X-ray characterisation of nanostructured materials

Oddershede, Jette

Publication date:
2008

Document Version
Publisher's PDF, also known as Version of record

Ph. D. Thesis by

Jette Oddershede

Department of Chemistry
Technical University of Denmark

December 2007

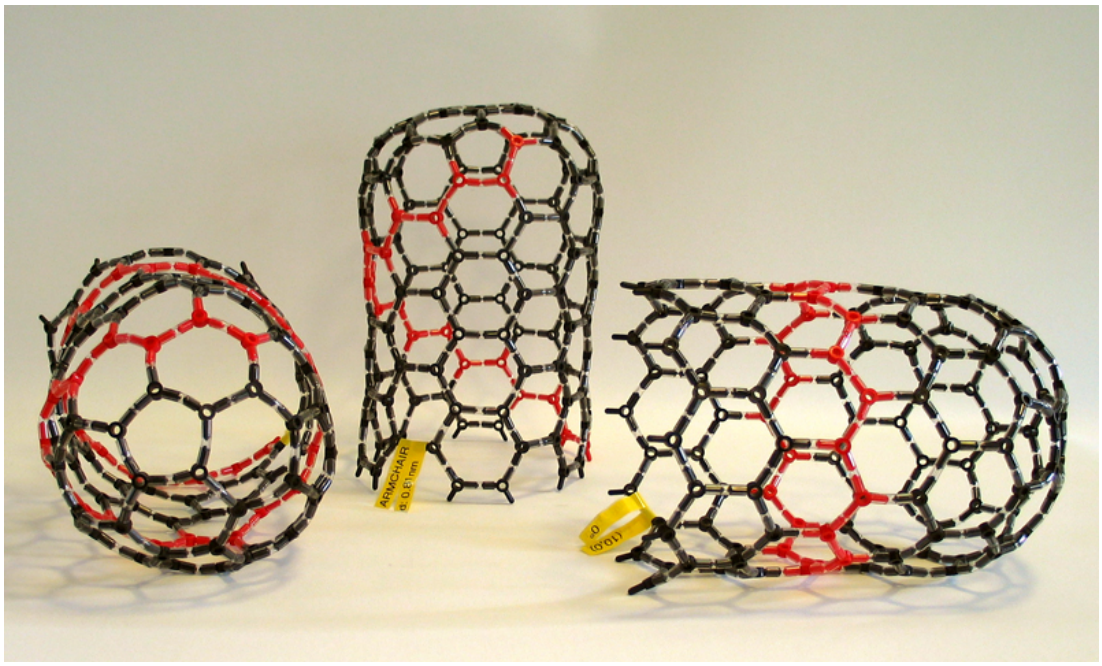

X-ray characterisation of nanostructured materials

Preface

The work presented in this Ph. D. thesis has been carried out at the Department of Chemistry, Technical University of Denmark from February 2003 to December 2007 under the supervision of Kenny Ståhl. It was funded by a grant from the Technical University of Denmark.

I would like to thank all of my collaborators who have contributed to the results of the present thesis: Kenny Ståhl for writing the Windows GUI to the Debye program, Anders Thygesen (Risø National Laboratory) for getting me involved in the cellulose project, Thomas L. Christiansen (Department of Manufacturing Engineering, Technical University of Denmark) for collaboration on expanded austenite, and Kurt Nielsen (Danish School of Conservation) for performing the PCA on the MWCNT simulated diffractograms.

I would also like to thank: Katarina Norén (I811, MAX-lab) for help on EXAFS, Flemming Grumsen (Department of Manufacturing Engineering) for recording TEM images, nano-lab.com and Claus Hviid Christensen (Department of Chemistry) for free MWCNT test samples, Susanne Helmark (Department of Chemistry) for photography work, Niels Thorup for proofreading, and the local workshop for designing a special sample holder.

My external research stay was at MAX-lab I811 during the commissioning in 2003–2004. In this connection I would like to thank the beamline manager, Stefan Carlson, for sharing his knowledge of how to build a beamline with me. I would also like to thank DANSCATT for funding my synchrotron trips.

Furthermore I would like to thank all of my past and present colleagues, especially my various "roommates" throughout the years, for making my time at the Department of Chemistry both pleasant and educational.

A special thanks goes to my supervisor, Kenny Ståhl, for help, encouragement and good spirits – even when I returned from my first maternity leave and told him that I was 3 months pregnant!

Finally I would like to thank my husband, Michael, and our sons, Frederik and Rasmus, for being my reason to hurry home every afternoon.

Jette Oddershede
December 2007

Publications

1. On the determination of crystallinity and cellulose content in plant fibres
   Thygesen, A., Oddershede, J., Lilholt, H., Thomsen, A. B. and Ståhl, K.
   Cellulose, (2005), 12(6): 563–576. (Appendix C.1)

2. Bulk characterization of multiwall carbon nanotubes
   Oddershede, J. and Ståhl, K.
   Z. Kristallogr., (2006) Suppl. 23: 325–330.(Appendix C.2)

3. Using X-ray diffraction and principal component analysis to determine structural properties for bulk samples of multiwall carbon nanotubes
   Oddershede, J., Nielsen, K. and Ståhl, K.
   Z. Kristallogr., (2007), 222(3–4): 186–192. (Appendix C.3)

4. Modelling the X-ray powder diffraction of nitrogen expanded austenite using the Debye formula
   Oddershede, J., Christiansen, T. L. and Ståhl, K.
   Submitted to J. Appl. Cryst. (Appendix C.4)

Presentations

1. Cellulose crystallinity in plant materials
   Thygesen, A., Oddershede, J., Lilholt, H, Thomsen, A. B. and Ståhl, K.
   Poster at DKM33, Pharmaceutical University of Denmark, 2003.

2. X-ray powder diffraction and pattern simulations of nanostructured materials
   Oddershede, J., Wess, T., Hiller, J. and Ståhl, K.
   Poster at ECM21, Durban, South Africa, 2003.

3. Diffraction from multiwall carbon nanotubes
   Oddershede, J. and Ståhl, K.
   Talk at DKM34, Risø National Laboratory, 2004.

4. Characterisation of bulk multiwall carbon nanotubes
   Oddershede, J., Nielsen, K. and Ståhl, K.
   Poster at EPDIC9, Prague, Czech Republic, 2004.

5. Modelling the X-ray powder diffraction of nitrogen expanded austenite
   Oddershede, J., Christiansen, T. L. and Ståhl, K.
   Poster at DKM37, University of Copenhagen, 2007.
   Poster at MAX-lab users meeting, 2007.

Summary

X-ray powder diffraction (XRPD) is an excellent tool for characterising the bulk structure of crystalline materials. Along with the growing interest in exploiting materials with decreasing particle sizes and increasing number of defects, factors that complicate the traditional interpretation of the experimental XRPD patterns, the need for new interpretation methods has arisen. The method described in the present thesis is by no means new, in fact it was developed by Debye in 1915. However, the Debye method it is rather computationally heavy, so in practise it is only applicable to the X-ray characterisation of nanostructured materials because of modern computers.

The Debye equation was implemented into a general GUI based program which is not custom-made to characterise a specific type of material as opposed to many earlier implementations. The Debye program is able to read a Crystallographic Information File (CIF), simulate the XRPD pattern given information about the nature of the sample and the experimental setup, and finally fit the simulated diffractogram to experimental XRPD data.

Three very different materials were studied using the Debye approach: 1) **Cellulose**, an organic polymer with a nanofibrous structure. The study was initiated based on the need for a reliable crystallinity determination from XRPD. It was shown that for future crystallinity determinations a new method based on Rietveld refinements should be preferred. If additional information about particle shape, size or size distribution is required, this can be obtained from Debye simulations. 2) **Nitrogen expanded austenite**, a highly defective material. Debye simulations confirmed that this material contains deformation stacking faults and that screw dislocations are abundant. A combined XRPD/EXAFS characterisation of nitrogen expanded austenite produced using a novel method showed that CrN formed even at temperatures below 450° where the mobility of Cr is very low. 3) **Carbon nanotubes**, a non-crystalline material with a periodic structure. It was shown that the mean bulk structural properties of the nanotubes can be obtained from XRPD using a combination of Debye simulations and parameterised Principal Component Analysis (PCA).

Røntgenkarakterisering af nanostrukturerede materialer

Man har traditionelt og med stor succes anvendt røntgendiffraktion til studiet af krystallinske materialer, men som partikelstørrelsen bliver mindre og interessen for at udnytte materialer med defekter større, bliver behovet for en god beskrivelse af disse effekters indvirkning på røntgendiffraktionseksperimentet stadig mere presserende. Metoden som er anvendt til fortolkning røntgendiffraktionsdata i indeværende afhandling blev oprindelig udviklet af Debye i 1915, men den er temmelig regnetung, så det er først med udviklingen af moderne computere at den er blevet praktisk anvendelig til karakterisering af nanostrukturerede materialer.

Debye's ligning er blevet implementeret i et generelt Debye-program. Programmet har en grafisk brugerflade og er i modsætning til mange af sine forgængere ikke er skræddersyet til en specifik materialetype. Debyeprogrammet kan læse en krystallografisk informationsfil (CIF), simulere diffraktogrammet ud fra information om de eksperimentelle forhold, partiklernes facon, størrelse og størrelsesfordeling, og endelig tilpasse det simulerede diffraktogram til eksperimentelle data.

Tre meget forskellige materialer er blevet studeret vha. Debye-metoden: 1) **Cellulose**, en molekylær krystal med en nanofibrøs struktur. Studiet blev initieret på baggrund af et behov for en troværdig krystallinitetsbestemmelse fra røntgendiffraktionsdata. Det blev vist at en ny metode baseret på Rietveldforfininger er at foretrække til fremtidige krystallinitetsbestemmelser, og at det er muligt at opnå yderligere information om partiklernes facon, størrelse og størrelsesfordeling fra Debye-simuleringer. 2) **Nitrogen-ekspanderet austenit**, et materiale med mange defekter. Debye-simuleringer har bekræftet at dette materiale indeholder deformationsstakningsfejl og at forekomsten af skruedislokationer er udbredt. Et kombineret EXAFS og røntgendiffraktionsstudie af nitrogen-ekspanderet austenit fremstillet på en ny måde viste at der blev dannet CrN selv ved temperaturer under 450°C hvor mobiliteten af Cr er meget lav. 3) **Kulstof nanorør**, et ikke-krystallinsk materiale med en periodisk struktur. Det blev vist at det er muligt at bestemme gennemsnitsstrukturen af nanorør i en prøve ud fra røntgendiffraktion vha. en kombination af Debye-simuleringer og parametriseret principal komponent analyse (PCA).

Contents

Abbreviations

BCC	Body Centered Cubic
BCT	Body Centered Tetragonal
CIF	Crystallographic Information File
DFA	Debye Function Analysis
EXAFS	Extended X-ray Absorption Fine Structure
FCC	Face Centered Cubic
FWHM	Full Width at Half Maximum
FT	Fourier Transform
GUI	Graphical User Interface
HRTEM	High Resolution Transmission Electron Microscopy
MSIC	Mixed Substitutional-Interstitial Cluster
MWCNT	MultiWall Carbon NanoTubes
PCA	Principal Component Analysis
PDF	Pair Distribution Function
RMS	Root Mean Square
SAXS	Small Angle X-ray Scattering
SWCNT	SingleWall Carbon NanoTubes
XANES	X-ray Absorption Near Edge Structure
XRPD	X-Ray Powder Diffraction
TEM	Transmission Electron Microscopy

Chapter 1

Introduction

Nanotechnology, nanoscience, nanomedicine, nanomaterials, nanostructures, nanodevices... The list is long and new items can be added every week, but it all boils down to the one same thing: The study and design of objects on the nanometer (10^{-9}m) length scale. Since the atomic radius is of the order 1Å (10^{-10}m), this is essentially on the atomic level. In connection with nanotechnology the terms top-down and bottom-up are frequently used. The top-down approach refers to the situation where the nanosized objects are constructed by breaking up larger entities, for instance with the motivation to improve the applicability of certain properties. It is not obvious whether the new nanoobjects will inherit the properties of their "parent" rendering them superior for the application. Taking on the bottom-up approach, the nanoobjects are built from smaller entities, in principle atom by atom. In reality the building blocks are somewhat larger, for instance surfactant molecules self-assembling into micelles. The nanosystems built in this way show properties without counterparts in the macroscopic world, and their nanoscopic size enables applications in places that have been inaccessible so far.

Irrespective of different motivations, interests and approaches to the field, every nanoscientist seeks to understand and characterise the very finest structural details of his or her specific nanoobject in order to explain, improve and exploit its properties. Many different characterisation techniques have been developed over the years, especially the different types of scanning probe microscopy as well as (High Resolution) Transmission Electron Microscopy ((HR)TEM) have proven most useful, not only for characterisation purposes but also to device design. These microscopy techniques are able to give detailed information on the structure of a limited number of nanoobjects, thus they are excellent local probes. As opposed to this, a number of more global probes exist: Extended X-ray Absorption Fine Structure (EXAFS), X-ray Absorption Near Edge Structure (XANES), Small Angle X-ray Scat-

tering (SAXS), and X-ray Powder Diffraction (XRPD) to mention some of the most important ones. Generally speaking these techniques give information on the average structure in a sample containing a large number of nanoparticles. The experiments still render information on the atomic arrangement (including defects), shape and size of the particles, but the interpretation is complicated by the inevitable presence of impurities and the fact that each structural parameter is distributed around the mean. The complementarity of the different characterisation techniques can be exploited to get a differentiated understanding of the material at hand.

This thesis will focus on the methods used to interpret XRPD patterns from nanostructured materials, the factors that complicate the interpretation and how to possibly improve interpretations in the future. Before going into this Chapter 2 is a short introduction to another X-ray based characterisation technique, namely EXAFS. Then Chapter 3 introduces the traditional methods for interpretation of XRPD data such as line profile analysis and Rietveld refinement, methods that roughly speaking treat the nanostructural details as perturbations of the infinitely periodic crystal structure. As opposed to this the Debye equation, and hence the possibility to calculate the diffraction from any collection of atoms, is introduced and a review of the relevant literature using this approach is presented. A description of how the Debye approach was implemented into the general Debye program is given in Chapter 4. Here some of the considerations made and problems encountered during the program design are described. In Chapter 5 the structure of cellulose is used as a test case for many of the basic features of the Debye program; crystallite shape, size, and size distribution. The study of cellulose was initiated based on the need for a reliable crystallinity determination from XRPD, and as a result two new methods based on Rietveld refinements and Debye simulations are suggested and evaluated. However, the real potential of the Debye method lies in the characterisation of defective and/or non-crystalline materials. Chapter 6 illustrates how Debye simulations can be used to characterise the structure of homogeneous and stress-free samples of nitrogen expanded austenite with large interstitial nitrogen occupancies, a material containing both deformation stacking faults and screw dislocations according to the simulations. In this chapter a combined XRPD/EXAFS characterisation of expanded austenite produced *via* a new synthesis route is also presented. As an example of the applicability towards non-crystalline materials with a periodic structure, Debye simulations for multiwall carbon nanotubes (MWCNTs) are presented in Chapter 7. Here a description of how parameterised Principal Component Analysis (PCA) can be used to keep track of how the various structural properties of the tubes affect the XRPD patterns is given. Finally Chapter 8 contains some concluding remarks.

Chapter 2

Principles of EXAFS

In the following the principles of X-ray absorption spectroscopy will be derived assuming the effects of diffraction to be negligible (Teo and Joy, 1981; Koningsberger and Prins, 1988; Jalilehvand, 2000). If a X-ray beam of intensity I_0 passes through a material of thickness x and linear absorption coefficient μ the intensity will be reduced to I by means of:

$$\ln(\frac{I_0}{I}) \ = \ \mu x \tag{2.1}$$

The value of μ depends on the concentration and the atomic number of the absorbing atom and on the energy of the X-ray beam. At certain energies the value of μ increases drastically. These energies correspond to the binding energies of the inner electrons (typically in the K- and L-shells) and are referred to as the atomic absorption edges. For iron the K-edge is situated at E=7.112keV. When scanning over the absorption edge of a particular atom the corresponding $\mu(E)$ function can be determined, and from this information about the chemical surroundings of the atom can be deduced. For energies above the absorption edge E_0 the electronic excitation caused by the X-ray absorption is coupled with the ejection of a photoelectron. This outgoing photoelectron will be backscattered by the surrounding atoms, and the interference between the outgoing and backscattered waves gives rise to the Extended X-ray Absorption Fine Structure (EXAFS). Single backscattering is the main reason for the EXAFS, but multiple scattering paths may also contribute.

The EXAFS function is defined as the modulation in the absorbance as a function of the energy, thus:

$$\chi(E) \ = \ \frac{\mu(E) - \mu_0(E)}{\mu_0(E)} \tag{2.2}$$

where $\mu(E)$ is the measured quantity and $\mu_0(E)$ is the atomic background absorption. $\mu_0(E)$ is obtained by spline fitting of the experimental data after these have been corrected for background effects, normalised, energy calibrated and converted to k-space. The choice of a good spline function is essential to the data analysis. In Figure 2.1 the Fe K-edge data of the as-nitrided sample described in detail in Section 6.2 is shown just before the k-space conversion, and in Figure 2.2 the $k^3\chi(k)$ which results after the spline fitting is given.

Figure 2.1 Fe K-edge absorption data for the as-nitrided sample described in Section 6.2 subjected to background subtraction and normalisation

---

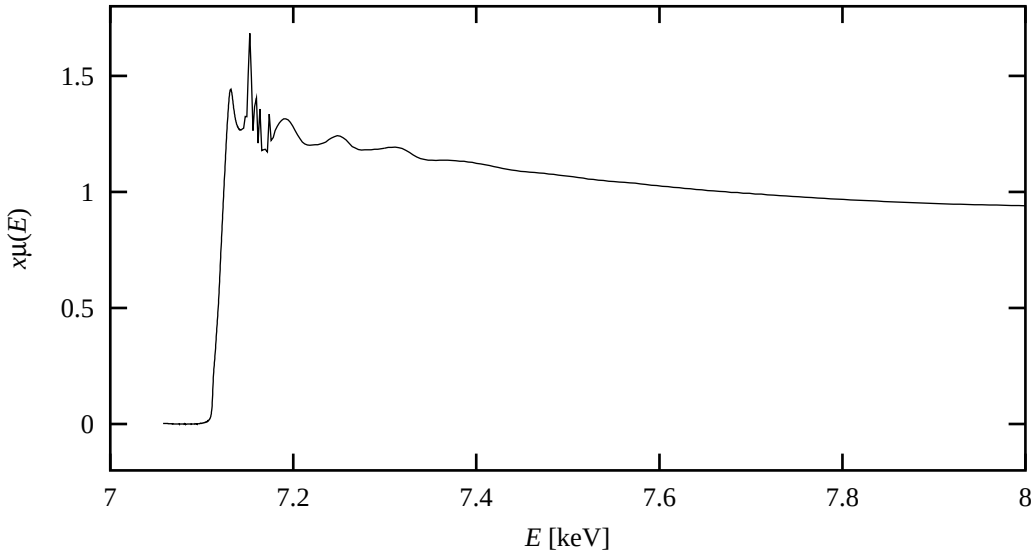

The EXAFS function of the central atom i can now be modelled in terms of the structure of the surrounding shells j responsible for the backscattering:

$$\chi_i(k) \;=\; \sum_j \; \frac{N_j S_0^2(k)}{k r_j^2} \; |f_j^{\text{eff}}(k)| \; e^{-2k^2\sigma_j^2} \; e^{-\frac{2r_j}{\Lambda(k)}} \; \sin(2kr_j + \phi_{ij}(k)) \qquad (2.3)$$

where N_j is the number of backscatterers in the j^{th} shell, r_j is the distance between the the central atom and the atoms in the j^{th} shell for single backscattering and half of the total path length for multiple scattering, $S_0^2(k)$ is the amplitude reduction factor, $f_j^{\text{eff}}(k)$ is the effective amplitude function for each path, σ_j^2 is the Debye-Waller parameter, $\Lambda(K)$ is the photoelectron

mean free path, and ϕ_{ij} is the phase shift due to the Coulomb potentials of atoms i and j.

A Fourier Transform of $k^3\chi(k)$ gives the pseudo radial distribution function which can be used to determine the values of r_j, see Figure 2.3. The k^3 weighting is frequently used to avoid information loss at high k-values because both $\chi_i(k)$ and $f_j^{\text{eff}}(k)$ goes as k^{-1}. Given the types and coordinates of all atoms within a certain distance of the central atom, the values of $f_j^{\text{eff}}(k)$, $\Lambda(K)$ and ϕ_{ij} for the possible scattering paths can be calculated *ab initio* by the FEFF7 program (Zabinsky et al., 1995). The WinXAS program (Ressler, 2004) can then be used to fit (2.3) to the experimental EXAFS by choosing the paths with the largest values of $|f_j^{\text{eff}}(k)|$ and refining the corresponding values of N_j, r_j and σ_j^2. The fitting can be performed in either k-space or R-space. The $S_0^2(k)$ factor arising mainly because of inelastic scattering events can also be refined, but it is proportional to N_j and correlates strongly with σ_j^2, so usually it is fixed to a value determined for a standard compound, or simply set to unity. Finally the energy scale offset ΔE_0, which of course correlates strongly with r_j, can be refined. As a measure of the quality of the fit the residual is often given:

$$R \;=\; \frac{\sum_i |y_i^{\text{exp}} - y_i^{\text{theo}}|}{\sum_i y_i^{\text{exp}}} \tag{2.4}$$

where y_i is either $\chi(k)$ or the FT, in which case the summation is over r.

Because of the limited amount of data only a limited number of paths and corresponding independent variables can be added and refined. Here the introduction of constraints into the refinement, for instance crystallographic symmetry between the different values of r_j, can be of help. The large correlations between the different parameters result in rather large standard deviations, for r_j this is at best 0.01Å while N_j is normally not refined because the determined values can only be trusted to within 25%. The Debye-Waller parameter contains contributions from both thermal vibrations and static disorder such that $\sigma^2 = \sigma^2_{\text{TV}} + \sigma^2_{\text{SD}}$.

The EXAFS data can be collected either in transmission or as fluorescence. In transmission the intensities I_0 and I of (2.1) are measured by absorption in two ion chambers placed before and after the sample respectively. The fluorescent signal corresponds to the K_α or L_α emission lines of the absorbing atom arising when the core hole in the inner shell is filled by an electron from a higher shell. The intensity of the fluorescence I_f can be measured, and the absorption μ is proportional to $\frac{I_f}{I_0}$.

Figure 2.2 The k^3-weighted EXAFS function indicating that only the data between k=4.2Å^{-1} and k=13.0Å^{-1} were used to produce the FT in Figure 2.3

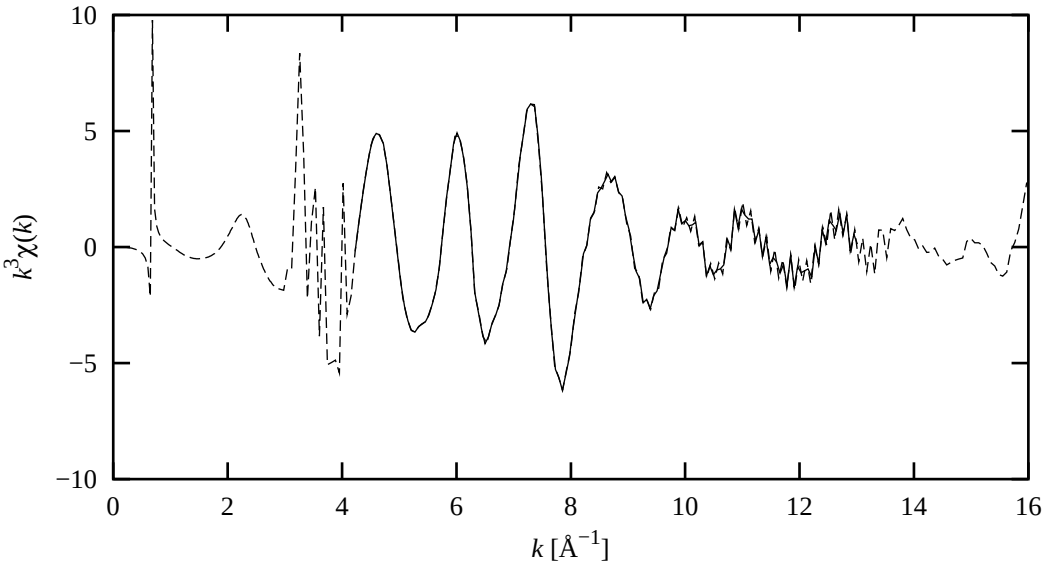

Figure 2.3 Fourier Transform of $k^3\chi(k)$ shown in Figure 2.2

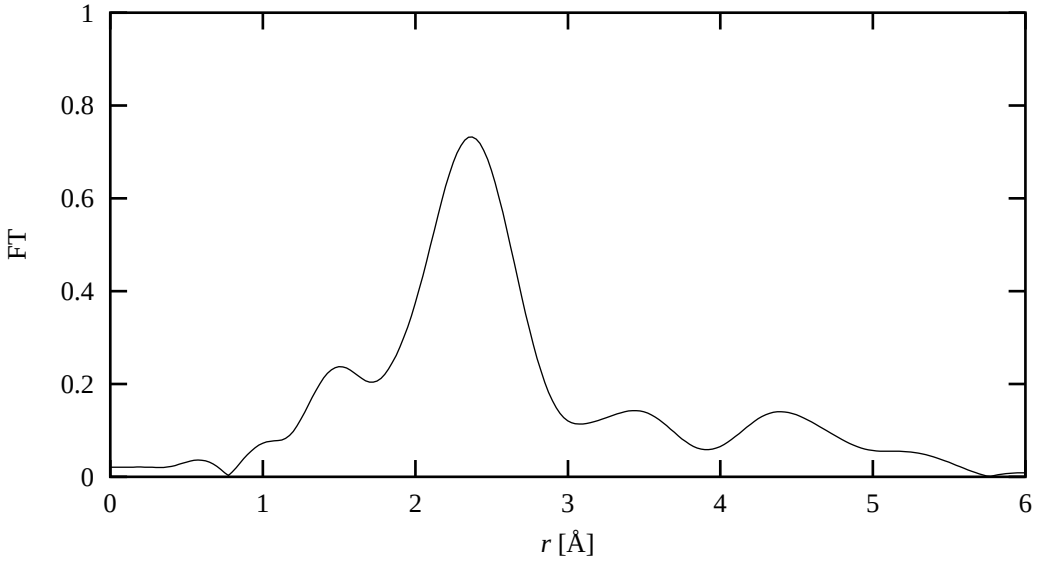

Chapter 3

X-ray powder diffraction from nanostructured materials

The Bragg intensity (I_{hkl}) measured for reflection hkl with scattering angle $2\theta_{hkl}$ in a XRPD experiment carried out on a crystalline sample is proportional to the Lorentz ($L_{\theta_{hkl}}$), polarisation ($P_{\theta_{hkl}}$) and reflection multiplicity (m_{hkl}) factors as well as to the square of the structure factor ($|F_{hkl}|^2$):

$$I_{hkl} \;=\; C\; L_{\theta_{hkl}}\; P_{\theta_{hkl}}\; m_{hkl}\; |F_{hkl}|^2 \tag{3.1}$$

where the structure factor F_{hkl} corresponding to the scattering from one unit cell is given by:

$$F_{hkl} \;=\; \sum_{j=1\ldots n} g_j\; f_j(\theta_{hkl})\; e^{-B_j\; \sin^2\theta_{hkl}/\lambda^2}\; e^{2\pi i(hx_j+ky_j+lz_j)} \tag{3.2}$$

Here the sum runs over the n atoms in the unit cell, g_j is the site occupancy, f_j the atomic scattering factor, and B_j the atomic temperature factor of the j^{th} atom (Bish and Post, 1989; Giacovazzo, 1992; Young, 1993; Langford and Louër, 1996).

The diffraction pattern calculated according to the above equations has zero background and the peaks have no width, a situation that is very far from that which can be observed experimentally. Background will always occur due to the presence of impurities, the experimental setup and peak overlap. A number of different factors, both related to the crystal structure and to factors such as the instrumentation and preferred orientation, contribute to the peak width. The shape and finite size of the crystals give rise to an order independent broadening, the size broadening, which also includes dislocation effects. Another type of broadening originating from the structure of the sample, the strain broadening, is order dependent and arises

because of variations in the d-spacing throughout the crystals. To conclude: the nanostructural details of the sample, both the infinitely ordered crystal structure and the nanoscale deviations from this, are reflected in the XRPD experiment, and the challenge is to extract the information.

3.1 Line profile analysis

Line profile analysis is the discipline of extracting information about the crystal structure from the line profiles of the experimental XRPD peaks. The experimentally determined peak profile is modelled as a convolution of structure related (due to particle size and strain) and instrument related peak broadening.

3.1.1 The Scherrer equation

The reciprocal relationship between the mean crystallite dimension (D_{hkl}) perpendicular to the $\{hkl\}$ planes and the particle size induced integral breadth of the corresponding diffraction peak (β^S_{hkl}) was first rationalised by Scherrer in 1918 and is today best known as the Scherrer equation (Scherrer, 1918):

$$\beta^S_{hkl} \;=\; \frac{K\,\lambda}{D_{hkl}\;\cos\theta_{hkl}} \tag{3.3}$$

where β^S_{hkl} is measured in radians on the 2θ-scale and can be obtained from the Full Width at Half Maximum (FWHM) of the diffraction peak, and K is the crystallite shape factor. K depends on the crystallite shape, but for all practical purposes K=1 can be applied (Klug and Alexander, 1974; Guinier, 1963; Warren, 1990). The Scherrer equation can be used to *estimate* the mean crystallite dimension D by averaging over a number of reflections, but it is not sufficiently accurate to determine the different dimensions of an anisotropically shaped crystal. Besides the approximation of K=1, this is mainly due to the fact that it is difficult to unambiguously determine β^S_{hkl} from the experimentally determined FWHM of the peaks without a model to describe the broadening arising from strain and instrumental effects.

3.1.2 Williamson-Hall plot

In 1944 Stokes and Wilson gave an expression for the strain (distortion) induced integral breadth (β^D_{hkl}) of reflection hkl (Stokes and Wilson, 1944):

$$\beta^D_{hkl} \;=\eta\;\tan\theta_{hkl} \tag{3.4}$$

where η is the apparent strain parameter. Assuming that the profiles are Lorentzian so that peak widths combine linearly, the total integral breadth arising from the crystal structure is given as:

$$\beta_{hkl} \; = \beta^S_{hkl} \; + \; \beta^D_{hkl} \tag{3.5}$$

Substituting (3.3) and (3.4) into (3.5) and rearranging under the assumption that K=1 and D_{hkl}=D for all hkl, one arrives at:

$$\beta_{hkl} \; \cos\theta_{hkl} \; = \; \frac{\lambda}{D} \; + \; \eta \; \sin\theta_{hkl} \tag{3.6}$$

A plot of the left-hand-side as a function of $\sin\theta_{hkl}$ for a number of reflections, known as a Williamson-Hall plot, offers the opportunity to estimate the crystallite size and strain from the intercept and slope of the best line through the points (Williamson and Hall, 1953). Again it can be no more than an *estimate* because of the assumptions made in the derivation of (3.6) concerning the Lorentzian peak shape and the isotropic crystallite size as well as the problems in deconvoluting the instrumental contributions from the FWHM of the experimental XRPD peaks.

3.1.3 Warren-Averbach analysis

The only information about the peak profiles utilised both in the Scherrer equation and in the Williamson-Hall plot is the integral breadths or FWHM of the peaks, hence these two methods are often referred to as integral breadth methods. However, much information about the crystal structure can be gained if the entire peak profiles are used. This philosophy is the basis of Fourier methods such as the Warren-Averbach analysis (Warren and Averbach, 1950; Warren and Averbach, 1952; Warren, 1990). Here the entire peak profile is expressed in terms of a Fourier series and the symmetric cosine terms (A_n) are then assumed to be the simple product of size (A^S_n) and strain (A^D_n) coefficients:

$$A_n(l) \; = \; A^S_n \; A^D_n(l) \tag{3.7}$$

Recall that only the strain broadening depends on the order l of the reflection. Rewriting (3.7) and introducing the expression for A^D_n assuming that n and l are small one arrives at:

$$\ln A_n(l) \; = \; \ln A^S_n \; - \; 2\pi^2 n^2 l^2 < e^2_n > \tag{3.8}$$

where $< e^2_n >$ is the mean-square strain. Thus a plot of $\ln A_n(l)$ versus l^2 offers the opportunity to estimate the crystallite size and strain from the intercept and slope of the best line through the points. The Warren-Averbach

method is more sensitive to peak overlap than the integral breadth methods because it is more difficult to obtain the entire peak profiles than simply the FWHM for overlapping peaks. Furthermore the number of applied reflections is usually limited since at least two and preferably more orders of the reflection need to be measured.

3.1.4 Recent progress in line profile analysis

Ungár and coworkers have modified both the Williamson-Hall plot and the Warren-Averbach analysis to the situation where the strain is caused by dislocations. The modification includes the introduction of new scaling factors, and results in the determination of the dislocation density (Ungar and Borbely, 1996). However, none of the above outlined methods used in classical line profile analysis can handle severely overlapping peaks. Furthermore, the methods all suffer from the fact that no actual information about the crystal structure except the hkl indices of the reflections is used in the interpretation. Methods of this type are often called pattern decomposition methods, as opposed to pattern modelling methods which aim at modelling all the peaks in the XRPD pattern based on physical parameters related to the structure of the sample. The most well-known pattern modelling method is no doubt the Rietveld approach which is discussed in the next section. Recently Scardi and Leoni have developed a whole powder pattern fitting/modelling approach and implemented it into the program PM2K. The approach is basically an extended Rietveld refinement procedure including a number of refinable physical parameters (*e.g.* domain shape, size and size distribution, lattice distortions, dislocations and faulting) that are not accounted for in the original Rietveld approach (Scardi and Leoni, 2002; Scardi and Leoni, 2003; Leoni et al., 2006). The method is rather computationally heavy and for a while it was only fully developed for FCC, BCC and HCP materials. However, recently a subroutine to handle dislocation effect for materials of any crystallographic symmetry was added (Leoni et al., 2007).

3.2 Rietveld refinement

Rietveld refinement is without comparison the most widely applied method to refine structural parameters from an experimental XRPD pattern. The formalism was devised by Rietveld in the 1960ies and states that the diffracted intensity at a the i^{th} step in 2θ can be calculated in the following way (Riet-

veld, 1967; Rietveld, 1969):

$$I(2\theta_i) \; = s \sum_{hkl} L_{\theta_{hkl}} \, P_{\theta_{hkl}} \, m_{hkl} \, |F_{hkl}|^2 \, PO_{hkl} \, \Phi(2\theta_i - 2\theta_{hkl}) \, + \, I_{bg}(2\theta_i) \quad (3.9)$$

Here s is the scale factor, PO_{hkl} is the preferred orientation function, $\Phi(2\theta_i - 2\theta_{hkl})$ is the reflection profile function, $I_{bg}(2\theta_i)$ is the background intensity at the i^{th} step and the remaining terms are defined as in (3.1) and (3.2). If the sample contains more than one phase, (3.9) can be extended to include a summation over the Bragg intensities originating from the different phases, and the relative contents of the phases can be calculated from the corresponding scale factors. Refinements are carried out by least squares minimisation of the residual:

$$S \; = \sum_i \; w_i \, (I_{\text{exp}}(2\theta_i) \; - \; I_{\text{calc}}(2\theta_i))^2 \quad (3.10)$$

where w_i is an experimentally determined weight, often $w_i = 1/I_{\text{exp}}(2\theta_i)$. Refinable parameters for each phase include: atomic coordinates, temperature factors and site occupancies for each atom in the unit cell, lattice parameters, a scale factor, a preferred orientation parameter, and a number of structure related profile parameters. The background function is a continuous function in 2θ, typically a polynomial, giving rise to several globally refinable parameters. Other globally refinable parameters include: a 2θ zero offset, the wavelength, and a number of peak profile parameters to describe instrumental broadening and peak asymmetry (Giacovazzo, 1992; Young, 1993; Langford and Louër, 1996).

Recalling that the peak profile must be modelled as a convolution of profile functions relating to different types of broadening it is not surprising that both Gaussian and Lorentzian forms and several different combination of these have been used to model the peak profiles (Young and Wiles, 1982). The Voigt peak profile function (Langford, 1978), which is the convolution of m Gaussian and n Lorentzian functions, offers the opportunity to interpret the refined profile parameters in terms of structure related physical quantities as outlined below. The reason for this is basically that the convolution of two Voigt functions is also Voigtian, thus the functional properties are conserved when the profiles relating to different types of peak broadening are combined. In reality the evaluation of the Voigt function is rather computationally heavy since it involves the complex error function, and the use of more easy-to-calculate functions such as the pseudo-Voigt (Wertheim et al., 1974) has proven useful despite the fact that the convolution of two pseudo-Voigt functions is no longer a pseudo-Voigt.

In 1958 Caglioti et al. suggested to model the instrumental peak broadening of an angle-dispersive neutron powder diffractometer as a Gaussian with a FWHM given according to (Caglioti et al., 1958):

$$\Gamma_G \;=\; \sqrt{U\tan^2\theta + V\tan\theta + W} \tag{3.11}$$

Because of its simplicity and fair performance, this expression (or variations of it) has since been adopted for the description of instrumental peak broadening in most Rietveld refinement programs, not only for neutrons and Gaussian peak profiles, but also for XRPD and a variety of different profile functions. Keeping with the derivations of section 3.1.2, it is often chosen to model the structure related peak broadening as a Lorentzian with a FWHM given as (Attfield and Cheetham, 1988):

$$\Gamma_L \;=\; \frac{X}{\cos\theta} \;+\; Y\;\tan\theta \tag{3.12}$$

Here X can be interpreted in terms of isotropic particle size and Y can be directly related to strain. The description of both size and strain according to (3.12) can be extended to the anisotropic case by replacing X with $X{+}X_e\cos\phi$ and Y with $Y{+}Y_e\cos\phi$, where ϕ is the angle between the scattering vector and the specified anisotropic direction, and the anisotropic size and strain coefficients are named X_e and Y_e, respectively (Larson and von Dreele, 2004).

The basis of the Rietveld approach is the structure factor giving the scattering from one unit cell, and the assumption that the entire crystal is built by a 3D repetition of a these where the total number of unit cells is so large that it can be considered infinite for all practical purposes. The diffraction effects arising from the finer nanostructural details such as finite crystal size and disorder are then handled via the introduction of analytical peak shape functions. The Rietveld approach offer the opportunity to apply a large number of different analytical peak shape functions and refine the corresponding parameters, however, not all of these can be directly related to either the structure or the experimental conditions, for instance the parameters U, V, and W of the Caglioti expression for the instrumental peak broadening (3.11) are merely empirical. The Rietveld interpretation of experimental XRPD data, where the nanostructural details of the sample are seen as a perturbation of the bulk crystal structure, is a typical top-down approach. It is not difficult to imagine a scenario where important information about the nanostructure of a highly disordered or even non-crystalline material could be gained from an XRPD experiment, and this is not possible by means of Rietveld refinement. For this purpose a bottom-up approach where

the structure is built atom by atom before the resulting XRPD pattern is calculated would be desirable, and such an approach does in fact exist.

3.3 The Debye equation

The desired bottom-up approach is by no means new, in fact the formalism which can be reached by averaging out the spatial dependence in (3.1) was presented by Debye in 1915. The statement, today known as the Debye formula/function/equation, is that the diffracted intensity from a powder sample (random spatial orientation) consisting of identical scattering objects (N scatterers each) can be calculated as a sum over all the interatomic distances (r_{ij}) without any assumption about crystallographic ordering (Debye, 1915):

$$I(Q) = \sum_{i,j=1...N} f_i(Q)\, f_j(Q)\, \frac{\sin(Qr_{ij})}{Qr_{ij}} \qquad \text{where } Q = 4\pi \sin\theta/\lambda \qquad (3.13)$$

So very simple and elegant, yet it is easily seen that the computational cost goes as the number of atoms squared.

The first application of the Debye formula to obtain information on particle size and structure was performed in 1941 (Germer and White, 1941) on spherical FCC Cu clusters of 13, 55 and 379 (only approximately) atoms and compared with ED experiments. In 1964 it was possible to explicitly calculate the diffraction from a 35Å cube of diamond (8000 atoms) with the aid of a computer (Tiensuu et al., 1964), and in 1993 the calculation of a spherical crystallite of SiC involving 10000 atoms was feasible (Bondars et al., 1993). Today a calculation for a box shaped crystallite of austenite including a particle size distribution (edge length between 10nm and 40nm and a maximum of $6.4{\cdot}10^6$ atoms, Table 4.2) can be done within a minute on a 2.8GHz/1GB RAM PC! With the computer power now at hand it is possible to perform the summation in (3.13) and obtain the diffractograms for structures large enough, complex enough and numerous enough to be of interest to the interpretation of experimental XRPD patterns, something that was not possible ten years ago.

3.3.1 Debye Function Analysis

The standard application of the Debye equation gives the diffraction pattern from a sample containing uniform particles with respect to structure, shape and size, but one TEM picture of any powder sample is enough to ascertain that a grain size distribution is always present in the real world.

An educated guess on the average particle size can be obtained by fitting a series of diffraction patterns simulated for different sizes to the experimental pattern, even if a combination of the different sizes would be a more correct description of the true sample.

In 1989 Hall and co-workers suggested the use of a new method called Debye Function Analysis (DFA) to describe the size and structure variations observed in experimental electron diffraction patterns of unsupported silver nanoparticles (Hall et al., 1989; Hall et al., 1991; Hall, 2000). The bulk structure of silver is FCC, but when the size is reduced to the nanoregime, icosahedral and decahedral multiply twinned particles are found along with the expected FCC cubeoctahedra, see Figure 3.1. The basic idea in DFA is to create a basis of simulated diffraction patterns for a range of different sizes and particle structures/shapes. The best fit to the experimental diffractogram is then sought as a linear combination (weights$\geq$0) of the basis functions, and the resulting weights are used to calculate the relative abundance of different particle types and the particle size distribution(s). It is important to emphasise that DFA gives the best fit to the distribution of interatomic distances in the sample *within* the chosen basis, thus it is not guarantied that the structure types used to set up the basis are actually present in the sample. In a recent review article (Hall, 2000) the discriminating powers of DFA were tested. A basis of seven different sizes of each of the three structure types shown in Figure 3.1 was used, and the "experimental data" were linear combinations of simulated diffraction patterns added a certain level of random noise, either simply the basis functions or patterns simulated after relaxing the basis structures with the aid of molecular dynamics. The results were good, especially with respect to estimating the mean diameter of the particles.

Figure 3.1 Ball models of multiply twinned particles: cubeoctahedron (A), decahedron (B), and icosahedron (C) (Mohr et al., 2003).

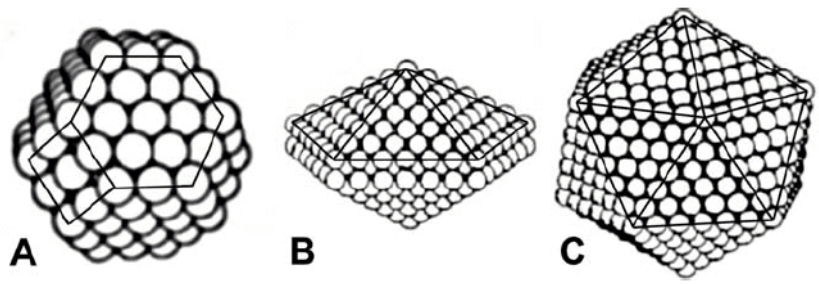

Vogel and co-workers have used DFA to obtain information about the active metal particles from *in situ* XRPD data of catalysts (Gnutzmann and Vogel, 1990; Vogel, 1998). The systems studied include: Pt/SiO_2 (Gnutzmann and Vogel, 1990; Hartmann et al., 1994), Au/alumina (Vogel et al., 1995), $Au/Mg(OH)_2$ (Vogel et al., 1996), $PtRu[N(Oct)_4Cl]_5$ and $PtRu[N(Oct)_4Cl]_5$/silica (Vogel et al., 1997), Pd/zeoliteY (Vogel et al., 1998b), Pd-$Pt[N(Oct)_4Cl]_5$ /C (Bönnemann et al., 1998a), Pt_3Sn[surfactant]/silica (Bönnemann et al., 1998b), Au/TiO_2 (Cunningham et al., 1999), and Pt-Ni/C (Yang et al., 2004).
Common to all of these is that the bulk metals/alloys display FCC structures, but like Ag the nanosized active particles present in the catalysts show multiple twinning. Knowing which active metal structure types and particle size distribution(s) are present in the catalysts and how these parameters change during reaction is important for the understanding of the catalytic activity and stability. It is by no means trivial to interpret XRPD data of supported and/or surfactant stabilised metal particles. When the catalyst loading is in the order of percent, the contribution from the support material and/or surfactants (which can be considered as background in this respect) constitutes by far the largest part of the diffraction pattern. However, if no epitaxial growth of the active nanoparticles onto the support is present, the experimental diffraction from the "free" metal particles can simply be obtained by subtracting the diffraction measured for the pure support material under the same experimental conditions (Gnutzmann and Vogel, 1990).

Despite the fact that DFA is rather sensitive to the choice of basis functions and background subtraction, the method offers important information on structure types and particle size distributions in nanostructured materials. It is therefore not surprising that a number of recent studies have employed DFA as a routine tool along with other techniques such as (HR)TEM, EXAFS and SAXS to study complex problems involving nanoparticles in the fields of catalysis and size-selective synthesis (Vogel et al., 1998a; Zanchet et al., 2000; Reetz et al., 2001; Mohr et al., 2003).

3.3.2 Applications of the Debye approach

The execution of the Debye equation (3.13) is greatly simplified if the system under study contains only one type of atoms. In the light of this it is hardly coincidental that the systems studied using DFA are all metals or at most binary alloys. This is also the case in other studies applying the Debye approach.

An extensive investigation of the nanostructure of SiC has been carried out by Palozs and coworkers. The studies include the effects of random layer stacking and surface reconstruction in small grains. The concept of an

apparent lattice parameter is introduced in order to account for the deviation from the bulk lattice parameter that are observed in Rietveld refinements on nanosized crystallites. Using simulated diffractograms as input for Rietveld refinements, the effects of crystallite size, surface relaxation and strain on the apparent lattice parameter are studied (Bondars et al., 1993; Pielaszek et al., 2002; Palosz et al., 2002; Palosz et al., 2003).

Cervellino, Giannini and Guagliardi have devised a whole pattern profile fitting procedure for mixtures of monatomic FCC-type materials (*c.f.* Figure 3.1) based on the Debye equation (Cervellino et al., 2003). Refinable are: background parameters (6^{th} order Young polynomial), a thermal parameter common to all structure types, and fractions, log-normal size distributions, and size related strain functions (uniform isotropic scaling of distances) for each structure type. The method was tested on simulated diffractograms added noise and applied to study thiol-capped Au-nanoparticles (Cervellino et al., 2004).

A similar fitting procedure has been developed by Kumpf and coworkers to study the structure of 1–5nm CdS, ZnS and ZnO nanoparticles by means of XRPD and Debye simulations. A reasonable starting set of parameters such as stacking fault probability, particle size and shape is first obtained by single particle modelling (Kumpf et al., 2005). From this parameter set 40 related sets are then created, and a diffractogram corresponding to each set is calculated by ensemble averaging over 50 single particles assuming that the parameters are distributed around the mean values given by the set in question. Finally an evolutionary algorithm is used to construct a new generation of 40 diffractograms, each being an ensemble average over 50 single particles, which fit the experimental data better than the previous generation, a step that can be repeated until convergence is reached (Kumpf, 2006).

A great advantage of the Debye approach as compared to Rietveld refinements is that the material under investigation need not be crystalline as long as it contains enough long range order to give rise to distinct diffraction peaks. Multiwalled carbon nanotubes are an excellent example of such a material, and the interpretation of the corresponding XRPD patterns with the aid of the Debye equation is thoroughly discussed in Chapter 7. Other samples of this type are layered structures such as: graphite (Andreev and Lundström, 1995; Yang and Frindt, 1996a; Andreev and Bruce, 2001), MoS_2 (Yang and Frindt, 1996a), or MnO_2/Li (Andreev and Bruce, 2001) with a turbostratic (random) stacking, and even single layers of MoS_2 or WS_2 (Yang and Frindt, 1996b).

Chapter 4

Implementation of the Debye equation

To facilitate the interpretation of the XRPD originating from any type of nanocrystalline material a simple, general and user-friendly implementation of the Debye equation was done. The idea was that the Debye program should focus on the effects of particle shape, size and size distribution and that it should be able to read and exploit the crystallographic information from a CIF. This of course limits the applications to crystalline samples containing neither strain nor defects, a rather idealised situation when considering nanostructured materials. On the other hand, it is important to have a firm grasp of the basic concepts before attacking more complicated matters. Therefore it was decided that the program should calculate the diffraction originating from crystals built up by a collection of entire and identical unit cells. The reason for this is obvious; by building the crystals in this way the 3D translational symmetry is unbroken and can thus be exploited during the execution of the program. Of course some crystals may offer the possibility to exploit an even higher symmetry, but as mentioned at the beginning it was intended to keep the program as simple and general as possible, and this also means using the *same* program for all compounds irrespective of space group.

The Debye program is written in Fortran and special attention has been made in order to ensure that the crystallographic parts of the program are correct. The choices made with respect to performance, CPU usage, input/output, *etc.* may not always be the most efficient ones, although the authors programming ability has improved significantly during the course of this work. The latest version of the Debye program can be downloaded from:
http://struktur.kemi.dtu.dk/kenny/powder_programs.html

4.1 Computational cost

One of the main issues in devising the Debye program – as for any computer program – is the computational cost. In order to understand the choices made for the present implementation, it is important to first review the different approaches taken by others.

4.1.1 Literature survey of Debye implementations

Recall the Debye equation as stated earlier:

$$I(Q) = \sum_{i,j=1...N} f_i(Q)\ f_j(Q)\ \frac{\sin(Qr_{ij})}{Qr_{ij}} \tag{4.1}$$

By introducing the distance multiplicity function, giving the multiplicity $m(r_{ij})$ for each interatomic distance, the Debye equation can be rewritten as:

$$I(s) = \sum_{m(r_{ij})\neq 0} m(r_{ij}) f_i(Q)\ f_j(Q)\ \frac{\sin(Qr_{ij})}{Qr_{ij}} \tag{4.2}$$

Now it is easily seen that the calculation of the diffracted intensity according to (4.2) is performed in two steps: 1) The setup of the distance multiplicity function, and 2) The summation over distinct distances for every value of Q needed to give a diffractogram of the desired accuracy.

Step 1) can actually be seen as two steps: 1a) The $N(N-1)/2$ distance calculations, a number which is less, the higher symmetry the system contains (Bondars et al., 1993; Grover and McKenzie, 2001), and 1b) The storage of the distinct distances and the corresponding multiplicities into an array. It should be noted that the distance multiplicity function is exact, however the performance of step 1b) will inevitably introduce round-off errors. Time spent to reduce the dimensionality of the array in step 1b) may very well be a good investment, since the computational cost in step 2) is proportional to the size of the array. One way to perform step 1b) is to choose a certain distance calculation accuracy (*e.g.* 0.01Å) and then round-off the actual distances according to this, a process often referred to as binning (Hall and Monot, 1991; Cervellino et al., 2006). An alternative and more accurate way to perform step 1b) is via Gaussian sampling (Cervellino et al., 2003; Cervellino et al., 2006), where a continuous atomic pair distance distribution is obtained after convolution of the distance multiplicity function with a Gaussian of a given width. The continuous pair distance distribution is then sampled on a grid with fixed step size to carry out the summation in step 2). An extensive

discussion on how to choose the width of the Gaussian and the size of the sampling step was published recently along with a method to estimate the error introduced in the calculated diffractogram depending on the choice of these parameters (Cervellino et al., 2006). A number of faster alternatives to the explicit summation in step 2) were also evaluated.

Another way to circumvent step 1) without explicitly calculating the $N(N-1)/2$ distances in step 1a) was described in a recent thesis (Kring, 2006). The approach is stochastic and the idea is to pick out nN atom pair at random ($n \ll N$) and assume that the corresponding interatomic distances are representative of the entire distance multiplicity function. Obviously this method performs much faster than the traditional route via step 1a), and tests have shown that it gives a fair estimate of the true diffraction pattern if Q is not too small.

Palosz and co-workers have devised a totally different calculation scheme to set up the pair correlation function which is their name for the distance multiplicity function (Marciniak et al., 1996; Pielaszek et al., 2002). The pair correlation function is calculated as the product of a radial distribution function and a shape distribution function. The radial distribution function describes the average electron density distribution around a reference atom as a function of the distance to this atom, while the shape distribution function gives the probability of finding a given interatomic distance within the crystal. Contrary to the calculation of the distance multiplicity function, which requires $N(N-1)/2$ operations, the calculation of the radial distribution function requires 2^3N operations only. (The term 2^3 arises because all positions of the reference atom must be considered.) The shape distribution function can only be given explicitly for spherical particles; expressions for other crystal shapes have to be calculated by means of Monte Carlo methods. Size and shape distributions can easily be included in the expression for the shape distribution function. The final addition, or rather integration since both the radial and shape distribution functions are continuous, is easily performed by Fast Fourier Transform.

4.1.2 The Debye program

In the present implementation the distance multiplicity function is a $10^6 \times 15$ array. The number of different atoms in the unit cell is limited to 5, giving a maximum of 15 different atom pairs. The number of different distances is limited to 10^6 and the multiplicities are stored using the binning principle, so the distance calculation accuracy is at most 10^{-6} times the maximum distance in the crystal. For nanoparticles with a diameter below 200nm this means a distance calculation accuracy no poorer than 0.002Å, and tests have shown that this does not introduce significant round-off errors.

The distance multiplicities are calculated and stored into the distance multiplicity array in the following way: For every possible vector $\mathbf{v}$ between two unit cells, the number of times this vector is found within the crystal is calculated. Only one of the vectors $\mathbf{v}$ and $-\mathbf{v}$ are considered, so unless $\mathbf{v}=\mathbf{0}$, the resulting multiplicity is doubled. The distances between all atom pairs situated in different unit cells separated by $\mathbf{v}$ are then calculated, and the atom pair types are determined. Finally the multiplicity is added into the corresponding positions of the distance multiplicity array. Assuming that the the crystal is built from entire and identical unit cells, the outlined procedure offers a significant reduction in the computational cost as compared to setting up an array of atomic coordinates and calculating all pairwise distances.

A distance multiplicity array built as described above is very easy to comprehend, but obviously it is not the best way to exploit the computers memory, considering that in most cases a large majority of the array simply contains the value 0. However, some tricks can be made in order not to read a larger part of it than necessary for the calculation of step 2). Once the array has been set up it is read once to determine the minimum and maximum distances, and for every distance in between these containing an entire row of 0's the entry in the first column is set to -1. Now when the addition in step 2) is performed by reading the distance multiplicity array for every value of Q, it is only done from the minimum to the maximum distance and rows starting with -1 are ignored.

The choice of exploiting the crystal symmetry to calculate the distance multiplicity function and storing this information into an array according to the binning principle before carrying out the explicit addition by means of (4.2) is in line with keeping it simple. For a majority of the compounds studied, the calculation time of step 2) is insignificant compared to the time spent in step 1), and if this is not the case then the entire calculation is extremely fast (*c.f.* Table 4.2), so it was deemed irrelevant to implement a faster and less comprehensible alternative.

4.2 Particle shape and size

Three different particle shapes are allowed by the Debye program: box, cylinder, and ellipsoid. When specifying which shape to use, the size must also be input. All three types are built from entire unit cells, rendering the curved crystallite surfaces in the case of cylinders and ellipsoids somewhat terraced. It should be noted that the cylinder axis and ellipsoid parameters must refer to the orthogonal coordinate system spanned by $\mathbf{a}^*$, $\mathbf{b}$ and $\mathbf{a}^* \times \mathbf{b}$. This untraditional choice of coordinate system was made to leave both the unique b-axis of the monoclinic cell setting and the unique c-axis of the hexagonal cell setting unchanged.

Box

The box shape is the simplest of the three. The particle consists of a repetition of $na \times nb \times nc$ unit cells along the a-, b- and c- axes respectively, so if either α, β or γ are different from 90°, the particle will be a parallelepiped instead of a box. The input values are na, nb and nc, so one must have an eye on the unit cell dimensions to get the desired particle size.

Cylinder

For a cylinder the direction of the cylinder axis as well as the length and radius must be given. A box of unit cells large enough to contain the cylinder is then constructed, and each cell is marked to determine whether or not it is part of the cylinder. This box of marked unit cells is then used when calculating the multiplicities as described in section 4.1.2.

Ellipsoid

The distance multiplicity calculations in the ellipsoid case runs in the same way as for the cylinder. The lengths of the ellipsoid axes along $\mathbf{a}^*$, $\mathbf{b}$ and $\mathbf{a}^* \times \mathbf{b}$ must be given, and it is noted that the special case of a sphere arises if these are set equal.

4.3 Particle size distribution

For the design of the Debye program it was chosen to go with a particle size distribution with a fixed aspect ratio, *i.e.* a fixed crystallite shape, assuming that the crystal growth starting from a given shape is proportional rather than linear. Having settled this, the problem of modelling a particle size distribution can be solved by explicit addition of powder patterns for a number of equally shaped crystallites of different size. This program feature applies to all particle shapes. Specifying the desired mass distribution function and an integer $m \in \{1, 2, \ldots, 9\}$, patterns for $2m{+}1$ crystals with dimensions of $1.0{-}0.1m$, $1.0{-}0.1(m{-}1)$,..., $1.0{+}0.1m$ times the input size (r_{in}) are added applying a set of weights corresponding to the distribution. The integer m thus defines how widely the mass distribution function should be sampled.

The mass distribution function can be either a uniform distribution (equal mass of all crystallite sizes), a Gaussian distribution (with the input dimension as mean and a spread of half the mean), a Weibull distribution or user-defined. The cumulative Weibull function has the form:

$$p(r) = 1 - \exp\left(-\left(\tfrac{r-\mu}{\alpha}\right)^{\gamma}\right) \tag{4.3}$$

where p is the probability, r is the crystallite dimension, μ is the location parameter, α is the scale parameter and γ is the shape parameter. This function was chosen because by setting $\mu = 0.05r_{in}$, $\alpha = 1.1r_{in}$ and $\gamma = 2.4$, a good fit to the mass distributions of the two NIST Standard Reference Materials (www.nist.gov/srm) Lanthanum Hexaboride (660a) and Silicon (640c) was achieved, see Figure 4.1. The mass distributions of these materials were determined by laser scattering, and the dimensions given in Figure 4.1 were divided by the particle size corresponding to p=0.5 (8.78μm for LaB_6 and 4.95μm for Si) to bring them on the same scale. The cumulative Weibull distribution with the specified parameters has a mean of $\mu{+}\alpha\,\Gamma(\frac{\gamma+1}{\gamma})$=$1.025r_{in}$, $p(0.1r_{in})$=0.0006 and $p(1.9r_{in})$=0.97.

From Figure 4.1 it seems that the very simple uniform distribution is not a very good approximation to the mass distribution observed in real powders, a Gaussian is considerably better but not as good as the Weibull distribution, especially for the fraction of low mass crystallites. If the particle size distribution is suspected to be very skew or displays several maxima, the program offers the possibility to design and test any such user-defined mass distribution function.

Figure 4.1 Cumulative crystallite mass percentages of NIST LaB_6 and Si shown along with the possible mass distribution functions of the Debye program. The value on the x-axis is the actual crystallite size r divided by the mean size r_{in}.

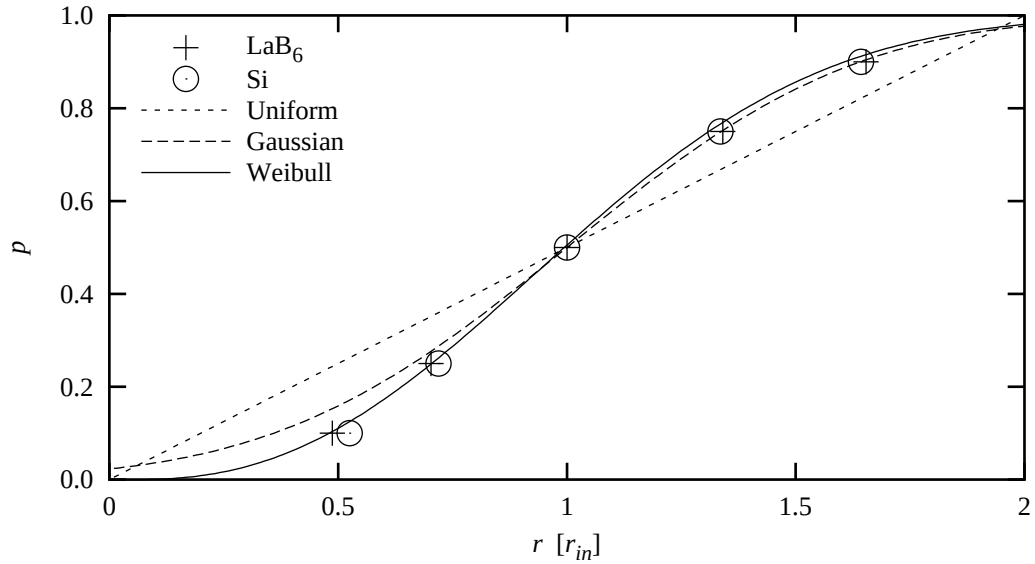

4.4 Benchmarks

The explicit addition of diffraction patterns to model a particle size distribution is obviously rather time consuming because the diffraction from a crystallite $1.0+0.1m$ times larger than the input size must be calculated. A benchmark study was set up to examine how the performance of the Debye program depends on the width of the particle size distribution. Two different materials that will be studied in more detail later, namely cellulose (Chapter 5) and austenite (Chapter 6), were chosen as model systems. As can be seen in Table 4.1 these two compounds have roughly the same density of atoms, so particles of similar volume contain the same number of atoms, and the calculation of the corresponding diffraction patterns by means of the Debye formula should in principle require comparable calculation times. However, because of the way the Debye program calculates the distance multiplicities this is certainly not the case. Diffractograms were simulated for box shaped, cylindrical and spherical particles with a size of 25–30nm as specified in Table 4.1 to test what the shape of the particles and the unit cell volume means for the calculation times of crystals with equal

amounts of atoms. 25–30nm is a fair size for many materials, so the calculation times of Table 4.2 may be taken as an indication of what to expect for other nanostructured materials.

First is should be noted that the calculation times given in Table 4.2 are split up so that the time it takes to calculates the distance multiplicity and the time it takes to do the actual summation of (4.2) are separated. The summation time is proportional to the following parameters: 1) The number of different atom pairs, 2) The maximum distance, 3) The distance calculation accuracy, and 4) The number of 2θ steps. 3) and 4) were kept equal for all simulations in the benchmark study. For cellulose the number of different atoms pairs is 6 while it is only 1 for austenite. However, it can be seen that for crystallites of the same shape and size, the summation times for cellulose are more like a factor of 10 times those of austenite. This is probably because cellulose is a molecular crystal with a continuous pair distribution, whereas austenite is a metal for which the pair distribution function is more discrete. The decrease in the maximum distance when going from a box shaped crystal over a cylinder to a sphere with equal volumes is reflected in the decreasing summation times. Finally the summation time goes as the maximum size $1.0+0.1m$ when applying a particle size distribution as expected.

The most interesting thing to be deduced from Table 4.2 is how the multiplicity calculation time depends on: 1) The sampling width of the particle size distribution, 2) The particle shape, and 3) The size of the unit cell. The calculation scheme applied to set up the distance multiplicity array for box shaped crystals where the limits of the crystal coincide with the surrounding box is very different from the cylinder and ellipsoid case where each unit cell in the surrounding box must be marked to determine whether or not it is part of the crystal. These differences are also reflected in how the different parameters influence the calculation times. From Table 4.2 it can be seen that for box shaped crystals the calculations performed for small unit cells containing a limited number of atoms (austenite) are much faster than those performed for large unit cell with many atoms (cellulose). The size dependence of the calculation time when applying a particle size distribution is $(1.0+0.1m)^5$ for crystals with small unit cells while it is $(1.0+0.1m)^3$ for larger unit cell materials.

For cylinders and ellipsoids it was immediately realized that the total number of unit cells needed to surround the shape of the crystal have a great impact on the time it takes to set up the distance multiplicity array, and therefore this number is also given for each calculation in Table 4.2. Here it seems that for cylinders and ellipsoids the multiplicity calculation time depends on the number of unit cells to a power of around 2.4. Considering that

Table 4.1 Structural data of the compounds used for the Debye benchmarks

	cellulose	austenite
space group	P 2_1	F -4 3 m
unit cell volume [Å^3]	658	40
atoms in unit cell	72	4
atomic density [Å^{-3}]	0.11	0.10
atom types	3	1
atoms in box with 25nm edge	$1.66{\cdot}10^6$	$1.56{\cdot}10^6$
atoms in cylinder of l=25nm and r=14nm	$1.68{\cdot}10^6$	$1.53{\cdot}10^6$
atoms in sphere with r=15.5nm	$1.66{\cdot}10^6$	$1.55{\cdot}10^6$
2θ steps	2501	2501
distance calculation accuracy [Å]	0.002	0.002

Table 4.2 Performance of the Debye program on a 2.8GHz/1GB RAM PC: multiplicity calculation time / intensity calculation time / number of unit cells in surrounding box

		cellulose	austenite	austenite[a]
shape	m	multi/sum/10^3uc	multi/sum/10^3uc	multi/sum/10^3uc
box	0	1min/189s/ 23	2s/ 13s/ 389	18s/ 18s/ 47
	3	2min/249s/ 51	8s/ 22s/ 857	41s/ 28s/104
	6	3min/307s/ 93	20s/ 31s/1602	79s/ 40s/195
	9	6min/365s/160	41s/ 43s/2686	128s/ 55s/314
cylinder	0	1min/171s/ 32	4h/ 11s/ 479	2min/ 17s/ 62
	3	3min/221s/ 66	27h/ 17s/1088	10min/ 25s/132
	6	10min/265s/122	/ /	36min/ 26s/249
	9	30min/282s/211	/ /	2h/ 32s/409
sphere	0	2min/133s/ 46	12h/ 8s/ 754	5min/ 14s/ 91
	3	6min/172s/101	63h/ 13s/1602	24min/ 13s/275
	6	19min/208s/186	/ /	2h/ 19s/389
	9	91min/234s/320	/ /	8h/ 23s/857

[a] Calculated for unit cells with an 8-fold volume

the number of unit cells goes as $(1.0+0.1m)^3$, this means that the calculation time when applying a particle size distribution to cylinders or ellipsoids goes roughly as $(1.0+0.1m)^7$.

In fact, because the austenite unit cell volume is so small, the number of unit cells needed to enclose a crystal with a diameter of 25–30nm is so large that the calculations applying a particle shape distribution take more than 24h. Therefore not all of these austenite calculations were performed. Instead the austenite unit cell was doubled in all 3 directions such that it contained 32 atoms rather than 4 atoms, hereby reducing the calculation times by a factor of around $8^{2.4}\sim150$. The improved calculation time is obtained at the expense of the crystal surface, which becomes slightly more terraced for the larger unit cells, but the difference is not detectable in the simulated diffraction patterns in the case of austenite.

It should be noted that every time 1 unit cell is needed to enclose a box shaped crystal, 1.3 unit cells are needed for the cylinder and 2.0 for the ellipsoid of similar volume, so if the box shape does not suffice, the cylinder should be tested before the ellipsoid to save calculation time. The benchmark study proves that in case of cylinders and ellipsoids it is worth considering a system with larger unit cells. Finally, before applying a particle size distribution, take a good look at Figure 4.1 and realize that a value of m=5 ($r\in[0.5r_{\text{in}};1.5r_{\text{in}}]$) or m=6 ($r\in[0.4r_{\text{in}};1.6r_{\text{in}}]$) covers most of the distribution. For the benchmark test cases there was virtually no difference in the diffractograms obtained for m=6 and m=9 besides the fact that the calculation time in the case of m=9 is more than doubled!

4.5 Instrumental corrections

This section is devoted to the corrections made by the program after the execution of the Debye equation (4.2). All of these are essentially convolutions of the intensity with a correction function, so the order in which they are performed is irrelevant. As explained in Appendix A the Lorentz factor is inherent to the Debye equation and therefore this correction need not be performed.

4.5.1 α_2 addition

When comparing with diffraction data measured with conventional X-rays using an experimental set-up where the α_2 contribution is not eliminated by the monochromator, the α_2 component should of course also be added in the simulations. This means that the α_1 and α_2 wavelengths and the popula-

tion of α_2 relative to α_1 must be given as input to the program. The most straightforward way to include the α_2 contribution would of be to perform the addition in (4.2) twice, once for each wavelength, and then add the resulting diffractograms using the input relative populations. However, this is rather time consuming, so instead (4.2) is only performed for the α_1 wavelength, and the α_2 contribution is then constructed from this. The result is a reduction in the number of steps to be performed for each value of 2θ from at most $15{\cdot}10^6$ (the number of entries in the distance multiplicity array) to around a handful (construct the α_2 contribution from the α_1 diffractogram, run a spline and resample to get the same step size).

4.5.2 Polarisation correction

If the Debye simulations are to be compared with experimental diffraction data collected using an unpolarised incident beam, that is conventional X-rays, the polarisation factor (Klug and Alexander, 1974):

$$P_\theta \;=\; \frac{1 \;+\; \cos^2 2\theta}{2} \tag{4.4}$$

must be used to correct the calculated intensities (*c.f.* (3.1)). This is chosen by turning on the polarisation correction in the Debye program. On the other hand, synchrotron radiation is linearly polarised in the plane of the ring, so if the diffraction experiment is carried out in the vertical plane, as is the case for the Huber G670 camera on beamline I711 at MAX-lab (Ståhl, 2000; Cerenius et al., 2000) where all synchrotron diffraction experiments described in the present thesis were performed, then P_θ=1 corresponding to no polarisation correction. If instead the experiment is performed in the horizontal plane of the synchrotron, then $P_\theta = \cos^2 2\theta$ (Als-Nielsen and McMorrow, 2000). This possibility is not currently implemented in the Debye program, so for experimental diffraction data of this type the polarisation correction must be performed on the raw data before comparing with simulations.

4.5.3 Instrumental broadening

A pseudo-Voigt instrumental peak broadening can be added in the Debye program. The pseudo-Voigt function is a linear combination of a Lorentzian and a Gaussian, $\eta L + (1-\eta)G$, where the mixing parameter $\eta \in [0,1]$ (Wertheim et al., 1974). The Lorentzian and the Gaussian share the same FWHM (Caglioti et al., 1958, *c.f.* (3.11)):

$$\Gamma \;=\; \sqrt{U\tan^2\theta + V\tan\theta + W} \tag{4.5}$$

while the mixing parameter is a polynomial in 2θ (Hill and Howard, 1985):

$$\eta \;=\; \eta_1 + \eta_2(2\theta) + \eta_3(2\theta)^2 \tag{4.6}$$

The six parameters: U, V, W, η_1, η_2, and η_3 can be input in the Debye program to describe the instrumental peak broadening. Every conventional X-ray diffractometer has its own instrumental peak profile that may change over time, and for synchrotron radiation the parameters must be determined anew at every visit (along with a wavelength calibration). This is done by measuring the diffraction from a standard reference material such as LaB_6 or Si with very accurately determined cell parameters (so the peak positions depend only on the wavelength and the 2θ zero off-set) and particle sizes of the order 1–10μm (which, according to the Scherrer equation (3.3), corresponds to a particle size broadening less than 0.02° in 2θ for λ=1.5Å and $2\theta \leq 120°$). Since the instrumental broadening is at least 0.08° in 2θ at low angles for state-of-the-art equipment at the same wavelength, it is reasonable to assume that the entire peak broadening of the standard reference material is instrumental in origin. Typical values of the instrumental parameters as determined from a Si standard for the Huber G670 camera on beamline I711 at MAX-lab in November 2005 (in connection with the collection of the expanded austenite data) are: U=0.023, V=−0.007, W=0.011, η_1=0.55, η_2=0.00, and η_3=0.00, which for λ=1.186Å corresponds to an instrumental peak broadening of 0.105° at 2θ=20° and 0.18° at 2θ=100° (the limits of the expanded austenite data).

4.5.4 Absorption correction

For comparison with diffraction data measured in transmission geometry on a sample mounted in a capillary of radius R it may be necessary to correct for absorption. This is done by interpolation in Table 5.3.5B of International Tables for X-ray Crystallography II (Kasper and Lonsdale, 1959) specifying the value of μR, where μ is the linear absorption coefficient of the material multiplied by some factor (typically around 0.5) to account for the packing inefficiency.

4.5.5 Guinier tangent angle correction

For the Guinier camera a correction term taking into account the variable sample to detector distance must be applied. The term takes on the form (Sas and de Wolff, 1966):

$$G_\theta \;=\; \frac{1}{\cos(2\theta - \psi)} \tag{4.7}$$

where ψ is the angle between between the specimen normal and crystal-reflected primary beam. The possibility to apply this correction is implemented into the Debye program for ψ=45°.

4.5.6 Auto-divergence slit

If the experimental diffraction pattern is measured with a Bragg-Brentano diffractometer equipped with an auto-diverge slit which keeps the illuminated length (A) of the sample fixed, then a correction term must be added to account for the variation in intensity due to the variable opening of the auto-divergence slit. The fixed illuminated length is given as (Philips Analytical X-ray Customer Support, 1992):

$$A \;=\; \frac{r\ \tan\delta_\theta}{\sin\theta} \tag{4.8}$$

where r is the goniometer radius and δ_θ is the divergence angle. Because the measured intensity must be proportional to δ_θ, the auto-divergence slit correction factor takes on the form:

$$\delta_\theta \;=\; \arctan(\frac{A\ \sin\theta}{r}) \tag{4.9}$$

This correction can be applied in the Debye program with A=12.5mm and r=173mm. For other values of A and r it is recommended that the experimental diffraction data are divided by δ_θ before they are compared with simulations.

4.6 GUI

To make the program as user-friendly as possible a Windows Graphical User Interface (GUI) was constructed. As stated in DebyeHelp.txt (Appendix B), which can be accessed *via* the GUI, the input instructions for the Debye program must be placed in an ascii file with the extension rec. The following will be a short introduction on how to get started with the program when a CIF containing the relevant crystallographic information exists. If this is not the case it is recommended to start from an existing rec file with the correct format and then perform the necessary corrections.

4.6.1 Simulations

Choose to start a new project from a CIF, give the name of the rec file to be created and the location where it should be placed along with the output files from the simulations and fitting. After browsing to the location of the CIF and selecting the correct file, the edit files menu appears (Figure 4.2). Here a project title and the format and name of the file containing the experimental XRPD pattern (optional, only required for fitting) can be given, and the names of the output files can be changed from the defaults given in DebyeHelp.txt. For the present demonstration of the program the experimental diffraction pattern of expanded austenite with an interstitial nitrogen occupancy of y_N=0.61 collected with a Guinier camera (capillary transmission) at MAX-lab was used along with the CIF of austenite (Häglund et al., 1993).

Figure 4.2 Project, edit files

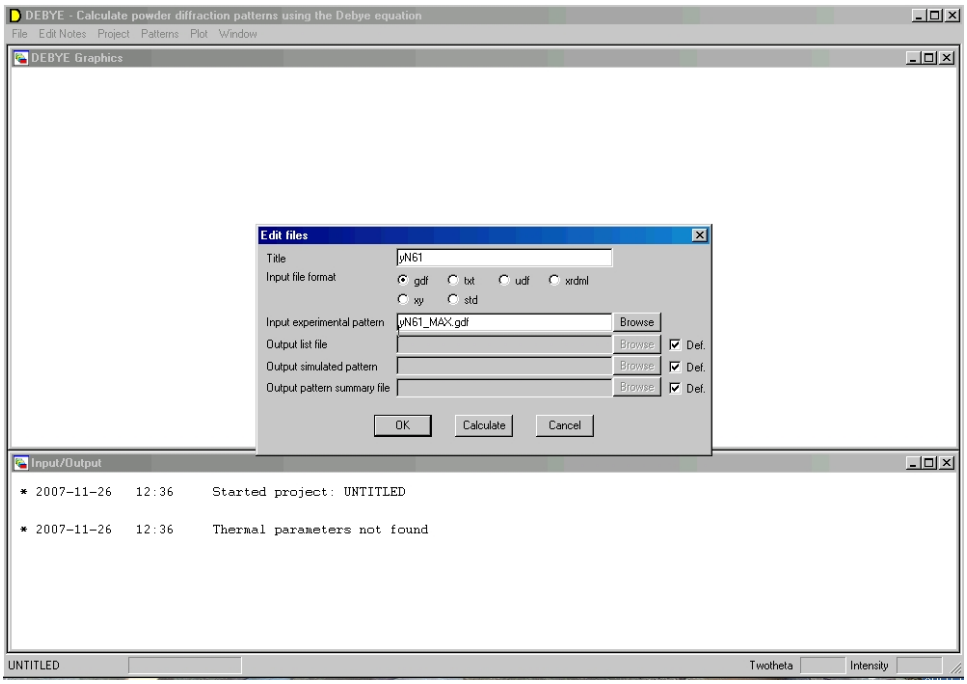

Then the edit structure menu containing the information obtained from the CIF appears (Figure 4.3). Because the imported CIF is for austenite, while the compound under study is expanded austenite, the lattice constant must be altered from 3.43Å to 4.0022Å. Furthermore the isotropic thermal parameter of the imported Fe atom must be changed to B_{Fe}=1Å^2, and the interstitial N atom with a site occupancy of g_{N}=0.61 and an isotropic thermal parameter of B_{N}=1Å^2 must be added. The thermal vibrations and site occupancies are included in the simulations by multiplying the atomic scattering factor $f_j(\theta)$ by $g_j\ e^{-B_j \sin^2\theta/\lambda^2}$ (*c.f.* (3.2)).

Figure 4.3 Project, edit structure

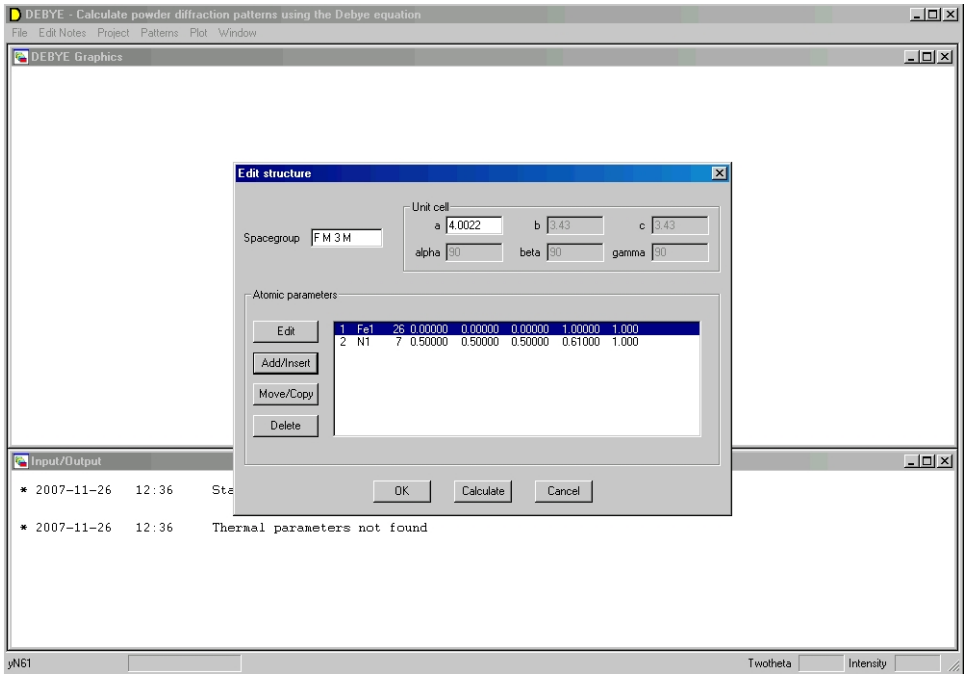

Finally the edit instructions menu (Figure 4.4), which is really the main menu of the Debye program, appears. Here all the important information for the specific simulation, both relating to the experimental conditions and to the nature of the sample, must be input. For the present example the experimental parameters described in Chapter 6 have been input: λ=1.186Å, 2θ limits, no polarisation correction (synchrotron data), Guinier geometry, absorption in cylindrical sample with μR=1.5, and instrumental peak profile parameters.

Figure 4.4 Project, edit instructions

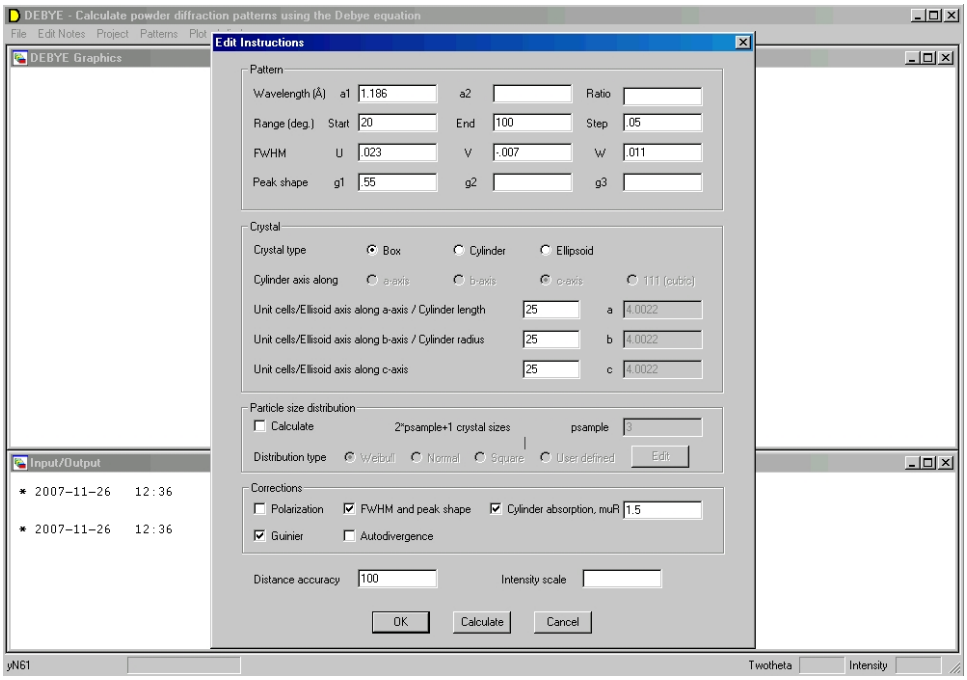

Based on the large differences in calculation times observed in the benchmark study the following general approach has been suggested to get a quick impression about the structure of a new material: 1) Always start by modelling the particles as box shaped to get an idea of the size and possible shape anisotropies, 2) Reduce the distance calculation accuracy and the number of 2θ steps to a minimum because the majority of the calculation time for the preliminary box simulations will be spent in the summation step, 3) If the box shape does not suffice, test the cylinder before the ellipsoid, 4) The Weibull mass distribution and m=3 (default values) serve as a good starting point for testing various particle size distributions, and 5) For the final simulation the distance calculation accuracy should be increased as much as possible and the 2θ step size should be set equal to the value of the experimental diffraction pattern used for comparison.

Finally a note on the intensity scale, I_{sca}, which is an integer. If $I_{\mathrm{sca}}<0$ the intensity output in the simulated xy file will be scaled so that $I_{\mathrm{max}}=-I_{\mathrm{sca}}$, if $I_{\mathrm{sca}}=0$ the intensity per unit cell will be output, and if $I_{\mathrm{sca}}>0$ the intensity per unit cell will be multiplied by I_{sca}. If a value of I_{sca} less than 1 is desired this can be achieved by reducing the site occupancy factors.

4.6.2 Fitting

After having set all the parameters for the simulation it is time to choose project, calculate (F3). The progress of the simulation can now be followed in the lower text window. Once the simulation is done the resulting XRPD pattern is shown in the upper graphical window. If an experimental pattern was imported, the simulated pattern is scaled to have the same maximum intensity (only for the view, not for the output xy file). Now choose pattern, fit pattern (F4) and a fit using the standard number of parameters: a scale factor, an overall temperature factor and 8 Chebyshev background parameters, is performed. Pressing F4 again leads to the fit patterns menu (Figure 4.5). Here it is possible to give the number of Chebyshev parameters to be refined (0–14) and indicated whether the scale factor, the overall temperature factor or both should be included in the refinements or simply set to some fixed value. It is also possible to change the value of the 2θ zero shift, but to avoid correlations it is not possible to refine this parameter. Every time a fit is performed, the graphical window is updated and the R-values and GooF are printed in the text window.

Figure 4.5 Patterns, fit pattern

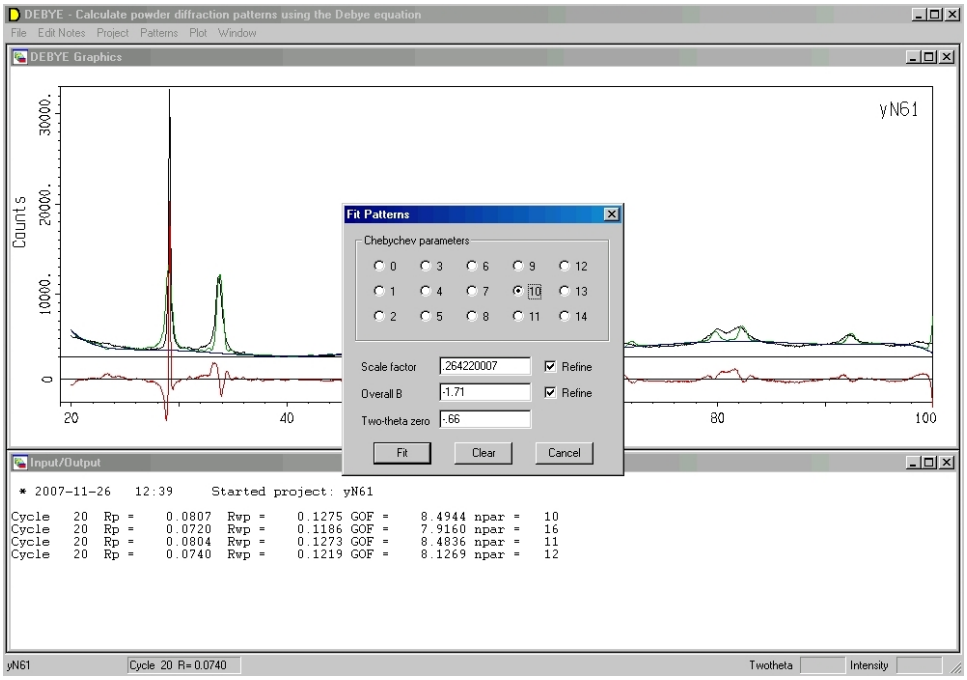

The example in Figure 4.5 is the fitting of the data simulated in Section 4.6.1 performed for: 8, 14, 9, and 10 Chebyshev background parameters. The 2θ zero shift was set to $-0.66°$ as determined for a Si-standard along with the other instrument parameters. The results of the simulations and fitting are written to a tabulated summary file which can be viewed by choosing patterns, table output. The tab file corresponding to the above example is given on page 35. From the R-values and the estimated standard deviations of the background parameters which are given in the tab file it can be concluded that 10 Chebyshev background parameters are sufficient. Furthermore, the refined value of the overall temperature factor strongly suggests that the input value of μR and/or the thermal parameters are too large. As will be shown in Chapter 6 the structure of expanded austenite contains deformation stacking faults that give rise to peak shifts, and screw dislocations which result in anisotropic peak broadening, so it is not surprising that the fit to a simulated pattern which does not take these effects into account is rather poor. However, taking into consideration that the preparation for a new project can be done within 10min and that the simulation itself only took 2s, a large amount of information about the structure can be gained within an hour by playing around with parameters such as: the site occupancy of nitrogen, the thermal parameters, the particles size, the size distributions, and the absorption correction.

It is also possible to determine the crystallinity, the fraction of intensity resulting from the simulated crystalline part of the sample, between any two values of 2θ and have this value output in the tab file. The crystallinity calculation feature is only valid if nothing but the amorphous scattering from the sample contributes to the background. The feature was developed for the cellulose study described in the next chapter, for the present example of expanded austenite it is irrelevant.

4.7 Upcoming features

The Debye program should be seen as a developing framework with the possibility to add new features in order to solve specific needs that appear during the study of real nanostructured materials. This section is devoted to some of the features that have been suggested and discussed as potential additions to the Debye program.

```
Wavelength(s)                    :   1.186000 A
Two-theta range                  :  20.000000 - 100.000000 deg.
    in steps of                  :                0.050000 deg.

Space group   :    F M 3 M

Unit cell     :   4.002200(.000000)  4.002200(.000000)  4.002200(.000000) A
                 90.00000(0.00000)  90.00000(0.00000)  90.00000(0.00000) deg.
   Volume     :                     64.106(  0.000) A**3



*10**4      x/a            y/b            z/c            SOF        B(A**2)

Fe1           0              0              0          1.000         1.0
N1         5000           5000           5000          0.610         1.0

Crystallite type: Box

  25 by    25 by    25 unit cells

Distance accuracy:    0.100E-01

No particle size distribution
Guinier correction performed
Absorption correction performed. MuR:   1.500
Peak function added:

Halfwidth parameters        :    0.02300  -0.00700   0.01100
Lorentzian parametrs        :    0.55000   0.00000   0.00000

Rp =  0.07   Rwp =  0.12   GOF =   8.13   12 parameters,  1601 observations


Parameter file                   : yN61.rec
Raw data file                    : yN61_MAX.gdf

Scale factor                     :  0.26422000(0.00720570)
Overall temp. fact. coeff.       : -1.7090( 0.2020) A**2

Two-theta zero :  -0.6600

Background parameters (Chebyshev type i) :

  -4095(   20)     -16(   35)    -347(   31)     706(   30)    -123(   29)
    250(   28)     -50(   26)      88(   26)     -50(   22)     263(   22)
```

As of present, the routines for modelling stacking faults and screw dislocations in FCC nitrogen expanded austenite described in Chapter 6 are only found in a modified non-GUI version of the Debye program. The intention is that these should be generalised and made applicable to other materials, but so far no steps have been made in this direction.

The possibility to choose the cylinder axis along the cubic [111] direction would be of interest to many materials. Based on the performance tests in Section 4.4 it has been proposed to let the program work internally with a hexagonal cell with the cubic [111] along the hexagonal [001] and a cell volume 3 times that of the cubic cell.

For the mass distribution functions shown in Figure 4.1 it has already been argued that the probability density below r=0.5r_{in} and above r=1.5r_{in} is very low. Therefore it has been suggested that it should be possible to work with user-defined particle sizes and an unequal amount of sampling steps on either side of the mean, as opposed to the current system where the sampling width of the mass distribution function is defined by the integer m and the corresponding sizes are given as $1.0-0.1m$, $1.0-0.1(m-1)$,..., $1.0+0.1m$. This would offer the opportunity to sample crystallite sizes for equal steps in p, *e.g.* $p(r_1)$=0.05, $p(r_2)$=0.10, $p(r_3)$=0.15, *etc.*... The structure of the program has already been prepared for this feature, but some details like whether the standard mass distribution functions should refer to equal steps in r (old) or in p (new) and whether more standard mass distribution functions should be implemented are still to be decided upon.

A correction for axial divergence, which is observed as a low angle peak asymmetry for some experimental XRPD patterns, is another possible feature that has been discussed. Different empirical convolution functions have been suggested (Finger et al., 1994), but it would be desirable if the applied function can be traced back to the geometry of the diffractometer.

Preferred orientation is one of the most problematic effects in the experimental XRPD patterns which is not taken into account in any way in the Debye program, in fact the derivation of the Debye equation assumes that no preferred orientation is present. Since the diffraction patterns simulated using the Debye formula contain no information about the indices or positions of the diffraction peaks, a subsequent correction for preferred orientation cannot be performed. The only possible way to perform a correction for preferred orientation is thus to derive a new variant of the Debye formula which includes the effects of preferred orientation, but the fact that no reports about any such attempt can be found in the literature strongly suggests that if the task is possible, it is difficult and it does not result in a simple expression such as the Debye formula.

Chapter 5

Cellulose — determining the crystallinity of a nanocrystalline material

The crystallinity of a plant fibre sample is defined as the mass fraction of crystalline cellulose in the dry matter. This measure is important for industrial applications of the plant fibres, for instance in the production of paper, pulp, strong composite materials or bioethanol. In the paper and pulp industry the crystallinity is closely monitored; a low crystallinity is desirable to avoid paper stiffness, because whereas the crystalline regions of cellulose are ordered and rigid the amorphous regions are random and flexible (van der Reyden, 1992). A fast and reliable measure of the crystallinity at the different stages of the composite fibre processing is vital because of the expected correlation between the cellulose crystallinity and the tensile strength of the fibres. During the production of bioethanol the cellulose in the plant fibres is enzymatically hydrolysed into monosaccharides, but different enzymes are used for crystalline and amorphous cellulose, so in order to tailor the best enzymatic mixture the crystallinity must be known.

XRPD has been used for crystallinity determinations for many years (Segal et al., 1959; Ruland, 1961; Vonk, 1973). Since cellulose is the only crystalline component in plant fibres, the problem of determining the crystallinity boils down to separating the amorphous and crystalline components of the XRPD patterns. This is, however, rather challenging for several reasons: 1) Compton and air scattering add to the amorphous background resulting in an underestimation of the crystallinity, so a good data collection strategy minimising these effects is needed, 2) Cellulose is a fibrous material, and the crystallites are needles along the fibre axis, so preferred orientation is unavoidable, and 3) The crystallites are nanosized, typically below 50Å in

diameter, so the diffraction peaks are severely broadened and overlap.

Traditional methods for crystallinity determinations in plant fibres such as the peak height ratio method (Segal et al., 1959) and the amorphous standard method (Ruland, 1961; Vonk, 1973) are straightforward and fast to use, but they tend to underestimate the crystallinity because they assume that the amorphous scattering curve touches the total diffractogram at one or more scattering angles. This assumption is wrong; the methods fail to account for the severe peak broadening and overlap that arises because of the small crystallite size and results in an amorphous scattering curve that lies below the total diffractogram at all scattering angles, *c.f.* Figure 5.3.

The crystalline component in higher plants is that of cellulose Iβ, and with the recent publication of the cellulose Iβ crystal structure (Nishiyama et al., 2002, see Table 5.1) it has become possible to use Rietveld refinements or Debye simulations for the crystallinity determinations. The application of these methods with the aim to determine the crystallinity in plant fibres has not been seen before and will therefore be the focus of the present chapter. In connection with this some comments on specific crystallographic challenges encountered during both the acquisition and the analysis of the diffraction data are in order. The study of cellulose crystallinity in plant fibre samples came about as a collaboration with scientists from Risø National Laboratory, and the entire publication which resulted from the project is attached in Appendix C.1 (Thygesen et al., 2005).

Table 5.1 Crystallographic data of cellulose Iβ (Nishiyama et al., 2002)

chemical formula	$C_{12}H_{20}O_{10}$
cell setting, space group	monoclinic, $P2_1$ (c unique)
a [Å]	7.784(8)
b [Å]	8.201(8)
c [Å]	10.380(10)
γ [°]	96.5
V [Å^3]	658.3(11)
Z	2

Figure 5.1 Data collection geometries, filter paper

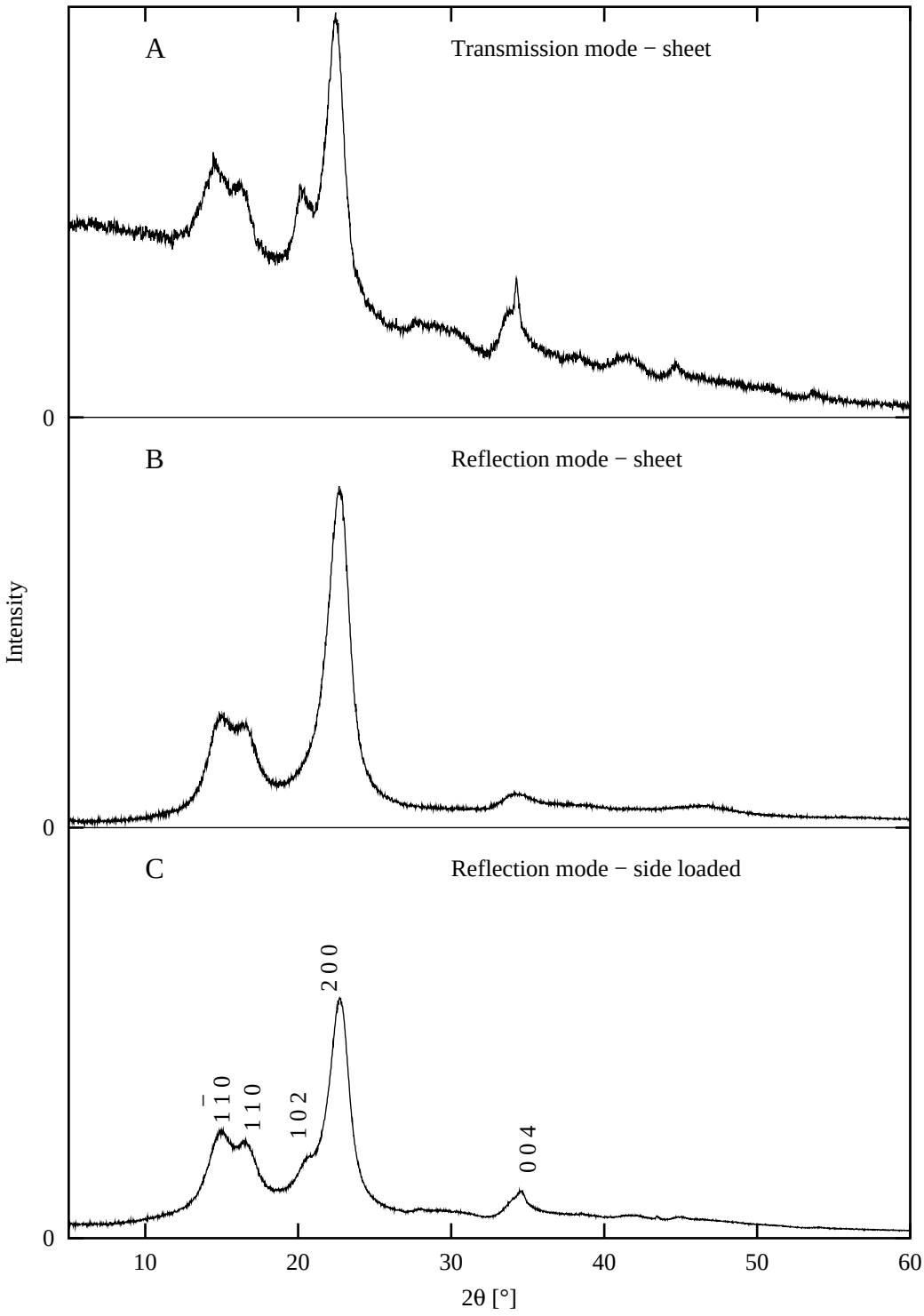
A
Transmission mode − sheet
0
B
Reflection mode − sheet
0
C
Reflection mode − side loaded
0
Intensity
1 1 0
1 1 0
1 0 2
2 0 0
0 0 4
10
20
30
40
50
60
2θ [°]

5.1 Data collection, sample preparation and preferred orientation

To determine the best experimental set-up for the crystallinity determinations, XRPD data of filter paper sheets (Frisenette ApS 165-70) were collected in both transmission (Huber G670 Guinier camera, CuKα_1 radiation, 2θ=1.4–100°, 0.005° step size, 30h) and reflection mode (Philips PW1820/3711 Bragg-Brentano geometry, auto-divergence slit, CuKα radiation, 2θ=5–60°, 0.02° step size, 15h), see Figure 5.1. Even though the measuring time of the transmission data is twice that of the reflection data, the signal-to-noise ratio is much poorer. Furthermore, it is impossible to separate the amorphous sample diffraction from the large air scattering component if the diffraction data are collected in transmission geometry, thus diffraction data for determining the crystallinity in plant fibres must be measured in reflection geometry.

As already mentioned the cellulose crystallites are needles, and in Bragg-Brentano geometry crystals of this shape tend to align with the preferred orientation vector (the growth direction) in the sample plane perpendicular to the scattering vector. Cellulose Iβ crystallises in space group $P2_1$ with the growth direction along the unique c-axis, so the $00l$ peaks will be severely suppressed compared to the $hk0$ peaks in reflection geometry, see Figure 5.1B.

To obtain a more random orientation of the cellulose crystallites a sample preparation procedure where the plant fibres were side loaded into a custom-made sample holder was devised. The sample holder shown in Figure 5.2 is made of 38mm×38mm×4mm stainless steel with a 20mm×15mm×2mm embrasure for the sample. The lid is made of 5mm plexiglas and can be mounted with 4 screws so that it can stand the pressure needed to prepare the sample while still enabling a visual inspection of the packing progress. Prior to packing the plant fibres were run through a knife mill with a 0.5mm sieve and wetted with distilled water. The fibre slurry was then pressed sideways into the sample holder using the piston, and excess water was removed through the oppositely situated drains. The pressed samples were allowed to air dry overnight before the diffractograms were recorded. The result of the new sample preparation procedure was a significant reduction but not a complete removal of the preferred orientation effects, see the diffractogram in Figure 5.1C.

In Rietveld refinements it is possible to correct for preferred orientation effects (*c.f.* (3.9)). One of the models most widely used is the March-Dollase preferred orientation function (March, 1932; Dollase, 1986):

$$PO_{hkl} = (r^2 \cos^2 \alpha + r^{-1} \sin^2 \alpha)^{-3/2} \tag{5.1}$$

Figure 5.2 Bragg-Brentano sample holder for side loading plant fibre samples to minimise preferred orientation effects

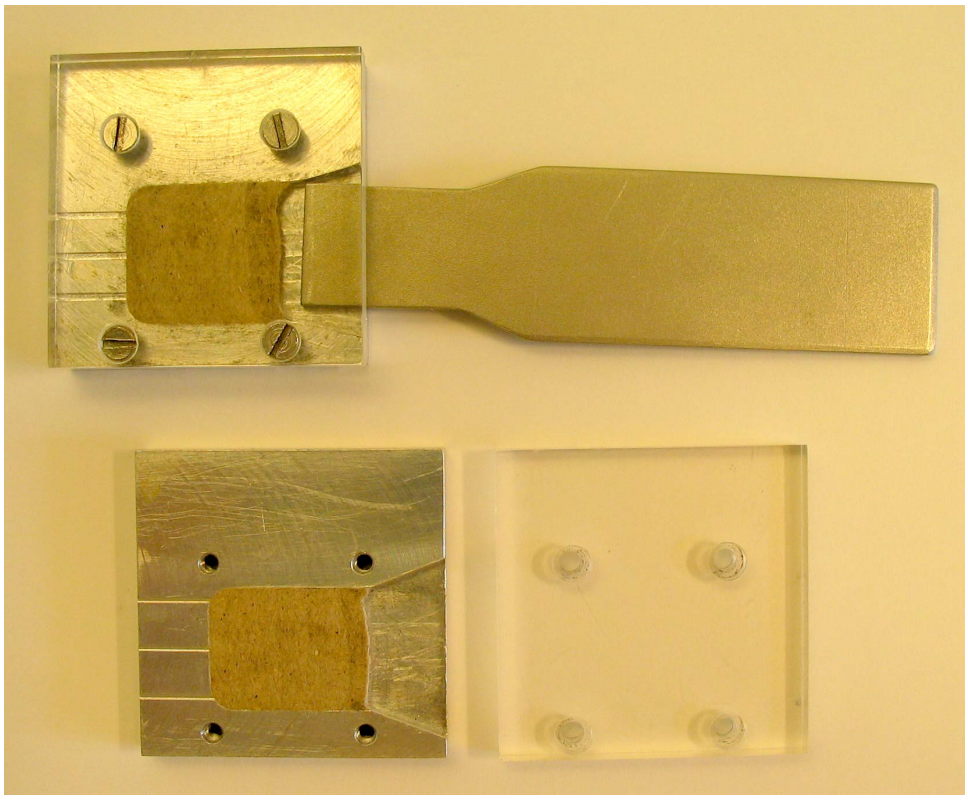

where α is the angle between the scattering vector and the preferred orientation vector, and r is the preferred orientation parameter. r=1 corresponds to no preferred orientation. To account for the experimentally observed peak intensities in the case of Bragg-Brentano diffraction from cellulose needles, reflections where $\sin^2 \alpha$ dominates over $\cos^2 \alpha$ should be given relatively more weight. This is done by increasing r.

A Debye simulation, however, assumes no preferred orientation since the derivation of the Debye equation includes an average over all orientations in space, thus it is not possible to quantify the extent of preferred orientation or obtain a perfect fit to the experimental diffraction data using the Debye approach.

5.2 Crystallinity determinations

The strategy for both the Rietveld refinements and the Debye approach is to obtain as good a fit to the crystalline part of the diffractograms as possible with the parameters at hand and then model the amorphous part – the background – as a Chebyshev polynomial of a given order. The crystallinity is then obtained as:

$$x_{\mathrm{CR}} = \int_{s_0}^{s_p} I_{\mathrm{CR}}(s) \cdot s^2 ds / \int_{s_0}^{s_p} I(s) \cdot s^2 ds \tag{5.2}$$

where $s=\frac{2\sin\theta}{\lambda}$ and the integration limits were chosen to include only the parts of the diffractograms containing visible crystalline intensity; s_0=0.11Å^{-1} (2θ=10°), and s_p=0.99Å^{-1} (2θ=50°).

Before giving detailed records of the two new methods for crystallinity determinations in samples containing cellulose – Rietveld refinements and Debye simulations – a more thorough description of the traditional methods and their pitfalls is in order. In Figure 5.3 the performance of all four methods is illustrated for a hemp sample and the resulting crystallinities are given. These should be compared to the fraction of cellulose in the samples; 0.63(3)g cellulose per g dry matter as determined by the method of strong acid hydrolysis (Kaar et al., 1991; Thygesen et al., 2005).

5.2.1 Peak height ratio

The mass fraction of crystalline cellulose in dry matter has frequently been determined by means of (5.3) using the height of the 200 peak (I_{200}, 2θ≈22.7°) and the minimum between the 200 and 110 peaks (I_{AM}, 2θ≈18°), see Figure 5.3A.

$$x_{\mathrm{CR}} = \frac{I_{200} - I_{\mathrm{AM}}}{I_{200}} \tag{5.3}$$

I_{200} represents both crystalline and amorphous material while I_{AM} represents amorphous material only. The expression requires that the amorphous material diffracts with the same intensity at 2θ≈18° and 2θ≈22.7°, and that the crystalline cellulose does not contribute to the intensity at 2θ≈18° (Segal et al., 1959).

Figure 5.3 Hemp crystallinity determinations

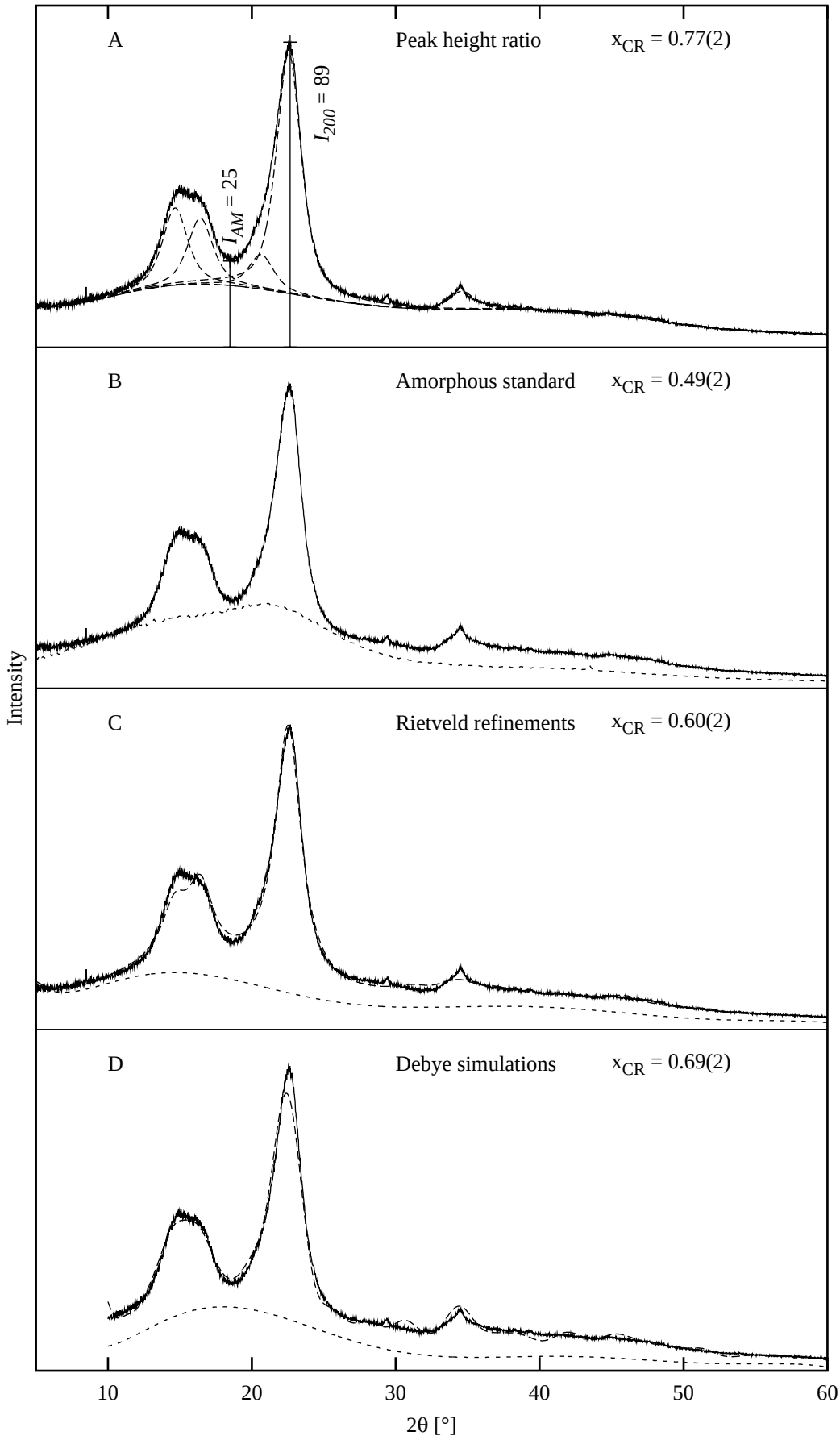
A
Peak height ratio
x_{CR} = 0.77(2)
I_{200} = 89
I_{AM} = 25
B
Amorphous standard
x_{CR} = 0.49(2)
C
Rietveld refinements
x_{CR} = 0.60(2)
D
Debye simulations
x_{CR} = 0.69(2)
Intensity
10
20
30
40
50
60
2θ [°]

The low computational cost of the peak height ratio method is probably the reason for its extensive use up to this day (Alexander, 1969; Buschle-Diller and Zeronian, 1992; Mwaikambo and Ansell, 1999; De Souza et al., 2002). However, because of the small crystallite sizes, the tails of the diffraction peaks extend far from the peak positions as illustrated in Figure 5.3A. Thus the actual background level is well below the diffraction curve of the partly crystalline cellulose sample, especially around $2\theta \approx 18^\circ$, so I_{AM} is overestimated. The same goes for I_{200} because of preferred orientation effects. There is also the effect that both the apparent cell parameters and the crystallite sizes vary considerably from species to species. This results in large variations in the I_{AM} levels, making the peak height ratio method very unreliable when comparing crystallinities, especially if the plant fibre samples have different origins. None of these points were mentioned in the original work (Segal et al., 1959), where the method was only used for differently purified cellulose samples all originating from cotton.

5.2.2 Amorphous standard

A way to separate the amorphous and crystalline contributions to the diffracted intensity and estimate the crystallinity was outlined by Ruland and Vonk (Ruland, 1961; Vonk, 1973). Here it is assumed that the Bragg peaks are sharp, *i.e.* the crystallites are large enough for the intensity between the diffraction peaks to be negligible. The amorphous part of the intensity is obtained by measuring the scattering of the compound on amorphous form. This amorphous diffractogram is then scaled by a factor $c(s)$ to bring it below the diffractogram of the partly crystalline compound. The scale factor $c(s)$ is allowed to vary continuously throughout the s-interval to meet the requirement that the crystalline diffraction intensity should be zero between some of the diffraction peaks (the diffractograms touch at several points). The use of a continuously varying scale factor seems incorrect in the light of Figure 5.3A, so for Figure 5.3B it was chosen to use a constant scale factor c to make the background touch the diffractogram in one point/interval only. Lignin was used as the amorphous standard, and finally the crystallinity was calculated from (5.2).

The amorphous standard method has the great advantage that it is a purely experimental approach. For more than a decade it has been widely accepted as one of the best ways to determine the crystallinity in cellulose samples (Fink and Walenta, 1994; Sao et al., 1994; Sao et al., 1997). However, the scaled amorphous background meets the diffractogram in the low angle region where the intensity is most poorly determined due to the fine adjustment of slits and the effects of axial divergence. This means that, besides the

fact that the definition of when the scale factor is correct for the curves to actually touch is rather subjective, the amorphous standard method is also very sensitive to instrumental inaccuracies. It should be added that the amorphous standard material must be chosen so that it resembles the amorphous component of the samples as closely as possible. Therefore the method can only be used to compare crystallinities of samples where the amorphous compositions can be assumed to be similar.

5.2.3 Rietveld refinements

To illustrate how the Rietveld method can be used to determine the crystallinity, refinements were carried out with a modified LHMP1 Rietveld program (Hill and Howard, 1986) for 2θ=5°–60°. The cellulose Iβ CIF was used as input and in the final model the following 16 parameters were refined (Thygesen et al., 2005 in Appendix C.1 states 17 parameters, this is a misprint): a scale factor, 10 Chebyshev background parameters, 2 Voigt peak profile parameters, 2 cell dimensions (a and b), and a preferred orientation parameter (along <0k0>, for unknown reasons this gave a superior fit to the expected <00l> direction). Due to the remaining preferred orientation effects the 00l reflections are still severely suppressed; in fact the diffraction pattern only contains three strong diffraction peaks that are all of the hk0 type. Therefore it was impossible to refine γ and c, the latter of which correlates strongly with the preferred orientation parameter. Neither could the 2θ zero shift be refined because of strong correlations to the cell parameters a and b. Instead c=10.35Å and γ=96.5° were fixed to average values given in the literature (Sarko and Muggli, 1974; Woodcock and Sarko, 1980; Simon et al., 1988; Sugiyama et al., 1991; Koyama et al., 1997; Finkenstadt and Millane, 1998; Nishiyama et al., 2002), and the 2θ zero shift was set to 0.0°. The crystallinity was calculated according to (5.2) based on the final fit shown in Figure 5.3C.

5.2.4 Debye simulations

For the crystallinity determination based on the Debye approach, the cell parameters and particle size estimations obtained from the Rietveld refinements (see Section 5.3.1) were used as input for the simulations along with the cellulose Iβ CIF. The values of c=10.35Å and γ=96.5° were used as for the Rietveld refinements, and the instrumental peak broadening parameters (U, V, W and η) were fixed at values obtained for a LaB_6 standard on the same diffractometer. A number of simulations varying the structural parameters (a and b as well as the particle shape, size and size distribution) stepwise one at the time as described in Section 5.3.2 were performed un-

til the values offering the best fit to the experimental diffractograms were achieved. The fitting procedure comprised of varying the scale factor of the simulated diffractogram and the coefficients of a 9^{th} order Chebyshev background polynomial for 2θ=10°–60°. The final fit is shown in Figure 5.3D.

As expected the amorphous standard method underestimates the crystallinity, whereas the value determined by the peak height ratio method is unreliable. Both the Rietveld refinements and the Debye simulations offer a good fit to the experimental diffractograms (*c.f.* Figure 5.3), the obtained crystallinities are consistent to within 15% for five different samples of very diverse origin, no systematic deviations are observed, and the determined crystallinities are all reasonable compared to the total cellulose contents in the plant fibre samples. Due to this consistency there is absolutely no reason to prefer one method over the other, so a recommendation can only be based on factors such as speed of calculation and user-friendliness.

Rietveld refinements of cellulose are by no means trivial. As for many other nanocrystalline materials with severe peak broadening and overlap the number of refinable parameters is limited, strong correlations among these are observed, and interpretation of the obtained parameters as physical quantities is questionable. Most importantly in connection to the present application, the background level is greatly affected by the choice of peak shape function since the different functions have very different tail shapes. However, bearing all this in mind it was still possible to find a satisfactory set of minimal refinement parameters. Having settled on a common set of refinement parameters, the Rietveld refinement procedure for crystallinity determination in plant fibres is very straightforward and fast to use and can be carried out using any Rietveld refinement program.

As opposed to this the Debye simulation procedure for the crystallinity determinations is rather complicated and time consuming, especially for the new user. Even though each simulation only takes about a minute on a standard PC, it still requires a lot of experience and effort to systematically vary the structural parameters and fit every resulting diffractogram to the experimental patterns. However, all of the involved parameters can be directly related to the physical structure of the sample, rendering Debye simulations an excellent reference procedure for a combined determination of the cellulose nanostructure and crystallinity in plant fibre samples.

In conclusion: Rietveld refinement is to be the preferred standard procedure for future determinations of the crystallinity in plant fibres due to the speed and straightforwardness of the method, while Debye simulations are to be preferred if time is not the issue and a more detailed understanding of the structure is required.

5.3 Particle shape, size and size distribution

Besides the application for determining the crystallinity, Debye simulations of cellulose Iβ are interesting for a number of other reasons: 1) As mentioned in Section 3.3.2 not many studies of organic compounds have been performed using the Debye approach, and 2) The cellulose crystallites are of a very anisotropic shape, yet they are small enough to make simulations fast, thus they may serve as an excellent test case for illustrating the effects of particle shape, size and size distribution. Before a presentation of some of the simulations varying these structural parameters, a description of how a set of starting values can be estimated from the Rietveld refinements is given.

From the transmission geometry XRPD data of filter paper shown in Figure 5.1A it is obvious that the cellulose Iβ particles are elongated, presumably cylindrical, along the unique c-axis of the $P2_1$ unit cell. This is confirmed by the preferred orientation effects observed for the reflection geometry XRPD data, and it agrees nicely with the crystal packing where the molecules are connected by strong covalent bonds in the c-direction while hydrogen bonds comprise the perpendicular interactions. For the filter paper transmission data in Figure 5.1A both Rietveld refinements and Debye simulations estimate the cylinder diameter to be 50(2)Å and the length to be 300(20)Å. These dimensions are a lot more realistic than the ones which can be obtained from reflection data, mainly because the transmission data are much less affected by preferred orientation. However, the following analysis serves to illustrate how much extra information about particle shape, size and size distribution can be obtained from reflection mode XRPD data when a good crystallinity determination is the top priority.

5.3.1 Rietveld refinements

During the Rietveld refinements the instrumental peak broadening was described by a Caglioti type expression (Caglioti et al., 1958, (3.11)) where U, V and W were fixed at diffractometer specific values as for the Debye simulations, while the particle size broadening was refined by means of two Voigt peak profile parameters, X and X_e. In addition to the Voigt parameters a direction is given, in this case the c-axis which is the fibre growth direction, making it possible to estimate the particle dimensions along and perpendicular to this (*c.f.* Section 3.2).

For the hemp samples Rietveld refinements estimated the crystallites to be 24Å cylinders with a diameter of 43Å, thus the term cylindrical hardly applies. There are several reasons for these poor particle size estimates: 1) The

Scherrer-type relationship between the Voigt peak profile parameters and the particle dimensions becomes inaccurate if the peaks are broadened and overlapping because the particles are nanosized, 2) The diffraction peaks needed to determine the dimension along the fibre axis are severely suppressed due to remaining preferred orientation effects, making an estimate of this dimension highly unreliable, and 3) The cylinder length determined by X-ray diffraction is the coherence length, which may be orders of magnitude shorter than the actual length of the fibres due to the presence of defects or bending.

5.3.2 Debye simulations

The working hypothesis for the Debye simulations is that the cellulose Iβ particles are cylindrical in shape. Once the length and diameter have been determined, simulations for box and ellipsoid shaped particle of similar size are presented for comparison. As mention in Section 5.1 it is not possible to take the remaining preferred orientation effects into account in any way during the Debye simulations, so the apparent cylinder length, giving the best fit between experiment and simulation, is underestimated as was observed for the Rietveld refinements. Since the values of the structural parameters are only varied systematically and not refined to give a minimum discrepancy between experiment and simulation, it is very likely that the suggested structure does not represent the global nor even a local minimum. The procedure of educated guessing by stepwise variation of the parameters one at the time is demonstrated in the following. Note that all the tabulated R-values used to determine the particle shape and size are determined with a 9^{th} order Chebyshev background polynomial in the fitting procedure, and that all the depicted diffractograms are given along with the experimental pattern of hemp for comparison and therefore are scaled accordingly.

Cylinder length

Fixing the cylinder diameter to the reasonable value of 43Å estimated from the Rietveld refinements, the cylinder length in the case of hemp was varied from 3 (31.05Å) to 7 (72.45Å) unit cells. The diffractograms only differ in the shape of the 004 and 102 peaks which, as expected, become more narrow the longer the cylinders (*c.f.* Figure 5.4 which is calculated for the optimal cylinder diameter of 38Å determined in the following section). Table 5.2 gives the obtained R-values describing the discrepancy between experiment and simulation. This is an excellent example demonstrating that the minimum R-value does not always point at the best structure. Visual inspection of the fits along with a genuine knowledge of the problem at hand (in this case the

Table 5.2 Hemp cylinder length

number of unit cells	3	4	5	6	7
cylinder length [Å]	31.05	41.40	51.75	62.10	72.45
R-value	0.0582	0.0603	0.0610	0.0641	0.0667

Figure 5.4 Hemp cylinder length

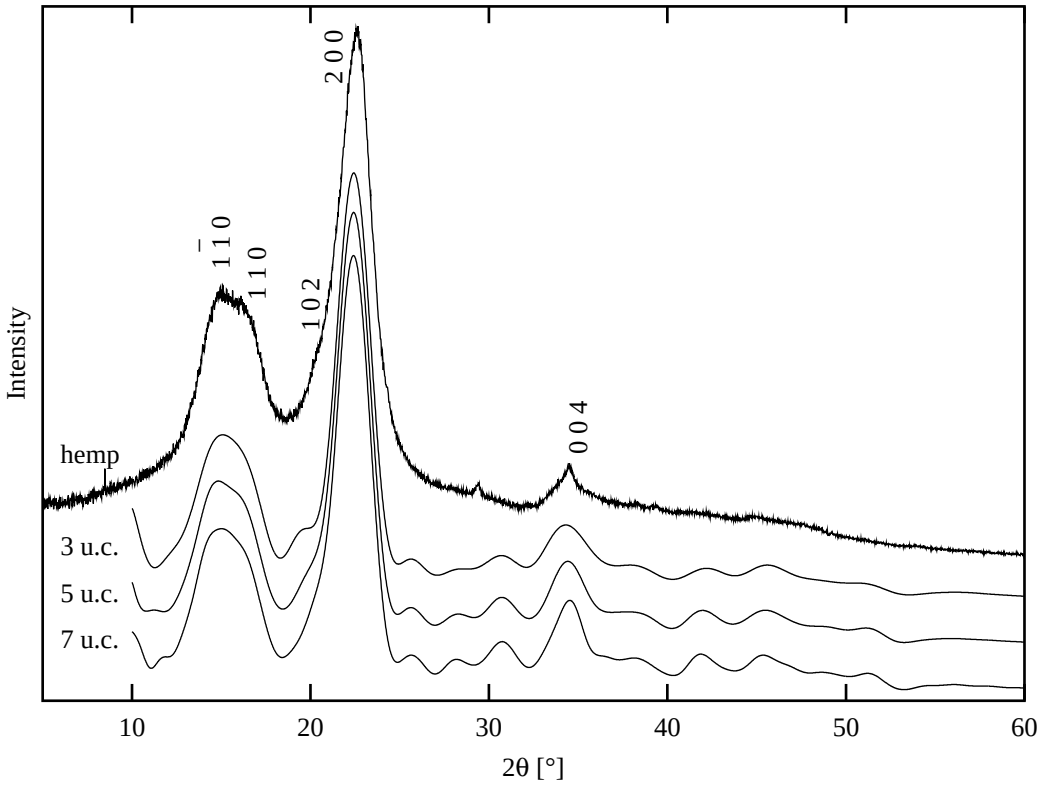

fact that the experimental diffractograms are severely affected by preferred orientation) led to the conclusion that a cylinder length of 5 unit cells is the best compromise.

Cylinder diameter

Having settled on a cylinder length of 5 unit cells, a series of simulations varying only the cylinder diameter was carried out and the resulting diffractograms were fitted to the experimental diffraction pattern giving the R-values of Table 5.3. Because the crystallites are built from entire unit cells in the Debye program, there is no difference between a diameter of 40Å and one of 43Å, and the same holds for 44Å and 46Å. The diffractograms corresponding to the different diameters given in Table 5.3 are depicted in Figure 5.5. It is immediately evident that the crystallite diameter has a great impact on the relative intensities of the $1\bar{1}0$ and 110 peaks. Furthermore it should be noted that the intensity of the 200 peak increases with increasing diameters as would be expected. From both the R-values and a visual inspection of the $1\bar{1}0/110$ doublet it is not difficult to conclude that the optimal diameter is 38Å. A new round of simulations varying the cylinder length with the diameter fixed at 38Å gave no reason to change the length from 5 unit cells.

Other particle shapes

The cylindrical nanoparticles giving the diffractogram that offers the best fit to the experimental diffraction pattern of hemp fibres are 52Å long, 38Å in diameter and consist of 95 entire unit cells of cellulose Iβ. The best way to mimic these dimensions for box or ellipsoid shapes crystallites are summarised in Table 5.4 along with the R-values resulting when fitting to the experiment. The corresponding diffractograms are shown in Figure 5.6 and again it is evident that the cylindrical crystallites offer the best fit around the $1\bar{1}0/110$ doublet, a fact that is also reflected in the lowest R-value.

Particle size distribution

The only particle size distribution applied for the Debye simulations in the final publication (Thygesen et al., 2005, Appendix C.1) was a manual addition of diffractograms calculated for particles with the same length and a radius of $\pm$1Å. The reason for this very crude way of applying a particle size distribution is that the project was terminated before the particle size distribution routine was implemented into the Debye program. The analyses presented in this section were therefore performed later. It should be noted that the conclusions drawn in the following regarding how to choose a mass

Table 5.3 Hemp cylinder diameter

cylinder diameter [Å]	34	36	38	40–43	44–46
R-value	0.0654	0.0639	0.0607	0.0610	0.0627

Figure 5.5 Hemp cylinder diameter

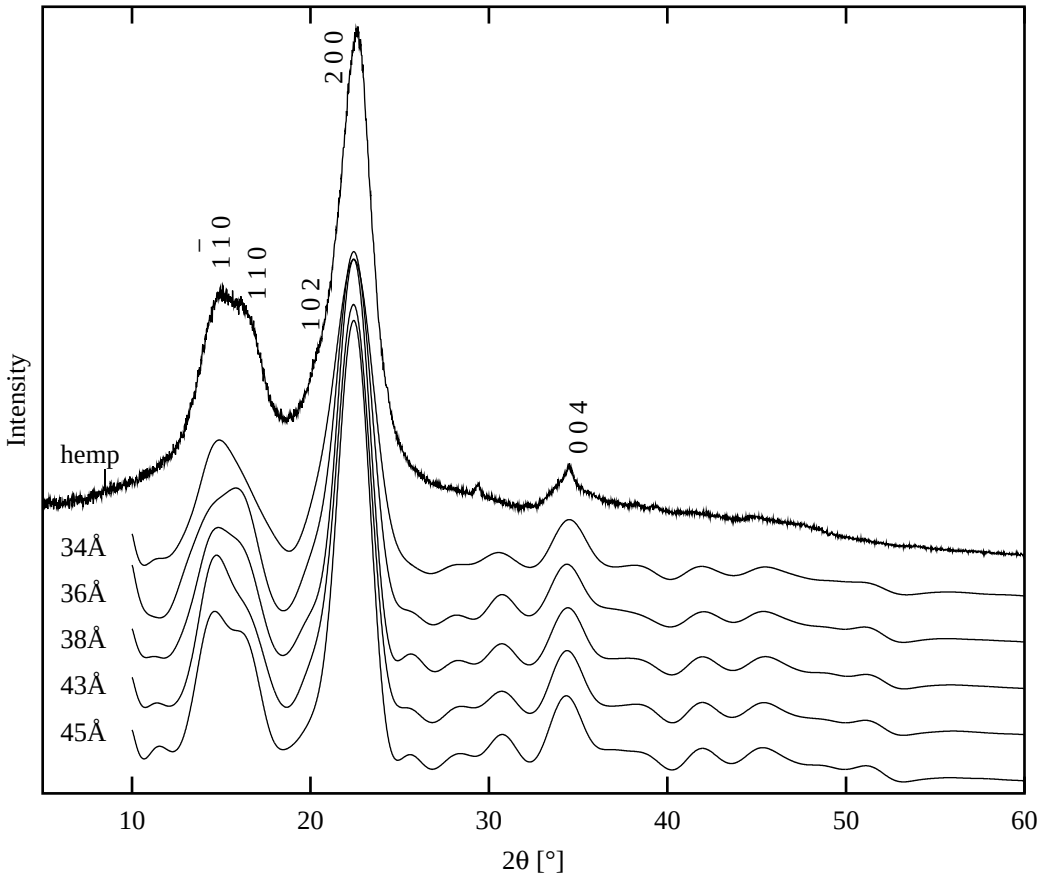

Table 5.4 Hemp particle shapes

particle shape	cylinder	box	ellipsoid
length along *c*-axis [Å]	52	52	66[a]
perpendicular dimension [Å]	38	40×33	44[a]
number of entire unit cells	95	100	93
R-value	0.0607	0.0632	0.0648

[a] The ellipsoid dimensions correspond to the maximum diameters.

Figure 5.6 Hemp particle shapes

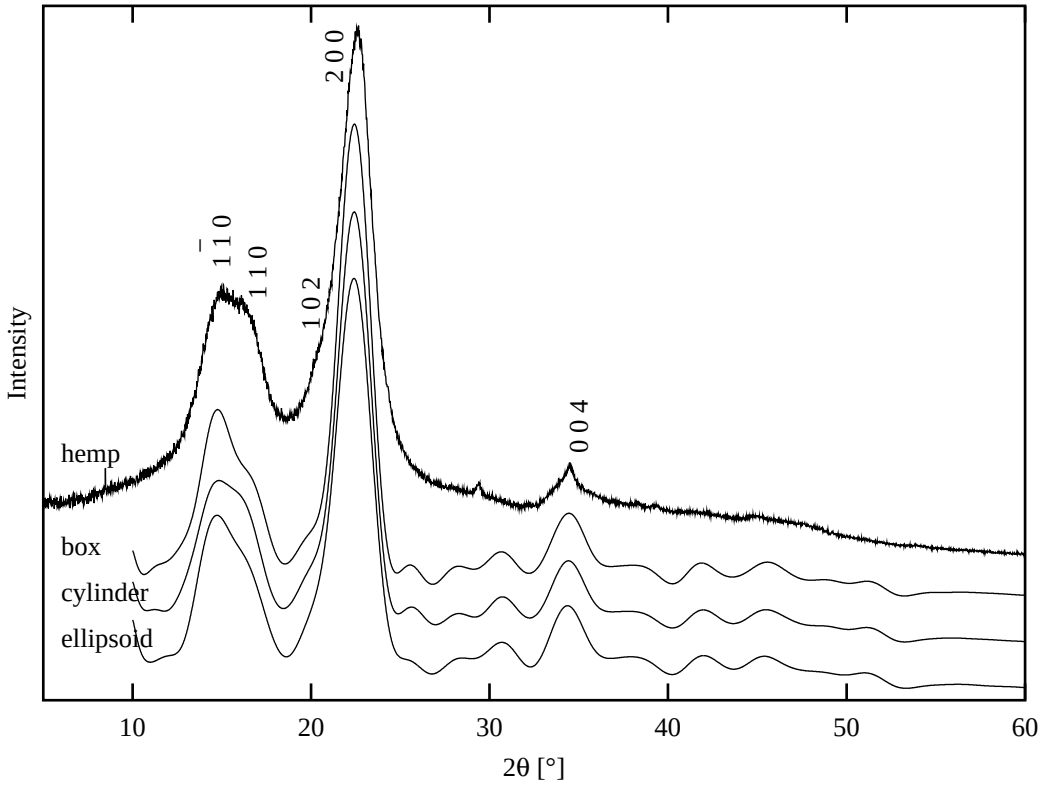

distribution function and how widely it should be sampled apply only to the particular type of nanocrystalline plant fibre samples presently under study, but the line of thoughts leading to the conclusions can be transferred to other studies.

In general the effects of adding a particle size distribution to the simulated diffractograms are mainly seen in the peak shapes, which become more narrow at the peak positions due to the presence of larger particles and broader at the bases due to the presence of smaller particles. This trend in peak shape change is hard to observe in the diffractograms of nanocrystalline cellulose Iβ simulated for different particle size distribution widths shown in Figure 5.7 because it drowns in the extreme particle size induced peak broadening. However, it can be seen that the relative intensities of the $1\bar{1}0/110$ doublet depend on the width of the particle size distribution. This is not surprising taking into consideration how even a small difference in the diameter affects the diffraction patterns in Figure 5.5.

As described in Section 4.3 the Debye program applies a particle size distribution by explicitly adding $2m+1$ diffractograms of sizes between $1.0-0.1m$ and $1.0+0.1m$ times the input size, where m is an integer between 1 and 9. Before the addition the diffractograms are scaled by a factor corresponding to one of the three mass distribution functions depicted in Figure 4.1. For nanosized particles as those of cellulose Iβ in the plant fibre samples it makes no sense to go beyond m=5 because this would correspond to crystallites with a volume less than $\frac{1}{8}$ of the input size, particles consisting of so few unit cells that they hardly deserve to be called crystalline, and as stated in the beginning of Section 5.2 the whole point of the Debye simulations is to model the *crystalline* part of the diffraction pattern in order to determine the crystallinity.

A number of simulations using the three possible mass distribution functions and varying m between 0 (no particle size distribution) and 5 were performed to determine the type of distribution and the value of m that give the best fit to the experimental hemp XRPD pattern. The corresponding R-values are given in Table 5.5. From this it can be seen that m=4 is superior for all distributions. Furthermore, Table 5.5 shows that the type of mass distribution function chosen is irrelevant for all practical purposes; applying different distributions result in diffractograms that are virtually identical. This is not entirely surprising considering that the distributions in Figure 4.1 are only sampled in a very limited number of points ($2m+1$) and differ very little between r=0.5 and r=1.5 (corresponding to m=5). Since the diffractograms simulated applying a uniform mass distribution function seem to give a marginally better fit to the experimental XRPD pattern these are the ones depicted in Figure 5.7.

Table 5.5 R-values for comparison hemp diffractograms, experimental and simulated using different particle size distributions

m	Uniform	Gaussian	Weibull
0	–	0.0607	–
1	0.0601	0.0597	0.0596
2	0.0589	0.0593	0.0595
3	0.0597	0.0585	0.0588
4	0.0574	0.0577	0.0578
5	0.0585	0.0583	0.0585

Figure 5.7 Hemp uniform particle size distribution

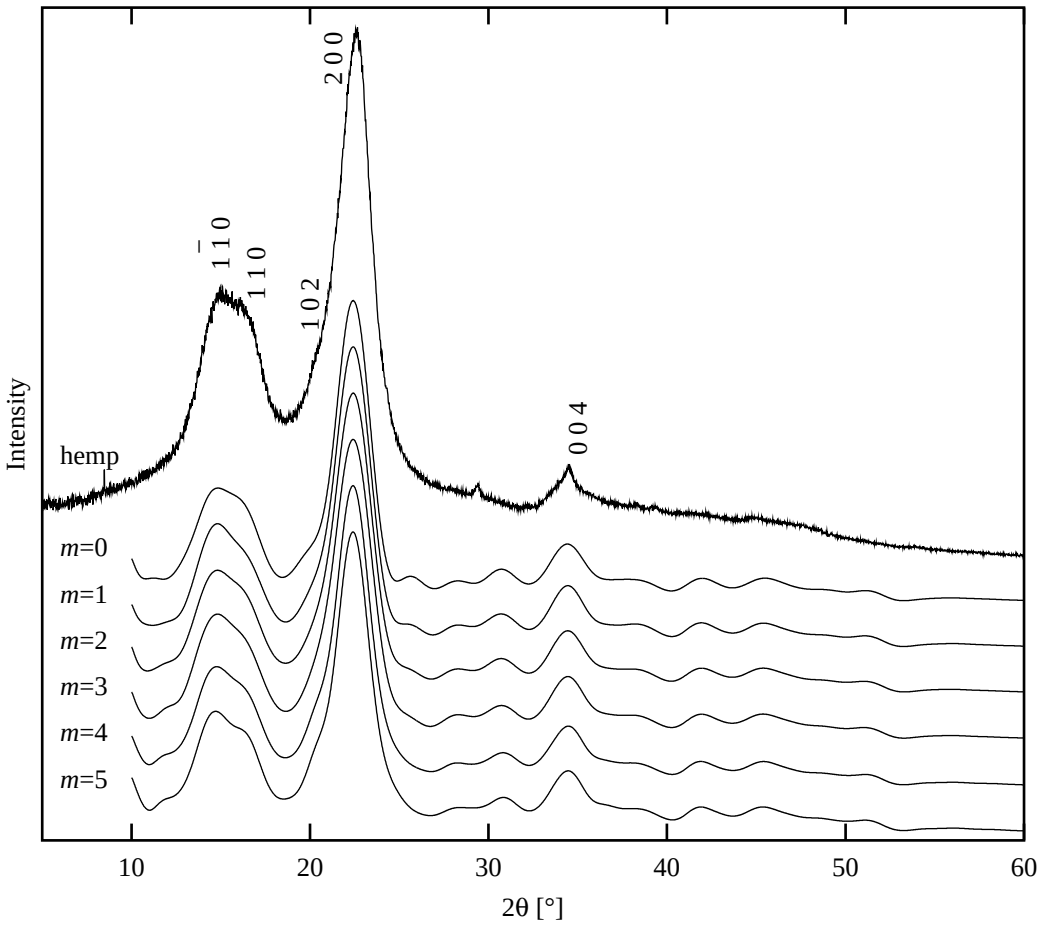

To check what happens with the apparent particle size when the peak profiles change as a result of applying a particle size distribution, Rietveld refinements on all the diffractograms simulated for various particle size distributions were carried out refining the same 16 parameters as described for the experimental diffractograms in Section 5.2.3. The particle dimensions estimated from the Voigt peak profile parameters during the Rietveld refinement are given in Table 5.6. Here it can be seen that the estimated dimensions are independent of m as they should be. The diameter estimates are excellent (perhaps except for the m=0 case where no particle size distribution is applied), whereas the lengths are consistently overestimated by more than 40% for all values of m. This is a good indication of how much (or how little) one can trust the Rietveld dimension estimates for nanosized particles. In this particular case the "experimental data" are even free of preferred orientation effects complicating the data analysis. However, it should be noted that in the Rietveld refinements the preferred orientation parameter refines to a value around 1.2 for all values of m, thus significantly different from the value of 1 which corresponds to no preferred orientation. The value of the b cell parameter also differs significantly from the true value used in the simulations, undoubtedly because of the severe peak overlap. The a cell parameter, on the other hand, refines nicely to the input value of 8.00Å, presumably because 200 is by far the strongest diffraction peak and thereby not as sensitive to either broadening or overlap as the remaining peaks.

Table 5.6 Cylinder diameters and lengths estimated from Rietveld refinements of the hemp diffractograms simulated using different particle size distributions

	Uniform		Gaussian		Weibull	
m	d [Å]	l [Å]	d [Å]	l [Å]	d [Å]	l [Å]
Input[a]			38	52		
0	–	–	46(1)	74(3)	–	–
1	41(1)	80(3)	41(1)	78(3)	41(1)	78(3)
2	39(1)	76(2)	39(1)	77(2)	39(1)	77(2)
3	37(1)	76(2)	39(1)	79(2)	38(1)	79(2)
4	39(1)	79(2)	39(1)	80(2)	39(1)	78(2)
5	39(1)	83(2)	40(1)	84(2)	39(1)	80(2)

[a] Mean values used as input for the simulations

In the light of Table 5.5, the very crude particle size distribution used in the publication (corresponding roughly to the uniform m=1 model adding three diffractograms, but using factors more like 0.95, 1.0, and 1.05 times the input dimensions instead of 0.9, 1.0, and 1.1 as for m=1) was not the best choice. This is also confirmed by the crystallinity of 0.69(2)g crystalline cellulose per g dry matter determined for hemp using the Debye approach with the crude particle size distribution. Recalling that the hemp sample contained only 0.63(3)g cellulose per g dry matter, this value is unrealistic. The particle size distribution offering the best fit to the experimental hemp diffractograms employs the uniform m=4 model, for which the crystallinity can be determined to be 0.64(2)g crystalline cellulose per g dry matter. This is in much better accordance with both the Rietveld refinements and the cellulose contents of the hemp samples, and thus serves to demonstrate the importance of taking the time to apply a proper particle size distribution.

5.4 Final conclusions

The ability to determine the crystalline fraction of cellulose in an efficient and reliable manner is essential for industrial applications of plant fibres. Considering that cellulose is the only crystalline component in the plant fibres, XRPD is an excellent tool for crystallinity determinations. It was shown that the diffraction data must be collected in reflection geometry to minimise unwanted air scattering contributions to the amorphous background. Cellulose is a fibrous material, so special attention must be made when preparing the samples for XRPD in order to minimise preferred orientation effects. An operational procedure for a custom-made sample holder was devised. The cellulose fibres are very thin, typically with diameters below 50Å, so the diffraction peaks are broadened and overlap. Traditional methods for crystallinity determinations (Segal et al., 1959; Ruland, 1961; Vonk, 1973) tend to underestimate the background contributions arising because of the nanosized particles and thus also the crystallinity. With the publication of the cellulose Iβ crystal structure (Nishiyama et al., 2002) Rietveld refinements taking full account of the broadened and overlapping peaks have become feasible. It was argued that this should be the preferred method for standard crystallinity determinations in the future because it can be performed using any readily available Rietveld refinement program with speed, ease and consistency.

Additional information about particle shape, size and size distribution can be obtained if time and effort is invested to do Debye simulations. The diameters of the cylindrical crystallites obtained from the Debye simulations are comparable with the microfibril diameters obtained in TEM studies (Bardage et al., 2004), while the lengths of the fibres are orders of magnitude smaller. Debye simulations of XRPD data collected in transmission geometry where the preferred orientation effects are almost negligible showed that remaining preferred orientation can only partly explain this length discrepancy, most likely the entire fibres do not scatter coherently due to the presence of bends and/or defects.

Chapter 6

Nitrogen expanded austenite

The surface hardness as well as wear and corrosion resistance of stainless steel can be significantly improved by nitriding or carburising the material at low temperature using a number of different techniques. This brings about a transformation of the surface adjacent region into so-called expanded austenite. The question of how to interpret the XRPD pattern of the resulting phase to extract the structural characteristics has been a matter of dispute for several years (Williamson et al., 1994; Sun et al., 1999; Marchev et al., 1999; Blawert et al., 1999; Menthe and Rie, 1999; Larisch et al., 1999; Bazaleeva, 2005; Borgioli et al., 2006; Fewell and Priest, 2007).

Hitherto, structural investigations of expanded austenite have relied on samples consisting of compositionally heterogeneous expanded austenite "layers" on bulk stainless steel substrates prepared by the use of plasma-based techniques. Unavoidably, samples of this type contain high compositionally induced compressive stresses which strongly affect the diffraction patterns. The diffraction patterns roughly correspond to that of FCC austenite with an expanded lattice due to the presence of interstitials, hence the name expanded austenite or γ_X where X is N or C depending on the nature of the interstitials. The peak positions, however, do no fit an ideal FCC lattice. This has led to the suggestion of two inherently different structural models: 1) The m-phase of tetragonal rather than cubic symmetry, and 2) Expanded austenite where the observed peak shifts are due to the presence of deformation stacking faults and/or residual stresses in the FCC lattice. The designation S-phase has also been used and usually refers to structural model 2.

Recently stress-free and homogeneous samples of nitrogen expanded austenite, a supersaturated solid solution of nitrogen in stainless steel with a homogeneity range of y_N=0.18 to y_N=0.61, were synthesised by gaseous nitriding of AISI316 stainless steel coupons under para-equilibrium conditions at low temperature (Christiansen and Somers, 2006).

Analysis of the corresponding XRPD patterns unambiguously confirmed the structure to be FCC with a deformation stacking fault probability between 0.01 and 0.04 to account for the peak shifts (Christiansen and Somers, 2004). Deformation stacking faults in a FCC lattice give rise to both peak shifts and peak broadening (Warren, 1990), but none of the traditional methods for XRPD analysis are able to take into account how the entire diffraction profile is affected. However, the Debye approach offers the possibility to simulate diffraction patterns of expanded austenite containing any combination of defects. In Section 6.1 it is analysed how the XRPD patterns are affected by the presence of screw dislocations, deformation and/or twin stacking faults, and finally the knowledge gained from the previous simulation studies is utilised to fit experimental diffraction data. The results of the simulation study were recently submitted to Journal of Applied Crystallography, see Appendix C.4.

Nitrogen contents as high as those observed in expanded austenite are obtained due to the high affinity between nitrogen and chromium, where nitrogen is believed to reside in the close vicinity of the supposed randomly distributed chromium atoms, *i.e.* short range order of N occurs. The thermodynamically more stable CrN does not form due to the low mobility of chromium at the nitriding temperature, only nitrogen is able to diffuse at a significant rate; thus nitrogen contents many times higher than the equilibrium solubility can be obtained. A fraction of the nitrogen content in expanded austenite, corresponding to y_{N}=0.18, is more tightly bound than the fraction between y_{N}=0.18 and y_{N}=0.61, and there are strong indications that the tightly bound nitrogen interacts with chromium, *i.e.* nitrogen trapping (Christiansen and Somers, 2006). EXAFS is a proficient tool for probing the local environment around each atom type in the metal lattice of nitrided or carburised steels. In particular the local structure of the chromium atoms is of interest in this respect, since it may shed a light on the actual occurrence of short range ordering of nitrogen atoms. The basic concepts of EXAFS are given in Chapter 2. The information that can be obtained comprises bond length, disorder (thermal and/or static) and the number of nearest neighbours. These parameters can be related to the presence/absence of interstitially dissolved elements in the immediate surroundings of the probed metal atom.

Hitherto, EXAFS investigations of short range order of nitrogen in stainless steel have been scarce (Oda et al., 1990; Kizler et al., 1994; Muñoz-Páez et al., 2002). The investigation by Oda et al. addressed nitrogen bearing 15Ni–15Cr austenitic stainless steel, *i.e.* nitrogen contents many time lower than for expanded austenite. The nitrogen atoms were found to form interstitial-substitutional complexes with chromium atoms. Kizler et al. investigated

conventionally salt bath nitrided foils of stainless steel AISI304 and AISI316. Unfortunately, neither nitriding temperature nor duration of nitriding is stated in this work. However, conventional nitriding is carried out at temperatures above 763K, *i.e.* in a temperature range where precipitation of CrN occurs. In this work it was reported that a strong lattice distortion was found around the Cr and Mo atoms, whereas only small lattice distortions could be observed in the neighbourhood of the Fe and Ni atoms. This observation was interpreted to indicate that dissolved nitrogen would prefer Cr and Mo as nearest neighbours, which would be consistent with the higher affinity of nitrogen towards Cr and Mo as compared to Fe and Ni. A recent investigation was carried out by Muñoz-Páez et al. on nitrided Cr, Mo, Mn and V alloyed ferritic steels. The authors state the occurrence of "new non-crystalline domains involving nitrogen", although there appears to be a striking resemblance to older work by Jack and co-workers on mixed cluster formation in low-alloyed ferritic steels (Jones et al., 1979). Cr, V and Mn were found to form austenitic FCC structures with the nitrogen atoms residing in the octahedral interstices upon nitriding, but in all cases a small fraction ($\frac{1}{4}$ to $\frac{1}{3}$) of the metal centers were found to retain the ferritic BCC structure. The investigation presented in Section 6.2 is a combined XRPD and EXAFS (Cr and Fe K-edge) characterisation of homogenously low temperature nitrided micrometer-sized AISI316 stainless steel flakes.

6.1 Debye simulations of expanded austenite

In the present study it was chosen to focus on how a variation of the particle size, the deformation and twin stacking fault probabilities, α and β, the screw dislocation density, ρ, and the interstitial nitrogen occupancy, y_{N}, affects the XRPD patterns of nitrogen expanded austenite. These variables describe the deviations from the overall periodic FCC structure, so it was necessary to substantially modify the original Debye program which is not able to handle any type of defects. Before describing how the atomic array that leads to the diffracted intensities is set up in the modified Debye program, a description of the global parameters describing the underlying FCC structure is in order. These were fixed to be identical for all simulations to limit the number of parameters and facilitate comparisons.

Global parameters

From Table 6.1 the weighted average atomic number of AISI316 stainless steel is 25.9, making it a reasonable first approximation to model all atoms

in the FCC lattice as Fe. The 'fault free' lattice parameters a_0 (one parameter for each value of y_N, *c.f.* Table 6.3) obtained in the conventional way were used as standard input for the simulations along with a thermal parameter set of B_{Fe}=B_{N}=1Å^2 which is reasonable at room temperature and agrees well with values obtained from Rietveld refinements. The anomalous dispersion corrections f' and f'' for both Fe and N at the relevant wavelengths were obtained *via* http://skuld.bmsc.washington.edu/scatter/. Finally instrumental peak broadening parameters of the pseudo-Voigt type were added (Caglioti et al., 1958; Wertheim et al., 1974).

Table 6.1 Chemical composition of AISI316 stainless steel

atomic name	Fe	Cr	Ni	Mn	Si	Mo
atomic number	26	24	28	25	14	42
atomic %	63.60	19.11	12.70	1.74	1.45	1.40

6.1.1 Building the structure atom by atom

The coordinate system chosen to model the nitrogen expanded austenite FCC structure is directed with the z-axis perpendicular to the (111) close packed layers which are situated in the xy-plane, thus a hexagonal cell setting.

Particle size in the simulations is realised by letting the atomic array be made up by m close packed layers each consisting of $m \times m$ Fe atoms. Hence a crystallite of size m=120 contains 120^3=1728000 Fe atoms and has a mean diameter of roughly 120·3Å=360Å. One parameter was deemed enough to describe the particle size since there is no reason to assume an anisotropic particle shape for a compound with a FCC structure.

Deformation stacking faults in a FCC structure are realised by changing the stacking sequence of the (111) close packed layers from ABCABCA to ABCACAB. In the program the atomic array is built up one close packed layer at the time, and each time a new layer is added a random number between 0 and 1 is generated. If the number is smaller than the input deformation stacking fault probability, α_{in}, a deformation stacking fault is introduced. The final deformation stacking fault probability, α, is defined as the number of deformation stacking faults in the atomic array divided by $m-1$, the number of new layers added. To get a physically realistic model

an average over several (typically 10) diffractograms simulated for the same value of α_{in} is used.

Twin or growth faults refer to the stacking sequence ABCACBA of the FCC (111) close packed layers as opposed to the normal ABCABCA order, thus a mirror plane is introduced and the stacking is reversed. After determining the stacking sequence of the (111) layers taking possible deformation stacking faults into account, the program reconsiders each layer, generates a random number between 0 and 1 and introduces a twin stacking fault by reversing the stacking of all subsequent layers if this random number is less than the input twin fault probability, β_{in}. Finally the twin fault probability, β, is calculated as an average over several simulations.

Screw dislocations with (111) slip planes, screw axes along [110] and one interatomic distance in displacement can be added to the structure after building the atomic array as described above. The desired screw dislocation density, ρ_{in}, typically in the order of 10^{15}–10^{16}m^{-2}, is input and the number of dislocations to which this corresponds for the given crystallite size is calculated. The number is then rounded off at random to one of the two nearest integers in a way that an average over several diffractograms should yield the desired real number. For a m=120 crystallite a dislocation density of 10^{15}m^{-2} corresponds roughly to one screw dislocation. A distance threshold to limit the dislocations from being placed too close to one another is calculated based on ρ_{in}, and the dislocations are then placed at random within the part of the crystallite that has the full thickness using the calculated distance threshold. The shortest distance between screw dislocations is printed in the output file along with the actual screw dislocation density, ρ. In order to keep the high symmetry of the atomic array (identical layers perpendicular to the screw dislocation axis) and thereby the high performance of the Debye calculations, no relaxation of the structure or removal of Fe atoms in the vicinity of the screw axes or slip planes is performed by the program. It should be noted that it was chosen to model the screw dislocations with slip planes extending to either side of the crystallite at random, see Figure 6.1. However, because screw dislocations appear when a stress is applied in a given direction, these were all modelled with the same chirality.

Interstitial nitrogen atoms can be placed at random in the octahedral interstices of the Fe FCC structure while building the atomic array. For every octahedral interstice a random number between 0 and 1 is generated, and if the number is less than y_{N}, a nitrogen atom is added. It was chosen not to place any nitrogen atoms at the crystallite surface or at stacking fault positions, the latter to avoid unrealistically short N–N distances or nitrogen atoms with tetrahedral coordination. Interstitial nitrogen atoms in the vicinity of screw dislocation axes and slip planes are removed during the

Figure 6.1 Section of a m=20 crystallite with y_N=0.6 viewed along the screw dislocation axis [110] with [111] directed upwards. Fe light gray, N dark gray. Note the stacking fault in the bottom of the picture (missing N layer) and the two screw dislocations with (111) slip planes.

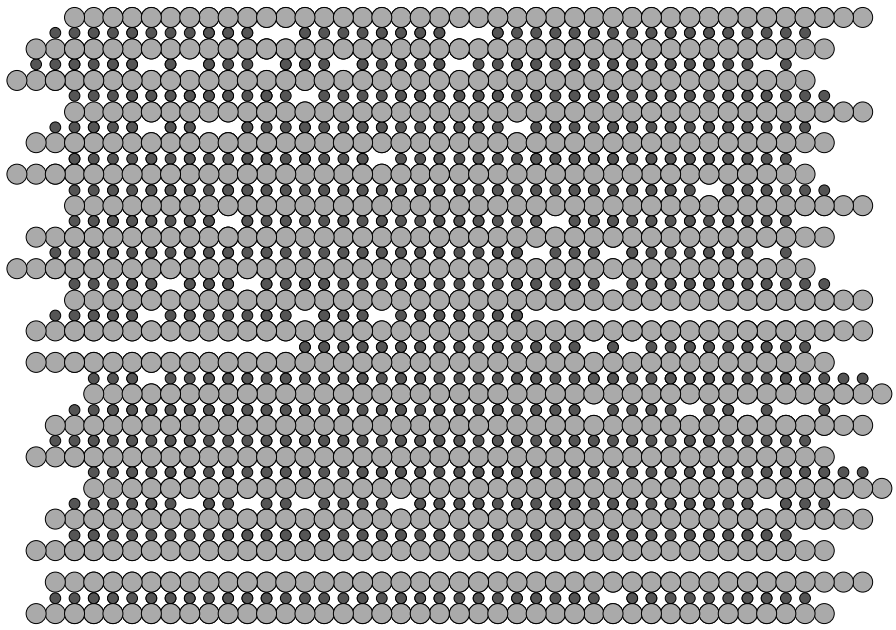

generation of the axes to avoid clashes.

Approach

The way the Fe FCC lattice is built makes it possible to exploit the symmetry of the atomic array to speed up the calculation of all the Fe–Fe interatomic distances. However, the interstitial nitrogen atoms are only introduced into a fraction of the octahedral interstices in the Fe FCC lattice, so the symmetry is broken and the Fe–N and N–N distances must be calculated for every atom pair, resulting in a substantial increase in calculation time. The reciprocal relationship between particle size and peak width is given by the Scherrer equation (3.3). Like the particle size, the presence of stacking faults and/or dislocations has great impact on the diffraction peak widths, but none of these parameters affect the integrated intensities. On the other hand, the introduction of nitrogen into the octahedral interstices alters the relative

intensities of the diffraction peaks, but has no impact on the peak widths. Based on these observations it was chosen to do a series of simulations of the Fe FCC lattice to analyse and possibly parameterise the effects of stacking faults, screw dislocations and a combination of these on the peak widths. The nitrogen atoms were left out because they do not contribute to the peak widths and because simulations without them are much faster as just argued.

6.1.2 Peak width analysis

In the following section the effects on the peak widths of varying α, β and ρ, both isolated and in combination, are analysed and parameterised. All the specified peak widths, β_{peak}, are integral breadths measured in degrees on the 2θ-scale for CoKα radiation. It is assumed that the individual contributions to the peak width add up in a Gaussian manner, thus:

$$\beta^2_{\text{peak}} = \beta^2_{\text{size}} + \beta^2_{\text{instr}} + \beta^2_{\text{sf}} + \beta^2_{\text{twin}} + \beta^2_{\text{sd}} + \dots \tag{6.1}$$

The $\beta^2_{\text{size}} + \beta^2_{\text{instr}}$ terms are simply taken as the squared integral breadths of the diffractogram simulated for the same size and instrumental parameters, but they can easily be parameterised using the Scherrer equation (β_{size}) and the pseudo-Voigt type instrument broadening (β_{instr}) as described previously.

Table 6.2 Stacking fault parameters

hkl	111	200	220	311	222
G_{hkl}	$\frac{1}{4}$	$-\frac{1}{2}$	$\frac{1}{4}$	$-\frac{1}{11}$	$-\frac{1}{8}$

Deformation stacking faults in a FCC lattice give rise to minor peak broadening effects as well as peak shifts of the type (Warren, 1990):

$$\Delta(2\theta_{hkl}) = 0.2756 \cdot \alpha \cdot G_{hkl} \cdot \tan\theta \tag{6.2}$$

where the deformation stacking fault parameter G_{hkl} is given according to Table 6.2. Since none of the other structural variables give rise to peak shifts, α can be determined from these. However, it is also necessary to parameterise the deformation stacking fault peak width contribution, β^2_{sf}, in order to fully understand the interplay between the different structural components. Figure 6.2 shows β^2_{sf} for α between 0.01 and 0.04 (the relevant interval for the experiments (Christiansen and Somers, 2004)). Each point in

the figure represents an average over 10 simulated diffractograms. For every value of α the peak width contributions are calculated for five different values of m, namely: 100, 200, 300, 400, and 500. Considering that the points group nicely around the trend lines, β^2_{sf} seems to be independent of particle size.

Figure 6.2 Calculated peak width contributions for different deformation stacking fault probabilities

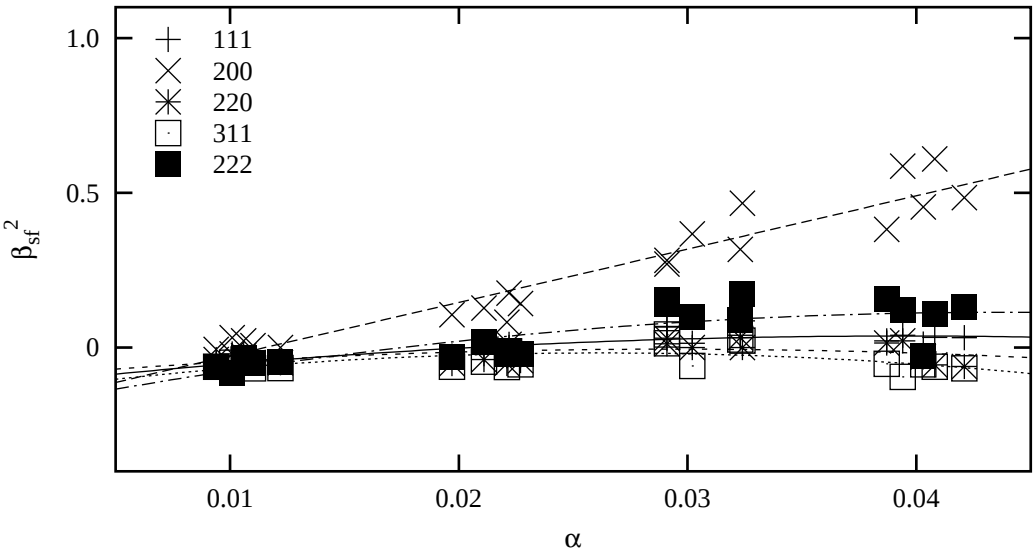

Twin faults in a FCC lattice result in asymmetric peak broadening (Warren, 1990). Simulations were performed for β between 0.01 and 0.04 since there was no reason to suspect a larger frequency of twin faults than of deformation stacking faults. For β in this interval the asymmetry was limited, so it was decided to focus only on the symmetric peak broadening effects, β^2_{twin}, depicted in Figure 6.3. As for the deformation stacking faults, each point represents an average over 10 simulated diffractograms and for every twin fault probability, β^2_{twin} is calculated for the same five values of m. From the figure it can be seen that β^2_{twin} is independent of particle size and only significantly different from zero for the 200 peak.

Screw dislocations of the type described above give rise to anisotropic peak broadening effects as seen from Figure 6.4. Note that the screw dislocation contribution, β^2_{sd}, to the 111 peak is significantly smaller than for the remaining peaks (except for 220), an effect that could potentially explain the large peak width anisotropies observed in the experimental diffractograms of

Figure 6.3 Calculated peak width contributions for different twin fault probabilities

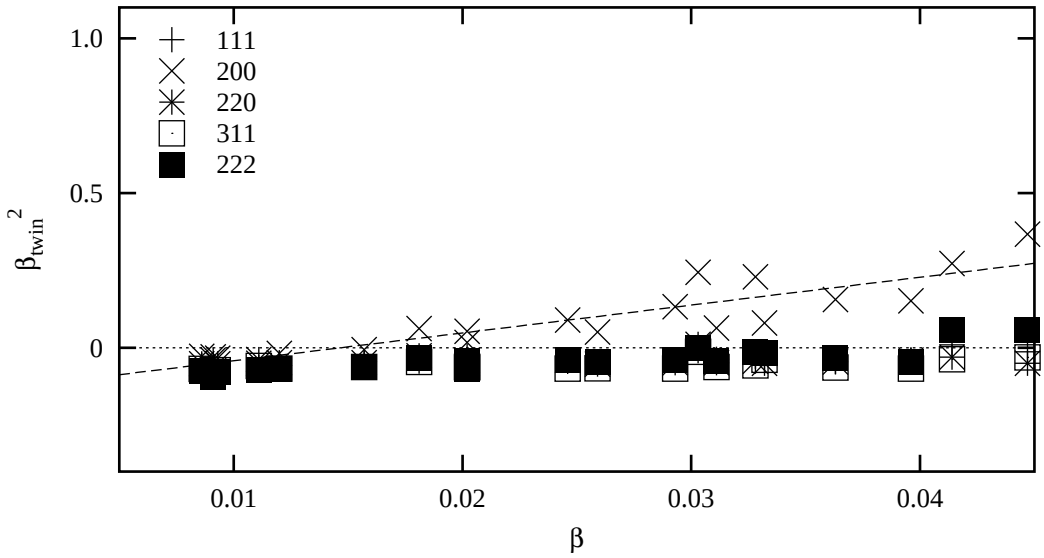

nitrogen expanded austenite (Figure 6.6 and Figure 6.7). The diffractograms used to construct Figure 6.4 are simulated for m=120 crystallites, so the labels on the x-axis correspond roughly to the number of screw dislocations in the crystallite, and each point represents an average over 10 simulated diffractograms. It can be seen that β_{sd}^2 is almost proportional to the screw dislocation density at low densities (trend lines forced through origo) and that it reaches a saturation level/maximum around $6{\cdot}10^{15}\mathrm{m}^{-2}$ which corresponds to a minimum distance between the individual screw dislocations around 65Å. The saturation/maximum could be the result of a shadowing effect where the addition of each new screw dislocation contributes less and less to the structure. If the shadowing effect is a function of the number of screw dislocations rather than the screw dislocation density, then β_{sd}^2 for a given screw dislocation density would be less the larger the crystallite. This effect was in fact observed and it is the reason why Figure 6.4, as opposed to Figure 6.2 and Figure 6.3, contains data for one value of m only.

Combining deformation stacking faults and screw dislocations it is not obvious whether the peak width contributions simply add up as $\beta_{\mathrm{sf}}^2 + \beta_{\mathrm{sd}}^2$, or whether the structural modifications correlate so strongly that

Figure 6.4 Calculated peak width contributions versus screw dislocation densities for m=120 crystallites

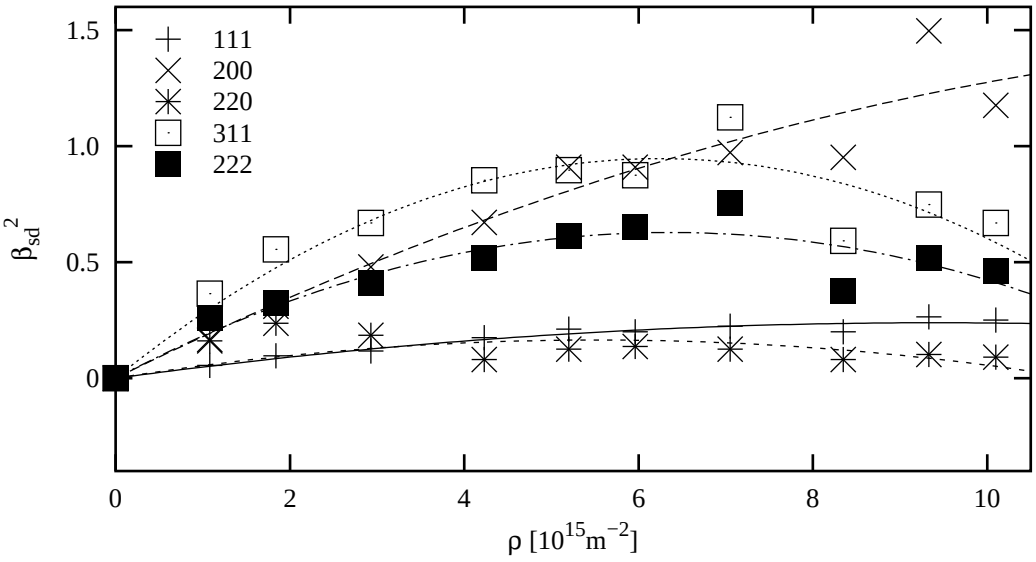

the resulting peak widths differ significantly from predictions based on the above analysis. The β^2_{twin} term was not considered because it only adds to the width of the 200 peak, which is also substantially broadened by the presence of both deformation stacking faults and screw dislocations. According to experimental XRPD patterns the 200 peak is no wider than the 220, 311 and 222 peaks, so twin faulting is bound to play a very minor part in the structure of nitrogen expanded austenite.

A number of diffractograms for m=120 crystallites with $\alpha\approx$0.03 and different values of ρ were simulated to test how well it is possible to predict the peak widths of diffractograms simulated for expanded austenite containing both deformation stacking faults and screw dislocations. For each value of ρ, Figure 6.5 shows the differences between the simulated peak widths β^2_{peak} and the peak widths predicted from parameterisation of size, instrumental broadening, deformation stacking faults (Figures 6.2) and screw dislocations (Figure 6.4). Each point in Figure 6.5 represents an average over 10 simulated diffractograms, and it should be noted that the differences are roughly constant and only differ significantly from 0 for the 200 (proportional to ρ) and 220 (constant) peaks. These extra peak width contributions, arising because of structural correlations between deformation stacking faults

and screw dislocations, are taken into account in the next section, where the parameterisation of the peak width contributions from different structural aspects derived in the present section is used to determine the model variables for Debye simulations that gives the best fit to the experimental diffractograms.

Figure 6.5 The difference between simulated and predicted peak widths for m=120 crystallites with $\alpha\approx$0.03 for various screw dislocation densities

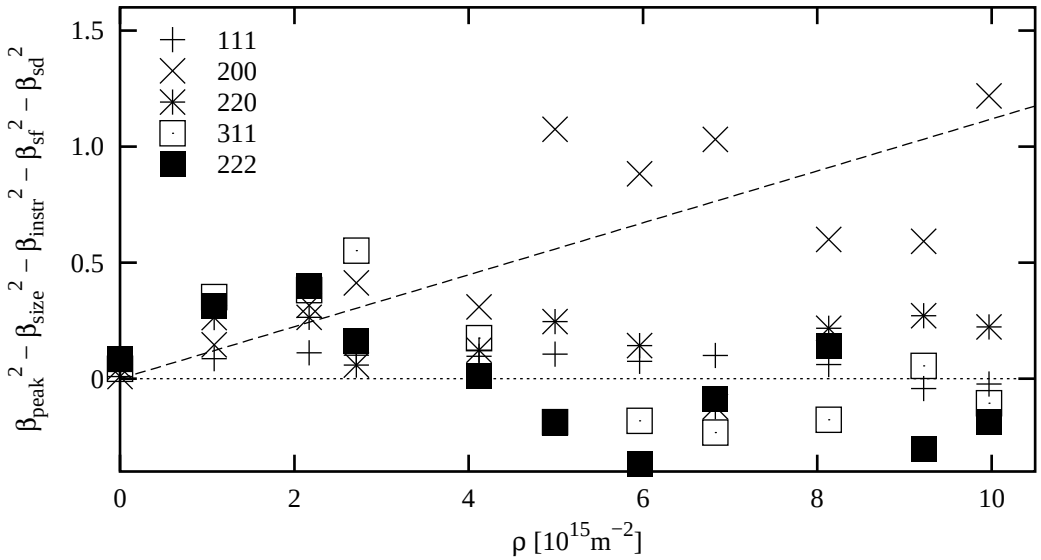

6.1.3 Experimental

XRPD data for expanded austenite samples with y_N=0.36, y_N=0.40 and y_N=0.58 were recorded using a Bruker D8 AXS diffractometer equipped with a Co anode (λ(CoKα_1)=1.78890Å, λ(CoKα_2)=1.79279Å) operating in Bragg-Brentano mode. The instrumental pseudo-Voigt peak profile parameters were obtained from a peak fit of a austenitised nitrogen-free AISI316 foil using the same diffractometer settings, assuming that the particle size in this sample is so large that the only significant contribution to the peak broadening is of instrumental origin.

Additionally synchrotron diffraction data for y_N=0.61 were collected in transmission mode with a HUBER G670 Guinier camera (λ=1.18608Å) at MAX-lab beamline I711 (Ståhl, 2000; Cerenius et al., 2000) with the sam-

ple mounted in a Ø=0.3mm capillary and Al-foils placed between sample and detector to reduce fluorescence. The short wavelength gives access to more diffraction peaks, and a much better signal to noise ratio can be obtained within minutes because of the high intensity of the synchrotron beam. The synchrotron data were corrected for 2θ zero shift (determined for a Si-standard along with the actual wavelength and the instrumental broadening), for the intensity profile related to the 45° Guinier tangent angle, and for absorption in a cylindrical sample with μR=1.5.

Fitting the experimental data

The modelling strategy to obtain the simulated diffractograms that best fit the experimental data consists of considering and including the already mentioned model variables — particle size, deformation and twin stacking fault probabilities, screw dislocation density, and interstitial nitrogen occupancy — one at the time. For the more advanced structural models the values of α,

Table 6.3 Fit parameters

y_N^a	a_0^a [Å]	α^a	bg^b	m	α	ρ [10^{15}m^{-2}]	y_N	R
0.36	3.8616	0.0142	3	120				0.0566
			3	120	0.014(8)			0.0567
			3	120	0.014(5)		0.3599(3)	0.0499
0.40	3.8848	0.0097	2	120				0.0615
			2	120	0.010(6)			0.0633
			2	120	0.010(9)		0.4000(2)	0.0553
0.58	3.9823	0.0274	3	120				0.0887
			3	120	0.027(9)			0.0879
			3	120	0.027(10)	2.1(3)		0.0871
			3	120	0.027(19)	2.0(4)	0.5799(3)	0.0681
0.61	4.0022	0.0362	12	120				0.0865
			12	120	0.036(12)			0.0731
			12	120	0.036(12)	3.9(5)		0.0711
			12	120	0.036(12)	3.9(5)	0.6100(3)	0.0551

[a] (Christiansen and Somers, 2004)
[b] Number of Chebyshev background parameters used for the background fit

ρ and y_N reported in Table 6.3 are mean values and estimated standard deviations obtained by averaging 10 simulated diffractograms. Table 6.3 also contains the final R-values obtained when fitting the simulated diffractograms to the experimental XRPD patterns using a scale factor and a number of Chebyshev background parameters.

The **particle size** can be estimated for the experimental diffractograms using the Scherrer equation. This yields particle sizes around 500Å perpendicular to {111} and around 200Å in all other directions, thus a large peak broadening anisotropy that cannot be correlated to particle size anisotropy because the {111} planes are found in four different orientations throughout the crystal due to the cubic space group symmetry. As a compromise it was decided to use m=120 crystallites corresponding to a particle size around 360Å, see Figure 6.6 for a fit to the synchrotron data. Considering that it is more than difficult to even estimate the mean particle size, it was deemed unnecessary to spend extra computer time on modelling the particle size distribution that will inevitably be present in the samples.

The **deformation stacking fault probabilities** were previously determined in the conventional way from the peak shifts (Christiansen and Somers, 2004). Simulations using a number of α values close to these were tested for each sample, but in each case the value of α leading to the best fit with the experimental data lay within the estimated standard deviation. Therefore it was decided simply to use the conventional α values as input for the final simulations. From Table 6.3 it can be seen that the models improved when the deformation stacking faults were taken into account; the R-values dropped as compared to the α=0 models, especially for the y_N=0.61 synchrotron data.

The **twin fault probabilities** were found to be zero for all samples. With the choice of m=120 and the conventional α values as described above, the 200 peaks of the simulated diffractograms for y_N=0.36 and y_N=0.40 are already wider than experimentally observed, so twin faulting which only adds to the 200 peak width (Figure 6.3) cannot be an issue. For the y_N=0.58 and y_N=0.61 samples the experimentally observed peak widths are better described by the presence of screw dislocations.

The **screw dislocation densities** were determined by least squares minimisation of the difference between the experimentally determined peak widths and the peak widths predicted using the parameterisation of peak broadening effects outlined above. According to this approach the model did not improve by adding screw dislocations to the simulations of the y_N=0.36 and y_N=0.40 samples. For the y_N=0.58 sample a dislocation density of $2{\cdot}10^{15}\mathrm{m}^{-2}$ refined, while $\rho{=}4{\cdot}10^{15}\mathrm{m}^{-2}$ was estimated for the y_N=0.61 sample. The R-values of Table 6.3 confirm that the models did in fact improve when screw dislocations were added to the structural models of the samples with

Figure 6.6 m=120, R=0.0865

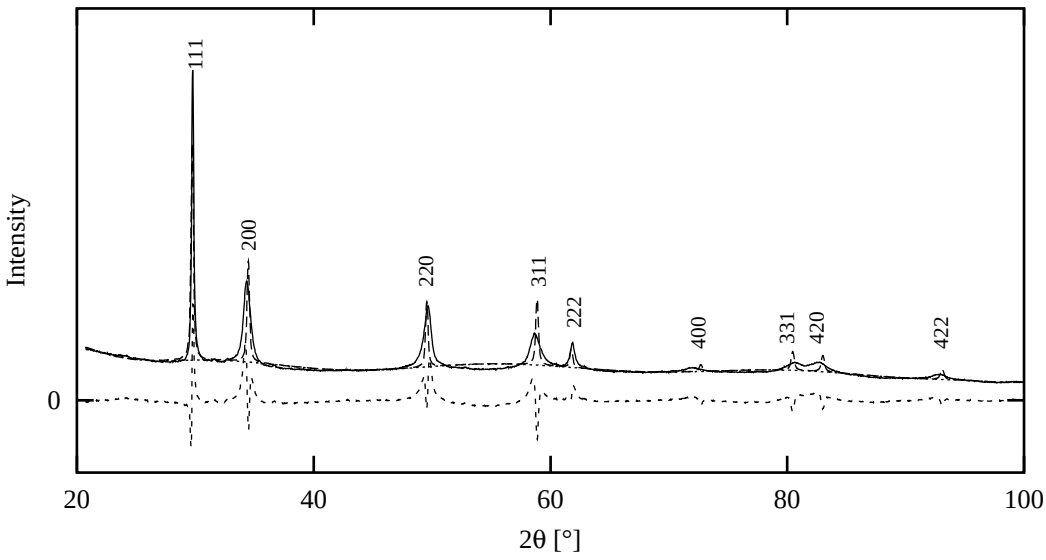

Figure 6.7 m=120, α=0.036(12), ρ=3.9(5)·10^{15}m^{-2}, y_{N}=0.6100(3), R=0.0551

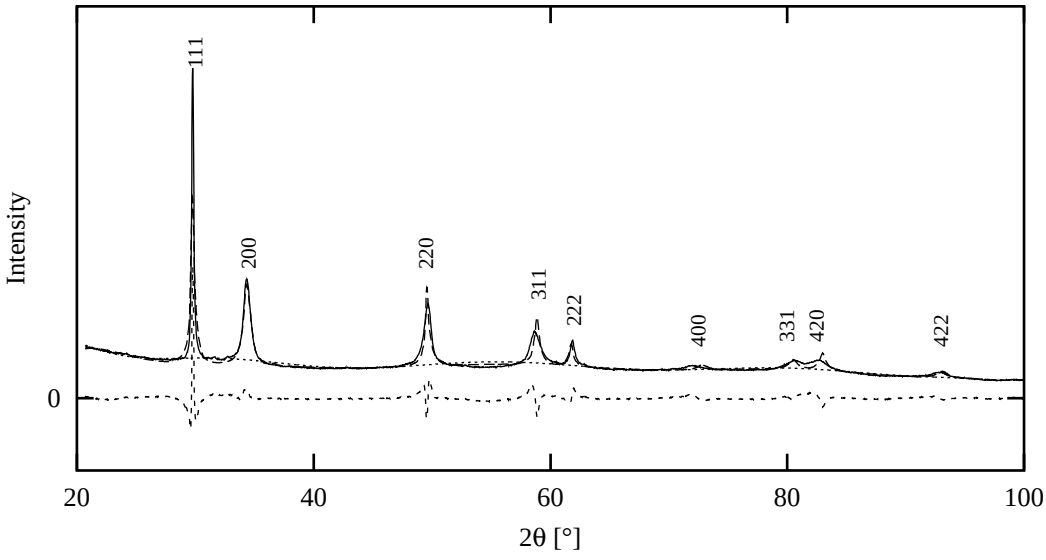

the highest nitrogen contents.

The **interstitial nitrogen occupancies** of the samples were determined using thermogravimetry, and these values were simply used as input for the simulations. As could be expected this lead to significant model improvements for all experiments, see Table 6.3 for R-values and Figure 6.7 for the final fit to the y_N=0.61 synchrotron data. It has long been known that the interstitial nitrogen atoms have a higher affinity towards Cr than towards Fe (Oda et al., 1990; Grujicic and Owen, 1995; Shankar et al., 1998; Bazaleeva, 2005). To test whether XRPD can be used to observe possible clustering of nitrogen around chromium, a model placing the nitrogen atoms in small clusters (55 atom cubeoctahedra) was tested. The resulting diffractogram was no different from the random nitrogen case, leading to the conclusion that it is impossible to detect nitrogen clustering by the use of XRPD.

6.1.4 Discussion

The first conclusion to be made is that the "fault free" lattice parameters are correct and that the structural models improve with the inclusion of deformation stacking faults. One of the main objectives for taking on the Debye approach was to check whether the numerical value of the traditionally determined α parameter actually corresponds to the deformation stacking fault probability, and based on the good correspondence between the two parameters this was found to be the case.

The experimentally determined XRPD patterns show extremely narrow 111 peaks corresponding to an unlikely particle size anisotropy since the {111} planes are oriented in four different directions throughout a crystal of FCC symmetry. The observed peak width anisotropies can be partly explained by the presence of screw dislocations in the atomic lattice since it was shown that the width of the 111 peak is affected much less by the presence of screw dislocations than most of the remaining peak widths.

From the widths of the 111 peaks in the experimental XRPD patterns it is obvious that the mean particle size of nitrogen expanded austenite is larger than the 360Å used for the simulations in the present study. Most likely a better fit would be obtained if the mean particle size was doubled and the peak width anisotropy was enhanced by increasing the screw dislocation density. However, calculation time is another non-negligible aspect in the choice of particle size; a m=120 simulation with y_N=0.6 can be performed within 48h on a 3GHz/1GHz standard PC, while doubling the mean particle size will increase the calculation time by a factor of 2^6=64. Hence it would no longer be feasible to test different parameters or average several diffractograms to obtain a distribution of α, ρ or y_N.

It is an approximation to model all atoms in the FCC framework as Fe, *c.f.* Table 6.1. Different atoms have different atomic radii which inevitably will result in local distortions of the FCC framework, distortions that were not considered in the simulations, but they are likely to be small if the atomic composition is random. The variations in scattering amplitudes and more importantly anomalous scattering contributions among the different atom types are other aspects that need to be considered. In order to quantify their importance, Rietveld refinements were carried out both modelling all atoms as Fe and using the correct atomic composition for AISI316 stainless steel. For the Co-data the refined thermal parameters increased by 20% in going from the Fe to the correct model, while the increase for the synchrotron data is hardly significant (2%). This agrees well with the observation that for the Co-data a better fit between simulations and experiments can be obtained if the thermal parameters are reduced. It was, however, decided to stay with the physically sound values of B_{Fe}=B_{N}=1Å^2 for all simulations.

If computational cost was not an issue it would be interesting to do another round of Debye simulations and test structural aspects such as: 1) Increasing the crystallite size along with the screw dislocation density to get a better fit to the anisotropic peaks widths, 2) Adding a particle size distribution, 3) Varying α, y_{N} and especially ρ in the search for a better fit to the experimental data, and 4) Modelling the FCC framework with the correct atomic composition to get the correct atomic radii, scattering factors and anomalous scattering contributions.

Taking all of these considerations into account the Debye approach, despite of the structural simplifications in order to make modelling feasible, offers valuable information about the structure of nitrogen expanded austenite that cannot be gained in any other way at present.

6.2 Combined XRPD and EXAFS characterisation

Whereas the nitrogen expanded austenite samples investigated in Section 6.1 were produced from foils, the following characterisation was performed for nitrided stainless steel flakes.

6.2.1 Nitriding of flakes

The stainless steel AISI316 flakes with thickness 0.4–1.2μm (325 mesh) were austenitised prior to nitriding by heating them at a rate of 30K/min to 1363K in an atmosphere of flowing H_2 (99.999%) followed by immediate cooling at a rate of 50K/min to the nitriding temperature. This annealing procedure ensured a full transformation of the cold worked flakes into austenite. Furthermore, the reducing hydrogen atmosphere removes the passive layer, consisting mainly of chromium(hydr)oxide, thus enabling subsequent nitriding of the flakes. Nitriding was carried out in a Netzsch STA449 simultaneous thermal analyzer for continuous monitoring of the sample weight. The nitriding temperature was 718K and nitriding was continued until a stationary weight gain was reached, suggesting that a para-equilibrium between nitrogen in the gas phase and in the stainless steel had been reached for the adjusted gas composition. The gas consisted of 9 vol.% N_2 and 91 vol.% NH_3, which corresponds to an infinitely high nitrogen activity (according to the dissociation equilibrium of ammonia). The flakes had to be exposed to the nitriding gas for 24h before a stationary weight was obtained. As compared to nitriding of stainless steel foils, where the surface can be activated by chemical dissolution of the passive chromium(hydr)oxide film followed by subsequent deposition of a Ni film of a few nanometers (Christiansen and Somers, 2006), the nitriding of the present samples proceeds rather sluggish. The reason for this could be that the H_2 activation at high temperature used in the present investigation is sensitive to the surface pollution, which will slow down the kinetics of nitrogen uptake. Furthermore, the flakes are produced by a ball milling method using organic lubricants, which can pollute the surface and make surface activation more difficult.

Nitriding under the above described conditions should give rise to a full transformation of austenite into nitrogen expanded austenite having an interstitial occupancy of y_N=0.61 (Christiansen and Somers, 2006). However, the overall nitrogen content in the as-nitrided sample (stationary nitrogen uptake) corresponded to y_N=0.51. Part of the batch of as-nitrided flakes was exposed to flowing hydrogen at 718K for 3h. This so-called denitriding

resulted in removal of the dissolved nitrogen atoms to y_N=0.18. During thermal exposure at 1363K the (de)nitrided flakes were partly sintered together in the crucibles, which necessitated some degree of mechanical processing in order to obtain a homogenous batch of powdered flakes for characterisation.

6.2.2 Characterisation methods

XRPD and Rietveld refinements

The XRPD data were collected using a Bruker D8 AXS diffractometer equipped with a Cr anode (λ(CrKα_1)=2.28962Å, λ(CrKα_2)=2.29352Å) operating in Bragg-Brentano mode. The different phases in the XRPD patterns were identified by means of search-match. In the subsequent Rietveld refinements the following parameters were refined: a scale factor, a Voigt peak profile parameter and lattice constants for each phase besides an overall 2θ zero shift and 3 Chebyshev background parameters. This gave a total of 18 parameters for both samples. The thermal parameters were set to B_{Cr}=B_{Fe}=B_N=1.0Å^2 for all phases.

For the expanded austenite phase an extra Voigt peak profile parameter coupled to the <111> direction was refined to account for the observed peak width anisotropy. This peak width anisotropy cannot be the result of anisotropic particle shapes because the {111} planes are found in four different orientations throughout the crystal due to the cubic space group symmetry. Rather it has been argued to result from the presence of deformation stacking faults and screw dislocations in the structure.

It should be noted that the nitrogen contents of the expanded austenite phases have not been refined, but rather calculated from the lattice parameter a (Christiansen and Somers, 2006). This was done to limit the number of parameters. For the denitrided sample the lattice parameter was outside the interval for which the linear relationship between a and y_N was determined, so the value of y_N=0.12 was estimated from an extrapolation towards the (y_N, a) pairs determined for y_N below 0.10. Finally the nitrogen contents of the martensite phase in the denitrided sample was set to 2 N atoms per 100 Fe atoms based on the c/a ratio (Cheng et al., 1990).

EXAFS

Cr and Fe K-edge EXAFS data were collected in transmission mode at MAX-lab beamline I811 equipped with a Si[111] double crystal monochromator (Carlson et al., 2006). Detuning to remove higher harmonics was performed. The samples were mounted on two pieces of tape, and the acquisition time was 70min per scan.

The analysis of the EXAFS data was performed in the WinXAS program (Ressler, 2004). For each sample 2–5 scans were averaged after energy calibrations performed using the E_0 values tabulated for Cr and Fe. Standard procedures were then used for the background subtraction, normalisation and spline fitting. The k-ranges used for the spline fittings and for the Fourier Transforms of $k^3\chi(k)$ are given in Table 6.4 and 6.5.

The phase and amplitude parameters used for the modelling of the EXAFS, which was performed in R-space, were obtained by FEFF7 *ab initio* calculations (Zabinsky et al., 1995). All samples were assumed to consist of a single cubic phase. In this way the crystallographic symmetry could be used to constrain the values of r_j together so that only one parameter, namely the cell constant which can easily be compared with tabulated values, was refined. Letting M denote either Cr or Fe, only paths corresponding to the first M–N shell (if present) and the first four M–M distances were added during the modelling. If a 3 atom multiple scattering path of the same r_j as the M–M path and a much higher value of $|f_j^{\text{eff}}|$ was found, this path was used on behalf of the M–M path to improve the fits significantly. Besides the cubic lattice constant, ΔE_0 and the values of σ_j^2 were refined. The amplitude reduction factor was maintained at S_0^2=1 for all refinements, because no literature values for similar systems were found.

The above described refinement procedure gave between 6 and 8 free variables (Table 6.4 and 6.5). It should be noted that both small deviations from the assumed cubic symmetry and the presence of additional phases with a similar local structure will result in increased values of σ_j^2, and that large values of σ_j^2 are in fact observed for all EXAFS refinements (Table 6.4 and 6.5). Information of additional phases obtained from other sources such as XRPD can be exploited to do a multi-phase refinement of the EXAFS data. The quality of the data is sufficient to justify the addition of more free variables, but the interpretation will be blurred by increasing correlations between the obtained parameters. From this point of view, and because the applied single cubic phase models are simple and easy to interpret, while the obtained residuals and fits (Figure 6.12) are as good as can be expected even from a multi-phase refinement, it hardly seems reasonable to engage in such.

Table 6.4 Cr EXAFS refinement data

as-nitrided	chromium nitride		CrN	F−4 3 m	
path	N_j	r_j [Å]	σ_j^2 [Å^2]	ΔE_0[eV]	S_0^2	R
Cr–N	6	2.06	0.0071	−0.35	1	10.0
Cr–Cr	12	2.91	0.0129			
Cr–Cr–N	12	4.12	0.0197			
Cr–Cr	24	5.05	0.0197	spline:	0.5–13.8Å^{-1}	
Cr–Cr–Cr	24	5.95	0.0209	FT:	3.0–11.0Å^{-1}	

denitrided	chromium nitride		CrN	F−4 3 m	
path	N_j	r_j [Å]	σ_j^2 [Å^2]	ΔE_0[eV]	S_0^2	R
Cr–N	6	2.07	0.0080	−0.25	1	12.0
Cr–Cr	12	2.92	0.0138			
Cr–Cr–N	12	4.13	0.0181			
Cr–Cr	24	5.06	0.0168	spline:	0.5–13.8Å^{-1}	
Cr–Cr–Cr	24	5.96	0.0183	FT:	3.0–11.0Å^{-1}	

Table 6.5 Fe EXAFS refinement data

as-nitrided	expanded austenite		γ-$FeN_{0.32}$	F−4 3 m	
path	N_j	r_j [Å]	σ_j^2 [Å^2]	ΔE_0[eV]	S_0^2	R
Fe–N	1.9	1.93	0.0064	6.54	1	11.9
Fe–Fe	12	2.73	0.0192			
Fe–Fe–N	3.8	3.86	0.0173			
Fe–Fe	24	4.73	0.0281	spline:	0.2–16.0Å^{-1}	
Fe–Fe–Fe	24	5.45	0.0368	FT:	4.2–13.0Å^{-1}	

denitrided	ferrite		α-Fe	I m 3 m	
path	N_j	r_j [Å]	σ_j^2 [Å^2]	ΔE_0[eV]	S_0^2	R
Fe–Fe	8	2.51	0.0104	7.39	1	12.5
Fe–Fe	6	2.90	0.0277			
Fe–Fe	12	4.10	0.0178	spline:	0.2–16.0Å^{-1}	
Fe–Fe	24	4.80	0.0140	FT:	3.3–14.9Å^{-1}	

6.2.3 Results

XRPD and Rietveld refinements

The recorded diffractograms are shown in Figure 6.8 and 6.9 along with the diffraction patterns of the different phases from the Rietveld refinements. For each sample four different phases were identified. The mass percentages of the different phases that can be derived from the scale factors are given along with the refined cell constants and final R_p values of the Rietveld refinements in Table 6.6. The corresponding nitrogen balances of the entire samples, determined from the mass fractions, are given in Table 6.7. For both of the investigated samples it should be noted that the diffraction peaks are generally were broad except for the 111 peak of expanded austenite. As illustrated in Section 6.1 many factors besides the particle size are likely to contribute to this observed broadening, for instance composition or stress variations, *i.e.* microstresses, as well as the presence of deformation stacking faults and screw dislocations.

The major component of the **as-nitrided** sample was determined to be an expanded austenite phase with y_N=0.50, as followed from the lattice parameter dependence on nitrogen content (Christiansen and Somers, 2006). CrN was found to be present in the as-nitrided sample with a mass fraction of 0.11, while the formation of CrN incorporating all of the chromium atoms would lead to a CrN mass fraction of 0.19. However, these two phases only comprise half of the total mass. The other half of the sample was found to consist of two different iron nitrides; FCC γ'-Fe_4N, and HCP ϵ-Fe_3N.

For the **denitrided** sample the phase with the largest mass fraction was found to be BCT martensite. Mechanical deformation of expanded austenite with a relatively low interstitial nitrogen content is known to result in martensite upon deformation (Venables, 1962). Mechanical deformation was introduced on removing the samples from the thermal analyzer, and was necessary because the flakes had sintered together during nitriding. In addition to martensite two austenite phases were identified. Judging from the lattice constants one phase is nitrogen-free austenite and the other is nitrogen expanded austenite with y_N=0.12. The final phase is CrN with a lattice constant slightly smaller than a=4.1480(5)Å (Nasr Eddine et al., 1977), suggesting that the nitrogen sublattice is not fully occupied. The mass fraction of CrN was determined to be 0.14, while the theoretical mass fraction corresponding to a total formation of CrN is 0.21.

Figure 6.8 Rietveld refinement of the as-nitrided sample

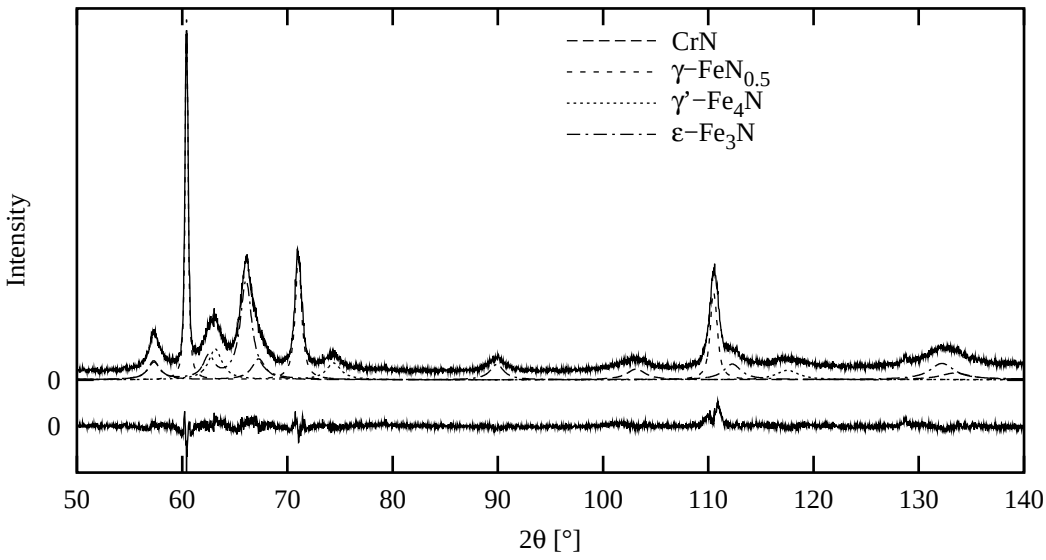

Figure 6.9 Rietveld refinement of the denitrided sample

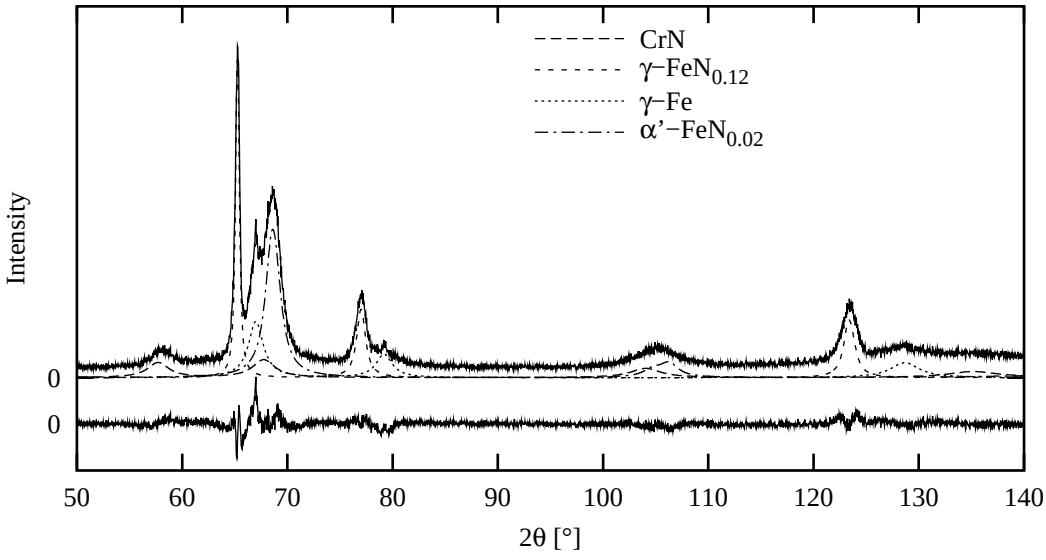

Table 6.6 Rietveld refinements

as-nitrided $R_p = 0.0883$				
	chromium	expanded	iron	iron
phase	nitride	austenite	nitride	nitride
abbreviation	CrN	γ-$FeN_{0.5}$	γ'-Fe_4N	ϵ-Fe_3N
structure	FCC	FCC	FCC	HCP
space group	F−4 3 m	F−4 3 m	P m −3 m	P 3 1 2
a [Å]	4.1356(8)	3.9425(2)	3.7892(7)	4.7784(13)
c [Å]				4.4141(8)
mass fraction	0.112(3)	0.388(3)	0.137(3)	0.363(4)
denitrided $R_p = 0.0912$				
	chromium	expanded		
phase	nitride	austenite	austenite	martensite
abbreviation	CrN	γ-$FeN_{0.12}$	γ-Fe	α'-$FeN_{0.02}$
structure	FCC	FCC	FCC	BCT
space group	F−4 3 m	F−4 3 m	F−4 3 m	I 4/m m m
a [Å]	4.1100(15)	3.6796(3)	3.5944(6)	2.8635(6)
c [Å]				2.8933(13)
mass fraction	0.135(4)	0.301(4)	0.199(5)	0.366(5)

Table 6.7 Nitrogen atoms per metal atom in the entire samples determined by various methods.

	thermo-balance	Rietveld refinement	EXAFS
as-nitrided	0.51	0.46	0.45
denitrided	0.18	0.17	0.19

EXAFS

From Figure 6.10 it can be seen that the chemical surroundings of Cr are identical for the as-nitrided and denitrided samples, while the environment of the Fe atoms is found to vary substantially with the nitrogen contents as illustrated in Figure 6.11. From the FT of the EXAFS data in Figure 6.12 it can be seen that the Fe atoms in the denitrided sample are found in nitrogen-free surroundings, whereas the octahedral interstices around the Fe atoms in the as-nitrided sample are partly occupied. As opposed to this the Cr atoms are found in nitrogen saturated surroundings for both samples. Thus the EXAFS data confirms that the nitrogen atoms have a much higher affinity towards Cr than towards Fe.

The single cubic phase fits to the **Cr EXAFS** data (Figure 6.12A and 6.12B) strongly suggest that the majority of the chromium atoms are present as CrN in both samples. The lattice constant refines to 4.12–4.13Å as compared to the literature value of 4.1480(5)Å (Nasr Eddine et al., 1977), while the refined values of σ_j^2 are all on the large side of the acceptable level. This indicates that a (small) fraction of the chromium atoms are found in chemical surroundings that are different from those of CrN; possibly within the expanded austenite, in the interface adjacent regions of the extremely small CrN particles or in the ϵ-Fe_3N of the as-nitrided sample. These findings are consistent with the Rietveld refinement which gave CrN mass fractions corresponding to trapping $\frac{2}{3}$ of the chromium atoms in CrN. The observed first neighbour Cr–N distances in the FT of the Cr EXAFS data (Figure 6.12A and 6.12B) are shorter than the expected first neighbour distances of both CrN (2.07Å), γ-$FeN_{0.5}$ (1.97Å, as-nitrided) and γ-$FeN_{0.12}$ (1.84Å, denitrided) because the phase shift ϕ_{ij} was not taken into account during the FT. If r_j of the outmost shell was constrained to the CrN lattice constant, the corresponding value of σ_j^2 became extremely large and the quality of the fit decreased dramatically. This value of r_j was therefore refined freely.

The local structure of **Fe** in the **as-nitrided** sample is found to be that of expanded austenite (Figure 6.12C). Refining the coordination number of N around the central Fe atom and constraining N_j of the Fe–Fe–N multiple scattering path to follow, the residual dropped from 14.5 to the final value of 11.9. For the Fe–N path the value of N_j=1.9, corresponding to y_N=0.32, resulted. However, the values of N_j, r_j and σ_j^2 determined by EXAFS do not correspond exclusively to the expanded austenite phase, they also reflect the two iron nitride phases that were identified from the XRPD analysis. This is the reason why the values of σ_j^2 are very large, except for the paths containing N where they correlate with the low occupancy.

Figure 6.10 Cr EXAFS

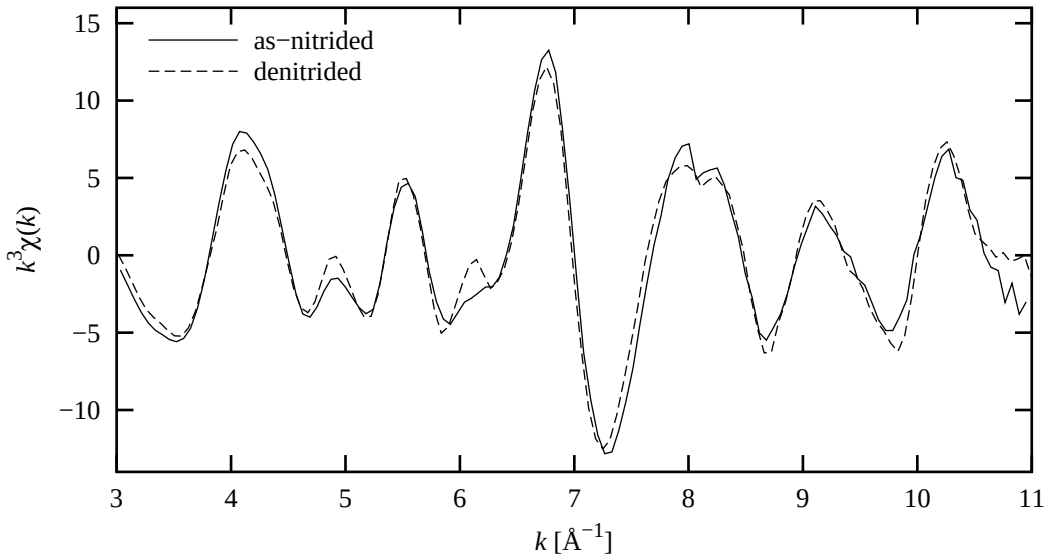

Figure 6.11 Fe EXAFS

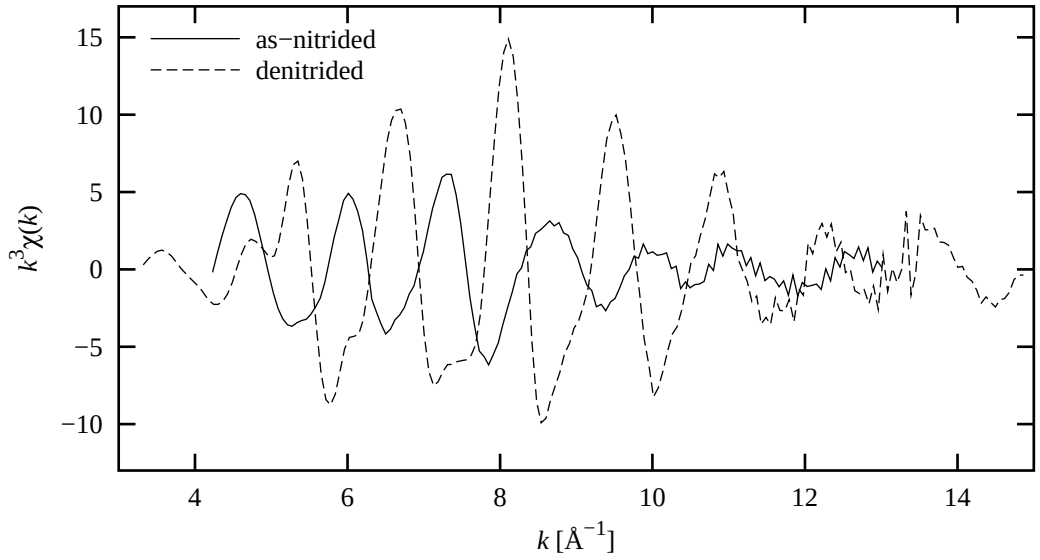

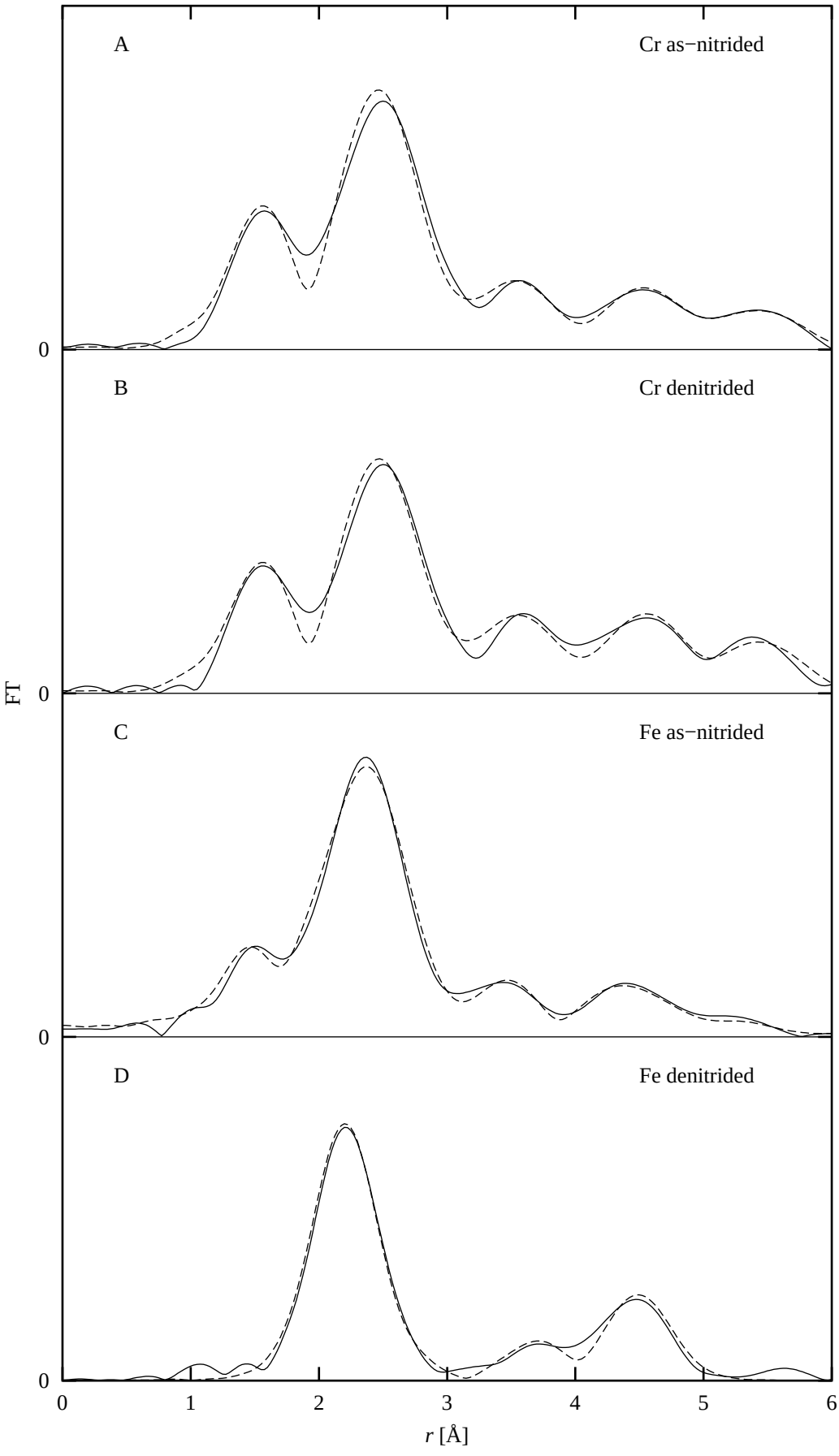
A
Cr as−nitrided
0
B
Cr denitrided
0
FT
C
Fe as−nitrided
0
D
Fe denitrided
0
0
1
2
3
4
5
6
r [Å]

Figure 6.12 Modelling of EXAFS Fourier Transforms

The FT of the **Fe** data for the **denitrided** sample (Figure 6.12D) does not contain the first Fe–N peak and it does not fit the FCC austenitic structure. Instead an acceptable identity can be found with the BCC structure of ferrite. As already argued the actual structure of the major phase is martensite, tetragonally distorted ferrite, but according to the Rietveld refinements the tetragonal distortion is almost negligible (c/a=1.01). For this reason, and because the process of constraining distances is more straightforward for cubic structures, ferrite was used for fitting the EXAFS data. The Rietveld refinements of the denitrided sample gave a mass fraction of austenitic phases of 0.50, while the mass fraction of martensite was determined to be 0.37. The fact that the fit to the EXAFS data is much poorer for the austenite FCC structure than for the ferrite BCC structure suggests that the sample used for EXAFS analysis was subjected to additional mechanical deformation during the preparation procedure. The coexistence of the martensite and austenite phases are reflected in the large values of σ_j^2 obtained from the fitting.

6.2.4 Discussion

Nitriding of thin stainless steel flakes for 24h results in the development of several phases. In addition to nitrogen expanded austenite also CrN, γ'-Fe_4N and ϵ-Fe_3N develop, yielding a total nitrogen content in the as-nitrided sample of 0.45–0.51 nitrogen atoms per metal atom (Table 6.7). This is significantly lower than the maximum solubility of y_N=0.61 for nitrogen expanded austenite, and it is a consequence of the formation of nitride phases during nitriding. CrN is expected to form prior to the iron based nitrides γ'-Fe_4N and ϵ-Fe_3N. The CrN development observed in the present samples could be associated with the relatively large surface area of the flakes, because CrN will most probably start to develop at the surface, where no strain energy effects are experienced upon nucleation. In the centre of the flakes expanded austenite is present. The development of CrN retracts Cr from solid solution in the austenite phase and effectively yields an austenitic structure rich in Fe and Ni. The iron based nitrides γ'-Fe_4N and ϵ-Fe_3N subsequently develop in the Cr denuded austenite as nitriding is carried out under conditions resulting in a high nitriding potential. Consequently, the mass fraction of nitrogen expanded austenite is lowered to 0.39.

After denitriding, the nitrogen content in expanded austenite is significantly lowered, resulting in a y_N of approximately 0.12 provided that the known linear relationship between nitrogen content and lattice parameter of expanded austenite (Christiansen and Somers, 2006) can be assumed valid in this (extrapolated) concentration range. This means that loosely bound nitrogen has been retracted and only tightly bound nitrogen resides in the expanded austenite; ostensibly the lower content of chromium in solid solution is responsible for the lower nitrogen content of tightly bound nitrogen, as compared to expanded austenite without CrN precipitates. The iron based nitrides γ'-Fe_4N and ϵ-Fe_3N present in the as-nitrided sample have disappeared and instead a nitrogen free austenite phase has developed. This change is reflected in the Fe EXAFS data where the chemical surroundings of the Fe atoms are found to change after denitriding, which for a large part can be attributed to the reduction of the formed iron nitrides. The presence of both expanded austenite and virtually nitrogen-free austenite is an immediate consequence of the precipitation of CrN, which obviously proceeds inhomogeneously. In the surrounding matrix the chromium content is lowered and no enhanced nitrogen content is dissolved. As a consequence of mechanical processing for sample preparation a large fraction of the sample is converted into martensite with relatively low nitrogen contents. The formation of martensite is more likely to occur in regions with low nitrogen content. Disregarding the presence of nitrides, a large fraction of nitrogen in the expanded austenite can be retracted and nitrogen residing in Fe-based nitrides in the as-nitrided sample can be fully retracted. The fraction of nitrogen bound as CrN and the fraction remaining in the expanded austenite after denitriding are not retractable in flowing hydrogen.

Rietveld refinements indicate that the mass fractions of CrN by XRPD are 0.11 and 0.14 for the as-nitrided and denitrided samples, respectively, while the corresponding theoretical values for the mass fractions of CrN if all chromium atoms should reside in the precipitates are 0.19 and 0.21. This implies that only $\frac{2}{3}$ of the chromium atoms in both samples are associated with CrN precipitates that display coherent XRPD. The remainder of the chromium atoms is associated with other phases. For the as-nitrided sample a fraction of the chromium atoms is expected to be found in the expanded austenite phase and in the ϵ-Fe_3N nitride. For the denitrided sample the remaining fraction of chromium should be found in the expanded austenite and in the deformation induced martensite phase. However, according to EXAFS the majority of the chromium atoms are associated with a Cr–N bond distance closely related to that of the chemical compound CrN in both the as-nitrided and denitrided sample. Hence, it is likely that more than $\frac{2}{3}$ of the chromium atoms should be bound as CrN. This implies that a fraction

of the formed CrN does not diffract coherently and cannot be detected with XRPD, only with short-range-order techniques such as EXAFS. The fact that almost all chromium atoms are associated with CrN is in opposition to the traditional interpretation of the formation of expanded austenite, which assumes that chromium is available in the austenite lattice for "trapping" of nitrogen without forming (chromium)nitrides. It is evident that expanded austenite still forms with high nitrogen contents even though the austenite matrix is seemingly denuded of chromium. An explanation to these observations is hypothesised in the following.

Nitriding of ferritic steels alloyed with a low contents of strong nitride formers *viz.* Cr, V, Ti, Mo, *etc.* can give rise to a significant hardening effect and abnormal nitrogen/metal ratios, higher than what can be accounted for by equilibrium metal nitride precipitates. This is due to formation of so-called mixed substitutional-interstitial clusters (MSIC), which are coherent platelets or clusters (GP zones) of nitrogen and strong nitride formers analogously to the GP zone formation in aluminium alloys (Jack, 1975; Jones et al., 1979). A matrix containing MSIC, *i.e.* a non-random solid solution, has the same unit cell as a random solid solution of the same concentration and only when precipitation occurs does the lattice parameter change to that of the depleted solid solution (Jones et al., 1979). Hence XRPD does not reveal the presence of the MSIC, only an increased lattice parameter. The prerequisite for this phenomenon is a large difference in the diffusivities of the interstitial and substitutional atoms. The same phenomenon possibly also occurs in nitrided austenitic Fe-35Ni-V,Nb alloys at 600–700°C (Driver et al., 1972).

In the present investigation the analogy to MSIC formation is straightforward; nitrogen in stainless steel at temperature lower than 723K diffuses many times faster than the substitutional elements *viz.* Cr. XRPD can only account for a part of the chromium atoms as CrN, whereas the remaining part does not give coherent diffraction. This could suggest the presence of mixed substitutional-interstitial solute-atoms clustering in austenitic stainless steel, thus leading to an enhanced solubility of nitrogen. MSIC of Cr and N could lead to abnormal solubility nitrogen in austenite (Fe surroundings). The ratio of N to Cr and Mo is approximately 3:1 in expanded austenite (Christiansen and Somers, 2006), which is somewhat similar to the ratios found for low-alloyed ferritic and austenitic alloys (Driver et al., 1972; Jones et al., 1979). Unfortunately, the present data are flawed by the fact the expanded austenite was not obtained homogeneously, but is influenced by the presence of both nitrides and mechanically induced martensite phases. Thus in order to verify or discard the above hypothesis further work is necessary; such work is under way.

6.3 Final conclusions

Debye simulations offer the opportunity to test how the XRPD patterns of nitrogen expanded austenite are affected by the presence of stacking faults and screw dislocations in combination, structural aspects that cannot be modelled using traditional XRPD analysis methods such as Rietveld refinements. The method is, however, limited by the particle size because the computational cost goes as the 6^{th} power of the average dimension. In the present case a mean diameter of 360Å was the limit. The simulations confirm the proposed presence of deformation stacking faults in homogeneous stress-free samples of nitrogen expanded austenite (Christiansen and Somers, 2004). The deformation stacking fault probability giving the best fit to the experimental XRPD pattern corresponds to the value conventionally determined from the peak shifts within the estimated standard deviation. There is no evidence to suggest that the structure of nitrogen expanded austenite contains twin or growth faults. Modelling screw dislocations into the structure of nitrogen expanded austenite results in diffraction patterns with peak width anisotropies that resemble the experimentally observed anisotropies. The fits to the experimental XRPD patterns show that the screw dislocation density increases with increasing interstitial nitrogen occupancy. The actual value of the screw dislocation density correlates strongly with the particle size and a better fit can probably be obtained if both are increased. Simulations of different ways to distribute the interstitial nitrogen atoms have shown that it is impossible to distinguish between clustering and a random distribution by means of XRPD.

Low temperature homogenously nitrided and denitrided micrometer-sized AISI316 stainless steel flakes were characterised by XRPD and EXAFS. Nitrogen expanded austenite was obtained in both the as-nitrided and denitrided samples, together with several other phases including CrN. The local structure of the Cr atoms was largely unaffected by denitriding in flowing hydrogen, whereas the Fe atoms experienced a change in chemical surroundings. Furthermore the local structure of the majority of Cr atoms was found to conform to the bond length of the chemical compound CrN, although only a fraction of the Cr atoms could be detected as CrN with XRPD. A possible explanation for this observation could be a phenomenon generally related to low-alloyed ferritic steel *i.e.* formation of mixed substitutional-interstitial clusters.

Chapter 7

Multiwall carbon nanotubes

The multiwall carbon nanotube (MWCNT) is no doubt the superstar molecule of nanoscience and nanotechnology. The tubes have a nanoscopic diameter (typically 1–50nm) and a microscopic length (up to 1mm), they are extremely strong and flexible, and they may act as either semiconductors or conductors depending on type. The suggested applications are numerous and include as different uses as: hydrogen storage, nanoelectronics, controlled drug delivery, and artificial muscles to mention a few. More than 25 years have passed since the discovery of MWCNTs was first reported along with a preliminary structural characteristic based on TEM and electron diffraction (Iijima, 1991). Ever since that time it has been obvious that the properties of MWCNTs are intimately linked to their structure, thus the ability to characterise a sample in a fast, cheap and reliable manner before taking further action is of vital importance for all applications.

Structural studies using TEM are relatively fast and very illustrative because they give an actual image of the structure. However, the technique suffers from the fact that it is a local probe and therefore unable to address the structure of the bulk. XRPD is the obvious choice of a global probe; even though the tubes are non-crystalline they display a periodic structure and thus give rise to distinct diffraction peaks. The interpretation of the diffraction pattern in terms of the relevant MWCNT structural properties is, however, not straightforward because of the non-crystalline nature of the samples.

Debye simulations have the potential to overcome this barrier considering that the XRPD pattern can be calculated for any scattering object irrespective of (lack of) symmetry. Even though MWCNTs are nanosized and powerful computers are easily accessible, it is too time consuming to perform simulations varying all relevant properties until a satisfactory fit is found for every new sample. Therefore the idea came about to construct a

large library of simulated MWCNT diffraction patterns covering a wide range of structural properties and then refer all experimental patterns to this.

During the construction of the library a number of challenges were encountered. First of all it was necessary to write a new version of the Debye program because the standard program described thus far can only be used for crystalline samples. For the design of the program it had to be defined which properties were of importance, both obvious things such as the dimensions of the tubes (length, diameter and wall thickness – both number of layers and interlayer spacing), but also more complex matters like chirality and the question of whether the MWCNTs are scrolls or built from concentric cylinders. Experimental XRPD patterns of MWCNT samples with variable purity and size specifications were collected in order to get an idea of the range of peak widths and asymmetries to be covered by the simulations. A thorough analysis of the effects of the various structural properties on the diffractograms was performed and the conclusions made from this study were used in a fitting approach to determine the structure of the MWCNT samples from the experimental XRPD patterns. The analysis and fitting results were presented as a poster at EPDIC-9 in Prague 2004 and summarised in the proceeding given in Appendix C.2 (Oddershede and Ståhl, 2006).

Based on the above described simulations and the MWCNT structural properties estimated from the XRPD patterns it was chosen to construct a library consisting of a total of 750 diffractograms (5 different radii, number of layers and interlayer spacings and 6 different lengths). As the analysis of the structural properties revealed that it is difficult to separate the diffraction effects arising from different properties, especially the diameter and the length, it was decided to perform a Principal Component Analysis (PCA) on the library. The hope was that the PCA method would be able to differentiate between the effects arising from the different properties, and eventually be of use in the determination of structural properties for real MWCNT samples. The findings of the PCA study were published in a special issue of Zeitschrift für Kristallographie devoted to State of the Art of Powder Diffraction, see Appendix C.3 (Oddershede et al., 2007). The contribution was invited based on the EPDIC-9 proceeding and it even made the front cover.

7.1 X-ray characterisation of MWCNTs

The idea of using Debye simulations to characterise the bulk structure of MWCNTs is not new, several studies of this type have already been reported (Koloczek et al., 2001; Koloczek and Burian, 2004; Koloczek et al., 2004; Koloczek et al., 2005). The simulated XRPD patterns have been compared to derive the effects of the different structural properties, to synchrotron XRPD data collected at λ=0.1067Å (Szczygielska et al., 2000) and λ=0.13Å (Hawelek et al., 2005), and to wide angle pulsed neutron data extending to $Q_{\max}$=60Å^{-1} (Burian et al., 2004). Furthermore, molecular dynamics simulations at different temperatures and defect concentrations have been combined with both Debye simulations and radial distribution function analysis, and comparisons with experimental neutron and XRPD data have been performed (Bródka et al., 2006; Bródka et al., 2007).

All of the experimental MWCNT diffraction data previously compared to Debye simulated XRPD patterns were originally collected to be used for radial distribution function analysis. The reduced radial distribution function (often also referred to as the pair distribution function or simply the PDF) is given as the Fourier Transform of the isotropically averaged scattering function:

$$4\pi r\,[\rho(r)-\rho_0] \;=\; \frac{2}{\pi}\int_0^{Q_{\max}} Q\,[\frac{I(Q)-f^2(Q)}{f^2(Q)}]\,\sin(Qr)\,W(Q)\,dQ \qquad (7.1)$$

where $W(Q)$ is the Lorch window function which reduces termination ripples and $Q_{\max}$ must be as large as possible to avoid spurious ripples (Burian et al., 1999a; Burian et al., 1999b; Dore et al., 2000; Szczygielska et al., 2000; Burian et al., 2004; Burian et al., 2005; Hawelek et al., 2005). The MWCNT PDFs were shown to be intermediate between the PDFs of graphite and turbostratic carbon. For small values of r the MWCNT PDF closely resembles that of graphite, indicating that the short range order (stacking of perfect graphene sheets) of the two compound is similar. For larger values of r a progressive deviation between the two PDFs is observed, presumably because the interlayer correlations in the MWCNTs are only preserved over a few layers due to the curvature of the graphene sheets.

When diffraction data are available beyond Q=20Å^{-1} it is natural to use the entire Q-range for comparisons with Debye simulated XRPD patterns. However, the statement of the present investigation is that the standard crystallographic Q-range between 1Å^{-1} and 6Å^{-1}, accessible with a wavelength of $\lambda\approx$1.5Å which in general gives better resolved diffraction peaks, carries sufficient information to enable a characterisation of the MWCNT bulk structure.

7.2 MWCNT structure

Both graphite and MWCNTs consist of honeycomb graphene sheets, but whereas the sheets are stacked along the *c*-axis in graphite (Table 7.1), they are rolled to build the carbon nanotubes (Figure 7.4). The term multiwall refers the situation where the tube walls consist of several graphene layers, as opposed to singlewall carbon nanotubes, SWCNTs. The MWCNT diffractograms closely resemble that of graphite and are therefore indexed accordingly, *c.f.* Figure 7.1 which shows the preliminary MWCNT diffractogram recorded at λ=1.509Å on an unspecified MWCNT sample to determine the experimental conditions (Section 7.5.2) and the Debye simulated diffractogram for a graphite crystal consisting of 20 graphene layers of 500Å×500Å. Many different models have been suggested to explain the course of the XRPD patterns, the simplest of which have been of the disordered graphite type refining structural properties such as the interlayer spacing, the crystallite size and the ordering within a single graphene layer (Shi et al., 1993; Reznik et al., 1995; Pasqualini, 1997).

In the MWCNT diffractograms peaks of $hk0$ (within a layer) and $00l$ (between layers) type dominate due to the limited correlation between different graphene sheets also referred to as turbostratic disorder (Reznik et al., 1995; Burian et al., 1999b; Lambin et al., 2002). The graphite 100 (2.95Å^{-1}) and 110 (5.11Å^{-1}) peaks are found in more saw-toothed versions due to the turbostratic stacking (Zhou et al., 1994; Maniwa et al., 2001) and/or the curvature of the graphene sheets (Lambin et al., 2002), whereas the peaks corresponding to the interlayer spacing, 200 (1.85Å^{-1}), 400 (3.70Å^{-1}), *etc.* are shifted to slightly lower Q-values than for graphite, reflecting the fact that the spacing between the multiple walls of the tubes is slightly larger (3.40Å) than the interlayer spacing of graphite (3.35Å).

Table 7.1 Crystallographic data of graphite (Wyckoff, 1963; Wikipedia)

chemical formula	$C_{graphite}$
cell setting, space group	hexagonal, $P6_3/mmc$
a [Å]	2.456
c [Å]	6.696
V [Å^3]	35.0
Z	2

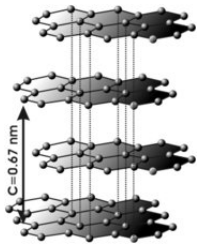

Figure 7.1 MWCNT and graphite diffractograms showing the graphite indices

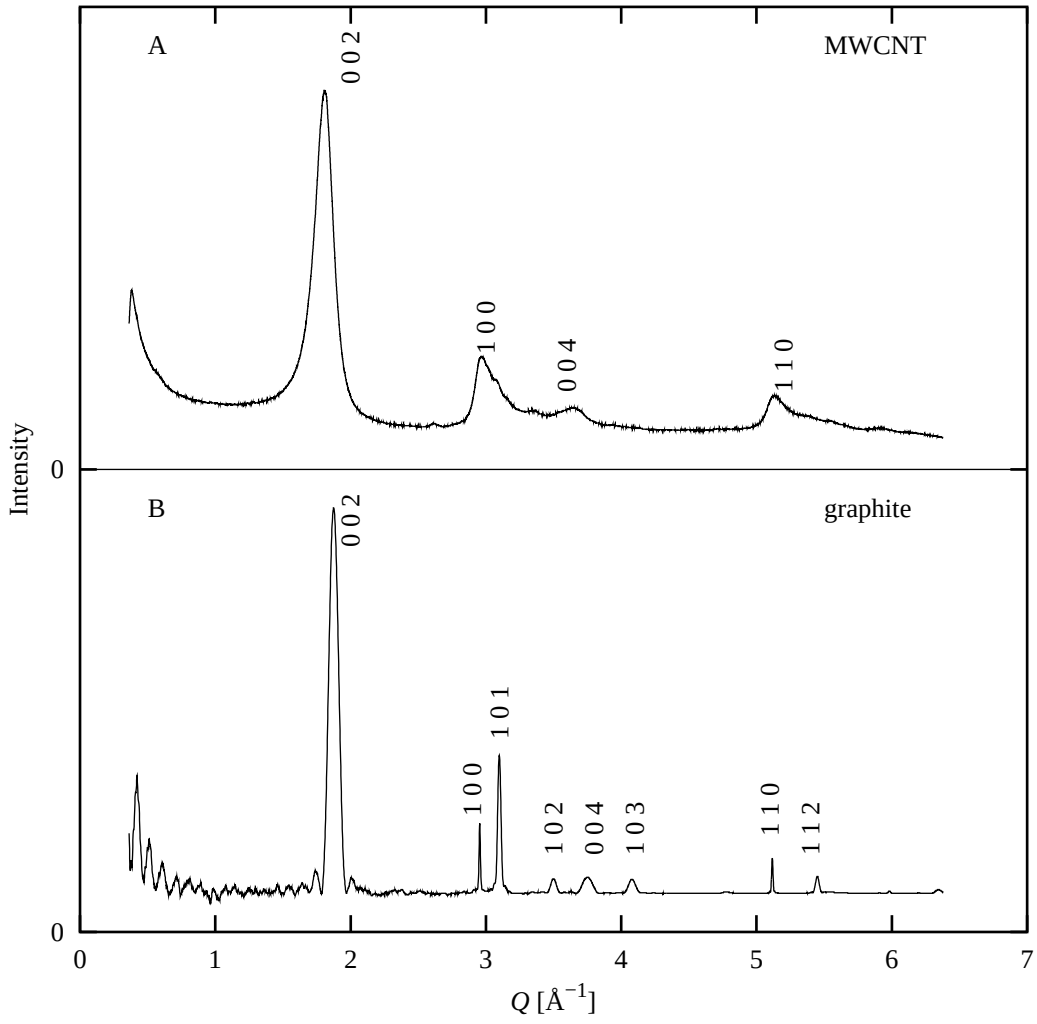

In the following the two main features that distinguish the MWCNT structure from that of graphite, namely the rolling direction determining the chirality of the tubes and the stacking of subsequent walls, either as concentric tubes or as scrolls, are described in detail.

7.2.1 Chirality

In order to construct a seamless cylinder from a graphene sheet the circumference of the cylinder must be chosen to correspond to a distance between two symmetry equivalent atoms in the graphene honeycomb lattice (White et al., 1993; Reznik et al., 1995; Lucas et al., 1996; Lambin and Lucas, 1997; Pasqualini, 1997; Amelinckx et al., 1999), *c.f.* Figure 7.2. The circumference vector C is defined by the pair (L,M) where L is the number of graphite unit cell lengths a in the horisontal direction and M is the number of a's in the direction making a 60° angle with the first. Thus the vector C given in Figure 7.2 corresponds to (L,M)=(10,4).

Figure 7.2 Definition of the MWCNT chiral angle α (Lambin and Lucas, 1997)

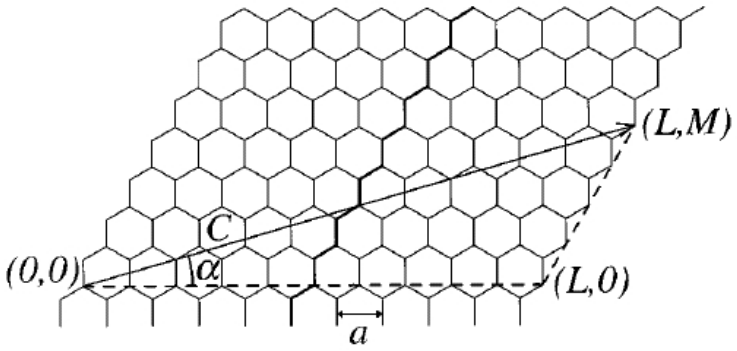

Figure 7.3 MWCNT sections for various chiral angles

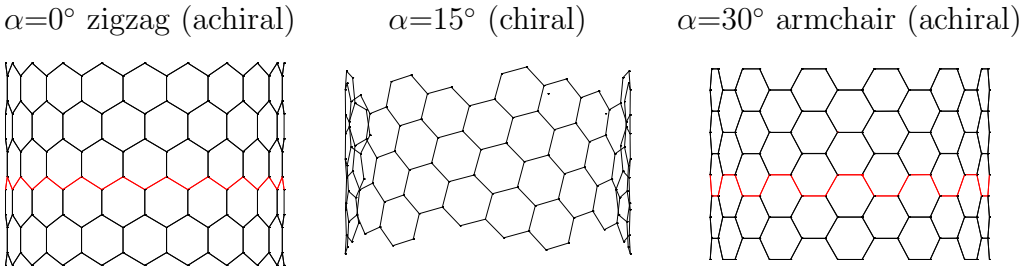

The chiral angle α is defined as the angle from (L,0) to (L,M), where $0 \leq M \leq L$, because these values of M are the only non-degenerate ones. This means that $0° \leq \alpha \leq 30°$. The two extremes M=0 (α=0°) and M=L (α=30°) correspond to lines of inflection in the graphene sheets and the resulting nanotubes contain the same type of mirror planes perpendicular to the cylinder axis, *c.f.* Figure 7.3. These tubes are achiral and have for obvious reasons been given the nicknames zigzag and armchair, respectively. For comparison a chiral or helical tube with α=15° is also given in Figure 7.3.

7.2.2 Concentric or scroll

The question of whether MWCNTs are built from concentric cylindrical tubes (Figure 7.4A) or as scrolls (Figure 7.4B) is still a matter of dispute. A variety of different approaches have been taken, among these also Debye simulations as shown later, but it has not been possible to draw any definitive conclusions as to the rolling characteristics (Zhou et al., 1994; Reznik et al., 1995; Bandow, 1997; Cumings and Zettl, 2000; Maniwa et al., 2001; Xu et al., 2001).

Figure 7.4 Rolling characteristics of MWCNTs, concentric (A) or scroll (B)

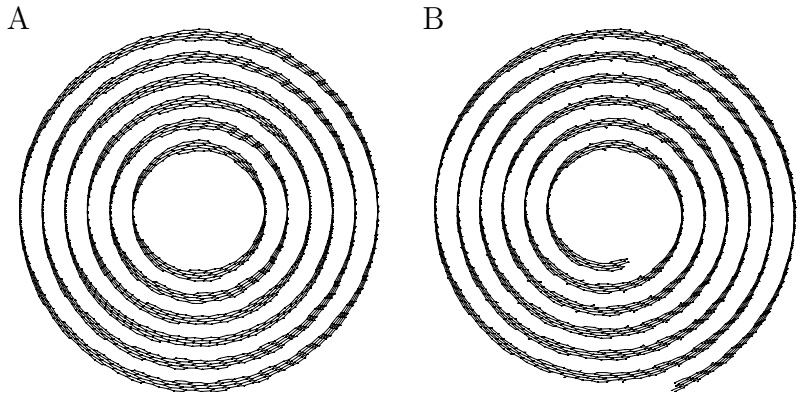

7.3 Program design

The program written to calculate the diffracted intensities for the MWCNTs by means of the Debye equation takes as input a number of the structural properties that will be defined in the following and calculates all the atomic positions corresponding to these structural specifications. No symmetry relations are used when calculating the interatomic distances and their multiplicities before the diffractogram calculation is performed according to (4.2), so for larger structures the program performs quite slowly. However, when the tubes are helical and the walls consist of several graphene layers (as is in principle always the case), the repeat distance along the cylinder axis can become extremely long and of variable length from layer to layer, so actually there is not much – if anything – to be gained from symmetry.

The C–C distance was taken to be 1.42Å as for graphite, while the thermal displacement parameter was set to B_{C}=2Å^2 as for C_{60} fullerenes at room temperature (Chow et al., 1992; Bürgi et al., 1993; Chen et al., 2002). To define the dimensions of the tubes the following properties were chosen as input for the program: The tube length l, the inner radius r, the number of graphene layers comprising the walls n, and the interlayer spacing between these d. From these properties the outer diameter *od* can easily be calculated for comparison with TEM observations.

If the tubes are scrolls a pair of (L,M) defining the rolling direction and the chiral angle must also be input, whereas in the case of concentric cylinders the desired n values of (L,M) are determined as those giving the best agreement with the radii $\{r,\ r+d,\ \ldots,\ r+(n-1)\mathrm{d}\}$. From this it is obvious that in the case of concentric cylinders it is impossible to control the values of both the chiral angle and the wall spacing. If it is chosen only to accept a small deviation in d as in the present implementation, one can of course start to search for the correct length of the circumference vector (L,M) around the desired value of α, but in the end a substantially different value of α is often needed to obtain an desired accuracy in d, and *vice versa* (Kociak et al., 2003).

In the coordinate system chosen to describe the MWCNT the z-axis runs through the centre of the tubes and the atomic coordinates referring to this axis range from 0 to l. The program offers the opportunity to model the tube as being bent into some input fraction of an entire circle. The corresponding radius of curvature r_c is then calculated and compared to the outer radius of the tube. To make sense r_c must be substantially larger than the tube radius, here a factor of 3 was chosen as the limit. The tube is then wrapped around the line $(x,r_c,0)$ so that the x-coordinates are unchanged whereas the y- and z-coordinates are modified.

The Debye program was equipped with a routine for writing all atomic coordinates into an input file for the molecular graphics program ATOMS (Dowty, 2000). In this way it was possible to check that all the structural properties of the MWCNTs were interpreted correctly before concentrating on the resulting diffractograms. Figure 7.3 and 7.4 are produced in this way.

7.4 Simulations

In the following it is described how the diffraction patterns change when the different MWCNT structural properties are varied one at the time. A relatively small standard size was chosen for the simulations to save CPU time: l=100Å, r=10Å, n=6, and d=3.40Å. For all simulations λ=1.509Å was used because this was the synchrotron wavelength at which the first experimental XRPD data were collected. All diffractograms are scaled to account for the different number of atoms and shown as a function of Q to facilitate comparison of simulations and experiments performed at different wavelengths.

7.4.1 Chirality

As noted previously it is only possible to test the effects of varying the chiral angle with a fixed interlayer spacing in the case of scroll type MWCNTs. From Figure 7.5A it is clear that the value of the chiral angle greatly affects the appearance of the diffractogram when the diameter of the tube is small; peaks corresponding to honeycomb lattice repeat distances directed along the length of the cylinder are extremely narrow (*c.f.* in particular the zigzag 100 and armchair 110 peaks), whereas peaks corresponding to lattice directions that are curved along the surface of the scroll are substantially broadened. Figure 7.5B shows that the effect is less pronounced for tubes with larger diameter (same values of l, n and d), but nevertheless still present contrary to the statement (Koloczek and Burian, 2004): "*. . . for wider carbon nanotubes no conclusion about chirality can be drawn from analysis of their diffraction patterns*". This conclusion was reached by comparing diffractograms for SWCNTs with diameters of 7Å and 70Å for three different values of α over the full Q-range up to $Q_{\max}$=24Å^{-1}, but Figure 7.5 unambiguously shows that the differences are in fact visible for even larger diameters if a more limited Q-range is consulted.

Considering that it is impossible to control the chiral angle during synthesis at the moment, as opposed to the dimensions, which to some extent can be controlled via the choice of catalysts (Liu et al., 2004; Zhang et al., 2005), α=15.3° corresponding to a tube circumference along (8,3) for scroll type MWCNTs was chosen as a reasonable average value for all simulations. Comparisons with the experimental diffractograms in Figure 7.11 support this choice.

Figure 7.5 Simulations showing the effects of varying (L,M) and thus the chiral angle α for scroll type MWCNTs with outer diameters of 55Å (A) and 135Å (B)

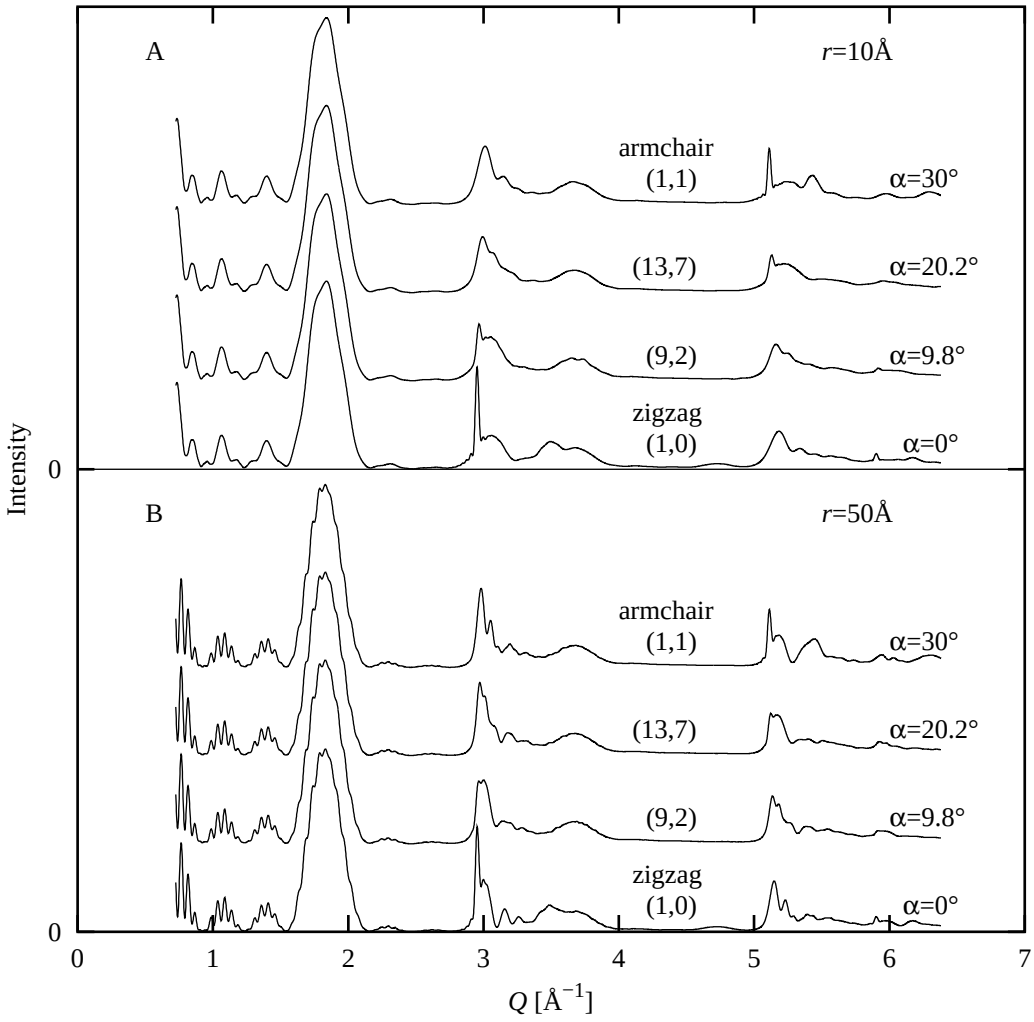

7.4.2 Concentric or scroll

In Figure 7.6 the PDF of a concentric and a scroll MWCNT with identical dimensions are shown. It is evident that the ripples in the PDF of the concentric tube arise because certain distances ($2(r+md)$, $m \in \{0,1,\ldots,n-1\}$) are overrepresented compared to others ($2(r+(m+\frac{1}{2})d)$). The ripples in the concentric PDF are in line with the previous observation that concentric cylinders with a very constant spacing d between adjacent cylinders give rise to a splitting of the interlayer $00l$ diffraction peaks (Koloczek and Burian, 2004). In Figure 7.7 the diffractograms corresponding to the PDFs are given, and the presence of the concentric cylinder ripples can be verified in the lower diffractogram.

Figure 7.6 Pair distribution function of concentric and scroll MWCNTs

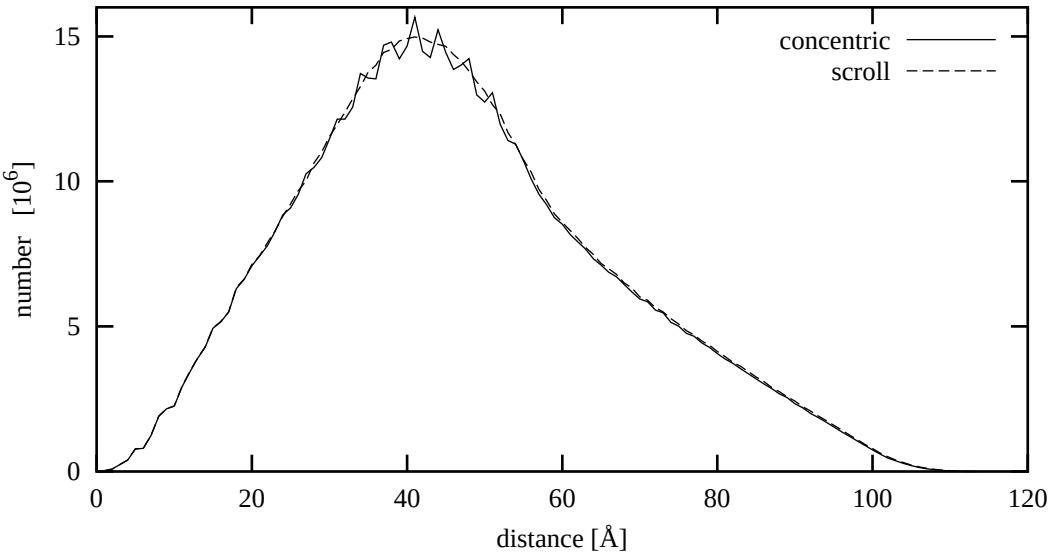

However, it can easily be shown that the positions of the ripples depend on the value of r, the inner radius, and that these splittings average out if a continuous distribution of different radii (a very realistic model of a true sample) is applied. The diffractogram corresponding to the concentric average is also shown and must be compared to the diffractogram simulated for a single scroll type MWCNT with a radius equal to the mean of the distribution used for the concentric average. As there is hardly any difference between these two, the conclusion must be that it is not possible to distinguish be-

tween averaged concentric cylinders and scrolls from a standard diffraction experiment.

Figure 7.7 Concentric or scroll type MWCNTs?

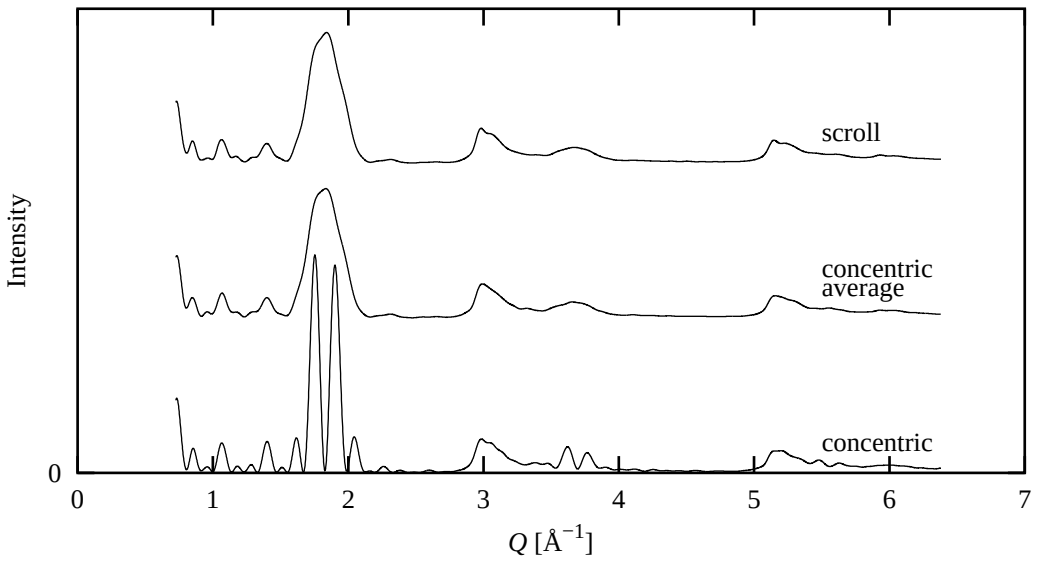

Since the scroll type simulations are much faster to perform because no average is required, and since only this type of simulations offer the opportunity to control the chirality, it was decided that all simulations performed in the present study should be for scroll type MWCNTs.

7.4.3 Length and diameter

The effects of varying the outer dimensions, the length or the diameter of the tubes, for fixed values of α, n and d have already been extensively described (Koloczek and Burian, 2004), but a short summary will be given here. Elongation of the tubes give sharper $hk0$ in-plane peaks as a simple size effect, *c.f.* the Scherrer equation (3.3) and Figure 7.8. Increasing the diameter has roughly the same effect, so from a visual inspection of the diffractograms only one size parameter corresponding roughly to the total number of scatterers can be determined. The length to diameter ratio must be calculated after assigning a reasonable value to one of the dimensions, typically the diameter since this is most easily estimated using TEM.

Figure 7.8 Simulations of bent MWCNTs

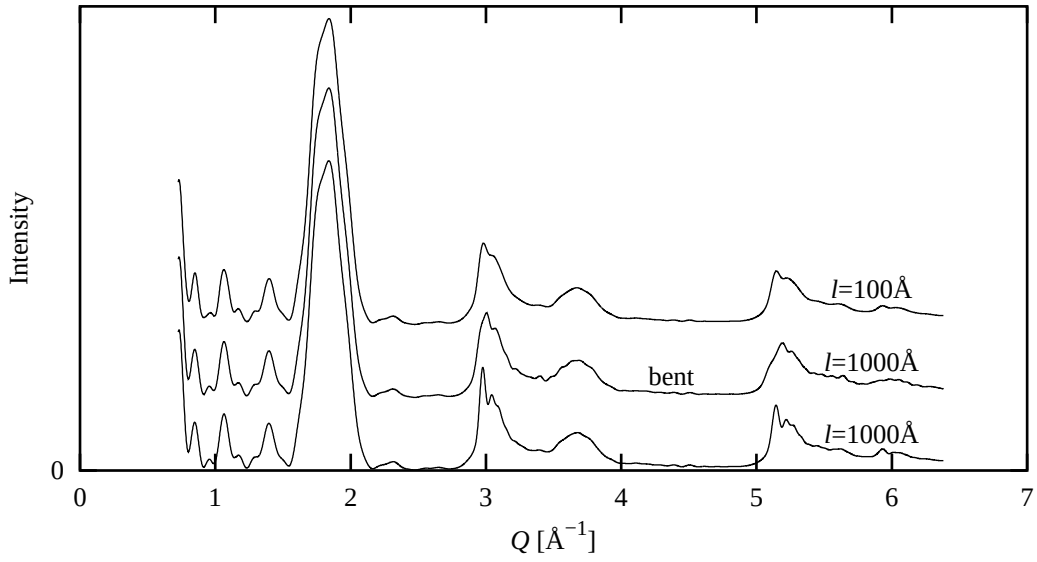

According to TEM the diameter of the MWCNTs is in the nanoregime while the length is of the order 1μm, but interpretation of the XRPD experiments inevitably leads to the conclusion that for the diameter to be nanoscopic the length must be of the order 100Å (Zhou et al., 1994; Koloczek et al., 2004) or even as short as 12Å (Koloczek et al., 2005). Based on analysis of TEM images a high concentration of defects has been suggested as the explanation to this discrepancy between physical dimension and coherent scattering length (Zhou et al., 1994). However, bending of the tubes is another possible explanation as seen from the simulations in Figure 7.8. Here it is illustrated how the diffraction pattern from a tube with a length of 1000Å resembles that of a tube with a length of only 100Å if the longer tube is bent into one tenth of a circle (corresponding to r_c=1600Å, *c.f.* for instance the nano15 TEM image in Figure 7.10), thus bending of a MWCNT makes it appear shorter in a XRPD experiment.

7.4.4 Wall structure

The term wall structure covers the effects giving rise to broadening of the 00l interlayer peaks. These have previously been characterised as falling into two distinct categories (Reznik et al., 1995; Burian et al., 1999a; Maniwa et al., 2001;

Lambin et al., 2002): size (arising from the wall thickness, thus the number of layers n) and strain (due to a distribution of interlayer spacings d). It is obvious that a finite number of layers n will lead to a broadening of the $00l$ peaks. Figure 7.9 illustrates the peak widths for different n, but it also shows that an average over several values of n leads to a cancellation of the low angle ripples, thus not surprisingly it can be concluded that a distribution of different wall thicknesses must be present in real samples. According to the Scherrer equation (3.3), the peaks are expected to be symmetric with widths inversely proportional to n for all orders of $00l$ if size is the only effect leading to a broadening of the $00l$ peaks. One look at the experimental diffractograms in Figure 7.11 is enough to conclude that the 004 peak is much wider than the 002 peak and that both peaks are asymmetric, thus strain broadening of the $00l$ peaks is indecisively present. The asymmetry can be modelled *via* a weighted average over diffractograms simulated for values of d between 3.35Å (the interlayer spacing in graphite) and 3.60Å using higher weights for the smaller spacings. This effect will cause a certain amount of order dependent broadening which must be compensated for by increasing the number of walls n.

Figure 7.9 Simulations showing the effect of varying the number of walls n

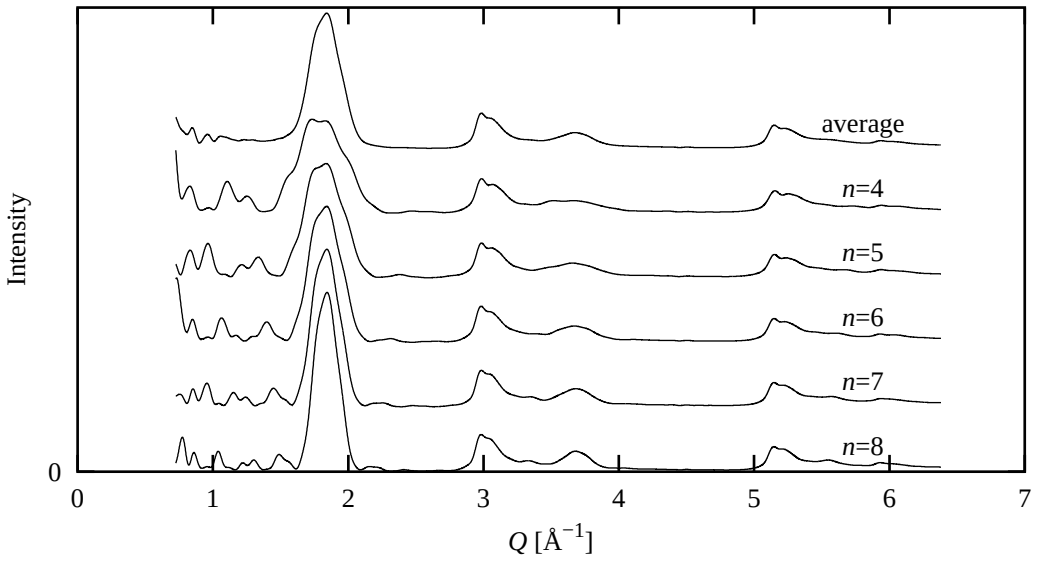

7.5 Experimental

The bulk structures of a number of MWCNT samples with different purity and dimensional specifications were characterised by means of XRPD and Debye simulations. The sample specifications and origin are given in Table 7.2.

Table 7.2 Specifications and origin of MWCNT samples

name	diameter [Å]	length [μm]	purity [%]	amount [g]	price [US$]	provider
sunnano	100–300	1–10	>90	10	30	www.sunnano.com
nano15	150±50	1–5	95	0.05	–	nano-lab.com
nano30	300±150	1–5	>95	0.05	–	nano-lab.com
bamboo	300±100	1–5	>95	0.05	–	nano-lab.com

7.5.1 TEM

TEM images of the samples described in Table 7.2 were recorded and a selection of these are shown in Figure 7.10. From the TEM images it seems that the diameter specified for the sunnano sample is reasonable. The images indicate that the sample contains impurity particles with a diameter around 100Å and a higher density than the MWCNTs, probably catalyst remnants. TEM, however, does not offer the opportunity to determine the nature or the concentration of these impurities as opposed to XRPD. Judging from Figure 7.10 the diameters of the nano15 and nano30 samples look alike, both samples contain MWCNTs with outer diameters of both 150Å and 300Å. The name bamboo is evident from the TEM images showing the sectioned MWCNTs, a structural characteristic that is also found for some of the other samples, but not to the same extent. Again the diameter specification for this sample seems reasonable, and the images suggest a non-negligible contents of catalyst particles. For all of the samples bending of the tubes seem to be more the rule than the exception, *c.f.* the discussion in Section 7.4.3 on how the tubes appear shorter in XRPD experiments if they are bent.

sunnano

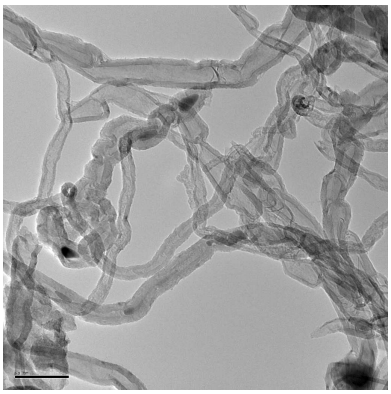

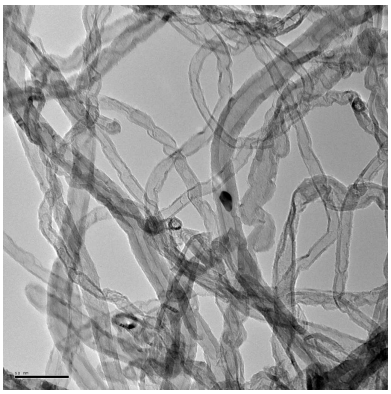

nano15

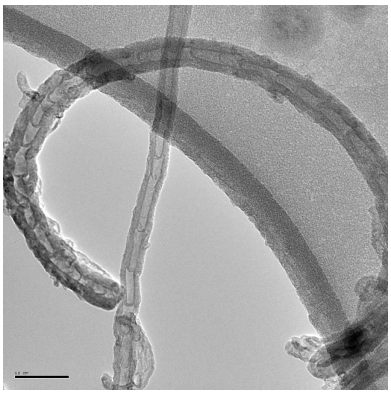

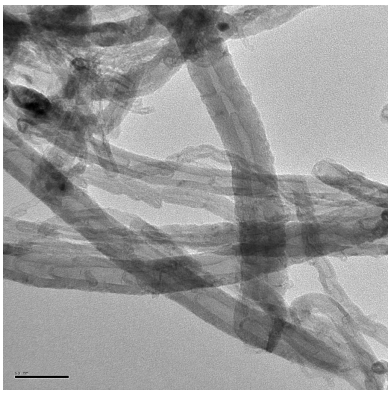

nano30

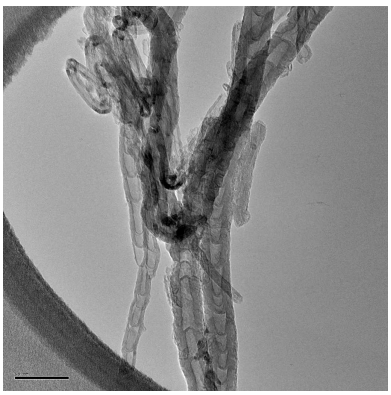

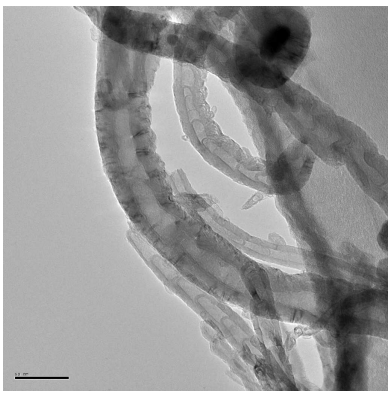

bamboo

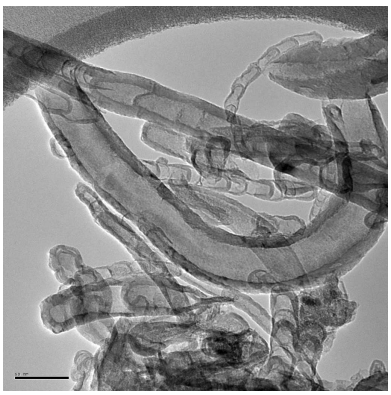

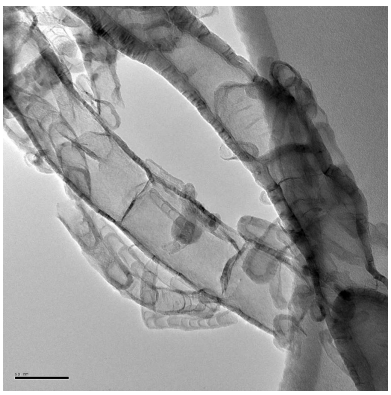

Figure 7.10 TEM images of MWCNT samples. Scale bar 500Å

7.5.2 XRPD

Collecting good experimental XRPD data of MWCNTs is not an easy task because of the low density and the poor scattering power of the samples. To obtain a high density sample the MWCNTs were pressed into tablets. These consisted of 50mg MWCNTs and were approximately 0.4mm thick yielding a density around 0.85gcm^{-3} compared to 2.1–2.2gcm^{-3} for graphite. Potential problems for this type of sample treatment are breaking of the tubes due to the pressure used to produce the tablets, and preferred orientation because the tube axes tends to orient perpendicular to the applied pressure. Preferred orientation affects the XRPD patterns much less if data collection is performed in transmission mode.

Besides this measuring times of more than 24h are needed to collect sufficiently good data if conventional X-rays are used. Therefore the experimental diffraction patterns were collected in transmission geometry using a HUBER G670 Guinier camera at MAX-lab beamline I711 (Ståhl, 2000; Cerenius et al., 2000). Preliminary tests to determine how to mount the tablets (with tape outside the illuminated area) and the exposure time (3min) were performed at λ=1.509Å. The actual data collections for the samples in Table 7.2 were performed later at λ=1.087Å. Both the wavelength, the 2θ zero shift of $-0.085°$ and the instrumental broadening parameters of the particular experimental setup, all parameters needed during the simulation and fitting procedures, were determined for a Si standard. The counting statistics of the MWCNT data were improved by adding 2 diffractogram for every sample.

Considering that a fast, cheap and reliable method for bulk structure characterisation of MWCNTs is sought, it is of course rather unfortunate that synchrotron radiation is needed to obtain sufficiently good experimental diffraction data to enable analysis. However, with the current development in the field of table-top synchrotrons, namely the compact light source of Lyncean Technologies Inc. (www.lynceantech.com), the concept of in-house routine characterisation for every new MWCNT batch may be possible in the near future.

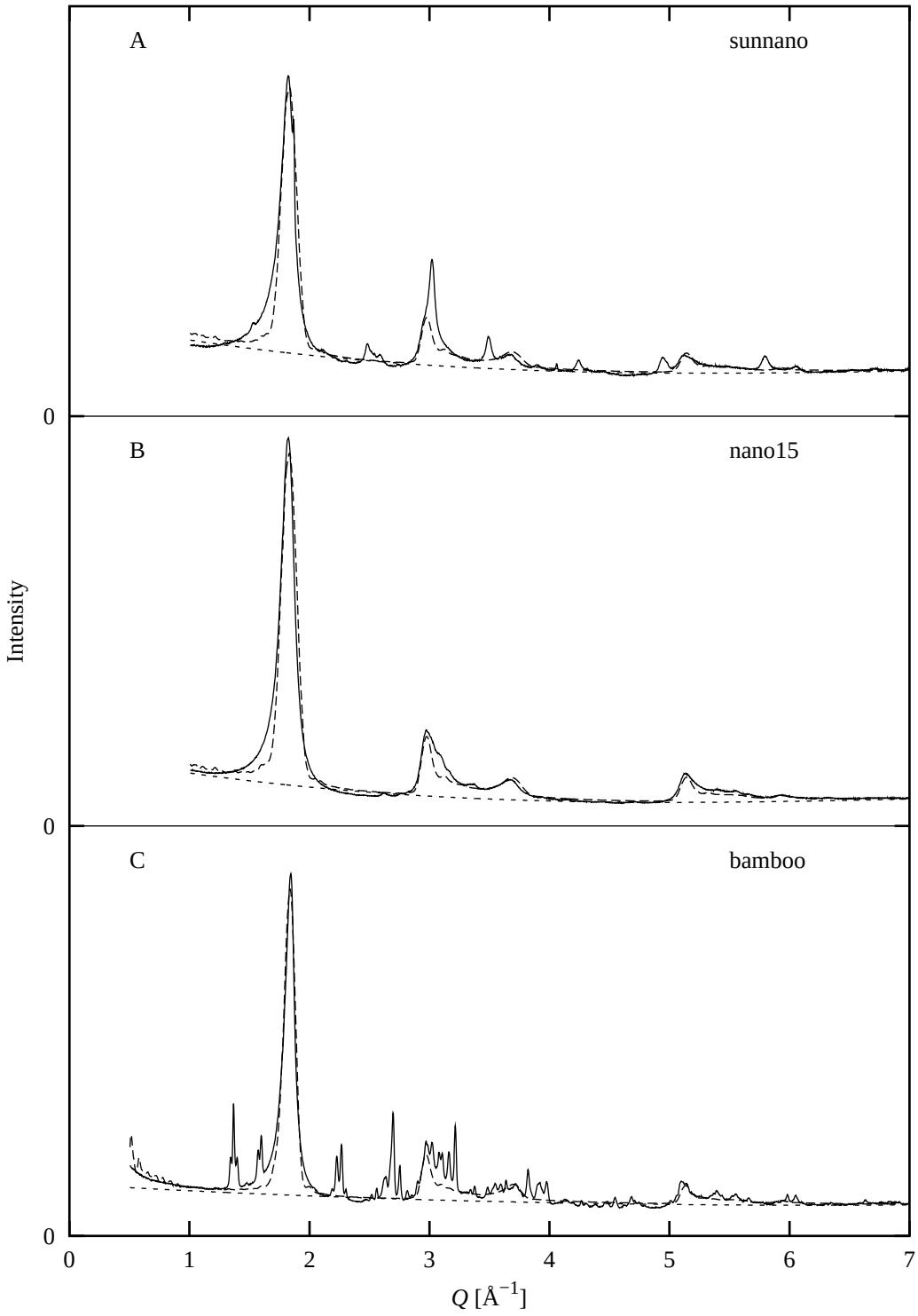
A
sunnano
B
nano15
C
bamboo
Intensity
0
0
0
0
1
2
3
4
5
6
7
Q [Å−1]

Figure 7.11 Fit between experiments and simulations according to Table 7.3

7.5.3 Fitting

The experimental diffractograms for the MWCNT samples in Table 7.2 were corrected for the intensity abberations related to the 45° Guinier tangent angle and for the 2θ zero shift of the current experimental setup. For fitting purposes the diffraction peaks clearly not related to MWCNT diffraction in the sunnano and bamboo samples were replaced by a smooth background curve. This was done to avoid mimicking of these false peaks in the subsequent fitting procedure where the simulated diffractograms were fitted to the experimental XRPD patterns by means of a scale factor and a Chebyshev polynomial to describe the background.

Taking advantage of the experience gained through the property studies, diffractograms covering a reasonable span in structural properties were simulated. As noted in Section 7.4.3 it is only possible to determine either l or r, so r=60Å was simply assigned based on the diameters observed in TEM. The structural characteristics of the samples were then determined as the property values used to simulate the diffractograms that, when fitted to the experiments, gave the lowest R_I-values ($R_I = \sum_i |I_i^{\text{exp}} - I_i^{\text{sim}}| / \sum_i I_i^{\text{exp}}$). The mean and spread of the structural properties leading to the best fits between experiments and simulations are given in Table 7.3 and the quality of the fit can be inspected in Figure 7.11. Considering that the experimental diffractograms for samples nano15 and nano30 are virtually identical, *c.f.* Figure 7.14, only one of these is shown. The fits in Figure 7.11 are excellent except for the low Q side of the 002 peak (perhaps even larger d-spacings than 3.60Å are present in the samples) and the high Q side of the 100 peak (possibly arising because the stacking of graphene layers is not completely turbostratic giving rise to a low intensity graphite 101 peak at 3.1Å^{-1}, *c.f.* Figure 7.1).

Besides the characteristics of the MWCNTs in terms of the mean and spread of the various structural properties, a XRPD analysis also offers the opportunity to detect and possibly identify impurities, especially crystalline components. In the sunnano sample a search-match indicates the presence of metallic alloys containing Ni, Al and/or Fe, elements all of which should be expected to be found in small amounts according to the provider. No crystalline impurities were detected in the nano15 and nano30 samples, but catalyst containing byproducts in the form of carbides of Fe, Co and/or Ni were found in the bamboo sample. Transmission geometry XRPD data are

Table 7.3 Structural characteristics of the MWCNT samples from fits of experimental XRPD patterns with Debye simulations

name	l [Å]	r [Å]	n	d [Å]	od [Å]	bg^a
sunnano	75	60	10–14	3.35–3.60	180–210	4
nano15	75	60	10–14	3.35–3.60	180–210	4
nano30	75	60	10–14	3.35–3.60	180–210	4
bamboo	100	60	16–20	3.35–3.60	220–250	4

[a] Number of Chebyshev background parameters used in the fitting procedure

not the best when trying to estimate the concentration of different components in a sample, because this type of scattering geometry gives rise to a significant amount of air scattering besides the sample related scattering.

7.6 Library of MWCNT diffractograms

The MWCNT structural properties that are of importance for most applications are the dimensions: The length l, the inner radius r (or alternatively and probably more accurately the outer diameter od), the number of concentric tubes n, and the spacing between these d. Based on the analysis of how these properties affect the simulated diffraction patterns and how simulated diffractograms compare with experimental XRPD pattern, a library of simulated MWCNT diffractograms with different dimensions designed to cover the size span typically found from experimental data was generated. The property values were varied according to Table 7.4, giving a total of $6{\cdot}5^3{=}750$ simulated diffractograms. Note that the outer diameter, which can be calculated as $od{=}2(r{+}(n{-}1)d)$, ranges from 53.5Å to 192Å.

All simulations for the library were performed for scroll type MWCNTs with a chiral angle of $\alpha{=}15.3°$. Numerous arguments for this choice have already been presented during the analysis of how the rolling characteristics affect the simulated diffractograms. No instrumental broadening was added in the simulations, this can always be added afterwards if it is deemed necessary. The diffractograms in the library give the intensity as a function of 2θ between 10° and 100° in steps of 0.02°. The wavelength used for the construction of the library was $\lambda{=}1.509$Å, the wavelength at which the first experimental data were obtained and the simulations to analyse the property effects were performed. This means that both experimental and simulated

Table 7.4 Property values used in the simulations

l [Å]	r[Å]	n	d[Å]
25	10	6	3.35
100	20	8	3.40
200	30	10	3.45
300	40	12	3.50
500	50	14	3.55
1000			

diffractograms were readily available for comparisons and testing. However, MAX-lab beamline I711 where the data was collected is a variable wavelength beamline, so the procedure of comparing experimental diffraction data with the library will in principle always include a wavelength conversion as well as a 2θ zero shift.

7.7 PCA

To analyse the differences between the 750 simulated diffractograms PCA was applied. The PCA was carried out on the 2θ-scale (λ=1.509Å) from 22° to 88° since tests proved the simulated background outside these limits to be a disturbing factor. There are two main reasons for using PCA. Firstly, the dimension of the problem will be strongly reduced, and secondly, it will be much easier to identify the effects of the nanotube properties. However, if this kind of analysis should be of any practical use, some kind of normalisation must be performed on the diffractograms; otherwise the experimental data must be brought to an absolute scale. PCA results in an orthogonal and optimal coordinate system, where orthonormal basis functions constitute the axes. The coordinate system is optimal in the sense that the best approximation of the 750 diffractograms in an m-dimensional subspace is found by linear combinations of the basis functions belonging to the m highest eigenvalues. If $\mathbf{D}$ is a matrix with elements D_{ji} proportional to the intensity at $2\theta_j$ for sample i, then $\mathbf{D}^t\mathbf{D}$ is a symmetric matrix with non-negative eigenvalues. PCA then consists of solving the eigenvalue problem $\mathbf{D}^t\mathbf{D}\mathbf{U} = \mathbf{U}\mathbf{\Lambda}$, where each column of $\mathbf{U}$ contains an eigenvector and $\mathbf{\Lambda}$ is the diagonal eigenvalue matrix with the eigenvalues sorted in a decreasing sequence. The orthonormal basis function matrix, $\mathbf{B}$, is then $\mathbf{B} = \mathbf{D}\mathbf{U}\mathbf{\Lambda}^{-\frac{1}{2}}$. Obviously, the number

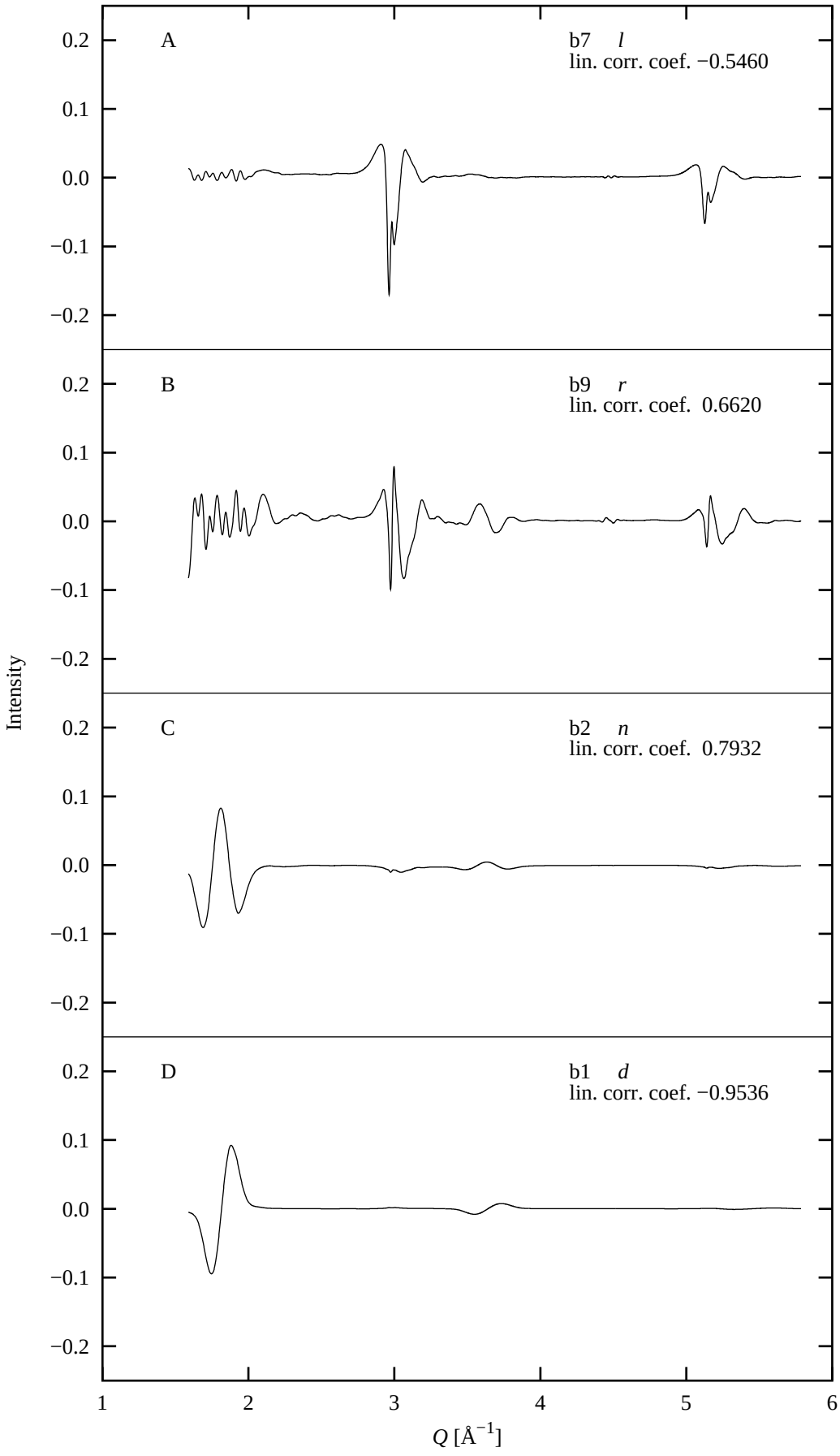
A
b7 l
lin. corr. coef. −0.5460
B
b9 r
lin. corr. coef. 0.6620
C
b2 n
lin. corr. coef. 0.7932
D
b1 d
lin. corr. coef. −0.9536
Intensity
Q [Å−1]
0.2
0.1
0.0
−0.1
−0.2
1
2
3
4
5
6

Figure 7.12 The basis functions from the PCA with the largest linear correlation coefficients to the four properties. b7 is the basis function with the 7^{th} highest eigenvalue and so on.

of basis functions is limited to the number of eigenvalues with significant non-zero values.

In the present case it was chosen to normalise the diffractograms such that the diagonal elements of $\mathbf{D}^t\mathbf{D}$ are equal to one. Furthermore, in order to enhance the discriminative power of the PCA, a slightly different approach was used. Before performing the PCA, the matrix $\mathbf{D}$ is replaced by $\mathbf{D} - \mathbf{M}$, where $\mathbf{M}$ is a matrix of the same rank and dimensions as $\mathbf{D}$ with identical columns each containing the average of the normalised diffractograms. With this setup the diagonal elements, $((\mathbf{D} - \mathbf{M})^t(\mathbf{D} - \mathbf{M}))_{ii}$, contain the sum of squared deviation between the average and the i^{th} diffractogram, and since the trace is invariant to any orthonormal transformation it is equal to the sum of eigenvalues. This means that it is possible to select an optimal number of basis functions, including the average, to account for any percentage of the total sum of squared deviations. Subsequently, the average diffractogram is orthogonalised and normalised and added to the number of basis functions. However, the normalisation destroys information, especially on the tube length. This implies that in order to be able to describe the effect of different tube lengths, basis functions of very little importance must be included. Tentatively, the 80 most important basis functions, including the average were chosen. These 80 basis functions account for 99.9994% of the total sum of squared deviations, and an approximation of the diffractograms by a linear combination of these basis functions leads to a maximum R_{I^2}-value $\left(R_{I^2} = \sqrt{\sum_i (I_i^{\text{obs}} - I_i^{\text{calc}})^2 / \sum_i (I_i^{\text{obs}})^2}\right)$ of 0.0014. The expansion coefficient or coordinate matrix, $\mathbf{C}$, is equal to $\mathbf{D}^t\mathbf{B}$. These coefficients should be related to the four nanotube properties, the values of which have been scaled to the interval between 0 and 1 to avoid that the properties are weighted differently.

To get an idea about the importance of the basis functions, the linear correlation coefficient between the coordinates and the tube properties were calculated for each basis function and each tube property. The four most important basis functions are shown in Figure 7.12. Whereas 7.12B is difficult to interpret, the basis functions in the 100 (Q: 2.8–3.2Å^{-1}) and 110 (Q: 5.1–5.4Å^{-1}) regions of 7.12A and in the 002 (Q: 1.8–2.2Å^{-1}) region of 7.12C have almost symmetrical shapes that are typical for changes in peak width. In 7.12D the shape in the 002 region is typical for a shift in peak position. This

agrees nicely with the observations made in the study of how the MWCNT properties affect the diffractograms; the width of the 100 and 110 in-plane peaks can be varied by altering the tube length, the width of the $00l$ peaks are controlled by varying the number of tubes walls, and a variation of the spacing between adjacent walls result in a shift of the $00l$ peak positions.

7.7.1 MWCNT properties from PCA

Since the basis functions given in Figure 7.12 are not the only ones with non-negligible correlation to the properties, it is obvious that some linear combination of the basis functions will lead to a better linear correlation, *i.e.* for each property it is possible to find the direction in the 80D space that maximises the linear correlation between the tube property and the coordinate in this direction. Any unit vector, $\mathbf{v}$, in the 80D space can be parameterised by 79 angles, α_j, $_{j=1...79}$ ($\alpha_{80} = 0$):

$$v_1 = cos(\alpha_1) \qquad v_j = cos(\alpha_j) \prod_{i=1}^{j-1} sin(\alpha_i), \ _{j=2...80} \tag{7.2}$$

A subspace omitting the m^{th} basis function is obtained by putting $\alpha_m = \frac{\pi}{2}$.

With 80 dimensions, the number of angular parameters amounts to 316, and with a total number of tube properties of 4·750=3000, this leads to an observation-to-parameter-ratio of less than 10. With excess parameters there is a risk that deficiencies in the model may be compensated for by these parameters, *e.g.* the large gap in length between 500 and 1000Å may be modelled correctly at 500 and 1000Å, but show an oscillatory behaviour in between, which may result in a very dubious prediction of the tube properties in this region. In an attempt to avoid these problems, the observation-to-parameter-ratio was fixed to at least 10. Consequently, the number of dimensions has to be reduced. Tentatively, 65 basis functions were selected for each direction. This gives a total of 256 angular parameters, leaving at most 44 parameters to describe the functional relationships between the properties and the coordinates. With a linear model only 8 of these are used. However, the necessity of using 80 basis functions in order to describe all diffractograms with a sufficient accuracy suggests that the problem is highly non-linear. Therefore, the 65 basis functions were selected in following way: For each basis function, the linear correlation coefficients were calculated between the property in question and the 1^{st}, 2^{nd} and 3^{rd} power of the coordinate, and the 65 basis functions with the highest sum of squared correlation coefficients were selected. The search for directions with maximum linear correlation was performed by numerical methods, and the linear

correlation coefficients obtained were: -0.9110, 0.9946, 0.9987, and 0.9998, for l, r, n, and d, respectively. Although some correlations seem very good, the estimated properties lie too far away from the true values used in the simulations.

It was chosen to use the four linearly optimised $\mathbf{v}_k$, $_{k=1\ldots4}$ vectors and the projections d_{ki} of the i^{th} diffractogram onto these as the starting point for the new model and then expand the linear description to include mixed higher order terms in d_{ki}. By trial and error a suitable model for property k of diffractogram i, p_{ki}, was obtained as a 4^{th} order polynomial of the type:

$$\begin{aligned} p_{ki} &= a_{k0} + a_{k1}d_{1i} + a_{k2}d_{1i}^2 + a_{k3}d_{1i}^3 + a_{k4}d_{1i}^4 + a_{k5}d_{1i}^3 d_{2i} + \ldots \\ &= \sum_{n_k} a_{kn_k} \prod_{h=1}^{4} d_{hi}^{m_{hn_k}} \end{aligned} \tag{7.3}$$

where n_k runs over the non-zero terms in the polynomial expansion for property k, $m_{hn_k} \in \{0, 1, 2, 3, 4\}$ and $\Sigma_{h=1}^{4} m_{hn_k} \leq 4$. The only exception was found for the length, here it was necessary to include a term proportional to d_{li}^5, where d_{li} denotes the projection of the i^{th} diffractogram onto the length vector.

The procedure to improve the model is then as follows: 1) For the present values of d_{ki}, determine the a_{1n_1} coefficients of (7.3) using least squares refinement, 2) Optimise the set of angles α_{1j}, $_{j=1\ldots79}$ used to define $\mathbf{v}_1$ in (7.2) to get the best estimate of p_{1i}. For every change in α_{1j}, d_{1i} will change, so a new set of a_{1n_1} must be determined, thus the optimisation procedure is rather time consuming, 3) In the same way optimise the α-angles for the other values of k, and 4) If the estimates of p_{ki} are not satisfactory, add more terms to the polynomials and repeat 1)–3).

Table 7.5 Fit quality for the final polynomial model

	l [Å]	r [Å]	n	d [Å]
max. deviation	-110.8	2.63	0.21	-0.0028
RMS deviation	30.2	0.66	0.06	0.0007
step size	75–500	10.00	2.00	0.0500

In Table 7.5 the maximum and root-mean-square (RMS) deviations taken over all diffractograms for each property are given. It can be seen that, except for the length, the maximum deviations are at the most 25% of the

step size between the values used to build the PCA library of diffractograms. Table 7.6 shows which terms are included in the polynomial expansions for each of the four properties, thus it gives an idea of which properties correlate the strongest. Looking at the large number of terms necessary to model the length it is not surprising that the maximum deviation of this property is much poorer. Contrary to what would be expected by comparing Figure 7.12C and D, hardly any correlation is found between the effects arising from the number of turns and the *d*-spacing. In fact these two properties are much easier to model than the length and inner radius, which correlate strongly, both internally and to the other properties. Figure 7.13 shows the final vectors $\mathbf{v}_k$ for each property. Even though these refined diffractograms are very complex in nature and offer no interpretation as was the case for the basis functions in Figure 7.12, some similarities between the two figures can still be found.

Table 7.6 Non-zero terms in the 4^{th} order polynomials of (7.3)

l	r	n	d
d_l	d_r	d_n	d_d
d_l^2	d_r^2	d_n^2	$d_d^3 d_r$
d_l^3	d_r^3	$d_n^3 d_r$	$d_d^2 d_r^2$
d_l^4	d_n	$d_n d_l^3$	$d_d^2 d_r d_l$
d_l^5	d_d	d_l^4	$d_d^2 d_r d_n$
$d_l d_d$	$d_r d_n$	$d_l d_r^2$	
$d_l d_r d_n$	$d_r^2 d_n$		
$d_l d_r d_n^2$	$d_r^2 d_d$		
$d_l d_r d_d^2$	$d_r d_l d_d$		
$d_l^2 d_r^2$	$d_r^3 d_n$		
$d_l^2 d_d^2$	$d_r^3 d_d$		
$d_l^3 d_r$	$d_r d_l^2 d_d$		
$d_l^3 d_n$	$d_r d_n^2 d_d$		
$d_r^2 d_d^2$			
$d_r d_n^3$			
d_n^4			

Figure 7.13 The optimised functions for the final model.

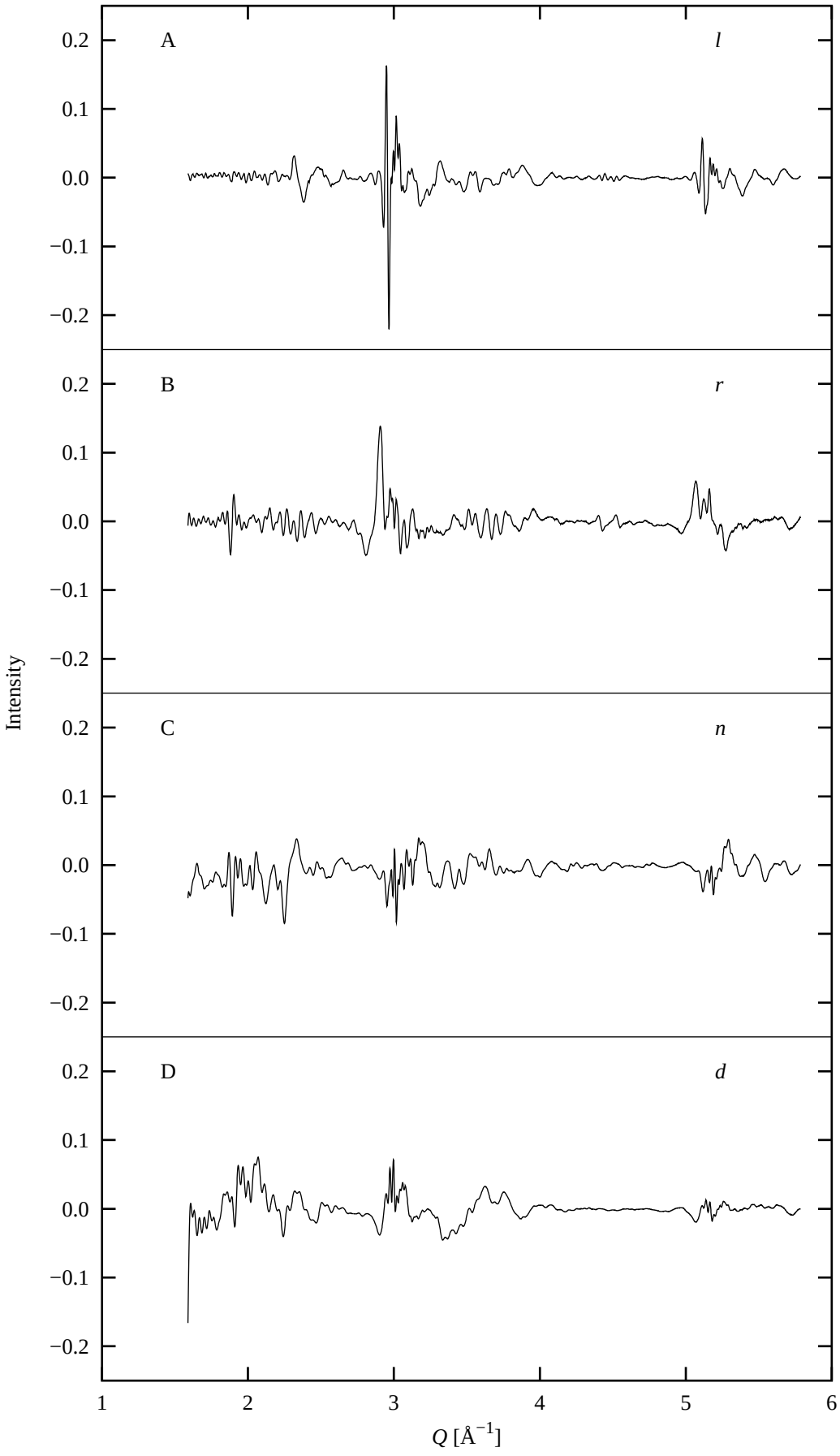
A
l
B
r
C
n
D
d
0.2
0.1
0.0
−0.1
−0.2
Intensity
1
2
3
4
5
6
Q [Å−1]

7.7.2 Applying PCA to estimate MWCNT properties from experimental XRPD data of bulk samples

The first 80 basis functions from the model calculations contain enough information to fit the 750 error-free simulated diffractograms with an acceptable accuracy. The large reduction in dimensionality indicates that the basis functions map the general features for error-free MWCNT diffractograms. However, the prediction of MWCNT structural properties from experimental diffractograms is carried out by fitting on the 2θ-scale (λ=1.509Å). Thus a number of problems can potentially complicate the analysis: Thermal displacement parameters differing from the B-factor of 2Å^2 used in the simulations, an experimental 2θ zero offset, diffractograms recorded at other wavelengths than the 1.509Å of the simulations, incorrect background correction, sample impurities, and/or structural parameters falling outside the intervals chosen for the PCA. In order to overcome some of these problems a separate algorithm was applied to modify the B-factor, 2θ zero shift and wavelength of the experimental diffractogram to obtain the best possible fit within the PCA basis. The method was tested on the four diffractograms given in Figure 7.14 and the predicted properties are given in Table 7.7.

Table 7.7 Predicted values for the diffractograms in Figure 7.14

	l [Å]	r [Å]	n	d [Å]	od [Å]	B-factor [Å^2]	2θ offset [°]	R_{I^2}-value
A	56	40.7	5.85	3.399	61	−0.003	0.40	0.0014
A[a]	100	40.0	6.00	3.400	60	0.000	0.40	
B	18	7.6	7.55	3.414	67	0.68	0.49	0.0384
C	−7	7.7	8.41	3.403	72	2.07	0.25	0.0384
D	18	7.5	8.48	3.410	73	1.97	0.14	0.0406

[a] True values for the simulated diffractogram A.

Figure 7.14 Predicting structural properties using PCA. The experimental diffractograms corrected for B-factor, 2θ offset and wavelength differences are shown along with the difference curves.

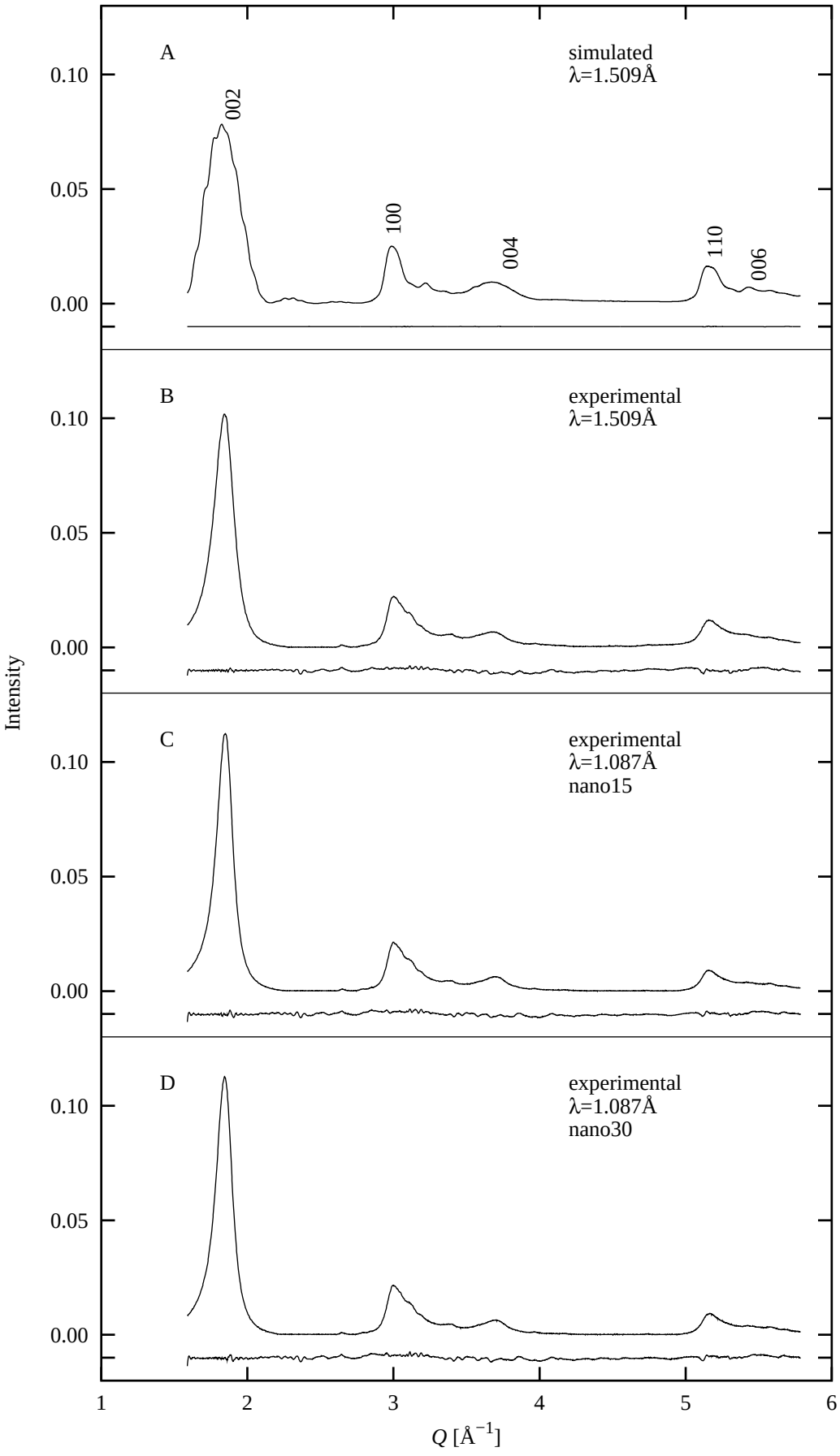
A
simulated
λ=1.509Å
002
100
004
110
006
B
experimental
λ=1.509Å
C
experimental
λ=1.087Å
nano15
D
experimental
λ=1.087Å
nano30
0.10
0.05
0.00
Intensity
1
2
3
4
5
6
Q [Å−1]

Diffractogram A is simulated for λ=1.509Å with a set of structural properties within the simulation limits. A B-factor of 0.000Å^2 was used in the simulation and the simulated diffractogram was offset by 0.40° before the prediction procedure. Since this diffractogram does not contain an experimental background or other instrumental abberations it is expected that a low R_{I^2}-value and a good property prediction should be obtained, which is indeed the case. This test case shows that the zero point and B-factor altering algorithm works satisfactorily.

Diffractogram B is recorded at λ=1.509Å and was subjected to an empirical background subtraction before the analysis. The quality of the fit and the reasonable predicted properties confirm that the PCA method can in fact be used to characterise MWCNT structural properties from experimental diffractograms and that an empirical background correction is sufficient.

Diffractograms C and D are recorded at λ=1.087Å on samples nano15 and nano30, respectively, and again empirical background corrections are performed. Despite the wavelength difference the fits to these diffractograms are of the same quality as for B, so the fact that it is almost impossible to obtain synchrotron diffraction data with no 2θ offset at the exact same wavelength as the one used to set up the PCA library seems to be a minor problem. Neither a TEM investigation of the samples (Figure 7.10) nor a XRPD and Debye fitting analysis (Table 7.3) suggest that the samples have different properties, despite the fact that the outer diameters specified by the provider were 150±50Å (nano15) and 300±150Å (nano30), respectively. The properties predicted from the PCA analysis are identical within one RMS deviation (except for d for which the difference is undoubtedly correlated to the erroneous difference in 2θ offset), so it is fair to say that the nano15 and nano30 samples are indistinguishable to the PCA method, as to the other MWCNT characterisation methods described.

Finally the bamboo diffractogram (Figure 7.11C) was also tested as an example of a sample containing impurities. This was more than the present implementation of the PCA was able to handle; all of the properties were predicted to unphysical values much larger than the upper limits used to set up the PCA library, and the 2θ offset refined to 1.18°. The reason for this is undoubtedly that the fitting algorithm tries to describe the diffraction arising from the crystalline impurities as MWCNT diffraction. Potential ways to overcome this problem could be to restrict the 2θ offset to 0° and to add a number of diffraction patterns for the most common impurities to the PCA library.

7.7.3 Concluding remarks on PCA

The above test cases have demonstrated that it is difficult to get a physically meaningful estimate of the average tube length from an experimental MWCNT diffractogram using the PCA method. The values determined fall below the lower limit used to set up the PCA library and are of the same size as the maximum and RMS deviations given in Table 7.5, which are rather poor despite the fact that they are obtained purely from error-free simulated diffractograms. The predicted inner diameters are also below the lower limit of the PCA library, so even though they are not physically unreasonable, they must be considered unreliable. A possible way to solve this problem would be to extend the PCA library to include smaller values of r. However, it is likely that more would be gained by improving the functional relationship between MWCNT properties and PCA basis functions, because the large number of terms needed to model l and r (Table 7.6) indicate that the polynomial model may be inadequate for modelling the correlation between these properties. Another manner in which to improve the model would be to select different, not necessarily connected, regions of the diffractograms for different properties to potentially reduce the loss of information on normalisation.

As mentioned earlier the broadening of the $00l$ peaks can be caused both by size (n) and strain (distribution of d). In a bulk sample the MWCNT structural properties are distributed around a mean, but the present PCA method can only estimate the mean and not the width of the distribution. Thus the potential strain broadening of the $00l$ peaks can only be modelled as a size broadening, leading to an underestimation of both the number of turns and the thermal displacement parameter. In Section 7.4.4 it was argued that strain broadening cannot be neglected, so the predicted values of n for all experiments are probably too low. To solve this problem it will be necessary to extend the library to include diffractograms simulated for larger values of n and to introduce distributions of properties. Since the PCA basis functions model all simulated diffractograms, a distribution of tube properties may be achieved by optimising distributions in the four property dimensions.

The performance of the PCA with regards to the distribution of chiral angles in the sample should also be tested. This implies that the PCA library must be substantially extended. In Table 7.8 a set of 5 values for each of l, r, n, d, and α are suggested, leaving a total of 5^5=3125 diffractograms to be simulated. However, with a maximum value of l=150Å which was shown to be sufficient, the time needed to set up the new library is probably comparable to the time spent to construct the present library of 750 diffractograms extending to l=1000Å. The intervals of n and d have been altered to include larger values to enable modelling of strain broadening. Judging from expe-

rience it could also be necessary to include diffraction patterns of the most common crystalline impurities in the PCA library.

Table 7.8 Suggested property values for a new PCA library containing 5^5=3125 diffractograms

l [Å]	r[Å]	n	d[Å]	α [°]
50	10	5	3.35	0.0
75	20	10	3.45	7.5
100	30	15	3.55	15.0
125	40	20	3.65	22.5
150	50	25	3.75	30.0

Applying this new library with property values carefully tailored based on experience and extending the analysis to include distributions of the properties it is likely that an even better understanding of the characteristics of bulk MWCNT samples can be reached. Furthermore, the increased number of library diffractograms makes it possible to improve the functional relationship between MWCNT properties and PCA basis functions without jeopardising the observation-to-parameter-ratio.

7.8 Final conclusions

To characterise the bulk structure of MWCNTs a global probe and a way to interpret the obtained data is needed. XRPD may serve as the probe due to the periodic but non-crystalline nature of the tubes. Furthermore XRPD makes it possible to detect and identify crystalline impurities. The local atomic structure and thus information about the nearest neighbour C–C distances, as well as the spacing and correlations between the graphene sheets can be determined from a PDF analysis of the XRPD data. Complementary to this the Debye formula is an excellent tool to simulate XRPD patterns of MWCNTs, and comparisons of simulated diffractograms have proven that the MWCNT structural properties affect the resulting XRPD patterns in a way that makes it possible to determine the structural properties of a bulk sample from an experimental diffractogram.

For the present Debye simulations the following properties were considered: The rolling type (concentric cylinders or scrolls), the chiral angle, the length, the inner radius, the number of walls and the spacing between these. Visual inspection and comparison of the diffractograms, both simulated and experimental, confirmed that all of the structural properties of the MWCNT bulk samples should be determined as distributions rather than as single values, and that some of the properties correlate strongly, especially the length and the diameter. The simulations proved that XRPD is not able to distinguish a sample consisting of concentric cylinders with a distribution of diameters from a scroll type sample. Modelling the MWCNTs as scrolls is fast and makes it possible to simultaneously control both the d-spacing and the chiral angle. A chiral angle of α=15.3°, a reasonable average value, was found to fit the experimental data well. It was shown that the Q-range from 1Å^{-1} to 6Å^{-1} accessible with a standard wavelength around λ=1.5Å is sufficient to extract the desired structural information. In the case of determining the chiral angle for large diameter MWCNTs the limited Q-range was even found to be superior. Finally it was shown that if the tubes are bent, as can often be seen in TEM images, the length will appear much shorter in an XRPD experiment.

To facilitate the determination of MWCNT bulk properties from experimental XRPD data, a library of diffractograms simulated for scroll type MWCNTs with α=15.3° and various values of l, r, n and d was constructed. The library was subjected to a PCA to limit the number of variables and identify the effects of the properties. Initial tests using a combination of PCA and basis function transformations showed that it is possible to directly obtain bulk structural properties from XRPD data of MWCNTs. The average values of inner radius, number of turns and d-spacing are well estimated with limited correlations, while the tube length cannot be estimated due to large correlations and the present type of samples largely affected by tube bending and defects. Experimental abberations like different thermal displacement parameters, 2θ offset, wavelength differences and experimental background can be effectively handled within the PCA approach. There is room for several improvements, especially the method performance with regards to varying the chiral angle and introducing distributions of the determined properties should be tested. This requires a substantial extension of the library of simulated diffractograms.

Chapter 8

Conclusions

The finer nanostructural details of a material are reflected in the XRPD pattern, but traditional interpretation methods such as Rietveld refinement are unable to extract the information. The general Debye program based on the Debye equation (Debye, 1915) was written to facilitate the characterisation of a special class of nanostructured materials, namely the nanocrystalline compounds. The program is able to read crystallographic information from a CIF, simulate the XRPD pattern given information about experimental setup, particle shape, size and size distribution, and finally fit the simulated diffractogram to experimental XRPD data. Traditionally the bottleneck of Debye simulations has been the computational cost, but with the present implementation which exploits the crystallographic symmetry to perform the summation over all interatomic distances, the diffractogram for a crystal containing 6 million atoms can be calculated within a minute on a standard PC. The Debye program should be seen as a developing framework for XRPD characterisation of nanostructured materials, a framework that can be added new features or modified more thoroughly in order to solve specific needs that appear during the study of real materials.

Three very different nanostructured materials have been studied in the present thesis using XRPD and the Debye approach in combination with complementary techniques such as Rietveld refinements, EXAFS and TEM. Except for the case of cellulose, this has been done using material-specific modifications of of the Debye program.

The study of **cellulose**, an organic polymer with a nanofibrous structure, was initiated because industrial applications of plant fibres require efficient and reliable crystallinity determinations. This can be done from XRPD, but the diffraction data must be collected in reflection geometry (to minimise unwanted air scattering contributions to the amorphous background) using a custom-made sample holder (to minimise preferred orientation of the cel-

lulose fibres). It was shown that Rietveld refinements taking full account of the broadened and overlapping diffraction peaks should be the preferred method for standard crystallinity determinations in the future because it can be performed using any readily available Rietveld refinement program with speed, ease and consistency. Additional information about particle shape, size and size distribution can be obtained if time and effort is invested to do Debye simulations, but because of remaining preferred orientation effects XRPD data collected in transmission geometry should be used if an accurate particle size determination is desired.

Debye simulations offer the opportunity to test how the XRPD patterns of stress-free and homogeneous **nitrogen expanded austenite**, a highly defective material with a large interstitial nitrogen occupancy, are affected by the presence of stacking faults and screw dislocations in combination. Because of the computational cost the Debye method is limited by the particle size, in the present case to a mean diameter of around 360Å. Comparisons with experimental XRPD patterns gave no evidence of twin or growth stacking faults, while both deformation stacking faults and screw dislocations were found to be abundant, the density of the latter increasing with the interstitial nitrogen occupancy. A XRPD characterisation of nitrogen expanded austenite produced using a novel method demonstrated that both the as-nitrided (y_N=0.51) and denitrided (y_N=0.18) samples consist of several phases, among these CrN even though the synthesis was performed below 450°C where the mobility of the Cr atoms is very limited. EXAFS data showed that the Fe atoms in the denitrided sample are found in nitrogen-free surroundings, whereas the octahedral interstices around the Fe atoms in the as-nitrided sample are partly occupied. As opposed to this the majority of the Cr atoms are found in nitrogen saturated surroundings corresponding to the chemical compound CrN in both samples, although only a fraction of the Cr atoms could be detected as CrN with XRPD. A possible explanation for this observation could be a phenomenon generally related to low-alloyed ferritic steel *i.e.* formation of mixed substitutional-interstitial clusters. The nitrogen expanded austenite samples produced in the traditional way only display one phase in the XRPD patterns. Performing Cr, Fe and Ni K-edge EXAFS on a number of these samples with various nitrogen contents would therefore offer valuable information about the distribution of nitrogen atoms in nitrogen expanded austenite without observable precipitation of coherent CrN.

To characterise the bulk structure of **multiwall carbon nanotubes**, a non-crystalline material with a periodic structure, the combination of XRPD and Debye simulations was found to be the ideal approach. It was shown that the Q-range from 1Å^{-1} to 6Å^{-1} accessible with a standard wavelength around λ=1.5Å is sufficient to extract the desired structural information.

For the present Debye simulations the following properties were considered: The rolling type (concentric cylinders or scrolls), the chiral angle, the length, the inner radius, the number of walls and the spacing between these. It was confirmed that all of the bulk structural properties should be determined as distributions rather than as single values, and the simulations proved XRPD unable to distinguish a sample consisting of concentric cylinders with a distribution of diameters from a scroll type sample. Finally it was shown that if the tubes are bent, as can often be seen in TEM images, the length will appear much shorter in an XRPD experiment. To facilitate the bulk characterisation of the MWCNTs from experimental XRPD data, a library of diffractograms simulated for various values of the above mentioned properties was constructed. The library was subjected to a principal component analysis to limit the number of variables and identify the effects of the correlating properties. Initial tests using a combination of PCA and basis function transformations showed that it is possible to directly obtain mean bulk structural properties from XRPD data of MWCNTs, but the method should be improved by adding the distributions of the determined properties.

The above described case studies performed using the Debye approach serve to illustrate that the method can be used to characterise nanostructured materials of technological importance. The general Debye program was written as an alternative to Rietveld refinements for nanocrystalline materials, and as such it has proven its purpose.

Appendix A

The Debye equation and the Lorentz correction

The Lorentz correction term $L_{\theta_{hkl}}$ is an angle-dependent term used to correct the squared scattering amplitudes $|F_{hkl}|^2$ in order to obtain the measured intensity I_{hkl}, *c.f.* (3.1). In an ideal world the reciprocal lattice consists of points which cross the infinitely thin surface of the Ewald sphere to give diffraction into a point detector. In reality the reciprocal lattice points have a small non-negligible volume due to the finite size of the crystals, the Ewald sphere has a thickness because the wavelength is not truly monochromatic, and the detector covers an area defined by the slit system. All of these deviations from ideality are the basis of the Lorentz correction. For XRPD data measured on a diffractometer with a fixed sample-to-detector-distance the Lorentz correction is given as:

$$L_\theta \;=\; \frac{1}{\sin 2\theta \;\sin\theta} \tag{A.1}$$

The Lorentz correction can be split up into two contributions; one arising because of the variation in time it takes the different reciprocal lattice "points" to cross the Ewald sphere, this is the so-called single crystal term, and one arising because the fraction of the scattering from a random powder that reaches the detector depends on the scattering angle, referred to as the powder diffraction term. The expressions for these contributions are derived in the following, assuming that the sample-to-detector-distance is kept constant.

A.1 Single crystal Lorentz correction

The Lorentz correction in the case of a single crystal diffraction experiment can be explained by means of the Ewald construction in Figure A.1. The crystal is placed at point A and rotated counterclockwise around an axis through A perpendicular to the plane of the paper with a constant angular velocity ω. This means that the reciprocal lattice is rotated with the same angular velocity around the origo O and that the reciprocal lattice point P with the scattering vector r^* and squared scattering amplitude $|F(r^*)|^2$ crosses the Ewald sphere. The intensity reaching the detector is proportional to the time it takes P to cross the Ewald sphere. Thus the Lorentz correction can be calculated as the constant velocity by which the Ewald sphere is rotated ($\omega\frac{1}{\lambda}$, where $\frac{1}{\lambda}$ is the radius of the Ewald sphere) divided by the angular dependent velocity component of point P along the radius of the Ewald sphere ($\omega\,|r^*|\cos\theta$, where $|r^*|=\frac{2\sin\theta}{\lambda}$):

$$L_\theta \;=\; \frac{\omega\frac{1}{\lambda}}{\omega|r^*|\cos\theta} \;=\; \frac{1}{2\sin\theta\cos\theta} \;=\; \frac{1}{\sin 2\theta} \qquad \text{(A.2)}$$

Figure A.1 The Lorentz correction in the single crystal case (Giacovazzo, 1992)

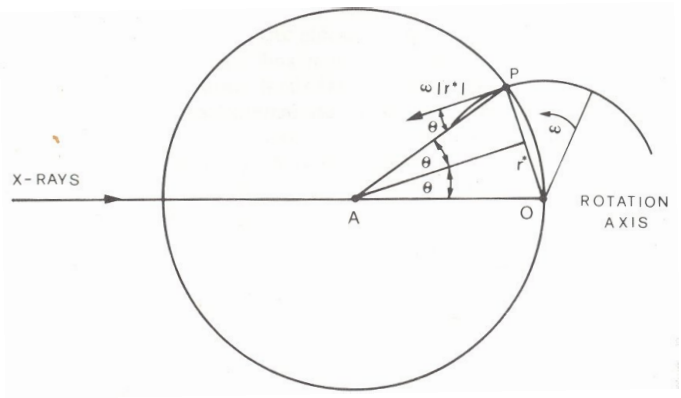

A.2 Lorentz correction for powder data

The scattering incident described above refers to a reciprocal lattice consisting of single points distributed in space dependent on the orientation of a single scattering crystal. For powder diffraction the scattering originates from a random powder consisting of an – in principle – infinite number of crystals with a random orientation. Therefore the reciprocal lattice points are smeared over the entire reciprocal lattice sphere of radius $|r^*|$. The nature of the Lorentz correction factor in this case can be explained by Figure A.2. Circle R′R′ is the intersection of the Ewald and reciprocal lattice spheres where the diffracted intensity is detected. Circle NN is where the normals to the diffraction planes giving rise to diffraction on the circle R′R′ fall, thus circle NN is a measure of the fraction of crystallites in the correct diffraction position. Using a point detector the measured intensity must be proportional to the circumference of circle NN (the larger the circle the more crystallites contribute to the scattering incident) and inversely proportional to the circumference of circle R′R′ (the detector and slit system has a fixed opening no matter the size of the scattering circle), thus:

$$L_\theta = \frac{2\pi R \sin(90-\theta)}{2\pi R \sin 2\theta} = \frac{\cos\theta}{\sin 2\theta} = \frac{1}{2\sin\theta} \tag{A.3}$$

Figure A.2 Lorentz correction for powder diffraction data (Lonsdale, 1948)

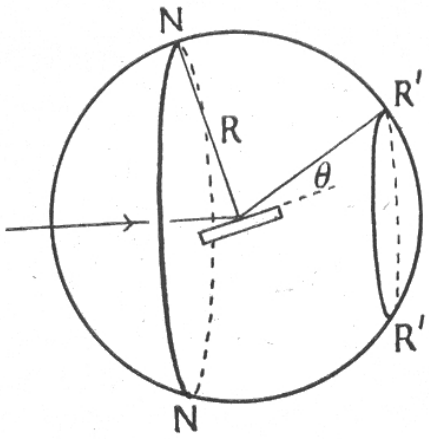

A.3 Lorentz correction for Debye simulations

To determine L_θ for Debye simulated data it is important to realise that the geometry of the scattering is the same as in section A.2, thus the squared scattering amplitude $|F(r^*)|^2$ which can be calculated by means of the Debye summation is smeared evenly over the entire surface of the reciprocal lattice sphere of radius $|r^*|$.

For a diffractometer with with a fixed sample-to-detector-distance consider a detector and slit system with a fixed angular opening of α by β radians; α on the 2θ scale corresponding to rotating the sample by $\frac{\alpha}{2}$ in Figure A.1, and β in the direction corresponding to a rotation around the incoming beam as in Figure A.2. Expressions for the fraction of crystallites in the correct diffraction position and for the fraction of the intensity actually hitting the detector must be determined for every scattering angle as in the derivation of (A.3). In each case it will be assumed that the fractions of the Ewald and reciprocal lattice spheres covered by the detector are so small that they can be taken to be rectangular without any loss of accuracy.

The fraction of crystallites in diffraction position is given by:

$$x_\theta^X = \frac{2\pi\frac{1}{\lambda}\frac{\alpha}{2}\cdot 2\pi\frac{1}{\lambda}\cos\theta\beta}{4\pi(\frac{1}{\lambda})^2} = \tfrac{1}{2}\pi\alpha\beta\cos\theta \qquad \text{(A.4)}$$

where denominator $4\pi(\frac{1}{\lambda})^2$ is the surface area of the Ewald sphere, and the numerator is the area of the rectangle covered by the normals to the scattering planes for which the scattered intensity hits the detector. It is assumed that $\alpha\sim 0$ so that $\cos\theta\sim\cos(\theta+\frac{\alpha}{2})$.

The fraction of the intensity measured is:

$$x_\theta^I = \frac{2\pi\frac{2\sin\theta}{\lambda}\frac{\alpha}{2}\cdot 2\pi\frac{\sin 2\theta}{\lambda}\beta}{4\pi(\frac{2\sin\theta}{\lambda})^2} = \tfrac{1}{4}\pi\alpha\beta\cos\theta \qquad \text{(A.5)}$$

where denominator $4\pi(\frac{2\sin\theta}{\lambda})^2$ is the surface area of the reciprocal lattice sphere, and the numerator arises because a certain rotation of the Ewald sphere around an axis through the sample position corresponds to the same rotation of the reciprocal lattice sphere around a parallel axis through the origo of the reciprocal lattice. Again it is assumed that $\alpha\sim 0$ so that $\sin 2\theta\sim\sin(2\theta+\alpha)$.

Seing that the fraction of the crystallites in diffraction position is proportional to the fraction of the intensity measured, the Lorentz factor for Debye simulated data simply becomes unity.

Appendix B

DebyeHelp.txt

```
2007-11-26
DEBYE

Simulation program for powder diffraction
Jette Oddershede and Kenny Stahl
Department of Chemistry
Technical University of Denmark
DK-2800 Lyngby, Denmark
kenny@kemi.dtu.dk


General:
The Debye simulation program calculates the XRPD pattern from a crystalline
sample by summing over all interatomic distances as stated by the Debye
equation (Debye, 1915, Ann. Phys. 46: 809). The crystallographic information
can be imported from a cif and modified if necessary. Additional information
about particle shape, size and size distribution can be supplied. The min,
max and step in 2theta as well as the wavelength can be altered to agree with
experimental XRPD data. Finally the simulated data can be convoluted with a
polarisation function, a pseudo-Voigt type instrument profile (Wertheim et al.,
1974, Rev. Sci. Instrum. 45(11): 1369) and functions related to the Guinier
diffraction geometry and absorption in cylindrical samples.

Limitations:
The program is presently limited to five different atom types.

Thermal parameters:
The program only works with isotropic thermal parameters, and these are
averaged to one per atom type. If the crystallographic information read from a
cif does not contain a Biso, it will be calculated from the anisotropic thermal
parameters in case these are given, otherwise the program defaults to Biso=0.
```

GUI:
The Windows GUI for the Debye program offers the opportunity to open an experimental XRPD pattern, simulate or open an earlier simulated diffractogram for comparison, and do a fit. The progress of the simulation and fitting can be followed in the lower text window while the diffraction patterns are shown in the upper graphical window. It is possible to zoom in the graphical window by holding down the left mouse button and dragging a window of the desired size.

Fitting:
During the fitting procedure the simulated diffractogram is scaled using either an ordinary scale factor, an overall temperature factor, or both. The background is modelled as a Chebyshev polynomial with a user-specified number of parameters (between 0 and 14). A 2theta zero shift can be manually added during the fitting procedure. The fitted parameters and their standard deviations are written on the rec file (see files below) and can be viewed via patterns, table output. Based on the fitted background it is possible to calculate the crystallinity, the fraction of intensity resulting from the simulated crystalline part of the sample, between any two values of 2theta. N.B. The crystallinity calculation is only valid if the background represents amorphous scattering from the sample only.

How to install:
Copy debye.exe, winpow.ini and DebyeHelp.txt (this file) into a common directory and make the appropriate correction to the winpow.ini file to define the default directory and the path leading to notepad.exe or some other text editor.

Files:
To do the simulations a name.rec input file in ascii format is needed. The input file can be constructed from scratch using the commands listed below. It is, however, much easier to import the crystallographic information from a cif and define the desired structural parameters via the GUI menus. If an experimental diffraction pattern is imported for fitting it is possible to obtain the following output files:

%name.out	List file summarising the simulation
%name.tab	Tabulated summary of simulation and fitting
%name.xy	Simulated diffractogram
%name.sum	2theta, experimental pattern, simulated and fitted pattern, difference, background.

Multiple simulations:
For more time-consuming calculations the Debye program offers the opportunity to run a series of simulations without having to start each simulation manually in the GUI. For this purpose all the rec files must first be constructed along with a file called anything.mlt containing the names of all the rec files to run, one name per line, eg:
name1.rec
name2.rec
name3.rec
Under file, open project choose the mlt file and select project, calculation.

```
Shortcut keys:
up arrow    Zoom out in graphical window
down  "     Zoom in        "
left  "     Move zoom window left
right "     Move zoom window right
F1          Return graphical window to full view
F2          Return graphical and text windows to original size
F3          Project, calculate
F4          Patterns, fit pattern
F5          File, save project as
F6          Project, edit files
F7          Project, edit structure
F8          Project, edit instructions
ctrl-I      Soft interupt of calculation
ctrl-T      Patterns, table output


List of records in the name.rec input file for the Debye simulations:

Required records:

SPGR  Space group symbol in the old Hermann-Mauguin notation with
      inversion centre at origo, e.g. P 21 21 21, P -3, P 63/M, F d d d.
      For rhombohedral space groups use the hexagonal setting.

CELL  Cell dimensions
      11-20  cell(1)     a [A]
      21-30  cell(2)     b [A]
      31-40  cell(3)     c [A]
      41-50  cell(4)     alpha [deg]
      51-60  cell(5)     beta  [deg]
      61-70  cell(6)     gamma [deg]

XYZ   Atomic coordinates
      11-14  atomname    Atom identifier
      18-20  atype       Atomic number
      21-30  x           Fractional coordinates
      31-40  y
      41-50  z
      51-60  sof         Site occupancy factor
      61-70  Biso        Isotropic temperature factor coefficient B=U8PI**2


Optional records:

TITL  11-78  Title of the job

PWDT  11-70  Name of experimental diffraction pattern file
```

```
FRMT  Input data format (optional)
      11-15              1  gdf (Huber)
                         2 - txt (Bruker)
                         3 - udf (Philips)
                         4 - xrdml (PANalytical)
                         5 - xy (general)
                         6 - std (general)

ELAM  Wavelengths (default: 1.54059, 0, 0 - CuKalpha1)
      11-20  lambda(1)   [A]
      21-30  lambda(2)   [A]
      31-40  lambda(3)   lambda2/lambda1 intensity ratio

ANOM  Anomalous dispersion corrections (defaults to MoKalpha, CuKalpha
      or CoKalpha depending on which wavelength is closest)
      11-14  atomname    Atom identifier
      21-30  fp          f'
      31-40  fpp         f''

DDIS  Distance calculation accuracy (default: 100)
      11-20  disacc      Reciprocal of the distance calculation accuracy [A-1]

DSHA  Particle shape (default: 1, 3)
      11-15  crysttype   1  box
                         2  cylinder
                         3 - ellipsoid
      16-20  cylaxis     1  a*
                         2  b
                         3  a*xb

DABC  Particle size
      If crysttype = 1: number of cells along the a-, b- and c-axis
      (default: 10, 10, 10)
      If crysttype = 2: cylinder dimensions [A]
      (default: 100., 50.)
      If crysttype = 3: ellipsoid dimension [A]
      (default:    50., 50., 50.)
      11-20  ncella/cyllen/ellips1
      21-30  ncellb/cylrad/ellips2
      31-40  ncellc/ellips3

DPSD  Particle size distribution (PSD) (default: 0, 3, 1)
      11-15  ptype         0  do not apply PSD
                           1  apply PSD
      16-20  psample       number of sizes sampled on
                           either side of the mean (max 9)
                           NB! Only sizes 1.0+-0.1 psample,
                           eg. 0.8, 0.9, 1.0, 1.1 and 1.2
```

```
                    times the input size (psample=2)
      21-25  distype      1  Weibull mass distribution
                         2  Gaussian      "
                         3  Uniform       "
                         4  User defined  "

DUS1  User defined mass distribution coefficients
      required for distype=4 (default: 0.,...,0.)
      11-20  puser(-9)    mass fraction of particles
      21-30  puser(-8)    with a size defined as
      31-40  puser(-7)    0.1, 0.2, 0.3, 0.4 etc times the input size
      41-50  puser(-6)
      51-60  puser(-5)
      61-70  puser(-4)
      71-80  puser(-3)

DUS2  User defined mass distribution coefficients
      11-20  puser(-2)
      21-30  puser(-1)
      31-40  puser(0)
      41-50  puser(1)
      51-60  puser(2)
      61-70  puser(3)
      71-80  puser(4)

DUS3  User defined mass distribution coefficients
      11-20   puser(5)
      21-30   puser(6)
      31-40   puser(7)
      41-50   puser(8)
      51-60   puser(9)

DTTH  2theta interval information and scale factor
      (default: 5., 50., 0.02, 0)
      11-20  ttmin       2thetamin  [deg]
      21-30  ttmax       2thetamax  [deg]
      31-40  ttdif       2thetastep [deg]
      41-50  ttsca       =0  intensity per unit cell is output
                         >0  intensity output for ttsca unit cells
                         <0  simulated pattern will be scaled to Imax=-ttsca

DCOR  Intensity corrections (default: 1, 0, 0, 0, 0, 1.)
      11-15  corrpol     0  no polarisation correction
                         1  polarisation correction
      16-20  corrpeak    0  no instrument profile
                         1  pseudo-Voigt instrument peak profile correction
      21-25  corrabs     0  no absorption correction
                         1  correct for absorption in cylindrical sample
      26-30  corrguin    0  no guinier correction
```

```
                    1  correct for 45 deg Guinier tangent angle
      31-35  corrauto   0 - no auto divergence slit
                        1 - auto divergence slit correction
      36-45  corrmur    value of muR for absorption correction

DPRO  pseudo-Voigt peak profile parameters (gL+(1-g)G)
      (default: 0., 0., 0.01, 0.5, 0., 0.)
      11-20  uu         FWHM
      21-30  vv         (Caglioti et al., 1958, Nucl. Instrum.
      31-40  ww         Methods 3(4): 223)
      41-50  g1         pseudo-Voigt mixing parameter
      51-60  g2         g = g1+g2(2theta)+g3(2theta)2
      61-70  g3         (Hill and Howard, 1985, J. Appl. Cryst. 18(3): 173)


Records added by the fitting routine:

SCAL  Scale factors (default: 1., 0.)
      11-22  scal       scale factor from fitting
      23-32  ovrl       overall temperature factor

ZETT  2theta zero shift (default: 0.) NB! Not refined
      11-20  zett       2theta zero shift

BKGR  Chebyshev background parameters (default: 0.,...,0.)
      NB! Three records, 0-14 Chebyshev parameters
      11-20  bkg1/bkg6/bkg11
      21-30  bkg2/bkg7/bkg12
      31-40  bkg3/bkg8/bkg13
      41-50  bkg4/bkg9/bkg14
      51-60  bkg5/bkg10

DCRY  Crystallinity (default: 5., 50., 0.)
      11-20  crystttmin  [deg]
      21-30  crystttmax  [deg]
      31-40  xtallinity  Crystallinity calculated
                         between crystttmin and crystttmax

DVAL  Fitting results
      11-20  fitpatrval  Pattern R-value from fit
      21-30  fitpatwrval Weighted pattern R-value
      31-40  fitpatgof   GooF from fit
      41-47  fitpatnpar  Number of fitted parameters
      48-54  nstep       Number of 2theta steps
```

Appendix C

Publications

C.1 On the determination of crystallinity and cellulose content in plant fibres

Thygesen, A., Oddershede, J., Lilholt, H., Thomsen, A. B. and Ståhl, K. (2005). *Cellulose*, 12(6): 563–576

Cellulose (2005) 12:563–576
DOI 10.1007/s10570-005-9001-8

On the determination of crystallinity and cellulose content in plant fibres

Anders Thygesen[1,2,*], Jette Oddershede[3], Hans Lilholt[1], Anne Belinda Thomsen[4] and Kenny Ståhl[3]
[1]*Materials Research Department, Risø National Laboratory, P.O. Box 49, DK-4000, Roskilde, Denmark;* [2]*Danish Centre for Forest, Landscape and Planning, The Royal Veterinary and Agricultural University, Højbakkegård Allé 1, DK-2630, Tåstrup, Denmark;* [3]*Department of Chemistry, Technical University of Denmark, Building 207, DK-2800, Lyngby, Denmark;* [4]*Biosystems Department, Risø National Laboratory, P.O. Box 49, DK-4000, Roskilde, Denmark; *Author for correspondence (e-mail: anders.thygesen@risoe.dk; fax: +45-4677-5758)*

Received 4 January 2005; accepted in revised form 17 June 2005

Key words: Cellulose, Crystallinity, Debye, Plant fibres, Rietveld, X-ray

Abstract

A comparative study of cellulose crystallinity based on the sample crystallinity and the cellulose content in plant fibres was performed for samples of different origin. Strong acid hydrolysis was found superior to agricultural fibre analysis and comprehensive plant fibre analysis for a consistent determination of the cellulose content. Crystallinity determinations were based on X-ray powder diffraction methods using side-loaded samples in reflection (Bragg-Brentano) mode. Rietveld refinements based on the recently published crystal structure of cellulose Iβ followed by integration of the crystalline and amorphous (background) parts were performed. This was shown to be straightforward to use and in many ways advantageous to traditional crystallinity determinations using the Segal or the Ruland–Vonk methods. The determined cellulose crystallinities were 90–100 g/100 g cellulose in plant-based fibres and 60–70 g/100 g cellulose in wood based fibres. These findings are significant in relation to strong fibre composites and bio-ethanol production.

Abbreviations: HPLC – High pressure liquid chromatography; DM – Dry matter

Introduction

Cellulose is technically a very interesting material. Plant fibres, as for instance hemp fibres, have high strength, low density and high sustainability, which can supplement glass fibres in composites (Hepworth et al. 2000; Madsen and Lilholt 2003). It has been shown empirically that the fibre tensile strength and elastic modulus depend on the cellulose content squared (Klinke et al. 2001). Due to the expected correlation between the tensile strength of the fibres and the cellulose crystallinity, it is of interest to find effective and reliable methods to determine the sample crystallinity of cellulose containing materials at different stages of processing. Plant fibre waste materials like corn stover and wheat straw have not proved useful for high performance composite materials due to their low cellulose content and bigger cell lumen resulting in low tensile strength. However, these

materials are useful for bioethanol production after pre-treatment and enzymatic hydrolysis of the cellulose and hemicellulose to monosaccharides (Felby et al. 2003; Varga et al. 2004). The enzymatic hydrolysis for converting cellulose to glucose substrate is mainly performed with exoglucanase for crystalline cellulose and endoglucanase for amorphous cellulose. Hence, it is valuable to know the amount of crystalline cellulose and amorphous cellulose, in the sample to develop enzyme mixtures optimized for the hydrolysis (Teeri and Koivula 1995; Thygesen et al. 2003).

Plant fibres are built essentially of cellulose, hemicellulose, lignin, pectin and minerals. Cellulose consists of both amorphous and crystalline regions. To determine the cellulose crystallinity in plant fibres, accurate determination of the cellulose content is needed, as cellulose is expected to be the only crystalline constituent. Cellulose consists of linear chains of poly[β-1,4-D-anhydroglucopyranose] ($C_{6n}H_{10n+2}O_{5n+1}$ (n = degree of polymerisation of glucose)), which crystallize through hydrogen bonding between the chains and has cellobiose as repeated unit (Figure 1a). The crystal structure of cellulose in higher plants is that of cellulose Iβ (Sarko and Muggli 1974; Nishiyama et al. 2002), which is monoclinic, space group $P2_1$, with the cellulose chains arranged along the unique c-axis (Figure 1b).

X-ray powder diffraction is an obvious method to study the sample crystallinity due to the diffraction peaks from cellulose crystals (Figure 2). However, all materials give rise to X-ray scattering, also the amorphous part of a sample. It is measured that hemicellulose and lignin have diffractograms similar to amorphous cellulose giving wide unspecific peaks (unpublished data). The

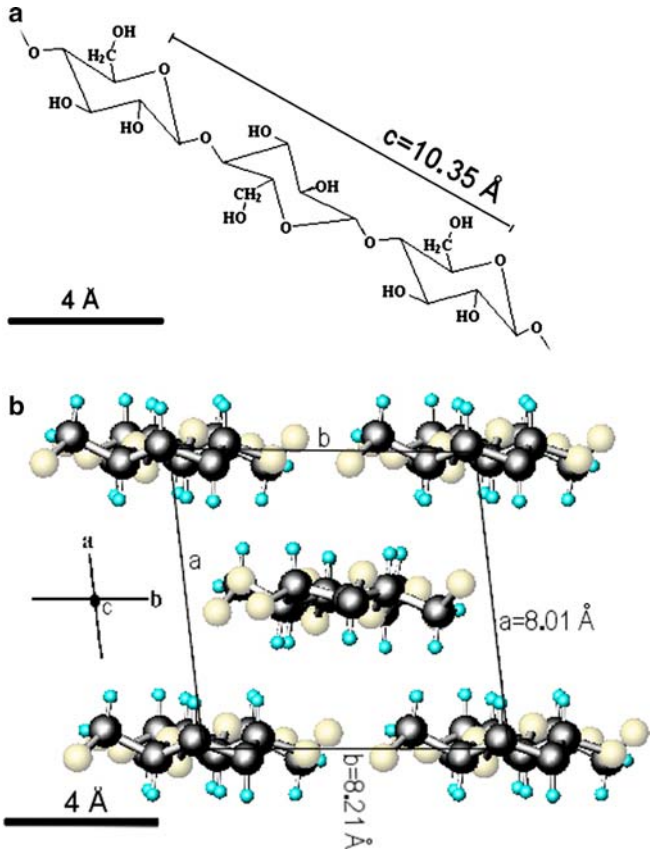

Figure 1. (a) The repeated cellobiose unit in cellulose as compared to the c-axis length. (b) The cellulose Iβ structure viewed along the unique c-axis of the $P2_1$ unit cell with the a- and b-axis in the paper plane (5 molecule chain ends are thereby shown).

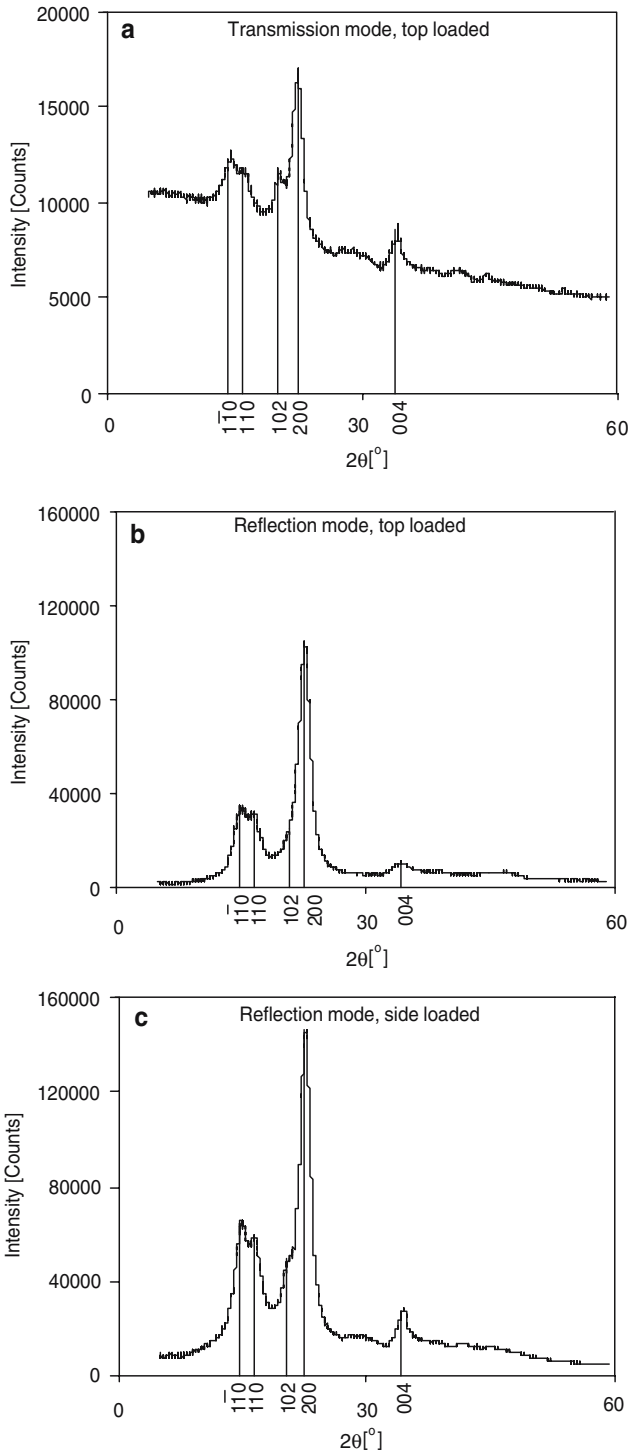

Figure 2. Diffractograms of filter paper measured in transmission mode (a) and reflection mode (b & c) to investigate the effect of diffraction geometry. Both top loaded (b) and side-loaded (c) paper samples are measured to see the effects of sample preparation and preferred orientation.

amorphous scattering will show up as a softly rising and decreasing background. Determination of the sample crystallinity is thus a problem of separating the amorphous from the pure crystalline part of a powder diffraction pattern. With well-crystallized samples, i.e. with large enough crystallites, this is rather simple as such crystallites give sharp diffraction peaks, which can be easily separated from the amorphous background. In the case of cellulose, the crystallites are very small, typically 20–50 Å in diameter, which will cause considerable peak broadening and serious peak overlap. Consequently, the separation of crystalline from amorphous scattering is no longer trivial. The crystallite diameter can be determined with X-ray diffraction based on the width of peaks representing directions perpendicular to the fibre axis (indices: 110, $1\bar{1}0$ and 200), while the crystallite length can be determined based on the width of peaks representing directions parallel with the fibre axis (index: 004) (Figure 2).

The scope of this paper is twofold. Firstly, we want to compare four different methods to assess the crystalline part of a cellulose diffraction pattern in order to determine the sample crystallinity: (1) Segal method, based on the intensity measured at two points in the diffractogram (Segal et al. 1959); (2) Ruland–Vonk method, based on a separate measurement of an amorphous standard scaled to the diffraction pattern (Ruland 1961; Vonk 1973); (3) Rietveld refinement method, based on refinements of the crystal structure, peak parameters and background (Rietveld 1967, 1969); and (4) Debye calculation method, where the crystalline scattering is calculated based on the crystal structure and crystallite size (Debye 1915). Secondly, we want to determine the cellulose content in plant fibres. For this purpose an accurate plant fibre analysis procedure is needed. The three most well known methods were compared: (1) Comprehensive plant fibre analysis (Browning 1967), (2) Agricultural fibre analysis (Goering and Van Soest 1970), and (3) Strong acid hydrolysis (Kaar et al. 1991). The samples used in the present study were purified cellulose (filter paper and Avicel cellulose), hemp fibres, Norway spruce and corn stover, which were chosen to cover a wide range of cellulose contents and biomass types. The samples were used without prior cellulose purification in the X-ray diffraction experiments to avoid modification of the cellulose structure.

Experimental

Materials

Organosolv lignin, (Aldrich 37, 101–7) was used as amorphous reference material. *Filter paper* (Frisenette ApS 165–70) and microcrystalline *Avicel cellulose* (Merck 2351) were used as purified cellulose materials. *Hemp fibres* (*Cannabis sativa* L., *Felina*) were hand peeled from the middle section of hemp stems (Thygesen et al., submitted). *Norway spruce* (*Picae abies*) was obtained from Ølstykke sawmill, Denmark, as a fresh, chipped and bark free material. The wood chips were dried at 20 °C for 7 days and ground with a hammer mill to 5 mm size. *Corn stover* from maize plants (*Zea Mays* L.) grown in Hungary in 2003 was recuperated following threshing in the combine harvester at grain harvest.

Chemical analysis

Before the plant fibre analyses, the samples were milled into particles that could pass a 1 mm sieve. The mineral content was determined by incineration of the raw samples at 550 °C for 3 h. *Comprehensive plant fibre analysis* is a gravimetric method used for fibres from agricultural plants and wood. Wax was extracted in chloroform, water-soluble components in water, pectin in EDTA solution, lignin in chlorite solution and hemicellulose in $NaOH + NaBO_3$ solution with weighing in between each step (Browning 1967). *Agricultural fibre analysis* is a gravimetric method used for analysis of agricultural lignocelluloses (Goering and Van Soest 1970). Non cell wall material (mainly pectin) is extracted in natrium-auryl-sulphate + EDTA + natrium-tetraborate + Na_2HPO_4 + ethylenglukolmonoethylether solution, hemicellulose in 0.5 M H_2SO_4 + cetyltrimethyl-ammonium-bromide solution and lignin in $KMnO_4 + Ag_2SO_4 + Fe(NO_3)_3 + AgNO_3 + KCH_3COO + CH_3COOH$ + butyl alcohol solution followed by filtration and treatment in oxalic acid + 70% ethanol. The amount of remaining solid material was weighed in between each step. *Strong acid hydrolysis* is an HPLC based method, in which the content of sugars in the fibres was measured after sample preparation by swelling in 12 M H_2SO_4 and following hydrolysis at dilute

H_2SO_4 (0.42 M) at 121 °C for 1 h (Kaar et al. 1991). The excess SO_4^{2-} was removed by $Ba(OH)_2$ addition. Shimadzu equipment was used in the HPLC-analysis. The column system used for woody samples consisted of a Rezex RPM column, a deashing cartridge and a security guard (Pb^{2+}) pre-column. The temperature was 80 °C, the eluent was H_2O and the flow rate was 0.6 ml/min. Glucose, xylose, galactose and mannose were detected refractometrically. The column system used for non-woody samples consisted of a Rezex ROA column and a security guard (H^+) pre-column. The temperature was 63 °C, the eluent was 4 mM H_2SO_4 and the flow rate was 0.6 ml/min. Glucose, xylose and arabinose were detected refractometrically.

X-ray powder diffraction

X-ray powder diffraction experiments were performed for sheets of filter paper in both transmission and reflection geometry to determine the best experimental mode. The transmission experiment was performed with a Huber G670 Guinier camera using CuKα_1 radiation. The thin samples were placed at a 45 ° angle to the primary beam and rocked during data accumulation. The data was collected for 30 h and in the 2θ-range 1.4–100 ° with a step size of 0.005°. For the reflection geometry measurements a Philips PW1820/3711 diffractometer with a symmetric θ-2θ Bragg-Brentano scattering geometry, CuKα radiation, a secondary graphite monochromator and an automatic divergence slit was employed. Data were collected in the 2θ-range 5–60° with a step size of 0.02° and a counting time of 20 s per step. The reflection mode intensities were corrected for the effects of the automatic divergence slit. No 2θ-dependent absorption correction is necessary for the symmetric Bragg-Brentano mode with the low-absorbing samples used in this study.

From the resulting diffractogram (Figure 2a) it was clear that the large air scattering contribution to the background of the transmission mode data made it very difficult to estimate the fraction of intensity originating from amorphous components in the sample. This effect was practically absent for the reflection mode diffractograms. Air scattering contributions along with Compton scattering comprise only a few percent of the continuously varying background, so no corrections for these effects were judged necessary. Thermal diffuse scattering (TDS) will contribute both to the continuous background and to the peak intensity and thereby to a large part cancel. However, it should be noted that the presence of uncorrected none-sample contributions to the background to some extent will result in reduced crystallinity values. On the other hand, the reflection mode diffractogram (Figure 2b) was greatly affected by preferred orientation, because the paper sheets consisted mainly of fibres in the lateral plane, giving too weak $00l$ peaks relative to the 110, $1\bar{1}0$ and 200 peaks. When loading fibrous samples into the sample holder from the top and flattening the X-ray illuminated surface, this effect is much enhanced. This effect could be reduced by cutting the sample into small pieces in a knife mill with a 0.5 mm sieve, wetting 0.5 g sample with distilled water, loading it into a sample holder from the side with respect to X-ray illuminated surface, and letting the 2 mm thick fibre sheet air dry overnight before the reflection mode diffractogram (Figure 2c) was recorded. To minimize preferred orientation and air scattering effects, it was therefore decided to perform all X-ray powder diffraction experiments in reflection mode on such side loaded samples. In addition, the number of counts was higher in the reflection diffractograms, which decreased the statistical uncertainty. Each sample was prepared and measured twice. The fibre sheets were dried at 105 °C after the X-ray diffraction experiments in order to determine the sample crystallinity based on the dry matter content.

Determination of the sample crystallinty

The sample crystallinity (g crystalline cellulose/100 g DM) is defined as the ratio of the amount of crystalline cellulose (cellulose Iβ) to the total amount of sample material (dry matter = DM), including crystalline and amorphous cellulose, lignin, hemicellulose, pectin, etc. The cellulose crystallinity is defined as 'g crystalline cellulose/100 g cellulose', and can be calculated as the ratio of the sample crystallinity to the cellulose content of the sample.

$$\text{Cellulose crystallinity} = \frac{\text{g crystalline cellulose}}{\text{g cellulose}} = \frac{\text{g crystalline cellulose/g DM}}{\text{g cellulose/g DM}} \quad (1)$$

Method 1: the Segal method

The sample crystallinity, x_{CR}, has frequently been determined by means of Equation 2 using the height of the 200 peak (I_{200}, $2\theta = 22.7°$) and the minimum between the 200 and 110 peaks (I_{AM}, $2\theta = 18°$) (Figure 3a). I_{200} represents both crystalline and amorphous material while I_{AM} represents amorphous material only.

$$x_{CR} = \frac{I_{200} - I_{AM}}{I_{200}} \quad (2)$$

The expression requires that the amorphous material diffracts with the same intensity at 18° and 22.7°, and that the crystalline cellulose does not contribute to the intensity at 18° (Segal et al. 1959).

Method 2: the Ruland–Vonk method

A way to separate the amorphous and crystalline contributions to the diffracted intensity and estimate the sample crystallinity has been outlined by Ruland (1961) and Vonk (1973). Here, it was assumed that the Bragg peaks are sharp, i.e. the crystallites are large enough for the intensity between the diffraction peaks to be negligible. The amorphous part of the intensity was obtained by measuring the scattering of the compound on amorphous form. This amorphous diffractogram was then scaled by a factor $c(s)$, where $s = 2 \sin \theta / \lambda$, to bring it below the diffractogram of the partly crystalline compound. The scale factor $c(s)$ was allowed to vary continuously throughout the s-interval to meet the requirement that the crystalline diffraction intensity should be zero between some of the diffraction peaks (the diffractograms touch at several points).

In the present work, lignin was chosen as the amorphous standard (c.f. Andersson et al. 2003). Because of the small crystallite sizes, the tails of the diffraction peaks extended far from the peak positions as illustrated in Figure 3a. This had the

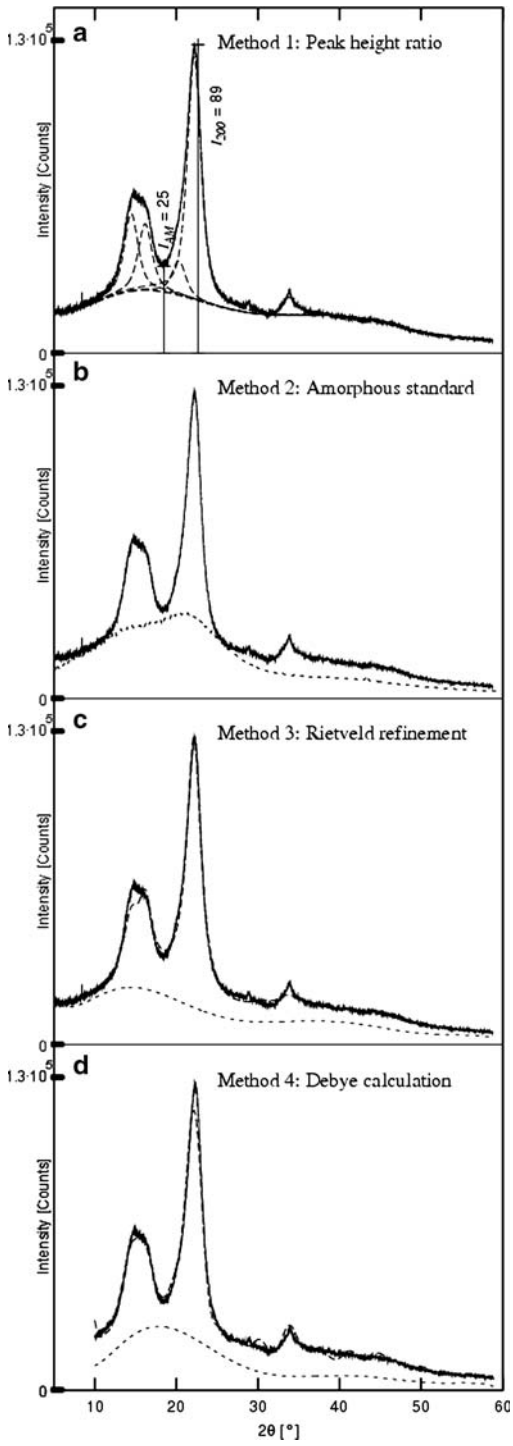

Figure 3. Determination of the crystalline cellulose contents in the hemp fibres measured with the Segal method (a), the Ruland-Vonk method (b), Rietveld refinement (c) and Debye calculation (d). For b, c and d the obtained fits for the amorphous and crystalline diffraction are shown.

effect that the actual background level was well below the diffraction curve of the partly crystalline cellulose sample for practically all scattering angles. The use of a continuously varying scale factor seemed incorrect in the light of Figure 3a, so in this study, it was chosen to use a constant scale factor c to make the background touch the diffractogram in one point/interval only (Figure 3b). Assuming that the intensity $I(s)$ at a given angle is the sum of the crystalline $I_{CR}(s)$ and amorphous $I_{AM}(s)$ contributions, the sample crystallinity was calculated from:

$$x_{CR} = \int_{s_0}^{s_p} I_{CR}(s) \cdot s^2 ds \Big/ \int_{s_0}^{s_p} I(s) \cdot s^2 ds \qquad (3)$$

The integration limits were in this work chosen so only the part of the diffractogram containing visible crystalline intensity was used, i.e. $s_0 = 0.11$ Å^{-1} ($2\theta = 10°$) and $s_p = 0.99$ Å^{-1} ($2\theta = 50°$).

Method 3: Rietveld refinement

The Rietveld method (Rietveld 1967, 1969) uses the full diffraction pattern in a least-squares fitting procedure to simultaneously fit unit cell, crystal structure, peak profile parameters, background, etc. The method requires knowledge of the crystal structure (unit cell, space group and atomic coordinates) as starting parameters. It is today the dominant method for obtaining structural information from powder diffraction data (Young 1993).

Refinements were performed with a modified LHMP1 Rietveld program (Howard and Hill 1986) with the cellulose Iβ crystal structure including thermal parameters from Nishiyama et al. (2002) as input. The best fit for all samples was obtained by refining one scale factor, 10 Chebyshev background parameters, 2 Voigt peak profile parameters, 2 cell dimensions (a and b) and one preferred orientation parameter along the $0k0$-direction (Figure 3c), giving a total of 17 refined parameters for all samples. The full-width half maximum parameters were fixed to values corresponding to those from a LaB_6 standard. The use of a Voigt profile function made it possible to estimate the crystallite dimensions relative to a given direction (here the fibre direction $00l$), but, because of the preferred orientation effects and the minimal size of the crystallites the estimates became quite poor, especially along the fibre direction. Finally the sample crystallinity was calculated using Equation 3 as outlined in Method 2, assuming that the fitted background comprised the amorphous contribution to the diffractogram.

Correct cell parameters of cellulose Iβ are essential to a proper fit. Both the Rietveld refinements of the present study and former studies of the cellulose Iβ crystal structure (Sarko and Muggli 1974; Woodcock and Sarko 1980; Simon et al. 1988; Sugiyama et al. 1991; Koyama et al. 1997; Finkenstadt and Millane 1998; Nishiyama et al. 2002) indicated large variations in the apparent unit cell dimension. It is clear that the true unit cell dimensions of cellulose Iβ are constant at constant temperature. The observed unit cell dimensions, however, are sensitive to the type of radiation (X-rays/neutrons/electrons), method (powder/fibre diffraction) and preparation method. In particular, the recorded 2θ-values depend on the actual penetration depth of the radiation, which directly affect the calculated/refined unit cell dimensions and strongly correlate to the 2θ zero-shift. Due to remaining preferred orientation effects, reflections unique to the c-direction were still severely suppressed. In fact, the cellulose diffraction patterns contained only three strong diffraction peaks, all of which have $l = 0$ (Figure 2). Several combinations of refined parameters were tried with the different samples with the objective to obtain the best possible fit of the crystalline diffraction. The final choice was to refine the a- and b-axis parameters and the preferred orientation parameter. The 2θ zero-shift was fixed to zero, the c-axis parameter to 10.35 Å and the gamma angle to 96.5°, which are average values given in the literature (Figure 1).

Method 4: Debye calculations

The basis of this method is the Debye formula (Debye 1915), which states that the diffracted intensity from a collection of atoms can be calculated as the sum over all interatomic distances r_{ij}:

$$I(s) = \sum_{i,j} f_i(s) f_j(s) \frac{\sin(2\pi s \cdot r_{ij})}{2\pi s \cdot r_{ij}} \qquad (4)$$

where s is defined as before and $f_i(s)$ is the atomic form factor of atom i. Thus, the method

requires a full set of atomic positions for a whole crystal, not just for one unit cell. Consequently, the effects from crystallite size and shape were inherent to the calculated diffractograms. A program was written to calculate the diffractograms for cellulose Iβ crystallites of different shapes and sizes exploiting the structural parameters including thermal parameters of Nishiyama et al. (2002). Both elliptical, cylindrical and box shaped crystallites, each consisting of an assembly of entire unit cells, were tested. The best correspondence to the experimental peak profiles was obtained if the diffractograms were simulated for crystallites of cylindrical shape with the cylinder axis along the fibre direction. To obtain a size distribution, the diffractogram was added to the intensities simulated for cylinders with radii of ± 1 Å. The simulated diffractograms were then fitted to the experimentally obtained patterns by means of a scale factor and a continuously varying background consisting of a 9th order Chebyshev polynomial (Figure 3d).

As with Rietveld refinements it was essential to use correct unit cell dimensions. Therefore, a number of simulations varying *a* and *b* simultaneously in steps of 0.05 Å were carried out. These diffractograms were fitted to the experimentally obtained diffractograms to determine the *a* and *b* parameters that best fitted the given sample. The length of the *c*-axis was fixed to 10.35 Å as argued for the Rietveld refinements (Figure 1). The crystallite size was identified from comparisons to simulated diffractograms with known crystallite dimensions, and the sample crystallinity was determined from the fitted background level using Equation 3 as outlined under Method 2.

Results

Chemical composition

The results of the chemical composition are presented in Table 1. The method that offered the best distinction between cellulose and hemicellulose, and thereby the best determination of these components, was the strong acid hydrolysis. The complex carbohydrates, cellulose and hemicellulose were hydrolysed into monomeric sugars, cellulose to glucose and hemicellulose to xylose, arabinose, galactose and mannose, which were subsequently determined by HPLC. Klason lignin is the insoluble residue after the sample preparation with H_2SO_4. The agricultural fibre analysis gave approximately the same cellulose and hemicellulose results with a lower standard deviation (Table 1), but the method is more laboriously demanding and in some cases unspecific. In comparison, the comprehensive plant fibre analysis gave unrealistically high contents of hemicellulose in the purified cellulose samples (filter paper and Avicel cellulose). Obviously, some cellulose was extracted in the hemicellulose extraction step of the comprehensive plant fibre analysis, a solution of NaOH and boric acid, making this step unspecific for hemicellulose. For Avicel cellulose, the reproducibility in this step was further complicated by the relatively small particle size of the Avicel cellulose, which resulted in extended dissolution, swelling and recrystallization of cellulose I into cellulose II (confirmed by X-ray diffraction). However, the first step in the comprehensive plant fibre analysis is recommended also in the strong

Table 1. Chemical composition of the plant materials measured by the three methods (g/100 g dry matter) and arranged according to: Results from comprehensive plant fibre analysis/agricultural fibre analysis/strong acid hydrolysis. The pooled standard deviations are shown for each method and component. Numbers in bold are results from the strong acid hydrolysis.

Material	Cellulose g/100 g	Hemi-cellulose g/100 g	Lignin g/100 g	Pectin g/100 g	Wax g/100 g	Water extractives g/100 g	Residual[a] g/100 g	Minerals g/100 g
Corn stover	33/32/**33**	33/31/**21**	14/6/**19**	1/–/–	3/–/–	10/–/–	–/24/**20**	**7**
Norway spruce	49/58/**49**	30/18/**20**	17/19/**29**	3/–/–		1/–/–	–/5/**2**	**0**
Hemp fibres	64/68/**63**	14/10/**10**	5/3/**6**	5/–/–	0/–/–	8/–/–	–/14/**17**	**4**
Filter paper	86/93/**84**	10/6/**6**	1/0/**0**	2/–/–	0/–/–	1/–/–	–/1/**8**	**0**
Avicel cellulose	–[b]/95/**87**	–[b]/4/**4**	1/0/**0**	1/–/–		1/–/–	–/0/**10**	**0**
Standard deviation	1.4/0.5/3.1	0.7/0.7/2.1	0.5/0.7/0.5	1.0/–/–	0.1/–/–	1.3/–/–	–/0.5/2.8	0.1

[a]Residual from agricultural fibre analysis and strong acid hydrolysis = pectin + wax + water extractives.[b]The swelling of the relatively small particles resulted in partial extraction of cellulose in the hemicellulose extraction step making the separation of these components impossible.

acid hydrolysis for specific extraction of wax, water-soluble components and pectin by ethanol, which is otherwise included in Klason lignin. The gravimetric extraction steps in the comprehensive plant fibre analysis resulted in consistent contents of 0–1 g/100 g dry matter (DM) for pectin, wax and water extractives in the purified cellulose samples, content levels that were within the uncertainty limits. In the other samples, the content of pectin, wax and water extractives were 1–5 g pectin/100 g DM, 0–3 g wax/100 g DM and 1–10 g water extractives/100 g DM (Table 1).

Crystallinity determinations

The results of the crystallinity and the crystallite dimensions are presented in Tables 2 and 3 and shown graphically in Figure 4.

Method 1: The Segal method

The Segal method (Segal et al. 1959) was very straightforward and fast to use, but the sample crystallinity of 47–83 g/100 g DM (Table 2) were found to be higher than the cellulose contents (Table 1) for both corn stover and hemp fibres (Figure 4). There are several reasons for these unrealistic results. Most importantly the cellulose crystallites are so small that peak overlap is bound to occur in the region around 18° for cellulose Iβ, giving too high values of I_{AM} (Figure 3a). The fact that I_{200} was overestimated due to preferred orientation added another element of uncertainty to the system. When comparing diffractograms for cellulose samples originating from different species there is also the effect that both the apparent cell parameters and the crystallite sizes vary considerably from species to species (Table 3). This results in large variations in the I_{AM} levels, making the Segal method very unreliable when comparing sample crystallinities in general. None of these points have been mentioned in the original work by Segal et al. (1959), where the method was used only for differently purified cellulose samples all originating from cotton. Since it is a simple method, it has been extensively utilized up to this day (Alexander 1969; Buschle-Diller and Zeronian 1992; Mwaikambo and Ansell 1999; De Souza et al. 2002), but the mentioned limitations and assumptions make it unreliable and incorrect.

Table 2. Sample crystallinity (g/100 g dry matter) with pooled standard deviations calculated for each X-ray diffraction method.

Material	Peak height ratio segal g/100 g DM	Amorphous standard (Ruland-Vonk) g/100 g DM	Rietveld refinement g/100 g DM	Debye calculation g/100 g DM
Corn stover	47	39	37	32
Norway spruce	47	56	33	32
Hemp fibres	77	49	60	69
Filter paper	83	72	57	61
Avicel cellulose	62	67	41	39
Standard deviation	1.5	1.4	1.6	2.0

Table 3. Crystallite dimensions of the cellulose in the plant materials calculated by Rietveld refinement and Debye calculation (Å). Numbers in parenthesis = standard deviations.

Material	Rietveld refinement		Debye calculation	
	Length[a] [Å]	Diameter [Å]	Length[a] [Å]	Diameter[b] [Å]
Corn stover	36(4)	30(1)	100	22(2)
Norway spruce	60(6)	30(1)	150	34(2)
Hemp fibres	24(2)	43(1)	50	36(2)
Filter paper	62(2)	60(1)	150	52(2)
Avicel cellulose	64(3)	39(1)	100	38(2)

[a]Along 00*l*. [b]Standard deviations arise from the ±1 Å distribution of the crystallite radii used in the simulations.

Method 2: Ruland–Vonk method

The Ruland–Vonk method as applied in the present study has the great advantage that it is a purely experimental approach to the determination of the sample crystallinity, giving values of 39–72 g/100 g DM (Table 2). However, for all the samples studied the scaled amorphous background touched the diffractogram somewhere in the 2θ-interval between 7 and 13°, thus in the low angle region, where the intensity is most poorly determined due to the fine adjustment of slits and the effects of axial divergence (Figure 3b). Therefore, besides the subjective definition of the scale factor, the Ruland–Vonk method is very sensitive to instrumental inaccuracies. It should be added that the amorphous standard material must be chosen so as to resemble the amorphous components in the samples. In the light of these observations the Ruland–Vonk method is difficult to apply to comparative studies of samples of different origin. Despite the problems mentioned above, the Ruland–Vonk method has been widely accepted as one of the best ways to determine the sample crystallinity in plant fibres during more than a decade (Fink and Walenta 1994; Sao et al. 1994, 1997).

Method 3: Rietveld refinement

During the last 30 years, Rietveld refinement has become the dominant method for refining structural information from powder diffraction when a preliminary structural model is known. Until recently such a model was not available for cellulose. However, with the publication of the cellulose Iβ crystal structure (Nishiyama et al. 2002), Rietveld refinement has become a feasible method for obtaining information about crystallite size and sample crystallinity from diffraction data. As soon as a minimum set of parameters has been found, it is straightforward to carry out refinements for a series of diffraction patterns with any of the Rietveld refinement programs available (Figure 3c).

The decision of which parameters to refine was not trivial for cellulose, since severe peak overlap gave very few resolved peaks (Figure 3a). The limited number of resolved peaks restricted the number of refinable parameters and resulted in large correlations between some of these. As already mentioned, the unit cell dimension in the *c*-direction was intimately linked to the preferred orientation. The unit cell lengths along the *a* and the *b* axis correlated strongly with the 2θ zero shift, and were in average fitted to 8.01 Å and 8.21 Å, respectively (Figure 1). Furthermore, the background level was greatly affected by the choice of peak shape function, since the peak tails extended very differently with different peak shape functions. However, bearing these correlations in mind, it was possible to find a common minimum set of refinement parameters suitable to all of the samples. That made the Rietveld refinement method consistent and straightforward to use, giving values of sample crystallinity in the range 33–60 g/100 g DM (Table 2).

Method 4: Debye calculation

As for the Rietveld refinements, the Debye calculation method requires that the cellulose crystal structure is known. While the entire Rietveld refinement procedure was implemented into one refinement program, the Debye calculation method required two different programs, one to simulate the diffractogram and one to fit the simulated diffractogram to the experimental data and determine the quality of the fit (Figure 3d). Every time a parameter such as the cell dimensions, the crystallite size or shape was changed, a new diffractogram had to be calculated by the simulation program and imported into the fitting program. The simulations are usually computationally heavy, scaling as the number of atoms in the crystallites squared. For crystallites as small as those of cellulose (diameter = 22–52 Å; length = 50–150 Å, Table 3) the simulation time was, however, no more than 1 min per diffractogram on a standard PC, so the bottleneck lies more in finding an appropriate set of parameters, systematically varying them and comparing the resulting diffractograms to the experimental diffraction patterns. Nevertheless, the Debye calculation method has one great advantage over the Rietveld refinement approach: The crystallite dimensions are not fitted by analytical peak profile functions but are included explicitly in the simulations. This fact made the Debye calculation method an excellent reference method for sample crystallinity determinations, giving values in the range 32–69 g/100 g DM (Table 2). It offered the most reliable estimate of the crystalline part of the diffraction pattern, but due to the computing efforts it is less suited as a standard method.

Discussion

Many earlier studies on crystallinity excluded the determination of the chemical fibre composition, so in fact only the sample crystallinity was determined and not the actual cellulose crystallinity. The strong acid hydrolysis was found superior for determination of the cellulose content due to chromatographic differentiation between the monomers in cellulose and hemicellulose (Table 1). The cellulose content in the examined samples was used to determine the cellulose crystallinity (g/100 g cellulose), which was used to evaluate the four investigated methods for crystallinity determination. However, all the three analysis methods seemed reliable when they are used to determine the mass balance over wet oxidation experiments with for example, wheat straw and hemp fibres as raw materials resulting in process recoveries of cellulose in the range 90–110% (Thygesen et al. 2003, 2004; Thomsen et al. 2005). Enzymatic hydrolysis resulted in up to 85% conversion of cellulose into glucose in pre-treated corn stover and pre-treated wheat straw, which seem reasonable. Based on these observations, the chemical analysis methods give reasonable results within an uncertainty interval of 10% of the measured value.

The best experimental mode in the X-ray diffraction experiments was reflection geometry during the measurements to avoid air scattering and obtain higher intensity, since the reflected and not the penetrated X-ray photons were counted (Figure 2). The use of side-loaded samples resulted in close to random orientation of the sample fibres so the ratio between the diffraction peak intensities was similar to the peaks in the diffractogram calculated by the Debye method. Therefore, the use of reflection mode for X-ray powder diffraction and side loading of samples are prerequisites for a reliable and optimal crystallinity determination.

The present comparative study showed that the most consistent and reliable methods for sample crystallinity determinations were the Rietveld and Debye methods. Both methods took full account of the overlapping and widely broadened diffraction peaks of cellulose (Figure 3a). The sample crystallinity determined by the Rietveld refinements and the Debye calculations were consistent and corresponded to realistic cellulose crystallinities below 100 g/100 g cellulose, cf. Figure 4. The Debye method was found an excellent reference method, but required extensive computation, and programs are not generally available. Rietveld refinement on cellulose was after some initial considerations concerning the parameter set, straightforward to carry out and gave consistent results. Combined with the facts that the cellulose Iβ crystal structure has been established (Nishiyama et al. 2002) and that Rietveld refinement

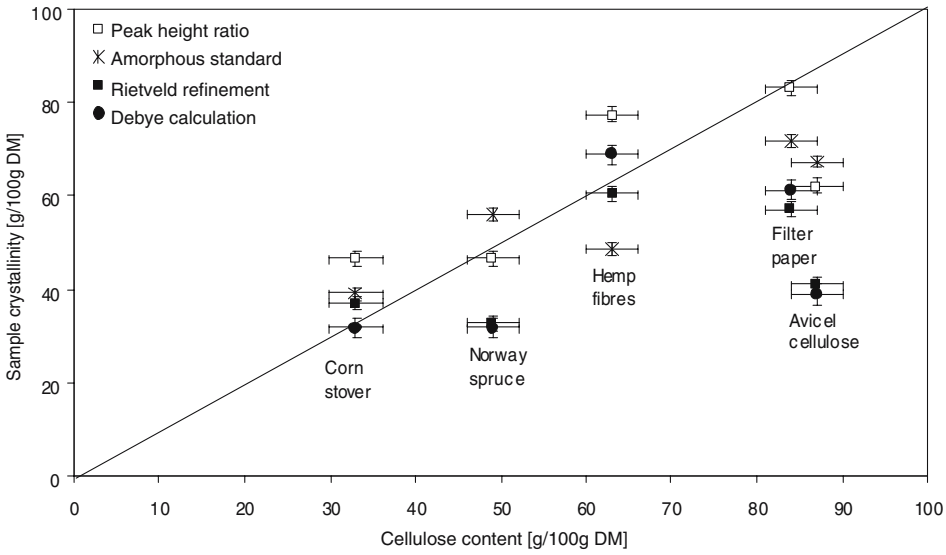

Figure 4. Comparison of the four methods for sample crystallinity determination combined with chemical analysis by the strong acid hydrolysis (g/100 g dry matter). The length of the error bars is one standard deviation.

programs are available, the Rietveld method should be the preferred method for sample crystallinity determinations of plant fibre samples. The Segal and Ruland–Vonk methods do not consider the effect of peak overlap contributing to the apparent background. As a result, the Segal and Ruland–Vonk methods will generally underestimate the sample crystallinity, compared both to the cellulose contents of the samples (Table 1 and Figure 4) and the Debye and Rietveld methods. However, the Ruland–Vonk method is still a robust method and if the peak overlap effect on the apparent background is taken into consideration, it may still be the preferred method when the true amorphous background can be determined experimentally.

Rietveld refinement and Debye calculations gave in addition, an estimate of the crystallite dimensions (Table 3). Reliable determination of the microfibril length was not possible by the Rietveld method due to the weak 004 reflection and peak overlaps. A more reliable determination was obtainable by the Debye method due to the manual fitting of the peaks. Bardage et al. (2004) have by transmission electron microscopy measured the microfibril diameter to 50 Å in Norway spruce pulp fibres, which is on the same level as determined by the Debye method in this study for filter paper (52 Å) and higher than for raw Norway spruce (34 Å) (Table 3). The determined crystallite diameter was thereby comparable or smaller than the microfibril diameter.

The results for cellulose content and crystallinity of the five samples are presented in Table 4 and compared in Figure 5. The corn stover and the hemp fibres are both plant-based and showed a high cellulose crystallinity of 90–100 g/100 g cellulose (full drawn line in Figure 5).

The Norway spruce sample had a cellulose crystallinity of 67 g/100 g cellulose (Table 4), which is comparable to previous findings in fresh Norway spruce (51–71 g/100 g cellulose) by X-ray diffraction (Andersson et al. 2003). The cellulose crystallinity was on the same level in filter paper (65 g/100 g cellulose) and was also comparable to the crystallinity of 68 g/100 g cellulose that has been measured in pine kraft pulp by ^{13}C-NMR by Liitia et al. (2003). The cellulose crystallinity of wood based materials was thereby found to be on

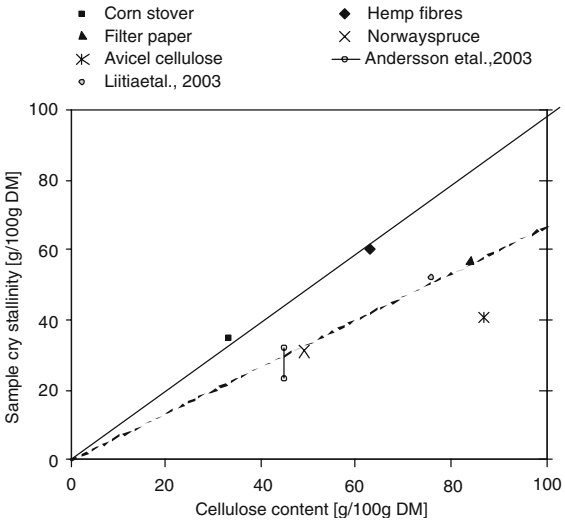

Figure 5. Sample crystallinity determined by Rietveld refinement compared to the cellulose contents measured by strong acid hydrolysis. The relationship for plant based materials (full drawn line) and the relationship for wood based materials (dotted line) are shown.

Table 4. Cellulose crystallinity (g/100 g cellulose) and contents (g/100 g dry matter) of cellulose, crystalline cellulose, amorphous cellulose and residual material, measured by the optimal methods: Strong acid hydrolysis and Rietveld refinement.

Material	Cellulose crystallinity g/100 g cellu.	Cellulose content g/100 g DM	Sample crystallinity g/100 g DM	Amorphous cellulose content g/100 g DM	Residual content
Corn stover	100	33	33	0	67
Norway spruce	67	49	33	16	51
Hemp fibres	96	63	60	3	37
Filter paper	68	84	57	27	16
Avicel cellulose	47	87	41	46	13
Norway spruce[a]	51–71	45	23–32	13–22	55
Pine kraft pulp[b]	68	76	52	24	24

[a]Andersson et al. (2003): Fresh Norway spruce analysed with X-ray powder diffraction and calculated with the Ruland–Vonk method.[b]Liitia et al. (2003): Norway spruce pulp analyzed with ^{13}C-NMR.

the same level, when determined by X-ray diffraction and by ^{13}C-NMR, and the pulping process had only slight effect on the cellulose crystallinity. The present data as well as the literature data are shown in Figure 5 and related by the dotted line, indicating a cellulose crystallinity of 60–70 g/100 g cellulose.

The Avicel cellulose originating from unspecified plant fibres had a low cellulose crystallinity (47 g/100 g cellulose), which shows that the very fine milling and hydrolysis during the cellulose purification decreased the cellulose crystallinity (Figure 5), compared to the plant fibres.

It should be mentioned that the improved methods for determination of cellulose content and cellulose crystallinity are fundamental for further investigations on how the cellulose microstructure affects the fibre strength and the enzymatic hydrolysis of cellulose to glucose. According to this investigation, the cellulose crystallinity is 90–100 g/100 g cellulose in plant-based fibres and 60–70 g/100 g cellulose in wood based fibres (Figure 5). Corn stover is a promising raw material for ethanol production and hemp fibres are interesting for fibre production. The high crystallinity in corn stover indicates that enzymatic hydrolysis for bioethanol production requires a high dosage of exoglucanase enzymes. The high content of cellulose and high crystallinity in hemp fibres indicates a high performance for strong composites.

Conclusions

- Among the investigated techniques, the best experimental mode was reflection geometry for the X-ray diffraction experiments to avoid air scattering, and using side-loaded samples to reduce the effect of preferred orientation.
- The Rietveld method was preferred for sample crystallinity determinations, since it took full account of the overlapping and widely broadened diffraction peaks of cellulose and gave consistent results.
- An accurate method for determination of the cellulose content is needed for determination of the cellulose crystallinity (g/g cellulose) in plant fibres. Strong acid hydrolysis followed by chromatographic measurement of monomers was chosen as the best of the tested methods.
- According to the novel methods, plant based materials have cellulose crystallinity of 90–100 g/100 g cellulose and wood-based materials have 60–70 g/100 g cellulose.
- Reliable methods for the determination of cellulose content and cellulose crystallinity are fundamental for further investigations on how the cellulose microstructure affects the fibre strength and for the development of methods for enzymatic hydrolysis of the cellulose.

Acknowledgements

This work was part of the project 'High performance hemp fibres and improved fibre networks for composites' supported by the Danish Research Agency of the Ministry of Science and of the project EFP Bioethanol part 2 J. nr. 1383/03–0002. Dr. Claus Felby is acknowledged as supervisor for Ph. D. student Anders Thygesen. Mr. Tomas Fernqvist and Mrs. Ingelis Larsen are acknowledged for technical assistance and Dr. Bo Madsen, Dr. Enikö Varga and Dr. Mette Hedegaard Thomsen are acknowledged for discussion and inspiration.

References

Alexander L.E. 1969. X-ray Diffraction Methods in Polymer Science. Wiley-Interscience, New York.

Andersson S., Serimaa R., Paakkari T., Saranpää P. and Pesonen E. 2003. Crystallinity of wood and the size of cellulose crystallites in Norway spruce (*Picea abies*). J. Wood Sci. 49: 531–537.

Bardage S., Donaldson L., Tokoh C. and Daniel G. 2004. Ultrastructure of the cell wall of unbeaten Norway spruce pulp fibre surfaces. Nordic Pulp Paper Res. J. 19(4): 448–452.

Browning B.L. 1967. Methods of Wood Chemistry. Interscience Publishers, A division of John Wiley & Sons, New york.

Buschle-Diller G. and Zeronian S.H. 1992. Enhancing the reactivity and strength of cotton fibres. J. Appl. Polym. Sci. 45(6): 967–979.

Debye P. 1915. Zerstreuung von Röntgenstrahlen. Ann. Phys. 46: 809–823.

De Souza I.J., Bouchard J., Methot M., Berry R. and Argyropoulos D.S. 2002. Carbohydrates in oxygen delignification. Part I: Changes in cellulose crystallinity. J. Pulp Paper Sci. 28(5): 167–170.

Felby C., Klinke H.B., Olsen H.S. and Thomsen A.B. 2003. Ethanol from wheat straw cellulose by wet oxidation pretreatment and simultaneous saccharification and fermentation. ACS Symposium Series 855: 157–174.

Fink H.P. and Walenta E. 1994. Röntgenbeugungsuntersuchungen zur übermolekularen Struktur von Cellulose im Verarbeitungsprozeß. Papier 48(12): 739–748.

Finkenstadt V.L. and Millane R.P. 1998. Crystal structure of Valonia cellulose Iβ. Macromolecules 31(22): 7776–7783.

Goering H.K. and Van Soest P.J. 1970. Forage fiber analyses (apparatus, reagents, procedures and some applications). Agricultural Research Service, USDA, Washington DC.

Hepworth D.G., Bruce D.M., Vincent J.F.V. and Jeronimidis G. 2000. The manufacture and mechanical testing of thermosetting natural fibre composites. J. Mater. Sci. 35(2): 293–298.

Howard C.J. and Hill R.J. 1986. LHMP: a computer program for Rietveld analysis of fixed wavelength X-ray and neutron powder diffraction patterns. AAEC (now ANSTO) Report M112. Lucas Heights Research Laboratory.

Kaar W.E., Cool L.G., Merriman M.M. and Brink D.L. 1991. The complete analysis of wood polysaccharides using HPLC. J. Wood Chem. Technol. 11(4): 447–463.

Klinke H.B., Lilholt H., Toftegaard H., Andersen T.L., Schmidt A.S. and Thomsen A.B. 2001. Wood and plant fibre reinforced polypropylene composites. In 1st world conference on biomass for energy and industry. James & James (Science Publishers), pp. 1082–1085.

Koyama M., Helbert W., Imai T., Sugiyama J. and Henrissat B. 1997. Parallel-up structure evidences the molecular directionality during biosynthesis of bacterial cellulose. Proc. Natl. Acad. Sci. USA 94(17): 9091–9095.

Liitia T., Maunu S.L., Hortling B., Tamminen T., Pekkala O. and Varhimo A. 2003. Cellulose crystallinity and ordering of hemicelluloses in pine and birch pulps as revealed by solid-state NMR spectroscopic methods. Cellulose 10: 307–316.

Madsen B. and Lilholt H. 2003. Physical and mechanical properties of unidirectional plant fibre composites – an evaluation of the influence of porosity. Compos. Sci. Technol. 63(9): 1265–1272.

Mwaikambo L.Y. and Ansell M.P. 1999. The effect of chemical treatment on the properties of hemp, sisal, jute and kapok for composite reinforcement. Angew. Makromol. Chem. 272: 108–116.

Nishiyama Y., Langan P. and Chanzy H. 2002. Crystal structure and hydrogen-bonding system in cellulose Iβ from synchrotron X-ray and neutron fiber diffraction. J. Am. Chem. Society 124(31): 9074–9082.

Rietveld H.M. 1967. Line profiles of neutron powder-diffraction peaks for structure refinement. Acta Crystallogr. 22: 151–152.

Rietveld H.M. 1969. A profile refinement method for nuclear and magnetic structures. J. Appl. Crystallogr. 2: 65–71.

Ruland W. 1961. X-ray determination of crystallinity and diffuse disorder scattering. Acta Crystallogr. 14: 1180–1185.

Sao K.P., Samantaray B.K. and Bhattacherjee S. 1994. X-ray study of crystallinity and disorder in ramie fiber. J. Appl. Polym. Sci. 52: 1687–1694.

Sao K.P., Samantaray B.K. and Bhattacherjee S. 1997. Analysis of lattice distortions in ramie cellulose. J. Appl. Polym. Sci. 66: 2045–2046.

Sarko A. and Muggli R. 1974. Packing analysis of carbohydrates and polysaccharides. 3. *Valonia* cellulose and cellulose-II. Macromolecules 7(4): 486–494.

Segal L., Creely J.J., Martin A.E. and Conrad C.M. 1959. An empirical method for estimating the degree of crystallinity of native cellulose using the X-ray diffractometer. Textile Res. J. 29: 786–794.

Simon I., Glasser L., Scheraga H.A. and Manley R.S. 1988. Structure of cellulose. 2. Low-energy crystalline arrangements. Macromolecules 21(4): 990–998.

Sugiyama J., Vuong R. and Chanzy H. 1991. Electron diffraction study on the two crystalline phases occuring in native cellulose from an algal cell wall. Macromolecules 24(14): 4168–4175.

Teeri T.T. and Koivula A. 1995. Cellulose degradation by native and engineered fungal cellulases. Carbohydr. Eur. 12: 28–33.

Thomsen A.B., Rasmussen S.K., Bohn V., Nielsen K.V. and Thygesen A. 2005. Hemp raw materials: The effect of cultivar, growth conditions and pretreatment on the chemical composition of the fibres. Risø National Laboratory. Report No.: R-1507.

Thygesen A., Thomsen A.B., Schmidt A.S., Jørgensen H., Ahring B.K. and Olsson L. 2003. Production of cellulose and hemicellulose-degrading enzymes by filamentous fungi cultivated on wet-oxidised wheat straw. Enzyme Microb. Technol. 32(5): 606–615.

Thygesen A., Thomsen M.H., Jørgensen H., Christensen B.H. and Thomsen A.B. 2004. Hydrothermal treatment of wheat straw on pilot plant scale, 2nd World Conference and Technology Exhibition on Biomass for Energy, Industry and Climate Protection, Rome, Italy, 10–15th May 2004.

Varga E., Reczey K. and Zacchi G. 2004. Optimization of steam pretreatment of corn stover to enhance enzymatic digestibility. Appl. Biochem. Biotechnol. 113(-16): 509–523.

Vonk C.G. 1973. Computerization of Rulands X-ray method for determination of crystallinity in polymers. J. Appl. Crystallogr. 6: 148–152.

Woodcock C. and Sarko A. 1980. Packing analysis of carbohydrates and polysaccharides. 11. Molecular and crystal-structure of native ramie cellulose. Macromolecules 13(5): 1183–1187.

Young R.A. (ed.) 1993. The Rietveld Method. Oxford University Press.

C.2 Bulk characterization of multiwall carbon nanotubes

Oddershede, J. and Ståhl, K. (2006).
***Z. Kristallogr.*, Suppl. 23: 325–330**

Bulk characterization of multiwall carbon nanotubes

Jette Oddershede[1] and Kenny Ståhl[1,*]

[1]Department of Chemistry, Technical University of Denmark, Building 207, DK-2800 Lyngby, Denmark
[*] Contact author; e-mail: kenny@kemi.dtu.dk

Keywords: carbon nanotubes, Debye equation, structure simulations

Abstract. The bulk structural properties of multiwall carbon nanotube samples can be estimated by comparing experimental X-ray powder diffractograms with simulations obtained using the Debye equation. Results typically indicate that the samples contain tubes with dimensions distributed within the following bounds: lengths of 5-15 nm, diameters of 15-25 nm, and walls 10-20 layers thick with a spacing between adjacent layers of 3.35-3.60 Å. The apparent short tube lengths obtained can be explained by the observed bending of the tubes. Furthermore it is possible to obtain information about impurities.

Introduction

Multiwall carbon nanotubes (MWCNTs) consist of several layers of rolled graphene sheets. Since this new type of material was discovered some 15 years ago [1] it has been studied extensively and the suggested applications have been numerous. Many of the studies have focused on the structure of the tubes because of the intimate structure/function relationship. Studies applying TEM and ED [2,3] are very illustrative, but both these structural probes suffer from the fact that they are local. The bulk properties of the sample depend on the average structure, which can only be determined in combination with a global probe. Powder diffraction is the obvious choice for studying the bulk structure of MWCNTs as the tubes are periodic in nature and give rise to distinct diffraction peaks. In addition, powder diffraction will detect crystalline impurities. Many different models have been suggested to explain the diffraction pattern arising from the MWCNTs. The simplest of these are of the disordered graphite type where structural parameters such as the interlayer spacing, the crystallite size and the ordering within a single graphene layer are refined [4-6]. Recently a more sophisticated approach taking into account the actual structure of the tubes has been suggested [7-9]. The basis for this approach is the Debye equation (1) stating that the diffracted intensity from a collection of scatterers can be calculated as a sum over all the interatomic distances r_{ij} [10].

$$I(Q) = \sum_{i,j} f_i(Q) f_j(Q) \frac{\sin(Qr_{ij})}{Qr_{ij}}. \qquad (1)$$

Here $Q = 4\pi \sin\theta / \lambda$ is the scattering vector. The method thus requires the calculation of all atomic positions for a given MWCNT structure followed by the application of equation (1) to obtain the diffractogram. The structural parameters of the MWCNTs can then be systematically varied and the simulated diffractograms compared to the experimental ones in order to obtain a qualified estimate of the bulk structure. Studies of the effects of varying different structural parameters have been carried out previously [7,8], but in a very wide Q-range (0-24 $Å^{-1}$). For these comparative studies a standard crystallographic Q-range (0-7 $Å^{-1}$) is sufficient, and using a longer wavelength will in general give higher angular resolution. The present work has by means of the Debye equation studied the effects of varying: I) the chiral angle, II) the rolling characteristics, III) the structure perpendicular to the tube, and IV) the bending of the tubes in comparison to experimental X-ray diffraction data from bulk MWCNT samples.

Simulations

The MWCNT diffractograms closely resemble that of graphite. Peaks of the *hk*0 (within a layer) and 00*l* (between layers) type dominate due to the limited correlation between different graphene sheets (turbostratic disorder) [3,5,11]. The graphite 100 (2.95 $Å^{-1}$) and 110 (5.11 $Å^{-1}$) peaks are found in a more saw-toothed version due to the turbostratic stacking [12,13] and/or the curvature of the graphene sheets [3]. The peaks corresponding to the interlayer spacing, 002 (1.85 $Å^{-1}$), 004 (3.70 $Å^{-1}$), etc. are shifted to slightly lower *Q*-values, reflecting the fact that the spacing between the multiple walls of the tubes is slightly larger (3.40 Å) than the interlayer spacing in graphite (3.35 Å).

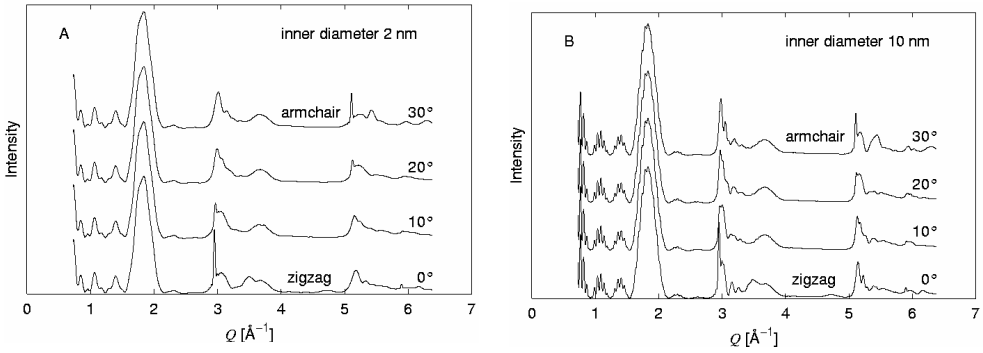

Figure 1. Variation of the chiral angle for different diameters.

I) Chiral angle. From figure 1A it is clear that the value of the chiral angle (the angle between the interatomic vector and the cylinder axis of the tube) greatly affects the appearance of the diffractogram when the diameter of the tube is small. Figure 1B shows that the effect is less pronounced for tubes with larger diameter (the tube length and wall thickness is the same for both diffractograms), but nevertheless it is still present contrary to the conclusions of Kołoczek et al.: *"...for wider carbon nanotubes no conclusion about chirality can be drawn from analysis of their diffraction patterns."* [8]. The reason for this conclusion is probably that the analyses were performed over the full *Q*-range of their simulated diffractograms (0-24 $Å^{-1}$), while the differences are better seen in the details of a more limited *Q*-range. Based on the observations concerning the chiral angle and the appearance of the ex-

perimental diffractograms given in figure 6 it was chosen to consistently use a chiral angle of 15° in the following.

II) Rolling characteristics. The question of whether the MWCNTs are structured as concentric cylinders or as scrolls (figure 2B) has been addressed a number of times [5,12-16] with very different approaches and results, without reaching a definite conclusion. It was previously noted [8] that concentric cylinders with a very constant d-spacing between adjacent cylinders give rise to a splitting of the interlayer diffraction peaks (figure 2A). However, it can easily be shown that these splittings average out if a continuous distribution of different tube diameters (a very realistic model of a true bulk sample) is applied. In figure 2A this average can be compared to the diffractogram simulated for a single scroll type MWCNT with a diameter corresponding to the mean of the distribution used for the concentric average. As there is hardly any difference between the concentric average and the scroll, the conclusion must be that it is not possible to distinguish between averaged concentric cylinders and scrolls from a standard diffraction experiment. Since the latter simulations are much faster to perform, only simulations for scroll type MWCNTs are presented in the following.

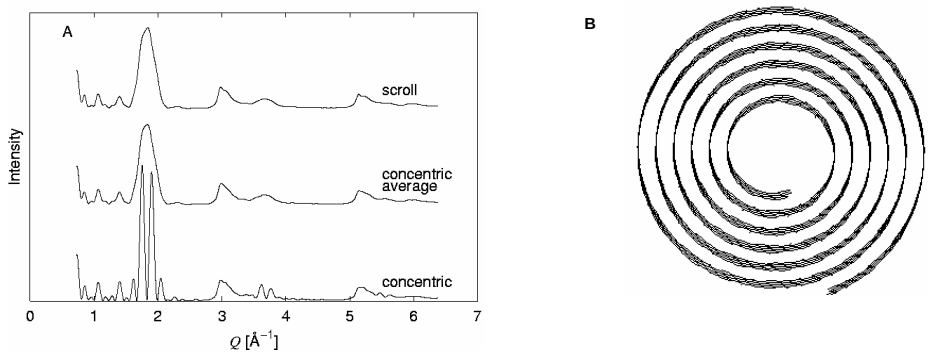

Figure 2. Concentric or scroll type tubes?

III) Structure perpendicular to the tube. Variations in the length and diameter of the MWCNTs affect only the *hk*0 peaks, and these effects have already been extensively described [8]. Instead focus was brought into the effects causing a broadening of the 00*l* interlayer peaks. These have previously been characterized as size (arising from the wall thickness) and strain (due to a distribution of d-spacings) broadening effects [3, 5, 11, 13].

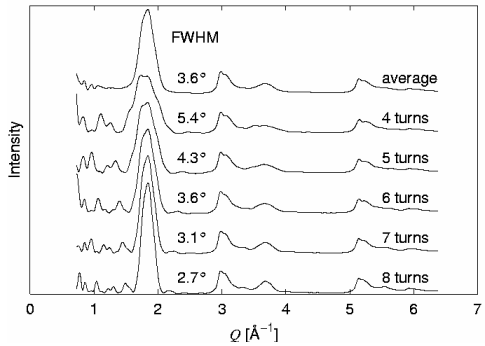

Figure 3. Effects of varying the wall thickness of the tubes.

It is obvious that a finite number of layers will lead to a broadening of the 00*l* peaks. In addition the simulations in figure 3 show that a true sample contains a distribution of different wall thicknesses, as the ripples at low *Q*-values disappear when an average is performed. From an inspection of the experimental diffractograms in figure 6 it is easily seen that a strain broadening of the 00*l* peaks is present, since the 004 peak is much wider as compared to the 002 peak than what would be expected if only size broadening was considered. Furthermore the experimentally observed broadening is asymmetric whereas size broadening is purely symmetric. The asymmetry can be modelled by letting the d-spacing vary between 3.35 Å and 3.60 Å with a higher probability of the smaller spacings.

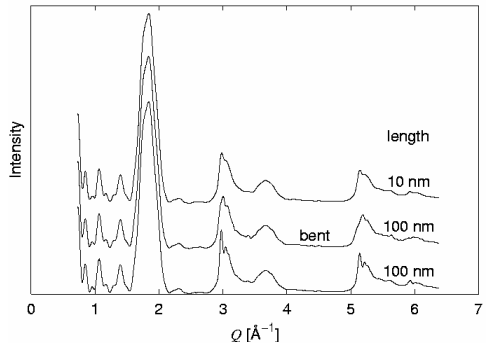

Figure 4. Effects of bending the tubes.

IV) Bending of the tubes. Figure 4 illustrates how the diffractogram from a tube with a length of 100 nm resembles that of a tube with a length of only 10 nm if the longer tube is bent with a 160 nm radius of curvature (compare with figure 5A). Defects in the tubes (figure 5) will have the same effect on the diffractogram; to make the tubes appear shorter than they actually are.

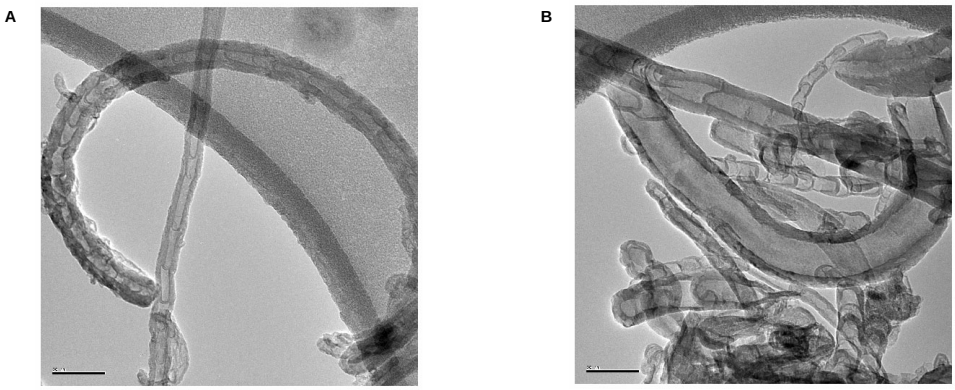

Figure 5. TEM images corresponding to the experimental diffractograms in figure 6 (scale bar 50 nm). A purchased as: Outer diameter 15 ± 5 nm, length 1-5 μm, and purity ~ 95 %. B purchased as: Outer diameter 30 ± 10 nm, length 1-5 μm, and purity > 95%..

Discussion

The simulated diffractogram in figure 6A is for a scroll type MWCNT with a chiral angle of 15°, an isotropic temperature factor coefficient of 2 $Å^2$ to describe the thermal motions, 10-14 turns, a length of 7.5 nm, an inner diameter of 12 nm (outer diameter 18-21 nm), and a distribution of d-spacings between 3.35 Å and 3.60 Å. The background is modelled by a 6^{th} order Chebyshev polynomial. The fit between experiment and simulations is excellent except for the low *Q* side of the 002 peak (perhaps even larger d-spacings than 3.60 Å are present in the sample) and the high *Q* side of the 100 peak (possibly arising because the stacking of graphene layers is not completely turbostratic giving rise to a low intensity graphite 101 peak at 3.1 $Å^{-1}$). The simulated diffractogram in figure 6B is for a MWCNT with 16-20 turns, an outer diameter of 22-25 nm and a length of 10 nm.

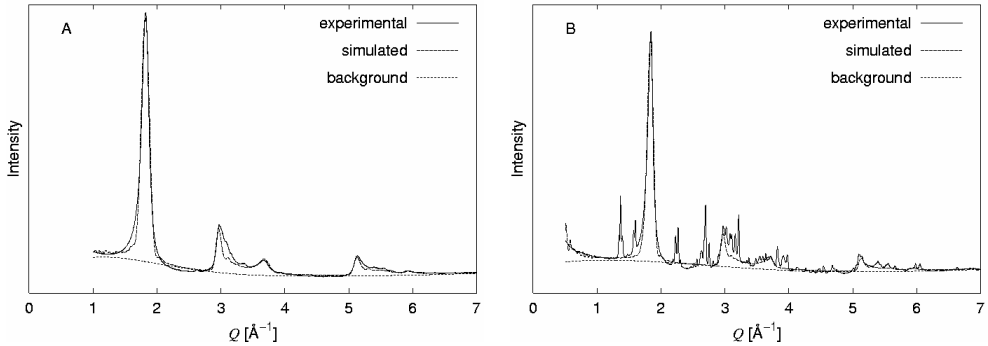

Figure 6. Experimental and simulated diffractograms corresponding to the TEM images in figure 5. The experimental diffractograms were recorded in transmission mode with a HUBER G670 Guinier camera (λ = 1.087 Å) at beam line I711 (MAXLAB, Lund, Sweden) on tablets pressed from 50 mg of commercial MWCNT samples.

The experimental diffractogram of figure 6B is recorded on a sample with contaminations from carbides of Fe, Co and/or Ni since these metals were used as catalysts in the fabrication of the MWCNTs. From the corresponding TEM image (figure 5B) it is obvious that this sample contains more impurities than the one shown in figure 5A, but how much more and which type of impurities it is not possible to tell from the TEM images. The increased amount of impurities is also evident from the experimental diffractograms in figure 6, but as opposed to the TEM technique X-ray diffraction offers the opportunity to identify the impurities.

The fact that even though TEM images demonstrate that the tubes are of the order 1 μm long, the simulations only indicate lengths in the order of 10 nm has been noted previously [9]. In the light of the simulations of bent MWCNTs in figure 4 and the TEM images in figure 5, the most probable explanation to this discrepancy is the bent shapes of the tubes. Previous TEM studies [12] have suggested that a high concentration of defects in the tubes could be another reason for coherence lengths in the order of only 10 nm.

Conclusions

Comparing experimental and simulated powder diffractograms, even in the standard *Q*-range 0-7 $Å^{-1}$, is an excellent way to determine bulk structural parameters for MWCNTs. It is possible to detect and identify impurities and to determine the average chiral angle, while concentric or scroll type tubes cannot be distinguished. Good estimates of the tube dimensions, i.e. length, diameter, wall thickness and interlayer spacing, and more importantly the distribution of these can be obtained from the comparisons. The simulations have made it evident that all of the structural parameters in the bulk samples should be determined as distributions rather than as single values.

One considerable problem still remains: the effects of the different parameters on the appearance of the diffractograms correlate strongly. A way to solve this correlation problem and more unambiguously quantify the experimental bulk tube dimensions is to conduct PCA (Principal Component Analysis) on diffractograms simulated for MWCNTs with different structural characteristics and extract basis functions corresponding to each parameter. It should then be possible to describe the experimental diffractograms as linear combinations of the basis functions, and to simply read the structural characteristics of the bulk samples from the coefficients. This development is in progress.

References

1. Iijima, S., 1991, *Nature*, **354**, 56.
2. Amelinckx, S., Lucas, A. & Lambin, P., 1999, *Rep. Prog. Phys.*, **62**, 1471.
3. Lambin, Ph., Loiseau, A., Culot, C. & Biró, L.P., 2002, *Carbon*, **40**, 1635.
4. Shi, H., Reimers, J.N. & Dahn, J.R., 1993, *J. Appl. Cryst.*, **26**, 827.
5. Reznik, D., Olk, C.H., Neumann, D.A. & Copley, J.R.D., 1995, *Phys. Rev. B*, **52**, 116.
6. Pasqualini, E., 1997, *Phys. Rev. B*, **56**, 7751.
7. Kołoczek, J., Kwon, Y.-K. & Burian, A., 2001, *J. Alloys Comp*., **328**, 222.
8. Kołoczek, J. & Burian, A., 2004, *J. Alloys Comp*., **382**, 123.
9. Kołoczek, J., Burian, A., Dore, J.C. & Hannon, A.C., 2004, *Diamond Rel. Mat.*, **13**, 1218.
10. Debye, P., 1915, *Ann. Phys.*, **46**, 809.
11. Burian, A, Dore, J.C., Fischer, H.E., Sloan, J. & Szczygielska, A., 1999, *Proceedings of SPIE*, **3725**, 107.
12. Zhou, O., Fleming, R.M., Murphy, D.W., Chen, C.H., Haddon, R.C., Ramirez, A.P. & Glarum, S.H., 1994, *Science*, **263**, 1744.
13. Maniwa, Y., Fujiwara, R., Kira, H., Tou, H., Nishibori, E., Takata, M., Sakata, M., Fujiwara, A., Zhao, X., Iijima, S. & Ando, Y., 2001, *Phys. Rev. B*, **64**, 073105.
14. Bandow, S., 1997, *Jpn. J. Appl. Phys*., **36**, 1403.
15. Cumings, J. & Zettl, A., 2000, *Science*, **289**, 602.
16. Xu, G., Feng, Z., Popovic, Z, Lin, J. & Vittal, J.J., 2001, *Adv. Mater.*, **13**, 264.

C.3 Using X-ray diffraction and principal component analysis to determine structural properties for bulk samples of multiwall carbon nanotubes

Oddershede, J., Nielsen, K. and Ståhl, K. (2007).
***Z. Kristallogr.*, 222(3–4): 186–192**

Z. Kristallogr. **222** (2007) 186–192 / **DOI** 10.1524/zkri.2007.222.3-4.186

Using X-ray powder diffraction and principal component analysis to determine structural properties for bulk samples of multiwall carbon nanotubes

Jette Oddershede[I], Kurt Nielsen[II] and Kenny Stahl*,[I]

[I] Department of Chemistry, Technical University of Denmark, Kemitorvet, 207, 2800 Lyngby, Denmark
[II] School of Conservation, Esplanaden, 34, 1263 Copenhagen K, Denmark

Received January 10, 2006; accepted April 10, 2006

Multiwall carbon nanotubes / Bulk structural properties / Debye simulations / Principal component analysis / X-ray powder diffraction

Abstract. It has been attempted to derive the structural properties of bulk multiwall carbon nanotubes (MWCNTs) from a combination of powder diffraction and principal component analysis (PCA). By a transformation of the direct PCA basis functions to a structural parameter set it was possible to obtain average values of inner radius, number of turns and *d*-spacing. The true tube lengths cannot be correctly estimated due to correlations to other properties, tube bending and defects in the tubes. Improvements can be expected by including distributions of the structural properties, further developing the functional relationships between the PCA and parameter functions and including the chiral angle (rolling direction) as a separate parameter.

1. Introduction

The bulk structural properties of multiwall carbon nanotube (MWCNT) samples can be estimated by comparing experimental X-ray powder diffractograms with simulations obtained using the Debye equation. So far the structural characteristics of the sample have been determined as the values used to simulate the diffractogram that, when fitted to the experiment, gave the lowest $R(I)$-value $\left(R(I) = \sum_i |I_i^{\text{obs}} - I_i^{\text{calc}}| / \sum_i I_i^{\text{obs}}\right)$ [1–4]. If there are no correlations between the different properties this procedure is straightforward, but this has been demonstrated not to be the case [4–8].

Applying principal component analysis (PCA) on simulated diffractograms a substantial reduction in dimensionality, typically a factor of 10, can be obtained. Furthermore, to facilitate the interpretation it would be useful to transform the directly obtained PCA basis functions into a coordinate set describing the MWCNT structural properties in terms of length, radius, number of turns and layer spacing. The present paper is an attempt to explore the use of PCA on simulated diffraction patterns combined with a basis function transformation to directly obtain the bulk structural properties of MWCNTs.

* Correspondence author (e-mail: kenny@kemi.dtu.dk)

2. Experimental MWCNT diffractograms

The experimental diffractograms are recorded in transmission mode with a HUBER G670 Guinier camera ($\lambda =$ 1509 Å or $\lambda = 1087$ Å) at Beamline I711, MAXLAB (Lund, Sweden) on 50 mg MWCNT samples pressed into tablets.

3. Simulation of MWCNT diffractograms

The basis for the simulations is the Debye equation [9] stating that the diffracted intensity from a collection of scatterers can be calculated as a sum over all the interatomic distances r_{ij}:

$$I(Q) = \sum_{i,j} f_i f_i \frac{\sin(Qr_{ij})}{Qr_{ij}} \quad \text{where} \quad Q = \frac{4\pi \sin\theta}{\lambda}$$

The method thus requires the calculation of all atomic positions for a given MWCNT structure followed by the application of the Debye equation to obtain the diffractogram.

The MWCNT structural parameters that are of importance for most applications are the dimensions: The length, the (inner) diameter, the number of concentric tubes, and the spacing between these. The focus of the present work has thus been on how to determine the average of these four properties for a bulk sample. In a bulk sample the MWCNTs display distributions of different dimensions, and the ultimate goal is to be able to determine not only the average dimensions but also their distributions. Another MWCNT characteristic is the distribution of chiral angles or rolling directions in the sample. The chiral angle is defined relative to the hexagonal axis in a graphene sheet and can take on values between the achiral

Table 1. Property values used in the simulations.

length [Å]	inner radius [Å]	no. of turns	*d*-spacing [Å]
25	10	6	3.35
100	20	8	3.40
200	30	10	3.45
300	40	12	3.50
500	50	14	3.55
1000			

extremes of 0° and 30°. However, as it is not possible to control this parameter during synthesis at the moment (as opposed to the dimensions, which to some extent can be controlled *via* the choice of catalysts) [10, 11], the determination of chiral angles was left out for the time being. Therefore all diffractograms simulated for the present study have a chiral angle of 15°, a reasonable average value [4].

A still disputed question is whether the MWCNTs are of the scroll type where one graphene sheet is rolled up, or built from separate concentric cylinders [5, 6, 12–15]. It was recently shown that it is not possible to distinguish between the diffraction patterns resulting from the two different structures if a distribution of different diameters is present in the sample with concentric cylinders [4]. As scroll type tubes are faster to simulate it was chosen to use this model. Finally a thermal displacement parameter of $B = 2\text{Å}^2$ was used consistently throughout the simulations.

On the basis of the considerations described above, a library of simulated MWCNT diffractograms with different dimensions designed to cover the size span typically found from experimental data was generated as the basis for the PCA. The property values were varied according to Table 1, giving a total of $6 \cdot 5^3 = 750$ simulated diffractograms.

4. PCA

To analyse the differences between the 750 simulated diffractograms PCA is applied. There are two main reasons for using PCA. Firstly, the dimension of the problem will be strongly reduced, and secondly, it will be much easier to identify the effects of the nanotube properties. However, if this kind of analysis should be of any practical use, some kind of normalisation must be performed on the diffractograms; otherwise the experimental data must be brought to an absolute scale. PCA results in an orthogonal and optimal coordinate system, where orthonormal basis functions constitute the axes. The coordinate system is optimal in the sense that the best approximation of the 750 diffractograms in an n-dimensional subspace is found by linear combinations of the basis functions belonging to the n highest eigenvalues. If $\mathbf{D}$ is a matrix with elements D_{ji} proportional to the intensity at $2\theta_j$ for sample i, then $\mathbf{D}^t\mathbf{D}$ is a symmetric matrix with non-negative eigenvalues. PCA then consists of solving the eigenvalue problem $\mathbf{D}^t\mathbf{D}\mathbf{U} = \mathbf{U}\mathbf{\Lambda}$, where each column of $\mathbf{U}$ contains an eigenvector and $\mathbf{\Lambda}$ is the diagonal eigenvalue matrix with the eigenvalues sorted in a decreasing sequence. The orthonormal basis function matrix, $\mathbf{B}$, is then $\mathbf{B} = \mathbf{D}\mathbf{U}\mathbf{\Lambda}^{-1/2}$. Obviously, the number of basis functions is limited to the number of eigenvalues with significant non-zero values.

In the present case we have chosen a normalisation of the diffractograms such that the diagonal elements of $\mathbf{D}^t\mathbf{D}$ are equal to one. Furthermore, in order to enhance the discriminative power of the PCA, we have used a slightly different approach. Before performing the PCA, the matrix $\mathbf{D}$ is replaced by $\mathbf{D} - \mathbf{M}$, where $\mathbf{M}$ is a matrix of the same rank and dimensions as $\mathbf{D}$ with identical columns each containing the average of the normalised diffractograms. With this setup the diagonal elements, $((\mathbf{D} - \mathbf{M})^t(\mathbf{D} - \mathbf{M}))_{ii}$, contain the sum of squared deviation between the average and the i-th diffractogram, and since the trace is invariant to any orthonormal transformation it is equal to the sum of eigenvalues. This means that we can select an optimal number of basis functions, including the average, to account for any percentage of the total sum of squared deviations. Subsequently, the average diffractogram is orthogonalised and normalised and added to the number of basis functions. However, the normalisation destroys information, especially on the tube length. Comparison of a set of normalised diffractograms for fixed inner radius, number of turns and *d*-spacing (Fig. 1) shows that the differences between the diffractograms are very small. This implies that in order to be able to describe the effect of different tube lengths, we have to include basis functions of very little importance. Tentatively, we have chosen the 80 most important basis functions, including the average. These 80 basis functions account for 99.9994% of the total sum of squared deviations, and an approximation of the diffractograms by a linear combination of these basis functions leads to a maximum $R(I^2)$-value $(R(I^2) =$

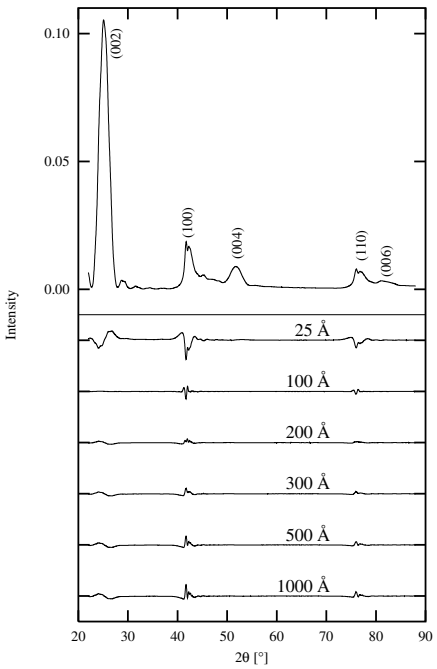

Fig. 1. Effects of varying the tube length for fixed inner radius (30 Å), number of turns (10) and *d*-spacing (3.45 Å). The normalised average diffractogram, which is shown at the top, has been subtracted from the normalised diffractograms simulated for each length. The diffraction peaks are named according to the graphite structure.

$\sqrt{\sum_i (I_i^{\text{obs}} - I_i^{\text{calc}})^2 / \sum_i (I_i^{\text{obs}})^2}$ of 0.0014. The expansion coefficient or coordinate matrix, **C**, is equal to $\mathbf{D}^t\mathbf{B}$. These coefficients should be related to the four nanotube properties, the values of which have been scaled to the interval between 0 and 1 to avoid that the properties are weighted differently.

To get an idea about the importance of the basis functions, we have, for each basis function and each tube property, calculated the linear correlation coefficient between the coordinates and the tube properties. The four most important basis functions are shown in Fig. 2. Whereas Fig. 2b is difficult to interpret, the basis functions in the (100) (2θ: 40–45° for $\lambda = 1509$ Å) and (110) (2θ: 75–80°) regions of Fig. 2a and in the (002) (2θ: 25–30°) region of Fig. 2c have almost symmetrical shapes that are typical for changes in peak width. In Fig. 2d the shape in the (002) region is typical for a shift in peak position.

5. Modelling the tube properties

Since the basis functions given in Fig. 2 are not the only ones with non-negligible correlation to the properties, it is obvious that some linear combination of the basis functions will lead to a better linear correlation, *i.e.* for each property we can find the direction in the 80D space that maximises the linear correlation between the tube property and the coordinate in this direction.

Any unit vector, $\boldsymbol{v}$, in the 80D space can be parameterised by 79 angles, α_j, $j = 1 \ldots 79$ ($\alpha_{80} = 0$):

$$v_1 = \cos(\alpha_1) \quad v_j = \cos(\alpha_j) \prod_{i=1}^{j-1} \sin(\alpha_i), \quad j = 2 \ldots 80 .$$

A subspace omitting the m-th basis function is obtained by putting $\alpha_m = \frac{\pi}{2}$. With 80 dimensions, the number of angular parameters amounts to 316, and with a total number of tube properties of 3000, this leads to an observation-to-parameter-ratio of less than 10. With excess parameters there is a risk that deficiencies in the model may be compensated for by these parameters, *e.g.* the large gap in length between 500 and 1000 Å may be modelled correctly at 500 and 1000 Å, but show an oscillatory behaviour in between, which may result in a very dubious prediction of the tube properties in this region. In an attempt to avoid these problems, we have fixed the observation-to-parameter-ratio to at least 10. Consequently, the number of dimensions has to be reduced. Tentatively, we have, for each direction, selected 65 basis functions. This gives a total of 256 angular parameters, leaving at most 44 parameters to describe the functional relationships between the properties and the coordinates. With a linear model only 8 of these are used. However, the necessity of using 80 basis functions in order to describe all diffractograms with a sufficient accuracy suggests that the problem is highly non-linear. Therefore, the 65 basis functions were selected in following way: For each basis function, the linear correlation coefficients were calculated between the property in question and the 1st, 2nd and 3rd power of the coordinate, and the 65 basis functions with the highest sum of squared correlation coefficients were selected. The search for directions with maximum linear correlation was performed by numerical methods, and the linear correlation coefficients obtained were: −0.9110, 0.9946, 0.9987, and 0.9998, for the length, inner radius, number of turns, and d-spacing, respectively. Although some correlations seem very good, the estimated properties lie too far away from the true values used in the simulations.

It was chosen to use the four linearly optimized $\boldsymbol{v}_k$, $k = 1 \ldots 4$ vectors and the projections d_{ki} of the i-th diffractogram onto these as the starting point for the new model and then expand the linear description to including mixed higher order terms in d_{ki}. By trial and error a suita-

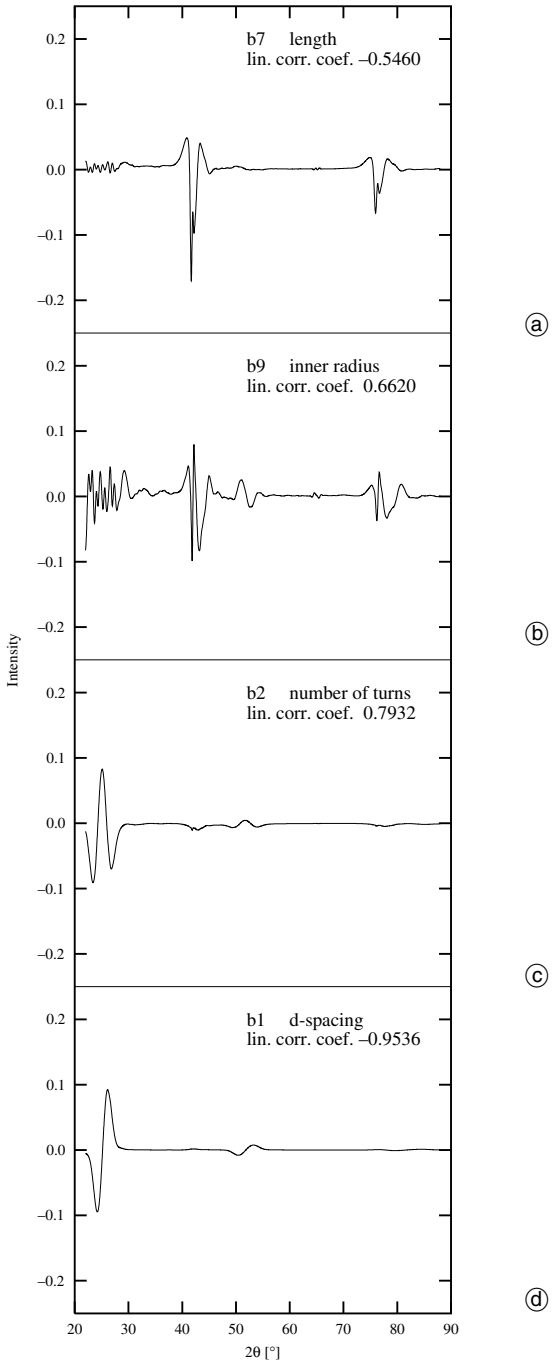

Fig. 2. The basis functions from the PCA with the largest linear correlation coefficients to the four parameters. b7 is the basis function with the 7th highest eigenvalue and so on.

Table 2. Fit quality for the final polynomial model.

	length [Å]	inner radius [Å]	no. of turns	*d*-spacing [Å]
max. deviation	−110.8	2.63	0.206	−0.0028
RMS deviation	30.2	0.66	0.061	0.0007

ble model for property k of diffractogram i, p_{ki}, was obtained as a 4-th order polynomial of the type:

$$p_{ki} = a_{k0} + a_{k1}d_{1i} + a_{k2}d_{1i}^2 + a_{k3}d_{1i}^3 + a_{k4}d_{1i}^4 + a_{k5}d_{1i}^3 d_{2i} + \ldots = \sum_{n_k} a_{kn_k} \prod_{l=1}^{4} d_{li}^{m_{ln_k}}$$

where n_k runs over the non-zero terms in the polynomial expansion for property k, $m_{ln_k} \in \{0, 1, 2, 3, 4\}$ and $\sum_{l=1}^{4} m_{ln_k} \leq 4$. The only exception was found for the length, here it was necessary to include a term proportional to d_{Li}^5, where d_{Li} denotes the projection of the i-th diffractogram onto the length vector.

The procedure to improve the model is then as follows:

- For the present values of d_{ki}, determine the a_{1n_1} coefficients using least squares refinement.
- Optimize the set of angles α_{1j}, $j = 1 \ldots 79$ used to define $\boldsymbol{v}_1$ to get the best estimate of p_{1i}. For every change in α_{1j}, d_{1i} will change, so a new set of a_{1n_1} must be determined, thus the optimization procedure is rather time consuming.
- In the same way optimize the α-angles for the other values of k.
- If the estimates of p_{ki} are not satisfactory, add more terms to the polynomials and repeat the above steps.

In Table 2 the maximum and rms deviations taken over all diffractograms for each property are given. It can be seen that, except for the length, the maximum deviations are at the most 25% of the step size between the values used to build the PCA library of diffractograms (Table 1). Table 3 shows which terms are included in the polynomial expansions for each of the four properties, thus it gives an idea of which properties correlate the strongest. Looking at the large number of terms necessary to model the length it is not surprising that the maximum deviation of this property is much poorer. Contrary to what would be expected by comparing Figs. 2c and 2d, hardly any correlation is found between the effects arising from the number of turns and the *d*-spacing. In fact these two properties are much easier to model than the length and inner radius, which correlate strongly, both internally and to the other properties. Figure 3 shows the final vectors $\boldsymbol{v}_k$ for each property. Even though these refined diffractograms are very

Table 3. Non-zero terms in the 4-th order polynomials.

length L	inner radius R	no. of turns T	*d*-spacing D
d_L	d_R	d_T	d_D
d_L^2	d_R^2	d_T^2	$d_D^3 d_R$
d_L^3	d_R^3	$d_T^3 d_R$	$d d_D^2 d_R^2$
d_L^4	d_T	$d_T d_L^3$	$d_D^2 d_R d_L$
d_L^5	d_D	d_L^4	$d_D^2 d_R d_T$
$d_L d_D$	$d_R d_T$	$d_L d_R^2$	
$d_L d_R d_T$	$d_R^2 d_T$		
$d_L d_R d_T^2$	$d_R^2 d_D$		
$d_L d_R d_D^2$	$d_R d_L d_D$		
$d_L^2 d_R^2$	$d_R^3 d_T$		
$d_L^2 d_D^2$	$d_R^3 d_D$		
$d_L^3 d_R$	$d_R d_L^2 d_D$		
$d_L^3 d_T$	$d_R d_T^2 d_D$		
$d_R^2 d_D^2$			
$d_R d_T^3$			
d_T^4			

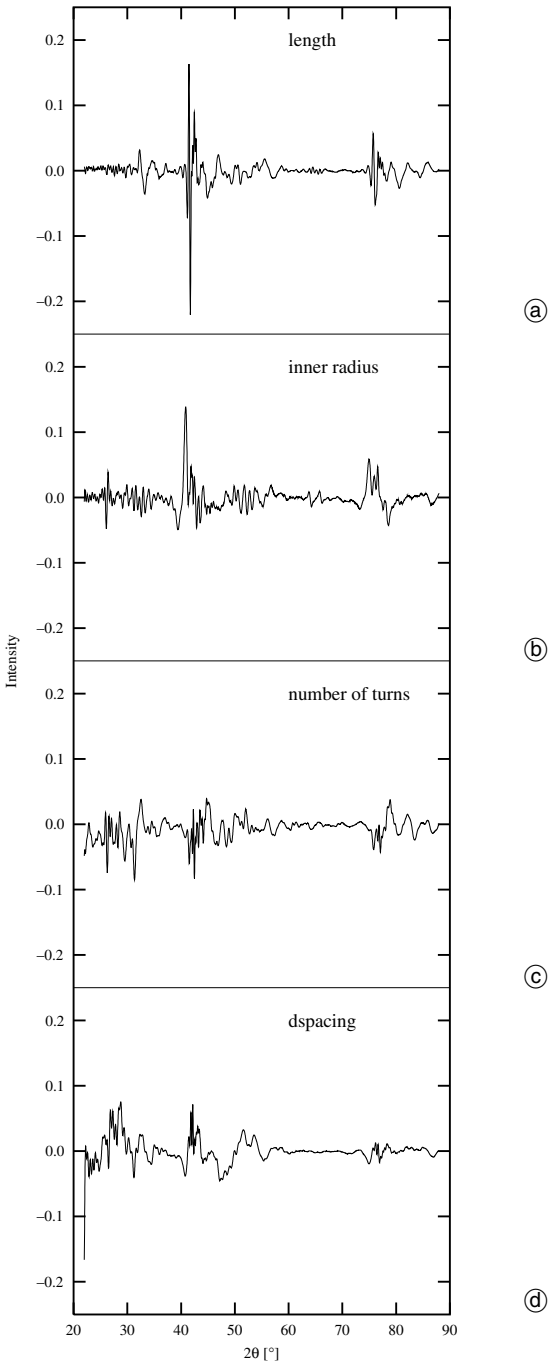

Fig. 3. The optimized functions for the final model.

complex in nature and offer no interpretation as was the case for the basis functions in Fig. 2, some similarities between the two figures can still be found.

6. Applying the method to estimate dimensions of experimental samples

The first 80 basis functions from the model calculations contain enough information to fit the 750 error-free simulated diffractograms with an acceptable accuracy. The large reduction in dimensionality indicates that the basis functions map the general features for error-free MWCNT diffractograms. However, a number of problems can potentially complicate the analysis when the model is used to predict structural properties from experimental diffractograms: Thermal displacement parameters differing from the B-factor of 2 Å^2 used in the simulations, an experimental 2θ zero offset, diffractograms recorded at other wavelengths than the 1.509 Å of the simulations, incorrect background correction, sample impurities, and/or structural parameters falling outside the intervals chosen for the PCA. In order to overcome some of these problems a separate algorithm was applied to modify the B-factor, 2θ zero shift and wavelength of the experimental diffractogram to obtain the best possible fit within the PCA basis. The method was tested on the four diffractograms given in Fig. 4 and the predicted properties are given in Table 4.

Diffractogram **A** is simulated for $\lambda = 1509$ Å with a set of structural properties within the simulation limits. A B-factor of 0.000 Å^2 was used in the simulation and the simulated diffractogram was offset by 0.40° before the prediction procedure. Since this diffractogram does not contain an experimental background or other instrumental abberations it is expected that a low $R(I^2)$-value and a good property prediction should be obtained, which is indeed the case. This test case shows that the zero point and B-factor altering algorithm works satisfactorily.

Diffractogram **B** is recorded at 1.509 Å and was subjected to an empirical background subtraction before the analysis. The predicted properties seem reasonable, perhaps apart from the rather short length, however one must recall the large rms and maximum deviations of this parameter.

Diffractograms **C** and **D** are recorded at 1.087 Å and again empirical background corrections are performed. Despite the wavelength difference the fits to these diffractograms are of the same quality as for **B**, so the fact that it

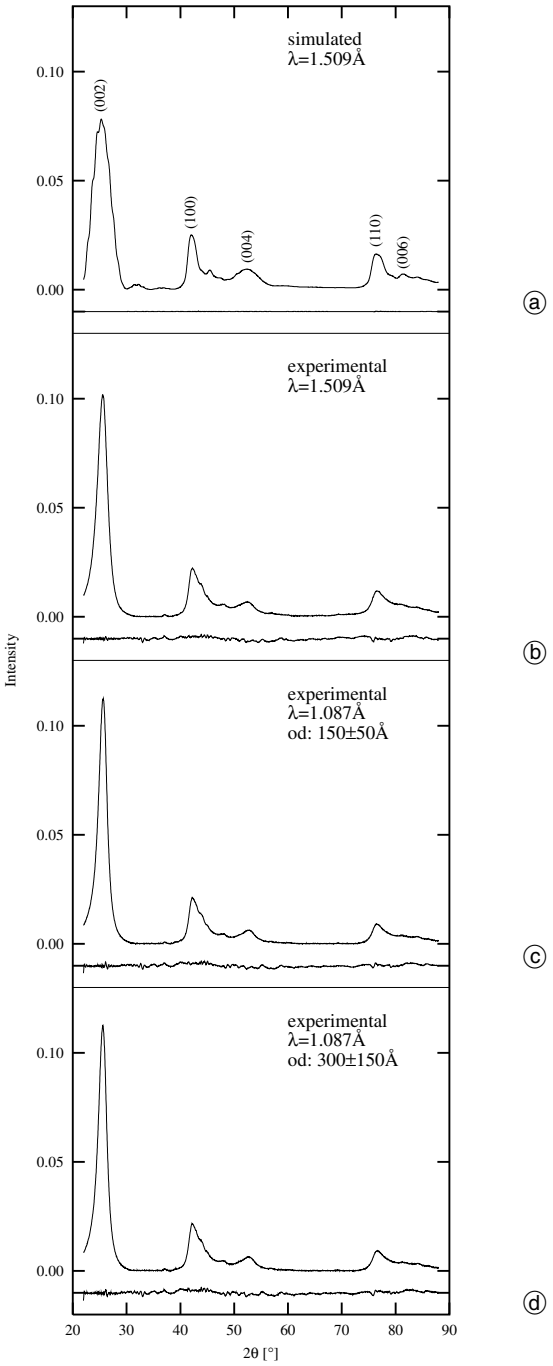

Fig. 4. Predicting structural properties using PCA. The experimental diffractograms corrected for B-factor, 2θ offset and wavelength differences are shown along with the difference curves. od: outer diameter reported by supplier.

Table 4. Predicted values for the diffractograms in Fig. 4.

Pattern	length [Å]	inner radius [Å]	no. of turns	d-spacing [Å]	outer diameter[a] [Å]	B-factor [Å^2]	2θ offset [°]	$R(I^2)$-value
A	56	40.7	5.85	3.399	61	0.003	0.40	0.0014
A[b]	100	40.0	6.00	3.400	60	0.000	0.40	
B	18	7.6	7.55	3.414	67	0.68	0.49	0.0384
C	7	7.7	8.41	3.403	72	2.07	0.25	0.0384
D	18	7.5	8.48	3.410	73	1.97	0.14	0.0406

a: Calculated as 2 · (inner radius + no. of turns · d-spacing)
b: True values for the simulated diffractogram **A**

is almost impossible to obtain synchrotron diffraction data at the exact same wavelength and 2θ zero point as the one used to setup the PCA library seems to be a minor problem. Furthermore it should be noted that the predicted properties (again except for the length) seem reasonable and for diffractogram 4**C** compare well to the values previously obtained by conventional comparison [4]. Neither a visual inspection of the diffractograms nor a conventional property fitting suggest that the two samples have different properties, and indeed this is confirmed by the PCA analysis, despite the fact that the samples were supplied with different outer diameter specifications (150 ± 50 Å for the sample in 4**C**, PCA predicts 72 Å on average, and 300 ± 150 Å for the sample in 4**D**, PCA predicts 73 Å on average). The TEM picture of the 300 ± 150 Å sample (Fig. 5, right) shows tubes with outer diameters of both 150 Å and 300 Å, but since TEM, as opposed to X-ray diffraction, is only a local probe, no definite conclusions about bulk structural properties can be drawn from this.

The above test cases have demonstrated that it is difficult to get a physically meaningful estimate of the average tube length from an experimental MWCNT diffractogram using the PCA method. The values determined are of the same size as the rms and maximum deviations given in Table 2, which are rather poor despite the fact that they are obtained purely from error-free simulated diffractograms. Furthermore, TEM images give evidence that the typical tube lengths are of the order 1 μm rather than around 100 Å as determined both here and in other X-ray diffraction studies [2–4, 12]. This suggests that the values obtained from diffraction experiments are not the actual tube lengths, but rather the lengths of the coherent scattering domains, which are several orders of magnitude shorter due to the presence of bends [4] and/or defects [3, 12] in the tubes (*cf.* Fig. 5).

It is well-known that broadening of the (00*l*) peaks can be caused both by size (number of turns) and strain (due to a distribution of *d*-spacings) [5–7, 16]. As mentioned earlier the structural parameters in a bulk sample are distributed around a mean, but the present PCA method can only estimate the mean and not the width of the distribution. Thus the potential strain broadening of the (00*l*) peaks can only be modelled as a size broadening, leading to an underestimation of both the number of turns and the thermal displacement parameter. For the diffractogram in Fig. 4c it has already been shown [4] that strain broadening cannot be neglected, so the number of turns predicted for this experiment is probably too low.

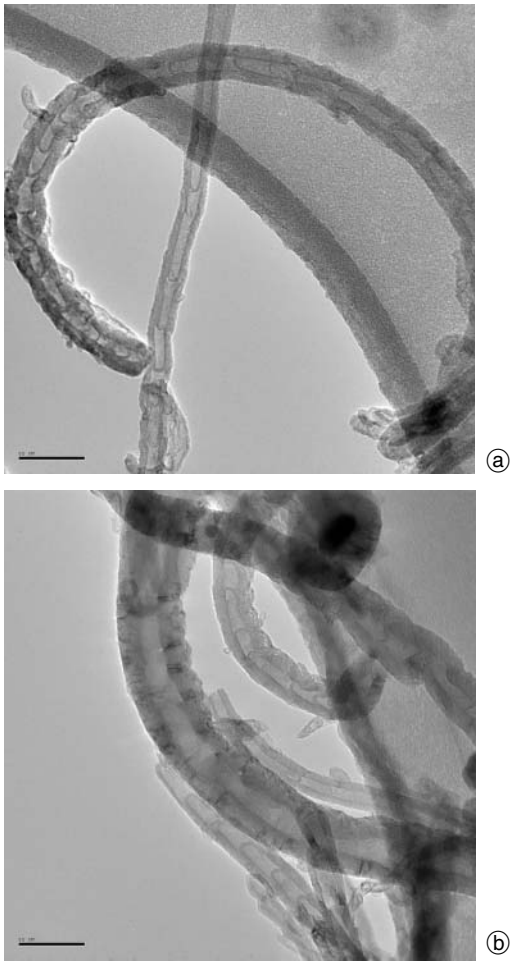

Fig. 5. TEM pictures of the MWCNT samples of Fig. 4c ((**a**), outer diameter: 150 ± 50 Å, PCA predicts 72 Å) and 4d ((**b**), outer diameter: 300 ± 150 Å, PCA predicts 73 Å). Scalebar 500 Å.

7. Conclusions

Initial tests using a combination of PCA and basis function transformations show that it is possible to directly obtain bulk structural properties from powder diffraction data of MWCNTs:

- The average values of inner radius, number of turns and *d*-spacing are well estimated with limited correlations.
- The tube length cannot be estimated due to large correlations and the present type of samples largely affected by tube bending and defects.
- Experimental abberations like different thermal displacement parameters, 2θ offset, wavelength differences and experimental background can be effectively handled.

The results are promising, but there are still several possibilities for improvements:

- Selecting different, not necessarily connected, regions of the diffractograms for different properties. This may reduce the loss of information on normalisation.
- The functional relationship between MWCNT properties and PCA basis functions should be improved. The large number of terms needed to model the length and inner radius indicates that the polynomial model may be inadequate for modelling the correlation between these properties.
- The method performance with regards to the distribution of chiral angles (or rolling directions) in the sample should be tested.
- It will be necessary to introduce distributions of properties. Since the PCA basis functions model all simulated diffractograms, a distribution of tube properties may be achieved by optimising distributions in the four property dimensions.

Acknowledgments. Haldor Topse A/S and nano-lab.com are acknowledged for MWCNT test samples. DANSYNC is acknowledged for financially supporting the synchrotron measurements.

References

[1] Koloczek, J.; Kwon, Y. K.; Burian, A.: Characterization of spatial correlations in carbon nanotubes modelling studies. J. Alloys and Compounds **328(1–2)** (2001) 222–225.

[2] Koloczek, J.; Burian, A.; Dore, J. C.; Hannon, A. C.: Model-based computation of powder diffraction patterns for carbon nanotubes. Diamond and Related Materials **13(4–8)** (2004) 1218–1221.

[3] Koloczek, J.; Hawelek, L.; Burian, A.; Dore, J. C.; Honkimaki, V.; Kyotani, T.: Modelling studies of carbon nanotubes – Comparison of simulations and X-ray diffraction data. J. Alloys and Compounds **401(1–2)** (2005) 46–50.

[4] Oddershede, J.; Stahl, K.: Bulk characterization of multiwall carbon nanotubes. Z. Kristallogr. Suppl. **23** (2006) 325–330.

[5] Reznik, D.; Olk, C. H.; Neumann, D. A.; Copley, J. R. D.: X-ray powder diffraction from carbon nanotubes and nanoparticles. Phys. Rev. B**52(1)** (1995) 116–124.

[6] Maniwa, Y.; Fujiwara, R.; Kira, H.; Tou, H.; Nishibori, E.; Takata, M.; Sakata, M.; Fujiwara, A.; Zhao, X.; Iijima, S.; Ando, Y.: Multiwalled carbon nanotubes grown in hydrogen atmosphere: An X-ray diffraction study. Phys. Rev. B**64(7)** (2001) 073105.

[7] Lambin, P.; Loiseau, A.; Culot, C.; Biro, L. P.: Structure of carbon nanotubes probed by local and global probes. Carbon **40(10)** (2002) 1635–1648.

[8] Koloczek, J.; Burian, A.: Computation of powder diffraction patterns for carbon nanotubes. Journal of Alloys and Compounds **382(1–2)** (2004) 123–127.

[9] Debye, P.: Zerstreuung von Röntgenstrahlen. Ann. Phys. **46** (1915) 809–823.

[10] Liu, J.; Fan, S.; Dai, H.: Recent Advances in Methods of Forming Carbon Nanotubes. MRS Bulletin **29(4)** (2004) 244–251.

[11] Zhang, J.; Albelda, T.; Liu, Y.; Canary, J. W.: Chiral Nanotechnology. Chirality **17** (2005) 404–420.

[12] Zhou, O.; Fleming, R. M.; Murphy, D. W.; Chen, C. H.; Haddon, R. C.; Ramirez, A. P.; Glarum, S. H.: Defects in Carbon Nanostructures. Science **3.263(5154)** (1994) 1744–1747.

[13] Bandow, S.: Radial Thermal Expansion of Puried Multiwall Carbon Nanotubes Measured by X-ray Diraction. Jpn. J. Appl. Phys **36** (1997) 1403–1405.

[14] Cumings, J.; Zettl, A.: Low-friction nanoscale linear bearing realized from multiwall carbon nanotubes. Science **289(5479)** (2000) 602–604.

[15] Xu, G.; Feng, Z.-C.; Popovic, Z.; Lin, J.-Y.; Vittal, J. J.: Nanotube structure revealed by highresolution X-ray diffraction. Advanced Materials **13(4)** (2001) 264–267.

[16] Burian, A.; Dore, J. C.; Fischer, H. E.; Sloan, J.; Szczygielske, A.: Structural studies of carbon nanotubes by wide-angle neutron scattering. Proceedings of SPIE **3725** (1999) 107–110.

C.4 Modelling the X-ray powder diffraction of nitrogen expanded austenite using the Debye formula

Oddershede, J., Christiansen, T. L. and Ståhl, K.
Submitted to J. Appl. Cryst.

Journal of Applied Crystallography

ISSN 0021-8898

Received 23 October 2007
Accepted 0 XXXXXXX 0000
Online 0 XXXXXXX 0000

Modelling the X-ray powder diffraction of nitrogen expanded austenite using the Debye formula

Jette Oddershede,[a]* Thomas L. Christiansen[b] and Kenny Ståhl[a]

[a]Department of Chemistry, Technical University of Denmark, 2800 Lyngby, Denmark, and [b]Department of Manufacturing Engineering, Technical University of Denmark, 2800 Lyngby, Denmark. Correspondence e-mail: jod@kemi.dtu.dk

Stress-free and homogeneous samples of nitrogen expanded austenite, a defect-rich FCC structure with a high interstitial nitrogen occupancy (between 0.36 and 0.61) have been studied using X-ray powder diffraction (XRPD) and Debye simulations. The simulations confirm the presence of deformation stacking faults in the structure, while twin or growth faulting can be ruled out. Screw dislocations are abundant and the dislocation density increases with the interstitial nitrogen occupancy. Whether the nitrogen atoms are clustered or distributed randomly among the octahedral interstices was found indistinguishable to XRPD.

1. Introduction

The surface hardness as well as wear and corrosion resistance of stainless steel can be significantly improved by nitriding or carburising the material at low temperature using a number of different techniques. This brings about a transformation of the surface adjacent region into so-called expanded austenite. The question of how to interpret the XRPD pattern of the resulting phase to extract the structural characteristics has been a matter of dispute for several years (Williamson *et al.*, 1994; Sun *et al.*, 1999; Marchev *et al.*, 1999; Blawert *et al.*, 1999; Menthe & Rie, 1999; Larisch *et al.*, 1999; Bazaleeva, 2005; Fewell & Priest, 2007).

Hitherto, structural investigations of expanded austenite have relied on samples consisting of compositionally heterogeneous expanded austenite "layers" on bulk stainless steel substrates prepared by the use of plasma-based techniques. Unavoidably, samples of this type contain high compositionally induced compressive stresses which strongly affect the diffraction patterns. The diffraction patterns roughly correspond to that of FCC austenite with an expanded lattice due to the presence of interstitials, hence the name expanded austenite or γ_X where X is N or C depending on the nature of the interstitials. The peak positions, however, do no fit an ideal FCC lattice. This has led to the suggestion of two inherently different structural models: 1) The m-phase of tetragonal rather than cubic symmetry, and 2) Expanded austenite where the observed peak shifts are due to the presence of deformation stacking faults and/or residual stresses in the FCC lattice. The designation S-phase has also been used and usually refers to structural model 2.

Recently stress-free and homogeneous samples of nitrogen expanded austenite with interstitial nitrogen occupancies, y_N, between 0.18 and 0.61 were synthesized by gaseous nitriding of AISI 316 stainless steel coupons under para-equilibrium conditions at low temperature (Christiansen & Somers, 2006). Analysis of the corresponding XRPD patterns unambiguously confirmed the structure to be FCC with a deformation stacking fault probability between 0.01 and 0.04 to account for the peak shifts (Christiansen & Somers, 2004). Complementary techniques such as TEM and theoretical calculations support this structural model (Borgioli *et al.*, 2006).

The approach taken in the present work is a whole pattern fitting procedure based on the Debye formula (Debye, 1915), which states that the diffracted intensity, $I(s)$, at a given wavevector, $s = \frac{4\pi \sin\theta}{\lambda}$, can be calculated as a sum over all interatomic distances, r_{jk}, without any assumptions regarding the periodic nature of the scattering object:

$$I(s) = \sum_{j,k} f_j f_k \frac{\sin(sr_{jk})}{sr_{jk}}$$

Thus it is in principle possible to build an atomic array of any structure and calculate the diffracted intensity. Here the term structure covers everything from crystallographic parameters like atomic composition and coordinates, thermal and lattice parameters over particle shape, size and size distribution to stacking faults, dislocations and disorder.

Whereas Rietveld refinements (Rietveld, 1967; Rietveld, 1969) and other traditional methods for XRPD analysis are not able to interpret the diffractograms in terms of parameters such as stacking fault probabilities and dislocation densities, Debye simulations offer the possibility to systematically vary these and analyse the resulting effects in the expanded austenite XRPD patterns. The knowledge gained from studies of this type can then be utilized to fit experimental diffraction data.

2. Experimental

XRPD data for expanded austenite samples with y_N=0.36, y_N=0.40 and y_N=0.58 were recorded using a Bruker D8 AXS diffractometer equipped with a Co anode (λ(CoKα_1)=1.78890Å, λ(CoKα_2)=1.79279Å) operating in Bragg-Brentano mode.

Additionally synchrotron diffraction data for y_N=0.61 were collected in transmission mode with a HUBER G670 Guinier camera (λ=1.18608Å) at MAXLAB beamline I711 (Cerenius *et al.*, 2000) with the sample mounted in a Ø=0.3mm capillary

IUCr macros version 2.1β1: 2007/05/15

and Al-foils placed between sample and detector to reduce fluorescence. The short wavelength gives access to more diffraction peaks, and a much better signal to noise ratio can be obtained within minutes because of the high intensity of the synchrotron beam. The synchrotron data were corrected for 2θ zero shift (determined for a Si-standard along with the actual wavelength and the instrumental broadening), for the intensity profile related to the 45° Guinier tangent angle, and for absorption in a cylindrical sample with μR=1.5.

3. Simulations

In order to analyse how the diffractograms of expanded austenite are affected by changing the different structural parameters, a program was written based on the Debye formula. The aim of this section is to define the parameters used to describe the structure and explain how these are used in the program to set up the atomic array that leads to the diffracted intensities.

3.1. Global parameters

To reduce the number of variables to a minimum it was necessary to choose a set of global parameters that were fixed to be identical for all simulations. From Table 1 the weighted average atomic number of AISI 316 stainless steel is 25.9, making it a reasonable first approximation to model all atoms in the FCC lattice as Fe. The 'fault free' lattice parameters a_0 (one parameter for each value of y_N, *c.f.* Table 3) obtained in the conventional way were used as standard input for the simulations along with a thermal parameter set of b_{Fe}=b_N=1Å^2 which is reasonable at room temperature and agrees well with values obtained from Rietveld refinements. The anomalous dispersion corrections f' and f'' for both Fe and N at the relevant wavelengths were obtained *via* http://skuld.bmsc.washington.edu/scatter/.

In the simulations an instrumental peak broadening of the pseudo-Voigt type was added (Caglioti *et al.*, 1958; Wertheim *et al.*, 1974). For the Co-data the parameters (u=0, v=0.0616, w=0.0176, γ_1=0.4) were obtained from a peak fit of a austenitised nitrogen-free AISI 316 foil using the same diffractometer settings assuming that the particle size in this sample is so large that the only significant contribution to the peak broadening is of instrumental origin. The instrument parameters for the synchrotron data (u=0.02323, v=−0.00714, w=0.01147, γ_1=0.55) were obtained from a Si-standard.

Table 1
Chemical composition of AISI 316 stainless steel

atomic name	Fe	Cr	Ni	Mn	Si	Mo
atomic number	26	24	28	25	14	42
atomic %	63.60	19.11	12.70	1.74	1.45	1.40

3.2. Model variables

In the present study it was chosen to focus on how a variation of the particle size, the deformation and twin stacking fault probabilities, α and β, the screw dislocation density, ρ, and the interstitial nitrogen occupancy, y_N, affects the XRPD patterns of nitrogen expanded austenite. Whereas the global parameters refer to the overall periodic FCC structure, the model variables describe the deviations from this ideal situation.

3.3. Building the structure atom by atom

The coordinate system chosen to model the nitrogen expanded austenite FCC structure is directed with the *z*-axis perpendicular to the (111) close packed layers which are situated in the *xy*-plane, thus a hexagonal cell setting.

Particle size in the simulations is realised by letting the atomic array be made up by m close packed layers each consisting of $m \times m$ Fe atoms. Hence a crystallite of size m=120 contains 120^3=1728000 Fe atoms and has a mean diameter of roughly 120·3Å=360Å. One parameter was deemed enough to describe the particle size since there is no reason to assume an anisotropic particle shape for a compound with a FCC structure.

Deformation stacking faults in a FCC structure are realised by changing the stacking sequence of the (111) close packed layers from ABCABCA to ABCACAB. In the program the atomic array is built up one close packed layer at the time, and each time a new layer is added a random number between 0 and 1 is generated. If the number is smaller than the input deformation stacking fault probability, α_{in}, a deformation stacking fault is introduced. The final deformation stacking fault probability, α, is defined as the number of deformation stacking faults in the atomic array divided by $m-1$, the number of new layers added. To get a physically realistic model an average over several (typically 10) diffractograms simulated for the same value of α_{in} is used.

Twin or growth faults refer to the stacking sequence ABCACBA of the FCC (111) close packed layers as opposed to the normal ABCABCA order, thus a mirror plane is introduced and the stacking is reversed. After determining the stacking sequence of the (111) layers taking possible deformation stacking faults into account, the program reconsiders each layer, generates a random number between 0 and 1 and introduces a twin stacking fault by reversing the stacking of all subsequent layers if this random number is less than the input twin fault probability, β_{in}. Finally the twin fault probability, β, is calculated as an average over several simulations.

Screw dislocations with (111) slip planes, screw axes along [110] and one interatomic distance in displacement can be added to the structure after building the atomic array as described above. The desired screw dislocation density, ρ_{in}, typically in the order of 10^{15}–10^{16}m^{-2}, is input and the number of dislocations to which this corresponds for the given crystallite size is calculated. The number is then rounded off at random to one of the two nearest integers in a way that an average over several diffractograms should yield the desired real number. For a m=120 crystallite a dislocation density of 10^{15}m^{-2} corresponds roughly to one screw dislocation. A distance threshold to limit the dislocations from being placed too close to one another is calculated based on ρ_{in}, and the dislocations are then placed at random within the part of the crystallite that has the full thickness using the calculated distance threshold. The shortest distance between screw dislocations is printed in the output file along with the actual screw dislocation density, ρ. In order to keep the high symmetry of the atomic array (identical layers

perpendicular to the screw dislocation axis) and thereby the high performance of the Debye calculations, no relaxation of the structure or removal of Fe atoms in the vicinity of the screw axes or slip planes is performed by the program. It should be noted that it was chosen to model the screw dislocations with slip planes extending to either side of the crystallite at random, see Figure 1. However, because screw dislocations appear when a stress is applied in a given direction, these were all modelled with the same chirality.

Interstitial nitrogen atoms can be placed at random in the octahedral interstices of the Fe FCC structure while building the atomic array. For every octahedral interstice a random number between 0 and 1 is generated, and if the number is less than y_N, a nitrogen atom is added. It was chosen not to place any nitrogen atoms at the crystallite surface or at stacking fault positions, the latter to avoid unrealistically short N–N distances or nitrogen atoms with tetrahedral coordination. Interstitial nitrogen atoms in the vicinity of screw dislocation axes and slip planes are removed during the generation of the axes to avoid clashes.

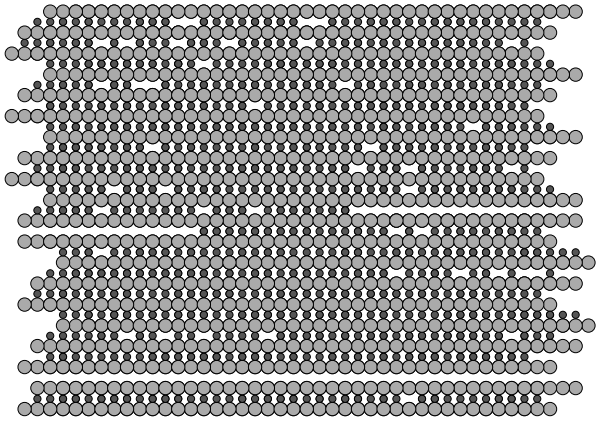

Figure 1
Section of a m=20 crystallite with y_N=0.6 viewed along the screw dislocation axis [110] with [111] directed upwards. Fe light gray, N dark gray. Note the stacking fault in the bottom of the picture (missing N layer) and the two screw dislocations with (111) slip planes.

3.4. Approach

The way the Fe FCC lattice is built makes it possible to exploit the symmetry of the atomic array to speed up the calculation of all the Fe–Fe interatomic distances. However, the interstitial nitrogen atoms are only introduced into a fraction of the octahedral interstices in the Fe FCC lattice, so the symmetry is broken and the Fe–N and N–N distances must be calculated for every atom pair, resulting in a substantial increase in calculation time.

The reciprocal relationship between particle size and peak width is given by the Scherrer equation (Scherrer, 1918). Like the particle size, the presence of stacking faults and/or dislocations has great impact on the diffraction peak widths, but none of these parameters affect the integrated intensities. On the other hand, the introduction of nitrogen into the octahedral interstices alters the relative intensities of the diffraction peaks, but has no impact on the peak widths.

Based on these observations it was chosen to do a series of simulations of the Fe FCC lattice to analyse and possibly parameterise the effects of stacking faults, screw dislocations and a combination of these on the peak widths. The nitrogen atoms were left out because they do not contribute to the peak widths and because simulations without them are much faster as just argued. Finally the results of these studies were exploited to simulate diffractograms for nitrided crystals to be compared with experimental data.

4. Results

4.1. Peak width analysis

In the following section the effects on the peak widths of varying α, β and ρ, both isolated and in combination, are analysed and parameterised. All the specified peak widths, β_{peak}, are integral breadths measured in degrees on the 2θ-scale for CoKα radiation. It is assumed that the individual contributions to the peak width add up in a Gaussian manner, thus:

$$\beta^2_{peak} = \beta^2_{size} + \beta^2_{instr} + \beta^2_{sf} + \beta^2_{twin} + \beta^2_{sd} + \ldots$$

The $\beta^2_{size} + \beta^2_{instr}$ terms are simply taken as the squared integral breadths of the diffractogram simulated for the same size and instrumental parameters, but they can easily be parameterised using the Scherrer equation (β_{size}) and the pseudo-Voigt type instrument broadening (β_{instr}) as described previously.

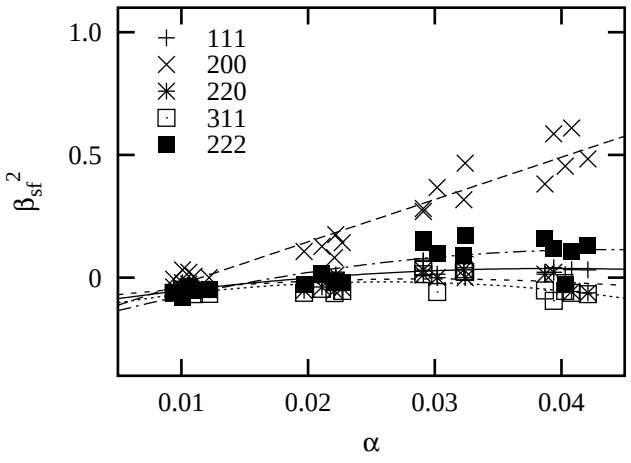

Figure 2
Calculated peak width contributions for different deformation stacking fault probabilities

Deformation stacking faults in a FCC lattice give rise to minor peak broadening effects as well as peak shifts of the type (Warren, 1990):

$$\Delta(2\theta_{hkl}) = 0.2756 \cdot \alpha \cdot G_{hkl} \cdot \tan\theta$$

where the deformation stacking fault parameter G_{hkl} is given according to Table 2. Since none of the other structural variables give rise to peak shifts, α can be determined from these.

IUCr macros version 2.1β1: 2007/05/15

Table 2
Stacking fault parameters

hkl	111	200	220	311	222
G_{hkl}	$\frac{1}{4}$	$-\frac{1}{2}$	$\frac{1}{4}$	$-\frac{1}{11}$	$-\frac{1}{8}$

However, it is also necessary to parameterise the deformation stacking fault peak width contribution, β_{sf}^2, in order to fully understand the interplay between the different structural components. Figure 2 shows β_{sf}^2 for α between 0.01 and 0.04 (the relevant interval for the experiments according to Christiansen & Somers (2004)). Each point in the figure represents an average over 10 diffractograms. For every value of α the peak width contributions are calculated for five different values of *m*, namely: 100, 200, 300, 400, and 500. Seeing that the points group nicely around the trend lines, β_{sf}^2 seems to be independent of particle size.

Twin faults in a FCC lattice result in asymmetric peak broadening according to Warren (1990). Simulations were performed for β between 0.01 and 0.04 since there was no reason to suspect a larger frequency of twin faults than of deformation stacking faults. For β in this interval the asymmetry was limited, so it was decided to focus only on the symmetric peak broadening effects, β_{twin}^2, depicted in Figure 3. As for the deformation stacking faults, each point represents an average over 10 diffractograms and for every twin fault probability, β_{twin}^2 is calculated for the same five values of *m*. From the figure it can be seen that β_{twin}^2 is independent of particle size and only significantly different from zero for the 200 peak.

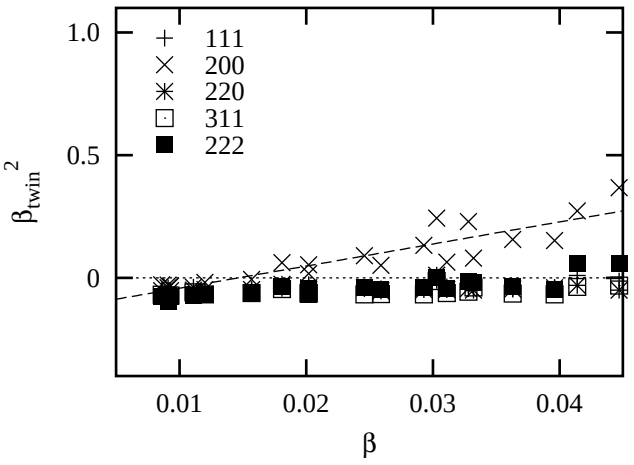

Figure 3
Calculated peak width contributions for different twin fault probabilities

Screw dislocations of the type described above give rise to anisotropic peak broadening effects as seen from Figure 4. Note that the screw dislocation contribution, β_{sd}^2, to the 111 peak is significantly smaller than for the remaining peaks (except for 220), an effect that could potentially explain the large peak width anisotropies observed in the experimental diffractograms of nitrogen expanded austenite (Figure 6 and Figure 7). The diffractograms used to construct Figure 4 are simulated for *m*=120 crystallites, so the labels on the *x*-axis correspond roughly to the number of screw dislocations in the crystallite, and each point represents an average over 10 diffractograms. It can be seen that β_{sd}^2 is almost proportional to the screw dislocation density at low densities (trend lines forced through origo) and that it reaches a saturation level/maximum around $6{\cdot}10^{15}\mathrm{m}^{-2}$ which corresponds to a minimum distance between the individual screw dislocations around 65Å. The saturation/maximum could be the result of a shadowing effect where the addition of each new screw dislocation contributes less and less to the structure. If the shadowing effect is a function of the number of screw dislocations rather than the screw dislocation density, then β_{sd}^2 for a given screw dislocation density would be less the larger the crystallite. This effect was in fact observed and it is the reason why Figure 4, as opposed to Figure 2 and Figure 3, contains data for one value of *m* only.

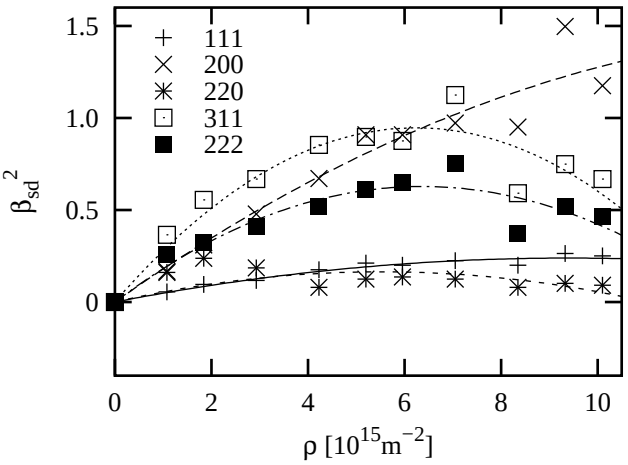

Figure 4
Calculated peak width contributions versus screw dislocation densities for *m*=120 crystallites

Combining deformation stacking faults and screw dislocations it is not obvious whether the peak width contributions simply add up as $\beta_{sf}^2 + \beta_{sd}^2$, or whether the structural modifications correlate so strongly that the resulting peak widths differ significantly from predictions based on the above analysis. The β_{twin}^2 term was not considered because it only adds to the width of the 200 peak, which is also substantially broadened by the presence of both deformation stacking faults and screw dislocations. According to experimental XRPD patterns the 200 peak is no wider than the 220, 311 and 222 peaks, so twin faulting is bound to play a very minor part in the structure of nitrogen expanded austenite.

A number of diffractograms for *m*=120 crystallites with $\alpha \sim 0.03$ and different values of ρ were simulated to test how well it is possible to predict the peak widths of diffractograms simulated for expanded austenite containing both deformation stacking faults and screw dislocations. For each value of ρ, Figure 5 shows the differences between the simulated peak widths β_{peak}^2 and the peak widths predicted from parameterisation of size, instrumental broadening, deformation stacking faults (Figures 2) and screw dislocations (Figure 4). Each point in Figure 5 represents an average over 10 diffractograms, and it should be

IUCr macros version 2.1β1: 2007/05/15

noted that the differences are roughly constant and only differ significantly from 0 for the 200 (proportional to ρ) and 220 (constant) peaks. These extra peak width contributions, arising because of structural correlations between deformation stacking faults and screw dislocations, are taken into account in the next section, where the parameterisation of the peak width contributions from different structural aspects derived in the present section is used to determine the model variables for Debye simulations that gives the best fit to the experimental diffractograms.

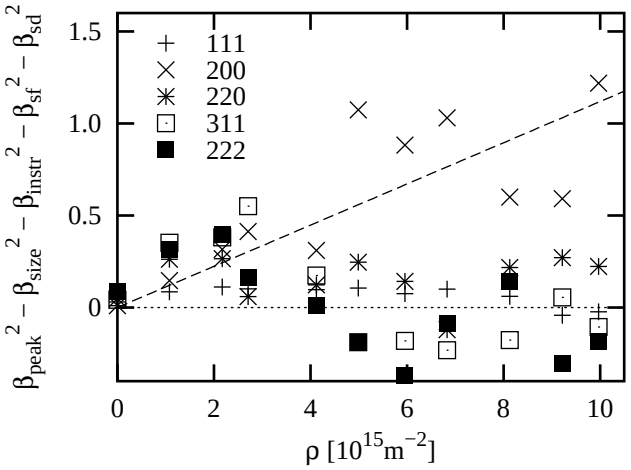

Figure 5
The difference between simulated and predicted peak widths for m=120 crystallites with $\alpha \approx 0.03$ for various screw dislocation densities

4.2. Fitting the experimental data

The modelling strategy to obtain the simulated diffractograms that best fit the experimental data consists of considering and including the already mentioned model variables — particle size, deformation and twin stacking fault probabilities, screw dislocation density, and interstitial nitrogen occupancy — one at the time. For the more advanced structural models the values of α, ρ and y_N reported in Table 3 are mean values and estimated standard deviations obtained by averaging 10 simulated diffractograms. Table 3 also contains the final R-values obtained when fitting the simulated diffractograms to the experimental XRPD patterns using a scale factor and a number of Chebyshev background parameters.

The **particle size** can be estimated for the experimental diffractograms using the Scherrer equation. This yields particle sizes around 500Å perpendicular to (111) and around 200Å in all other directions, thus a large peak broadening anisotropy that cannot be correlated to particle size anisotropy because the (111) planes are found in four different orientations throughout the crystal due to the cubic space group symmetry. As a compromise it was decided to use m=120 crystallites corresponding to a particle size around 360Å, see Figure 6 for a fit to the synchrotron data. Seing that it is more than difficult to even estimate the mean particle size, it was deemed unnecessary to spend extra computer time on modelling the particle size distribution that will inevitably be present in the samples.

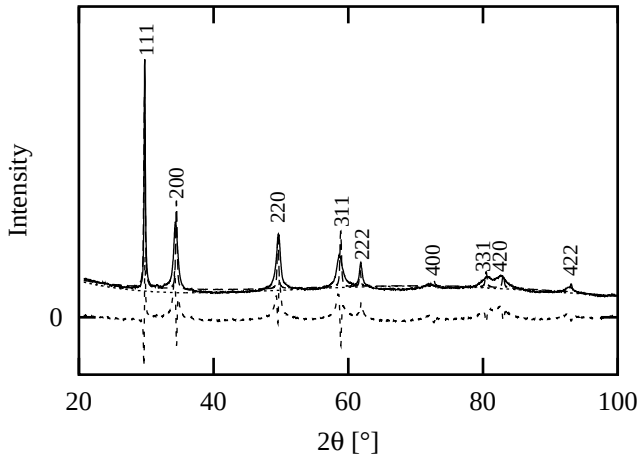

Figure 6
m=120, R=0.0865

The **deformation stacking fault probabilities** were previously determined in the conventional way from the peak shifts (Christiansen & Somers, 2004). Simulations using a number of α values close to these were tested for each sample, but in each case the value of α leading to the best fit with the experimental data lay within the estimated standard deviation. Therefore it was decided simply to use the conventional α values as input for the final simulations. From Table 3 it can be seen that the models improved when the deformation stacking faults were taken into account; the R-values dropped as compared to the α=0 models, especially for the y_N=0.61 synchrotron data.

The **twin fault probabilities** were found to be zero for all samples. With the choice of m=120 and the conventional α values as described above, the 200 peaks of the simulated diffractograms for y_N=0.36 and y_N=0.40 are already wider than experimentally observed, so twin faulting which only adds to the 200 peak width (Figure 3) cannot be an issue. For the y_N=0.58 and y_N=0.61 samples the experimentally observed peak widths are better described by the presence of screw dislocations.

The **screw dislocation densities** were determined by least squares minimisation of the difference between the experimentally determined peak widths and the peak widths predicted using the parameterisation of peak broadening effects outlined above. According to this approach the model did not improve by adding screw dislocations to the simulations of the y_N=0.36 and y_N=0.40 samples. For the y_N=0.58 sample a dislocation density of $2{\cdot}10^{15}$m^{-2} refined, while $\rho{=}4{\cdot}10^{15}$m^{-2} was estimated for the y_N=0.61 sample. The R-values of Table 3 confirm that the models did in fact improve when screw dislocations were added to the structural models of the samples with the highest nitrogen contents.

The **interstitial nitrogen occupancies** of the samples were determined using thermogravimetry, and these values were simply used as input for the simulations. As could be expected this lead to significant model improvements for all experiments, see Table 3 for R-values and Figure 7 for the final fit to the y_N=0.61 synchrotron data. It has long been known that the interstitial nitrogen atoms have a higher affinity towards Cr than towards Fe (Oda *et al.*, 1990; Grujicic & Owen, 1995; Shankar

IUCr macros version 2.1β1: 2007/05/15

et al., 1998; Bazaleeva, 2005). To test whether XRPD can be used to observe possible clustering of N around Cr, a model placing the nitrogen atoms in small clusters (55 atom cubeoctahedra) was tested. The resulting diffractogram was no different from the random nitrogen case, leading to the conclusion that it is impossible to detect nitrogen clustering by the use of XRPD.

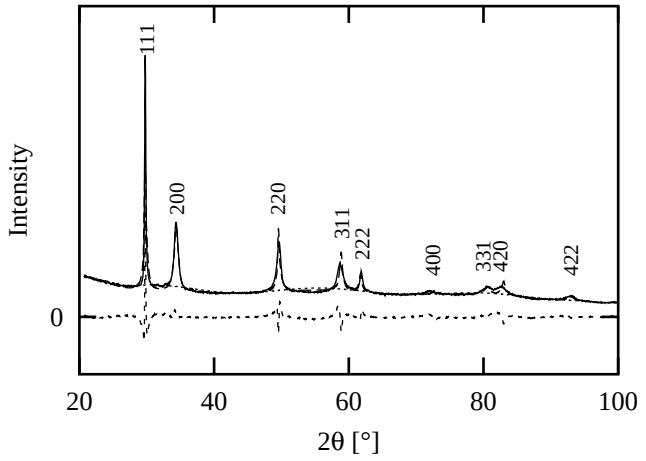

Figure 7
m=120, α=0.036(12), ρ=3.9(5)·10^{15}m^{-2}, y_N=0.6100(3), R=0.0551

5. Discussion

The first conclusion to be made is that the 'fault free' lattice parameters are correct and that the structural models improve with the inclusion of deformation stacking faults. One of the main objectives for taking on the Debye approach was to check whether the numerical value of the traditionally determined α parameter actually corresponds to the deformation stacking fault probability, and based on the good correspondence between the two parameters this was found to be the case.

The experimentally determined XRPD patterns show extremely narrow 111 peaks corresponding to an unlikely particle size anisotropy since the (111) planes are oriented in four different directions throughout a crystal of FCC symmetry. The observed peak width anisotropies can be partly explained by the presence of screw dislocations in the atomic lattice since it was shown that the width of the 111 peak is affected much less by the presence of screw dislocations than most of the remaining peak widths.

From the widths of the 111 peaks in the experimental XRPD patterns it is obvious that the mean particle size of nitrogen expanded austenite is larger than the 360Å used for the simulations in the present study. Most likely a better fit would be obtained if the mean particle size was doubled and the peak width anisotropy was enhanced by increasing the screw dislocation density. However, calculation time is another non-negligible aspect in the choice of particle size; a m=120 simulation with y_N=0.6 can be performed within 48h on a 3GHz/1GHz standard PC, while doubling the mean particle size will increase the calculation time by a factor of 2^6=64. Hence it would no longer be feasible to test different parameters or average several diffractograms to obtain a distribution of α, ρ or y_N.

It is an approximation to model all atoms in the FCC framework as Fe, c.f. Table 1. Different atoms have different atomic radii which inevitably will result in local distortions of the FCC framework, distortions that were not considered in the simulations, but they are likely to be small if the atomic composition is random. The variations in scattering amplitudes and more importantly anomalous scattering contributions among the different atom types are other aspects that need to be considered. In order to quantify their importance, Rietveld refinements were carried out both modelling all atoms as Fe and using the correct atomic composition for AISI316 stainless steel. For the Co-data the refined thermal parameters increased by 20% in going from the Fe to the correct model, while the increase for the synchrotron data is hardly significant (2%). This agrees well with the observation that for the Co-data a better fit between simulations and experiments can be obtained if the thermal parameters are reduced. It was, however, decided to stay with the physically sound value of b=1Å^2 for all simulations.

If computational cost was not an issue it would be interesting to do another round of Debye simulations and test structural aspects such as: 1) Increasing the crystallite size along with the screw dislocation density to get a better fit to the anisotropic peaks widths, 2) Adding a particle size distribution, 3) Varying α, y_N and especially ρ in the search for a better fit to the experimental data, 4) Modelling the FCC framework with the correct atomic composition to get the correct atomic radii, scattering factors and anomalous scattering contributions, and 5) Considering a nonuniform distribution of the different atom types in the FCC lattice. Will the higher affinity of N towards Cr than towards Fe lead to a clustering of N (or possibly CrN) resulting in a number of local distortions in the FCC lattice to accommodate areas where the austenite framework is expanded more or less? And if yes, is this detectable with XRPD? The local structure of Cr and Fe in stress-free and homogeneous samples of nitrogen expanded austenite with large interstitial nitrogen occupancies is the subject of an upcoming combined XRPD and EXAFS study (Oddershede *et al.*, in preparation).

Taking all of these considerations into account the Debye approach, despite of the structural simplifications in order to make modelling feasible, offers valuable information about the structure of nitrogen expanded austenite that cannot be gained in any other way at present.

6. Conclusions

- Debye simulations offer the opportunity to test how the XRPD patterns of nitrogen expanded austenite are affected by the presence of stacking faults and screw dislocations in combination, structural aspects that cannot be modelled using traditional XRPD analysis methods such as Rietveld refinements.
- The Debye approach has the advantage that the modelled structural modifications are physically present in the structure and not simply convolutions of the XRPD pattern with empirical functions.

IUCr macros version 2.1β1: 2007/05/15

- The method is, however, limited by the particle size seing that the computational cost goes as the 6^{th} power of the average dimension. In the present case a mean diameter of 360Å was the limit.
- The simulations confirm the proposed presence of deformation stacking faults in homogeneous stress-free samples of nitrogen expanded austenite (Christiansen & Somers, 2004). The deformation stacking fault probability giving the best fit to the experimental XRPD pattern corresponds to the value conventionally determined from the peak shifts within the estimated standard deviation.
- There is no evidence to suggest that the structure of nitrogen expanded austenite contains twin or growth faults.
- Modelling screw dislocations into the structure of nitrogen expanded austenite results in diffraction patterns with peak width anisotropies that resemble the experimentally observed anisotropies. The fits to the experimental XRPD patterns show that the screw dislocation density increases with increasing interstitial nitrogen occupancy. The actual value of the screw dislocation density correlates strongly with the particle size and a better fit can probably be obtained if both are increased.
- Simulations of different ways to distribute the interstitial nitrogen atoms have shown that it is impossible to distinguish between clustering and a random distribution by means of XRPD.

Financial support by the Danish Research Agency under grant 274-05-0230 is gratefully acknowledged.

References

Bazaleeva, K. O. (2005). *Metal Science and Heat Treatment*, **47**(9–10), 455–461.

Blawert, C., Mordike, B. L., Jirásková, Y. & Schneeweiss, O. (1999). *Surface & Coatings Technology*, **116--119**, 189–198.

Borgioli, F., Fossati, A., Galvanetto, E., Bacci, T. & Pradelli, G. (2006). *Surface & Coatings Technology*, **200**(18–19), 5505–5513.

Caglioti, G., Paoletti, A. & Ricci, F. P. (1958). *Nucl. Instrum. Methods*, **3**(4), 223–228.

Cerenius, Y., Ståhl, K., Svensson, L. A., Ursby, T., Oskarsson, Å., Albertsson, J. & Liljas, A. (2000). *J. Synchrotron Rad.* **7**(4), 203–208.

Christiansen, T. & Somers, M. A. J. (2004). *Scripta Materialia*, **50**(1), 35–37.

Christiansen, T. & Somers, M. A. J. (2006). *Metal. Mater. Trans. A*, **37A**, 675–682.

Debye, P. (1915). *Ann. Phys.* **46**, 809–823.

Fewell, M. P. & Priest, J. M. (2007). *Surf. Coat. Technol.* .

Grujicic, M. & Owen, W. S. (1995). *Acta Metall. Mater.* **43**(11), 4201–4211.

Larisch, B., Brusky, U. & Spies, H.-J. (1999). *Surface & Coatings Technology*, **116--119**, 205–211.

Marchev, K., Landis, M., Vallerio, R., Cooper, C. V. & Giessen, B. C. (1999). *Surface & Coatings Technology*, **116--119**, 184–188.

Menthe, E. & Rie, K.-T. (1999). *Surface & Coatings Technology*, **116--119**, 199–204.

Oda, K., Kondo, N. & Shibata, K. (1990). *ISIJ International*, **30**(8), 625–631.

Oddershede, J., Christiansen, T. & Ståhl, K. (in preparation).

Rietveld, H. M. (1967). *Acta Cryst.* **22**(1), 151–152.

Rietveld, H. M. (1969). *J. Appl. Cryst.* **2**(2), 65–71.

Scherrer, P. (1918). *Göttinger Nachrichten*, **2**, 98.

Shankar, P., Sundararaman, D. & Ranganathan, S. (1998). *J. Nucl. Mater.* **254**(1), 1–8.

Sun, Y., Li, X. Y. & Bell, T. (1999). *J. Mater. Sci.* **34**(19), 4793–4802.

Warren, B. E. (1990). *X-ray diffraction*. Dover Publications Inc.

Wertheim, G. K., Butler, M. A., West, K. W. & Buchanan, D. N. E. (1974). *Rev. Sci. Instrum.* **45**(11), 1369–1371.

Williamson, D. L., Ozturk, O., Wei, R. & Wilbur, P. J. (1994). *Surface & Coatings Technology*, **65**, 15–23.

Table 3
Fit parameters

y_N [a]	a_0 [Å] [a]	α [a]	bg [b]	m	α	ρ [10^{15}m^{-2}]	y_N	R
0.36	3.8616	0.0142	3	120				0.0566
			3	120	0.014(8)			0.0567
			3	120	0.014(5)		0.3599(3)	0.0499
0.40	3.8848	0.0097	2	120				0.0615
			2	120	0.010(6)			0.0633
			2	120	0.010(9)		0.4000(2)	0.0553
0.58	3.9823	0.0274	3	120				0.0887
			3	120	0.027(9)			0.0879
			3	120	0.027(10)	2.1(3)		0.0871
			3	120	0.027(19)	2.0(4)	0.5799(3)	0.0681
0.61	4.0022	0.0362	12	120				0.0865
			12	120	0.036(12)			0.0731
			12	120	0.036(12)	3.9(5)		0.0711
			12	120	0.036(12)	3.9(5)	0.6100(3)	0.0551

[a] Christiansen & Somers (2004)
[b] Number of Chebyshev background parameters used for the background fit

Bibliography

Alexander, L. E. (1969). *X-ray Diffraction Methods in Polymer Science*. Wiley-Interscience.

Als-Nielsen, J. and McMorrow, D. (2000). *Elements of modern X-ray physics*. John Wiley and Sons.

Amelinckx, S., Lucas, A., and Lambin, P. (1999). Electron diffraction and microscopy of nanotubes. *Rep. Prog. Phys.*, 62: 1471–1524.

Andreev, Y. G. and Bruce, P. G. (2001). Peak-shape analysis using the general Debye equation. *Mater. Sci. Forum*, 378–381: 148–153.

Andreev, Y. G. and Lundström, T. (1995). Simulation of powder diffraction diagrams for disordered and imperfect graphitic layers. *J. Appl. Cryst.*, 28(5): 534–539.

Attfield, J. P. and Cheetham, A. K. (1988). Synchrotron X-ray and neutron powder diffraction studies of the structure of α-$CrPO_4$. *J. Appl. Cryst.*, 21(5): 452–457.

Bandow, S. (1997). Radial thermal expansion of purified multiwall carbon nanotubes measured by X-ray diffraction. *Jpn. J. Appl. Phys*, 36: 1403–1405.

Bardage, S., Donaldson, L., Tokoh, C., and Daniel, G. (2004). Ultrastructure of the cell wall of unbeaten Norway spruce pulp fibre surfaces. *Nordic Pulp and Paper Research Journal*, 19(4): 424–428.

Bazaleeva, K. O. (2005). Mechanisms of the influence of nitrogen on the structure and properties of steel (a review). *Met. Sci. Heat Treat.*, 47(9–10): 455–461.

Bish, D. L. and Post, J. E., editors (1989). *Modern powder diffraction*, volume 20 of *Reviews in mineralogy*. Mineralogical Society of America.

Blawert, C., Mordike, B. L., Jirásková, Y., and Schneeweiss, O. (1999). Structure and compostion of expanded austenite produced by nitrogen plasma immersion ion implantation of stainless steels X6CrNiTi1810 and X2CrNiMoN2253. *Surf. Coat. Technol.*, 116–119: 189–198.

Bondars, B., Gierlotka, S., and Palosz, B. (1993). Program for simulation of diffraction pattern of small particles. *Mater. Sci. Forum*, 133–136: 301–306.

Bönnemann, H., Brijoux, W., Brinkmann, R., Schulze Tilling, A., Schilling, T., Tesche, B., Seevogel, K., Franke, R., Hormes, J., Köhl, G., Pollmann, J., Rothe, J., and Vogel, W. (1998a). Selective oxidation of glucose on bismuth-promoted Pd-Pt/C catalysts prepared from $NOct_4Cl$-stabilized Pd-Pt colloids. *Inorg. Chim. Acta*, 270(1–2): 95–110.

Bönnemann, H., Britz, P., and Vogel, W. (1998b). Structure and chemical composition of a surfactant-stabilized Pt_3Sn alloy colloid. *Langmuir*, 14(23): 6654–6657.

Borgioli, F., Fossati, A., Galvanetto, E., Bacci, T., and Pradelli, G. (2006). Glow discharge nitriding of aisi 316l austenitic stainless steel: Influence of treatment pressure. *Surf. Coat. Technol.*, 200(18–19): 5505–5513.

Bródka, A., Koloczek, J., and Burian, A. (2007). Application of molecular dynamics simulations for structural studies of carbon nanotubes. *J. Nanosci. Nanotechnol.*, 7(4/5): 1505–1511.

Bródka, A., Koloczek, J., Burian, A., Dore, J. C., Hannon, A. C., and Fonseca, A. (2006). Molecular dynamics simulation of carbon nanotube structure. *J. Mol. Struct.*, 732–793: 78–81.

Bürgi, H.-B., Restori, R., and Schwarzenbach, D. (1993). Structure of C_{60}: Partial orientational order in the room-temperature modification of C_{60}. *Acta Cryst. B*, 49(5): 832–838.

Burian, A., Dore, J. C., Fischer, H. E., and Sloan, J. (1999a). Structural studies of multiwall carbon nanotubes by neutron diffraction. *Phys. Rev. B*, 59(3): 1665–1668.

Burian, A., Dore, J. C., Fischer, H. E., Sloan, J., and Szczygielske, A. (1999b). Structural studies of carbon nanotubes by wide-angle neutron scattering. *Proceedings of SPIE*, 3725: 107–110.

Burian, A., Dore, J. C., Hannon, A. C., and Honkimaki, V. (2005). Complementary studies of structural characteristics for carbon materials with X-rays and neutrons. *J. Alloys and Compounds*, 401(1): 18–23.

Burian, A., Koloczek, J., Dore, J. C., Hannon, A. C., Nagy, J. B., and Fonseca, A. (2004). Radial distribution function analysis of spatial atomic correlations in carbon nanotubes. *Diamond and Related Materials*, 13(4–8): 1261–1265.

Buschle-Diller, G. and Zeronian, S. H. (1992). Enhancing the reactivity and strength of cotton fibres. *J. Appl. Polym. Sci.*, 45(6): 967–979.

Caglioti, G., Paoletti, A., and Ricci, F. P. (1958). Choise of collimators for a crystal spectrometer for neutron diffraction. *Nucl. Instrum. Methods*, 3(4): 223–228.

Carlson, S., Clausén, M., Gridneva, L., Sommarin, B., and Svensson, C. (2006). XAFS experiments at beamline I811, MAX-lab synchrotron source, Sweden. *J. Synchrotron Rad.*, 13(5): 359–364.

Cerenius, Y., Ståhl, K., Svensson, L. A., Ursby, T., Oskarsson, Å., Albertsson, J., and Liljas, A. (2000). The crystallography beamline I711 at MAX II. *J. Synchrotron Rad.*, 7(4): 203–208.

Cervellino, A., Giannini, C., and Guagliardi, A. (2003). Determination of nanoparticle structure type, size and strain distribution from X-ray data for monatomic f.c.c.-derived non-crystallographic nanoclusters. *J. Appl. Cryst.*, 36(5): 1148–1158.

Cervellino, A., Giannini, C., and Guagliardi, A. (2004). Quantitative analysis of gold nanoparticles from synchrotron data by means of least-squares techniques. *Eur. Phys. J.*, 41(4): 485–493.

Cervellino, A., Giannini, C., and Guagliardi, A. (2006). On the efficient evaluation of Fourier patterns for nanoparticles and clusters. *J. Comput. Chem.*, 27(9): 995–1008.

Chen, X., Yamanaka, S., Sako, K., Inoue, Y., and Yasukawa, M. (2002). First single-crystal X-ray structural refinement of the rhombohedral C_{60} polymer. *Chem. Phys. Lett.*, 356(3–4): 291–297.

Cheng, L., Böttger, A., de Keijser, T. T., and Mittemeijer, E. J. (1990). Lattice parameters of iron-carbon and iron-nitrogen martensites and austenites. *Scripta Metall. Mater.*, 24: 509–514.

Chow, P. C., Jiang, X., Reiter, G., Wochner, P., Moss, S. C., Axe, J. D., Hanson, J. C., McMullan, R. K., Meng, R. L., and Chu, C. W. (1992). Synchrotron X-ray study of orientational order in single crystal C_{60} at room temperature. *Phys. Rev. Lett.*, 69(20): 2943–2946.

Christiansen, T. and Somers, M. A. J. (2004). On the crystallographic structure of the S-phase. *Scripta Materialia*, 50(1): 35–37.

Christiansen, T. and Somers, M. A. J. (2006). Controlled dissolution of colossal quantities of nitrogen in stainless steel. *Metall. Mater. Trans. A*, 37A: 675–682.

Cumings, J. and Zettl, A. (2000). Low-friction nanoscale linear bearing realized from multiwall carbon nanotubes. *Science*, 289(5479): 602–604.

Cunningham, D. A. H., Vogel, W., Torres Sanchez, R. M., Tanaka, K., and Haruta, M. (1999). Structural analysis of Au/TiO_2 catalysts by Debye function analysis. *J. Catal.*, 183(1): 24–31.

De Souza, I. J., Bouchard, J., Methot, M., Berry, R., and Argyropoulos, D. S. (2002). Carbohydrates in oxygen delignification. Part I: Changes in cellulose crystallinity. *J. Pulp Paper Sci.*, 28(5): 167–170.

Debye, P. (1915). Zerstruung von Röntgenstrahlen. *Ann. Phys.*, 46: 809–823.

Dollase, W. A. (1986). Correction of intensities for preferred orientation in powder diffractometry: Application of the March model. *J. Appl. Cryst.*, 19(4): 267–272.

Dore, J., Burian, A., and Tomita, S. (2000). Structural studies of carbon nanotubes and related materials by neutron and X-ray diffraction. *Acta Physica Polonica A*, 98(5): 495–504.

Dowty, E. (2000). Atoms version 5.1 for windows.

Driver, J., Handley, J. R., and Jack, K. H. (1972). Substitutional-interstitial solute-atom interactions in nitrided austenitic steel. *Scand. J. Metall.*, 1(5): 211–216.

Fewell, M. P. and Priest, J. M. (2007). High-order diffractometry of expanded austenite using synchrotron radiation. *Surf. Coat. Technol.*

Finger, L. W., Cox, D. E., and Jephcoat, A. P. (1994). A correction for powder diffraction peak asymmetry due to axial divergence. *J. Appl. Cryst.*, 27(6): 892–900.

Fink, H. P. and Walenta, E. (1994). Röntgenbeungungsuntersuchungen zur übermolekularen Struktur von Cellulose im Verarbeitungsproceß. *Papier*, 48(12): 739–748.

Finkenstadt, V. L. and Millane, R. P. (1998). Crystal structure of Valonia cellulose Iβ. *Macromolecules*, 31(22): 7776–7783.

Germer, L. H. and White, A. H. (1941). Electron diffraction studies of thin films. *Phys. Rev.*, 60(6): 447–455.

Giacovazzo, C., editor (1992). *Fundamentals of crystallography.* International Union of Crystallography, Oxford University Press.

Gnutzmann, V. and Vogel, W. (1990). Structure sensitivity of the standard Pt/SiO_2 catalyst EuroPt-1 to H_2 and O_2 exposure by in situ X-ray diffraction. *J. Phys. Chem.*, 94(12): 4991–4997.

Grover, R. F. and McKenzie, D. R. (2001). An effecient *ab initio* calculation of powder diffraction intensity using Debye's equation. *Acta Cryst. A*, 57(6): 739–740.

Grujicic, M. and Owen, W. S. (1995). Models of short-range order in a face-centered cubic Fe-Ni-Cr alloy with a high concentration of nitrogen. *Acta Metall. Mater.*, 43(11): 4201–4211.

Guinier, A. (1963). *X-ray diffraction*. W.H. Freeman and Company.

Häglund, J., Fernández Guillermet, A., Grimvall, G., and Körling, M. (1993). Theory of bonding in transition-metal carbides and nitrides. *Phys. Rev. B*, 48(16): 11685–11691.

Hall, B. D. (2000). Debye function analysis of structure in diffraction from nanometer-sized particles. *J. Appl. Phys.*, 87(4): 1666–1675.

Hall, B. D., Flüeli, M., Monot, R., and Borel, J.-P. (1989). Electron diffraction on unsupported ultrafine silver particles. *Z. Phys. D – Atoms, Molecules and Clusters*, 12(1–4): 97–101.

Hall, B. D., Flüeli, M., Monot, R., and Borel, J.-P. (1991). Multiply twinned structures in unsupported ultrafine silver particles observed by electron diffraction. *Phys. Rev. B*, 43(5): 3906–3917.

Hall, B. D. and Monot, R. (1991). Calculating the Debye-Scherrer diffraction pattern for large clusters. *Computers in Physics*, 5: 414–417.

Hartmann, N., Imbihl, R., and Vogel, W. (1994). Experimental evidence for an oxidation/reduction mechanism in rate oscillations of catalytic CO oxidation of Pt/SiO_2. *Catalysis Letters*, 28(2–4): 373–381.

Hawelek, L., Koloczek, J., Burian, A., Dore, J. C., Honkimaki, V., and Kyotani, T. (2005). Application of image plate for structural studies of carbon nanotubes by high-energy X-ray diffraction. *J. Alloys and Compounds*, 401(1–2).

Hill, R. J. and Howard, C. J. (1985). Peak shape variation in fixed-wavelength neutron powder diffraction and its effect on structural parameters obtained by Rietveld analysis. *J. Appl. Cryst.*, 18(3): 173–180.

Hill, R. J. and Howard, C. J. (1986). ANSTO Report M122. Technical report, Lucas Heights Research Laboratories, Australia.

Iijima, S. (1991). Helical microtubules of graphitic carbon. *Nature*, 354(6348): 56–58.

Jack, K. H. (1975). Nitriding. *Heat Treat. '73 Conf. Proc.*, pages 39–50.

Jalilehvand, F. (2000). *Structure of Hydrated Ions and Cyanide Complexes by X-ray Absorption Spectroscopy.* PhD thesis, Royal Institute of Technology, Stockholm.

Jones, D. M., Stephenson, A., Hendry, A., and Jack, K. H. (1979). Strengthening by mixed cluster formation in nitrided low-alloy steels. *Strength of Metals and Alloys*, 5: 737–742.

Kaar, W. E., Cool, L. G., Merriman, M. M., and Brink, D. L. (1991). The complete analysis of wood polysaccharides using hplc. *J. Wood Chem. Technol.*, 11(4): 447–463.

Kasper, J. S. and Lonsdale, K., editors (1959). *International Tables for X-ray Crystallography*, volume II. The Kynoch Press.

Kizler, P., Frommeyer, G., and Rosenkrantz, R. (1994). Localization of nitrogen atoms in nitrogen alloyed austenitic and ferritic stainless steels by EXAFS studies. *Z. Metallkd.*, 85(10): 705–708.

Klug, H. P. and Alexander, L. E. (1974). *X-ray diffraction procedures.* John Wiley and Sons, 2. edition.

Kociak, M., Hirahara, K., Suenaga, K., and Iijima, S. (2003). How accurate can the determination of chiral indices of carbon nanotubes be? *Eur. Phys. J. B*, 32(4): 457–469.

Koloczek, J. and Burian, A. (2004). Computation of powder diffraction patterns for carbon nanotubes. *J. Alloys and Compounds*, 382(1–2): 123–127.

Koloczek, J., Burian, A., Dore, J. C., and Hannon, A. C. (2004). Model-based computation of powder diffraction patterns for carbon nanotubes. *Diamond and Related Materials*, 13(4–8): 1218–1221.

Koloczek, J., Hawelek, L., Burian, A., Dore, J. C., Honkimaki, V., and Kyotani, T. (2005). Modelling studies of carbon nanotubes - Comparison of simulations and X-ray diffraction data. *J. Alloys and Compounds*, 401(1–2): 46–50.

Koloczek, J., Kwon, Y. K., and Burian, A. (2001). Characterization of spatial correlations in carbon nanotubes-modelling studies. *J. Alloys and Compounds*, 328(1–2): 222–225.

Koningsberger, D. C. and Prins, R., editors (1988). *X-ray absorption.* John Wiley and Sons.

Koyama, M., Helbert, W., Imai, T., Sugiyama, J., and Henrissat, B. (1997). Parallel-up structure evidences the molecular directionality during biosynthesis of bacterial cellulose. *Proc. Natl. Acad. Sci. USA*, 94(17): 9091–9095.

Kring, A. (2006). Computer simulations of X-ray diffraction from gold nanoparticles. Master's thesis, University of Copenhagen.

Kumpf, C. (2006). Structure determination of very small (1–5nm) nano-particles. *Appl. Phys. A*, 85(4): 337–343.

Kumpf, C., Neder, R. B., Niederaenk, F., Luczak, P., Stahl, A., Scheuermann, M., Joshi, S., Barglik-Chory, C., Heske, C., and Umbach, E. (2005). Structure determination of CdS and ZnS nanoparticles: Direct modelling of synchrotron-radiation diffraction data. *J. Chem. Phys.*, 123(22): 224707.

Lambin, P., Loiseau, A., Culot, C., and Biro, L. P. (2002). Structure of carbon nanotubes probed by local and global probes. *Carbon*, 40(10): 1635–1648.

Lambin, P. and Lucas, A. A. (1997). Quantitative theory of diffraction by carbon nanotubes. *Phys. Rev. B*, 56(7): 3571–3574.

Langford, J. I. (1978). A rapid method for analysing the breadths of diffraction and spectral lines using the Voigt function. *J. Appl. Cryst.*, 11(1): 10–14.

Langford, J. I. and Louër, D. (1996). Powder diffraction. *Rep. Prog. Phys.*, 59(2): 131–234.

Larisch, B., Brusky, U., and Spies, H.-J. (1999). Plasma nitriding of stainless steels at low temperatures. *Surf. Coat. Technol.*, 116–119: 205–211.

Larson, A. C. and von Dreele, R. B. (2004). *General Structure Analysis System (GSAS) manual*. Los Alamos National Laboratory Report LAUR: 86–748.

Leoni, M., Confente, T., and Scardi, P. (2006). PM2K: a flexible program implementing whole powder pattern modelling. *Z. Kristallogr.*, Supp. 23(1): 249–254.

Leoni, M., Martinez-Garcia, J., and Scardi, P. (2007). Dislocation effects in powder diffraction. *J. Appl. Cryst.*, 40(4): 719–724.

Liu, J., Fan, S., and Dai, H. (2004). Recent advances in methods of forming carbon nanotubes. *MRS Bulletin*, 29(4): 244–251.

Lonsdale, K. (1948). *Crystals and X-rays*. G. Bell and Sons Ltd.

Lucas, A. A., Bruyninckx, V., and Lambin, P. (1996). Calculating the diffraction of electrons or X-rays by carbon nanotubes. *Europhys. Lett.*, 35(5): 355–360.

Maniwa, Y., Fujiwara, R., Kira, H., Tou, H., Nishibori, E., Takata, M., Sakata, M., Fujiwara, A., Zhao, X., Iijima, S., and Ando, Y. (2001). Multiwalled carbon nanotubes grown in hydrogen atmosphere: An X-ray diffraction study. *Phys. Rev. B*, 64(7):073105.

March, A. (1932). Mathematische Theorie der Regelung nach der Korngestalt bei affiner Deformation. *Z. Kristallogr.*, 81: 285–297.

Marchev, K., Landis, M., Vallerio, R., Cooper, C. V., and Giessen, B. C. (1999). The m phase layer on ion nitrided austenitic stainless steel (III): an epitaxial relationship between the m phase and the γ parent phase and a review of structural identifications of this phase. *Surf. Coat. Technol.*, 116–119: 184–188.

Marciniak, H., Gierlotka, S., and Palosz, B. (1996). *Ab Initio* calculations of diffraction patterns of submicron powders. *Mater. Sci. Forum*, 228–231: 39–42.

Menthe, E. and Rie, K.-T. (1999). Further investigation of the structure and properties of austenitic stainless steel after plasma nitriding. *Surf. Coat. Technol.*, 116–119: 199–204.

Mohr, C., Hofmeister, H., and Claus, P. (2003). The influence of real structure of gold catalysts in the partial hydrogenation of acrolein. *J. Catal.*, 213(1): 86–94.

Muñoz-Páez, A., Peruchena, J. I. F., Espinós, J. P., Justo, A., Castañeda, F., Díaz-Moreno, S., and Bowron, D. T. (2002). Experimental evidences of new nitrogen-containing phases in nitrided steels. *Chem. Mater.*, 14: 3220–3222.

Mwaikambo, L. Y. and Ansell, M. P. (1999). The effect of chemical treatment on the properties of hemp, sisal, jute and kapok for composite reinforcement. *Angew. Makromol. Chem.*, 272: 108–116.

Nasr Eddine, P. M., Bertaut, E. F., Roubin, M., and Pâris, J. (1977). Etude cristallographique de $Cr_{1-x}V_xN$ á basse temperature. *Acta Cryst. B*, 33(10): 3010–3013.

Nishiyama, Y., Langan, P., and Chanzy, H. (2002). Crystal structure and hydrogen-bonding system in cellulose Iβ from synchrotron X-ray and neutron fiber diffraction. *J. Am. Chem. Soc.*, 124(31): 9074–9082.

Oda, K., Kondo, N., and Shibata, K. (1990). X-ray absorption fine structure analysis of institial (C, N)-substitutional (Cr) complexes in austenitic stainless steels. *ISIJ International*, 30(8): 625–631.

Oddershede, J., Nielsen, K., and Ståhl, K. (2007). Using X-ray diffraction and principal component analysis to determine structural properties for bulk samples of multiwall carbon nanotubes. *Z. Kristallogr.*, 222(3–4): 186–192.

Oddershede, J. and Ståhl, K. (2006). Bulk characterization of multiwall carbon nanotubes. *Z. Kristallogr.*, Suppl. 23: 325–330.

Palosz, B., Grzanka, E., Gierlotka, S., Stelmakh, S., Pielaszek, R., Bismayer, U., Neuefeind, J., Weber, H.-P., and Palosz, W. (2002). Diffraction studies of nanocrystals: Theory and experiments. *Acta Phys. Polonica A*, 102(1): 57–82.

Palosz, B., Grzanka, E., Gierlotka, S., Stelmakh, S., Pielaszek, R., Lojkowski, W., Bismayer, U., Neuefeind, J., Weber, H.-P., and Palosz, W. (2003). Application of X-ray powder diffraction to nano-materials – determination of the atomic structure of nanocrystals with relaxed and strained surfaces. *Phase Transitions*, 76(1–2): 171–185.

Pasqualini, E. (1997). Concentric carbon structures. *Phys. Rev. B*, 56(12): 7751–7754.

Philips Analytical X-ray Customer Support (1992). *X'PERT SYSTEM User Guide*, 2. edition.

Pielaszek, R., Gierlotka, S., Stelmakh, S., Grzanka, E., and Palosz, B. (2002). X-ray characterization of nanostructured materials. *Diffusion and Defect Data*, 208–209: 187–200.

Reetz, M. T., Winter, M., Breinbauer, R., Thurn-Albrecht, T., and Vogel, W. (2001). Size-selective electrochemical preparation of surfactant-stabilized Pd-, Ni- and Pt/Pd colloids. *Chem. Eur. J.*, 7(5): 1084–1094.

Ressler, T. (2004). Winxas version 3.10.

Reznik, D., Olk, C. H., Neumann, D. A., and Copley, J. R. D. (1995). X-ray powder diffraction from carbon nanotubes and nanoparticles. *Phys. Rev. B*, 52(1): 116–124.

Rietveld, H. M. (1967). Line profiles of neutron powder-diffraction peaks for structure refinement. *Acta Cryst.*, 22(1): 151–152.

Rietveld, H. M. (1969). A profile refinement method for nuclear and magnetic structures. *J. Appl. Cryst.*, 2(2): 65–71.

Ruland, W. (1961). X-ray determination of cellulose crystallinity and diffuse disorder scattering. *Acta Cryst.*, 14(11): 1180–1185.

Sao, K. P., Samantaray, B. K., and Bhattacherjee, S. (1994). X-ray study of crystallinity and disorder in ramie fiber. *J. Appl. Polym. Sci.*, 52: 1687–1694.

Sao, K. P., Samantaray, B. K., and Bhattacherjee, S. (1997). Analysis of lattice distortions in ramie cellulose. *J. Appl. Polym. Sci.*, 66(10): 2045–2046.

Sarko, A. and Muggli, R. (1974). Packing analysis of carbohydrates and polysaccharides. 3. *Valonia* cellulose and cellulose-II. *Macromolecules*, 7(4): 486–494.

Sas, W. H. and de Wolff, P. M. (1966). Intensity corrections for the Guinier camera. *Acta Cryst.*, 21(5): 826–827.

Scardi, P. and Leoni, M. (2002). Whole powder pattern modelling. *Acta Cryst. A*, 58(2): 190–200.

Scardi, P. and Leoni, M. (2003). *Diffraction Analysis of the Microstructure of Materials*, chapter Whole Powder Pattern Modelling: Theory and Applications, pages 51–91. Springer.

Scherrer, P. (1918). *Göttinger Nachrichten*, 2: 98.

Segal, L., Creely, J. J., Martin, A. E., and Conrad, C. M. (1959). An empirical method for estimating the degree of crystallinity of native cellulose using the X-ray diffractometer. *Textile Res. J.*, 29: 786–794.

Shankar, P., Sundararaman, D., and Ranganathan, S. (1998). Clustering and ordering of nitrogen in nuclear grade 316LN austenitic stainless steel. *J. Nucl. Mater.*, 254(1): 1–8.

Shi, H., Reimers, J. N., and Dahn, J. R. (1993). Structure-refinement program for disordered carbons. *J. Appl. Cryst.*, 26: 827–836.

Simon, I., Glasser, L., Scheraga, H. A., and Manley, R. S. (1988). Structure of cellulose. 2. Low-energy crystalline arrangements. *Macromolecules*, 21(4): 990–998.

Ståhl, K. (2000). The Huber G670 imaging-plate Guinier camera tested on beamline I711 at the MAX II synchrotron. *J. Appl. Cryst.*, 33(2): 394–396.

Stokes, A. R. and Wilson, A. J. C. (1944). The diffraction of X-rays by distorted crystal aggregates – I. *Proc. Phys. Soc. Lond.*, 56(3): 174–181.

Sugiyama, J., Vuong, R., and Chanzy, H. (1991). Electron diffraction study of the two crystalline phases occuring in native cellulose for an algal cell wall. *Macromolecules*, 24(14): 4168–4175.

Sun, Y., Li, X. Y., and Bell, T. (1999). X-ray diffraction characterisation of low temperature plasma nitrided austenitic stainless steels. *J. Mater. Sci.*, 34(19): 4793–4802.

Szczygielska, A., Jabłońska, A., Burian, A., Dore, J. C., Honkimaki, V., and Nagy, J. B. (2000). Radial distribution function analysis of carbon nanotubes. *Acta Phys. Pol. A*, 98(5): 611–617.

Teo, B. K. and Joy, D. C., editors (1981). *EXAFS Spectroscopy.* Plenum Press.

Thygesen, A., Oddershede, J., Lilholt, H., Thomsen, A. B., and Ståhl, K. (2005). On the determination of crystallinity and cellulose content in plant fibres. *Cellulose*, 12(6): 563–576.

Tiensuu, V. H., Ergun, S., and Alexander, L. E. (1964). X-ray diffraction from small crystallites. *J. Appl. Phys.*, 35(6): 1718–1720.

Ungar, T. and Borbely, A. (1996). The effect of dislocation contrast on X-ray line broadening: A new approach to line profile analysis. *Appl. Phys. Lett.*, 69(21): 3173–3175.

van der Reyden, D. (1992). Recent scientific research in paper conservation. *J. Am. Inst. Conserv.*, 31(1): 117–138.

Venables, J. A. (1962). The martensite transformation in stainless steel. *Phil. Mag.*, 7(1): 35–44.

Vogel, W. (1998). X-ray diffraction from clusters. *Cryst. Res. Technol.*, 33(7–8): 1141–1154.

Vogel, W., Bradley, J., Vollmer, O., and Abraham, I. (1998a). Transition from five-fold symmetric to twinned fcc gold particles by thermally induced growth. *J. Phys. Chem. B*, 102(52): 10853–10859.

Vogel, W., Britz, P., Bönnemann, H., Rothe, J., and Hormes, J. (1997). Structure and chemical composition of surfactant-stabilized PtRu alloy colloids. *J. Phys. Chem. B*, 101(51): 11029–11036.

Vogel, W., Cunningham, D. A. H., Tanaka, K., and Haruta, M. (1996). Structural analysis of $Au/Mg(OH)_2$ during deactivation by Debye function analysis. *Catalysis Letters*, 40(3–4): 175–181.

Vogel, W., Duff, D. G., and Baiker, A. (1995). X-ray structure of a new hydrosol of gold clusters. *Langmuir*, 11(2): 401–404.

Vogel, W., Knözinger, H., Carvill, B. T., Sachtler, W. M. H., and Zhang, Z. C. (1998b). Mass diffusion effects in large zeolite Y aggregates on Pd cluster size distribution: A combined in situ EXAFS/XRD study. *J. Phys. Chem. B*, 102(10): 1750–1758.

Vonk, C. G. (1973). Computerization of Rulands X-ray method for determination of crystallinity in polymers. *J. Appl. Cryst.*, 6(2): 148–152.

Warren, B. E. (1990). *X-ray diffraction*. Dover Publications Inc.

Warren, B. E. and Averbach, B. L. (1950). The effect of cold-work distortion in X-ray patterns. *J. Appl. Phys.*, 21: 595–599.

Warren, B. E. and Averbach, B. L. (1952). The separation of cold-work distortion and particle size broadening in X-ray patterns. *J. Appl. Phys.*, 23(4): 497–498.

Wertheim, G. K., Butler, M. A., West, K. W., and Buchanan, D. N. E. (1974). Determination of the Gaussian and Lorentzian content of experimental line shapes. *Rev. Sci. Instrum.*, 45(11): 1369–1371.

White, C. T., Robertson, D. H., and Mintmire, J. W. (1993). Helical and rotational symmetries of nanoscale graphitic tubules. *Phys. Rev. B*, 47(9): 5482–4588.

Williamson, D. L., Ozturk, O., Wei, R., and Wilbur, P. J. (1994). Metastable phase formation and enhaced diffusion in f.c.c. alloys under high dose, high flux nitrogen. *Surf. Coat. Technol.*, 65: 15–23.

Williamson, G. K. and Hall, W. H. (1953). X-ray line broadening from filed aluminium and wolfram. *Acta Metall.*, 1(1): 22–31.

Woodcock, C. and Sarko, A. (1980). Packing analysis of carbohydrates and polysaccharides. 11. Molecular and crystal structure of native ramie cellulose. *Macromolecules*, 13(5): 1183–1187.

Wyckoff, R. W. G. (1963). *Crystal Structures*, volume 1. Interscience Publishers, 2. edition.

Xu, G., Feng, Z.-C., Popovic, Z., Lin, J.-Y., and Vittal, J. J. (2001). Nanotube structure revealed by high-resolution X-ray diffraction. *Advanced Materials*, 13(4): 264–267.

Yang, D. and Frindt, R. F. (1996a). Powder X-ray diffraction of turbostratically stacked layer systems. *J. Mater. Res.*, 11(7): 1733–1738.

Yang, D. and Frindt, R. F. (1996b). Powder X-ray diffraction of two-dimensional materials. *J. Appl. Phys.*, 79(5): 2376–2385.

Yang, H., Vogel, W., Lamy, C., and Alonso-Vante, N. (2004). Structure and electrocatalytic activity of carbon-supported Pt-Ni alloy nanoparticles toward the oxygen reduction reaction. *J. Phys. Chem. B*, 108(30): 11024–11034.

Young, R. and Wiles, D. B. (1982). Profile shape functions in Rietveld refinements. *J. Appl. Cryst.*, 15(4): 430–438.

Young, R. A., editor (1993). *The Rietveld method*. International Union of Crystallography, Oxford University Press.

Zabinsky, S. I., Rehr, J. J., Aukudinov, A., Albers, R. C., and Eller, M. J. (1995). Multiple scattering calculations of X-ray absorption spectra. *Phys. Rev. B.*, 52(4): 2995–3008.

Zanchet, D., Hall, B. D., and Ugarte, D. (2000). Structure population in thiol-passivated gold nanoparticles. *J. Phys. Chem. B*, 104(47): 11013–11018.

Zhang, J., Albelda, T., Liu, Y., and Canary, J. W. (2005). Chiral nanotechnology. *Chirality*, 17: 404–420.

Zhou, O., Fleming, R. M., Murphy, D. W., Chen, C. H., Haddon, R. C., Ramirez, A. P., and Glarum, S. H. (1994). Defects in carbon nanostructures. *Science*, 263(5154): 1744–1747.